Dynamic Evolution of C-type Asteroids Inferred from Carbonaceous CM Chondrites

Cameron James Floyd

BSc (Hons), University of Glasgow
MSc (Res), University of Glasgow

Thesis submitted in fulfilment of the requirements for the degree of

Doctor of Philosophy

School of Geographical and Earth Sciences

College of Science and Engineering

University of Glasgow

January 2024

Abstract

The Mighei-like (CM) group of carbonaceous chondrites are water and carbon-rich meteorites which have been identified as the most chemically primitive chondrites available to study. Their high indigenous water and carbon content has led authors to hypothesise that these meteorites may be at least partly responsible for organic and water delivery to Earth during the early solar system. The CM chondrites are therefore the subject of significant scientific interest.

Spectroscopic analysis has identified C-type asteroids as the likely parent body(ies) for the CM chondrites. Whilst incorporated into these body(ies) the CM chondrites experienced an array of secondary alteration processes including aqueous alteration, brecciation, deformation and space weathering. This thesis seeks to examine the effects deformation, brecciation and space weathering.

For this thesis ten CM chondrites spanning a range of petrologic subtypes were studied. Using a combination of high resolution 2D (SEM and EDS) and 3D (XCT) techniques CM chondrite chondrule sizes and orientations were analysed and relationships between the different deformation and alteration mechanisms investigated.

Chondrule sizes were investigated in ten of the CM chondrites. Analysis was conducted in 2D, following a standardised measurement method developed during this project, and in 3D using established techniques. The limitations and benefits associated with 2D and 3D measurement techniques are discussed and the outcomes of several stereological correction models compared. The results presented in this thesis highlight several challenges associated with the use of stereological correction models and suggests that an adapted version of an existing correction model provides the most reliable 2D-3D correction.

The results of the chondrule size analysis reveal the CM average chondrule size is significantly smaller than previously reported and more akin to those of CO chondrites. Chondrule sizes, shapes and abundances are also observed to vary between constituent clasts in meteorite breccias. Upon petrologic classification of clasts and lithologies it is found that a negative correlation exists between

chondrule size and petrologic subtype, with chondrule sizes increasing with a greater degree of aqueous alteration. It is suggested that this relationship is a consequence of a size sorting process influencing initial chondrule accretion to the parent body followed by a aqueous alteration which varied in intensity as a function of depth.

3D chondrule orientation analysis was conducted on five CM chondrites to determine the strength and orientation of any chondrule-defined fabric. Results revealed that chondrule defined fabrics are commonplace within the CM chondrites and that 3D techniques are best suited to fabric detection and characterisation. Inter-clast and chondrite variations in chondrule fabrics are observed with instances of both consistency and variability in fabric strength and orientation between clasts.

Significant chondrule deformation was also observed in all chondrites with chondrules deviating significantly from a compact shape. Chondrule deformation even in chondrites with the weakest fabrics is interpreted as evidence for a prolate original chondrule shape during accretion. This finding reconciles the paradox between low shock stage within the CM chondrites and observable fabrics and alignment.

During this thesis 3D XCT analysis is shown to be an important and powerful tool for studying CM chondrites. XCT analysis facilitates accurate, ‘true’ values for chondrule size and orientation to be determined and its further use within the CM group is encouraged.

The potential usefulness of the WN etching technique for damage track analysis of space weathered olivine grains is reviewed. It is suggested that future use of the technique on CM chondrite thin sections could yield useful information regarding the accretionary histories of the CM parent body(ies). In particular, such work may improve our understanding of the previously observed inhomogeneous distribution of track-rich grains in the clastic matrix and our understanding of regolith turnover processes acting on the body.

Table of Contents

List of Tables

List of Figures

Acknowledgements

I firstly wish to thank my supervisors Martin Lee and Lydia Hallis for their support and encouragement throughout the last 4.5 years. Thanks especially to Martin for always providing thoughtful discussion, thorough feedback at all hours of the day, and for all your support, especially over the past 12 months. I certainly owe you a few caterpillar shaped goods. Thanks, must also go to Luke Daly whose infectious enthusiasm and inciteful discussions have been so helpful in preventing me from falling down a rabbit hole.

To Aine O'Brien and Sammy Griffin who helped guide me through the first few years of research life and introduced me to the quirks of GES. To all my other colleagues within GES thank you for putting up with my rantings and making the last 4.5 years so enjoyable – Amanda Stubbs, Faisal Khudhur, Danjuma Kwetishe, Pierre-Etienne Martin, Laura Jenkins, Yusuff Sarnoh, Kang Xie, Fakhri Bintang, Chralie Rex, Beth Langley and Heather Gibson.

To James Hodgson and Alasdair Ireland for keeping me sane over the COVID pandemic when we were confined to quarters, and for always having time for dinner or a drink. To Catriona, Alice F, John, Logan, Alice D, Sam, Laura, Remi, Stuart, Claire, Rupert, Eadie and Tom for always providing adventurous distractions either on the water, up a hill, or very occasionally on a bike. Thanks also to Dr. Jonathan Bell and George Elderfield for their support, cricket-based discussion, and whose own PhD journeys have provided significant motivation for finishing this thesis.

To my family and especially my parents, thank you for your steadfast support since I began my journey at Glasgow University as an undergraduate more than 9 years ago. Mum and dad, I am now officially finished being a student and I promise to get a job.

To my partner Maia, I thank you for always being there on the good days and the bad! Without all your support I would not have finished this PhD and I will be forever grateful for everything you have done for Team Flizzle during the last 4.5 years.

Finally, I must thank Rebecca Stables. Your love and support was a great comfort during this PhD and the lessons you taught me were invaluable during the last few years. I wish you could see me as I hit the submit button on this thesis.

Author’s Declaration

I declare that this dissertation is the result of my own work and has not been submitted for any other degree at the University of Glasgow or any other institution.

Cameron James Floyd

Definitions/Abbreviations

Acronym	Definition
2D	Two Dimensional
3D	Three Dimensional
AA	Azimuth angle
ALH	Allan Hills
ANSMET	US Antarctic Search for Meteorites
AOA	Amoeboid Olivine Aggregates
AR	Aspect Ratio
BO	Barred Olivine
BSE	Backscatter Electron
CAI	Calcium-Aluminium Inclusion
CB	Carbonaceous Bencubbin type meteorite
CH	Carbonaceous ALH85085 type meteorite
CIS	Chondrule Image Segmentation
CK	Carbonaceous Karoonda type meteorite
CL (chondrite)	Carbonaceous Loongana type meteorite
CL	Cathodoluminescence
CM	Carbonaceous Mighei type meteorite
CO	Carbonaceous Ornans type meteorite
CR	Carbonaceous Renazzo type meteorite
CT	Computed Tomography
C-ung	Carbonaceous ungrouped type meteorite
C-value	Strength parameter used to describe fabric strength
CV	Carbonaceous Vigarano type meteorite
CY	Carbonaceous Yamato type meteorite
EBSD	Electron Backscatter Diffraction
ECAS	Eight-Color Asteroid Survey
EDS	Energy Dispersive X-ray Spectroscopy
FGR	Fine-grained Rim
GCR	Galactic Cosmic Ray
GOP	Granular Olivine-Pyroxene chondrule type
GP	Granular Pyroxene chondrule type
JAXA	Japan Aerospace Exploration Agency
K-parameter	Shape parameter used to describe fabric shape
LAP	LaPaz Icefield - a collection site for ANSMET
LEW	Lewis Cliff - a collection site for ANSMET
LON	Lonewolf Nunataks - a collection site for ANSMET
MAB	Main Asteroid Belt
MASCam	A wide-angle camera associated with the MASCOT lander and the Hayabusa 2 mission
MASCOT	The Mobile Asteroid Surface Scout, a small lander associated with the Hayabusa 2 mission
NASA	National Aeornautics and Space Administration
NEA	Near Earth Asteroid
NEO	Near Earth Object
$npFe_0$	Nano-phase iron particle

ORSIRIS-REx	Origins, Spectral Interpretation, Resource Identification and Security - Regolith Explorer, the space craft associated with Bennu sample return
PAR	Primary Accretionary Rock
PCP	Poorly Characterised Phase
PO	Porphyritic Olivine chondrule type
POP	Porphyritic Olivine Pyroxene chondrule type
PP	Porphyritic Pyroxene chondrule type
QUE	Queen Alexandra Range - a collection site for ANSMET
RELAB	Reflectance Experiment Laboratory
RP	Radial Pyroxene chondrule type
SCO	Scott Glacier - A collection site for ANSMET
SCR	Solar Cosmic Ray
SE	Secondary Electron
SEM	Scanning Electron Microscopy
SEP	Solar Energetic Particle
SMASSII	Small Main-belt Asteroid Spectroscopic Survey Phase II
STEM	Scanning Transmission Electron Microscopy
SW	Solar Wind
TCI	Tochilinite Cronstedtite Intergrowth
TEM	Transmission Electron Microscopy
WN	Chemical etchant used for damage track revelation in olivine
XCT	X-ray Computed Tomography

Presentations of this Work

Journal Publications: Work conducted during this project has been included in the manuscripts listed below. Where a manuscript is not included in this thesis a brief statement of personal contribution is provided.

- Lee, M. R., et al. (2024) Impact melt in the Cold Bokkeveld CM2 carbonaceous chondrite and the response of C-complex asteroids to hypervelocity collisions (*Accepted with minor revisons)*. *Contribution*: XCT and SEM analysis of Cold Bokkeveld sample.
- Floyd, C. J. et al. (2024) CM Carbonaceous Chondrite Petrofabrics and their Implications for Understanding the Relative Chronologies of Parent Body Deformation and Aqueous Alteration, *Meteoritics and Planetary Science (Accepted with minor revisions)*
- Floyd, C. J., et al. (2023) Chondrule Sizes within the CM Carbonaceous Chondrites and Measurement Methodologies, *Meteoritics and Planetary Science (Accepted with minor revisions)*
- Daly, L. D., et al (2023) Brecciation at the grain scale within the lithologies of the Winchcombe CM carbonaceous chondrite, *Meteoritics and Planetary Science 59* (5), 1068-110. *Contribution*: XCT and SEM analysis of Winchcombe samples, including petrofabric and chondrule analysis.
- Lee, M. R., et al. (2023) Extended timescales of carbonaceous chondrite aqueous alteration evidenced by a xenolith in LaPaz Icefield 02239 (CM2), *Meteoritics and Planetary Science 58* (5), 672-687. *Contribution*: SEM analysis of LAP 02239 sample and contributions to discussion.
- King, A. J., Daly, L., et al. (2022) The Winchcombe meteorite, a unique and pristine witness from the outer solar system, *Science Advances 8* (46), eabq3925. *Contribution*: XCT analysis of all Winchcombe samples collected including petrofabric analyses.
- Lee, M.R., et al. (2021) CM carbonaceous chondrite falls and their terrestrial alteration, *Meteoritics and Planetary Science 56* (1), 34-48. *Contribution*: SEM and Raman spectroscopy analysis of a suite of CM chondrites.

- Suttle, M. D., et al. (2023) The Winchcombe meteorite – A regolith breccia from a rubble pile CM chondrite asteroid, *Meteoritics and Planetary Science 59* (5), 1043-2067. *Contribution*: XCT and SEM analyses of Winchcombe samples.
- Jenkins, L.E., et al. (2023) Winchcombe: An example of rapid terrestrial alteration of a CM chondrite, *Meteoritics and Planetary Science 59* (5), 988-1005. *Contribution*: SEM and Raman spectroscopy analysis of Winchcombe samples alongside discussion contributions.
- O'Brien, A. C., et al. (2022) The Winchcombe Meteorite: one year on, *Astronomy and Geophysics 63* (1), 1.21-1.23. *Contribution*: Discussion relating to the then ongoing research into the Winchcombe meteorite as an ECR.

Conference Abstracts: Work conducted during this project has been included in the following conference abstracts:

- Floyd, C. J., et al. (2023) CM Chondrite Chondrules and their Relationship to Petrologic Subtype, *86th Annual Meeting of the Meteoritical Society*, abstract# 6096
- Floyd, C. J., et al. (2023) Unravelling Petrofabrics in Brecciated CM Chondrite Cold Bokkeveld, *54th Lunar and Planetary Science Conference*, abstract# 1477
- Floyd, C. J. & Lee, M. R. (2022) A New Record of Chondrule Sizes within the Carbonaceous CM chondrites and Implications for Understanding the CM-CO Clan, *85th Annual Meeting of the Meteoritical Society,* abstract# 6088
- Floyd, C. J. & Lee, M. R. (2022) The CIS Method: A Proposed Standardised Protocol for Measuring and Reporting Sizes of Chondrules and other Chondritic Objects, *85th Annual Meeting of the Meteoritical Society,* abstract# 6087
- Floyd, C. J., et al. (2022) Brecciation on the Aguas Zarcas Parent Body Revealed Using Clast Petrofabrics, *53rd Lunar and Planetary Science Conference*, abstract# 1470

- Floyd, C. J., & Lee, M. R. (2021) Chondrule Size Variation within CM Chondrite Lithologies, *84th Annual Meeting of the Meteoritical Society*, abstract# 6091
- Lee, M. R., et al. (2021) A Xenolith from an early formed parent body in the CM carbonaceous chondrite LaPaz Icefield 02239, *84th Annual Meeting of the Meteoritical Society*, abstract# 6176
- Floyd, C. J., Lee, M. R. (2021) Size Analysis of Chondrules and their Rims in CM Carbonaceous Chondrites, *52nd Lunar and Planetary Science Conference*, abstract# 1337

Chapter 1 Introduction

1.1 Asteroids

Asteroids are bodies of rock and/or metal that are remnants of the early solar system having not been accreted into the terrestrial planets during their formation at ~4.6 Gyr (Bottke et al. 2021; Carry 2012; Gaffey 2011). Generally considered to have diameters <1000 km, asteroids have an array of different compositions reflecting their formation conditions and evolution; for example, those asteroids that have experienced differentiation and those that have not (Asphaug, 2009; Gaffey, 2011). Owing to their generally small size and therefore limited amounts of radiogenic nuclei originally within their interiors, most asteroids are not differentiated and have instead evolved through predominantly external forces such as collision, high energy particle bombardment and external heating (Carry 2012).

Whilst there has been a significant amount of observational science conducted on asteroids, much of what we know of their composition and mineralogy is from the study of meteorites, with the link between asteroids and meteorites long-established using spectral analysis (Chapman 1996; Chapman and Salisbury 1973; DeMeo et al. 2022; Pieters and McFadden 1994). Whilst this spectroscopy has been able to link asteroid types with meteorite classes, determining exact meteorite parent bodies within the asteroid population remains a significant challenge.

Sample return missions such as the concluded Japan Aerospace Exploration Agency's (JAXA) missions Hayabusa 1 and Hayabusa 2; alongside the recently completed National Aeronautics and Space Administration's (NASA) ORSIRIS-REx mission (Figure 1.1) hope to deepen our understanding of asteroid/meteorite relationships by ground truthing spectral observations with sample analysis. However, whilst sample return missions afford an opportunity to correlate observational spectral data with geological material, only three asteroids have been sampled and the total returned sample load remains small with <1g returned by Hayabusa1, 5.4g returned by Hayabusa2 and a goal of at least 60g to be returned by the ORSIRIS-Rex mission (Lauretta et al. 2017; Tsuda et al. 2022; Yoshikawa et al. 2021). Compared to the 71,688 meteoritic samples which have been collected and catalogued by the Meteoritic Bulletin, these sample return missions whilst important represent a fraction of the extra-terrestrial material available for laboratory study. This thesis therefore sets out to investigate some of the processes involved in asteroid formation and evolution by examining the meteoritic record. Given the recent return of material by the NASA ORSIRIS-REx mission this thesis will focus on C-complex asteroids and meteoritic material believed to be comparable.

To fully understand the context of this research it is first useful to introduce asteroids, their locations within the solar system, taxonomy and how they have been linked to meteorites.

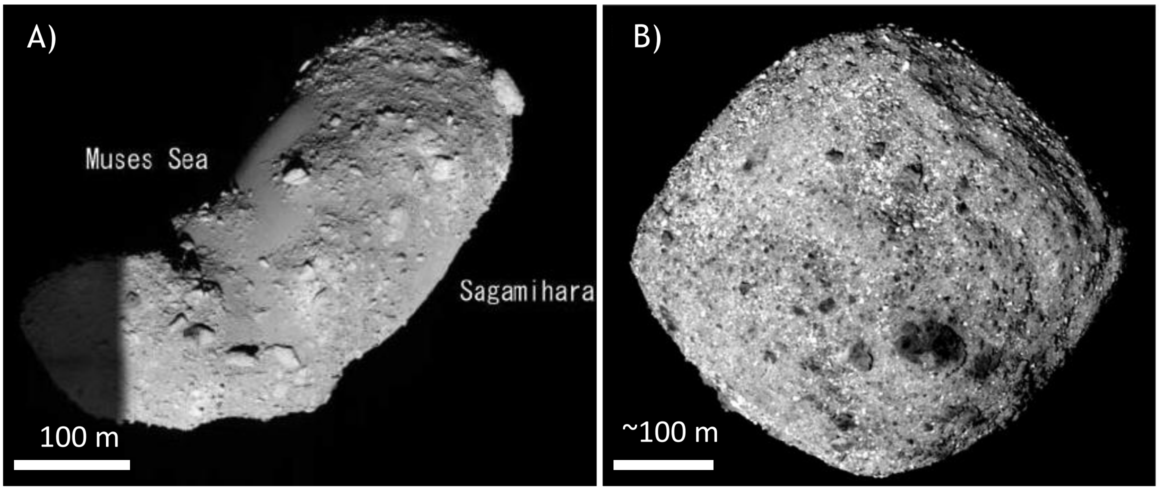

Figure 1.1*. Spacecraft collected images of A) Asteroid Itokawa, the subject of the Hayabusa mission which returned the first asteroid samples to Earth in 2010. Image source* Fujiwara et al., (2006). *B) Asteroid Bennu, subject of the NASA ORSIRIS-REx mission which returned material to Earth in September 2023. Image source* Lauretta et al. 2019).

1.1.1 Asteroid Locations

Asteroids can be classified in the first instance as belonging to one of three populations within the solar system: Near Earth Objects (NEOs), the Main Asteroid Belt (MAB), and the Trojan group. These different regions and their positions within the solar system are illustrated in Figure 1.2. Asteroids classified as belonging to either the NEOs or MAB are the focus of this research and so they are described in more detail in the following sections.

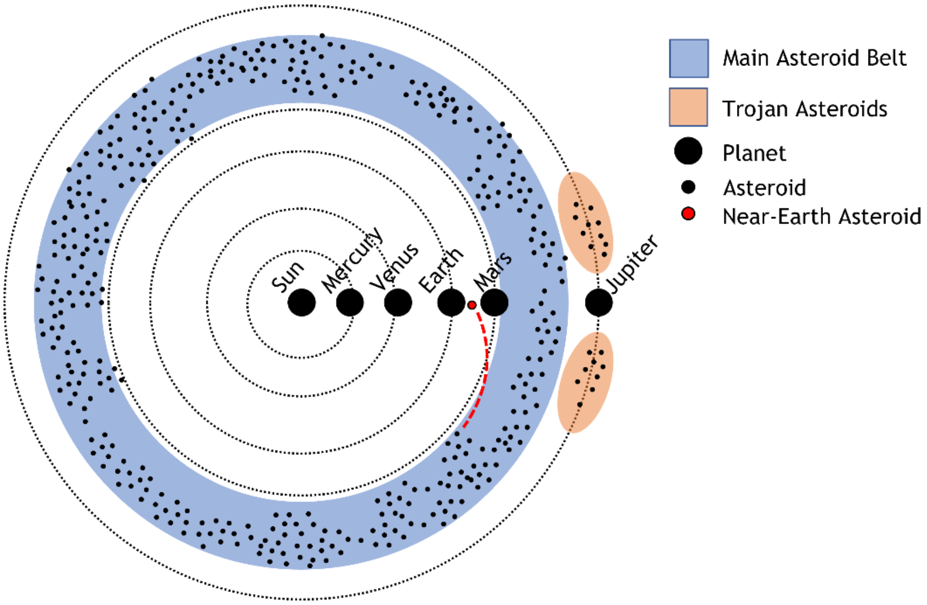

Figure 1.2. *Schematic illustration of the approximate locations of the two major asteroid belts within the solar system. The dashed red line illustrates a MAB asteroid which has transitioned into a Near-Earth asteroid following either collision or 'leaking'*

1.1.1.1 Near Earth Objects (NEOs)

NEOs include asteroids and comets that have an aphelion distance (Q) ≥0.983 and a perihelion distance (*q*) ≤1.3 AU (Morbidelli and Michel 2014). Asteroids classified as NEOs are referred to as Near Earth Asteroids (NEAs) and being closest to Earth pose the greatest threat of Earth impact (Harris and D'Abramo, 2015). There are only ~1000 NEAs larger than 1km with many believed to have originated from the MAB, having either been 'bumped' into a close Earth orbit as a result of collisions or, leaked from the MAB on timescales of tens of millions of years (Morbidelli 1999; Morbidelli and Michel 2014). Two NEAs are the focus of significant scientific interest at the time of writing are Asteroid 162173 (Ryugu) and Asteroid 101955 (Bennu), which are the subjects of the recently returned Hayabusa2 and ORSIRIS-REx missions, respectively (Lauretta et al. 2017; Watanabe et al. 2017).

1.1.1.2 Main Asteroid Belt (MAB)

The MAB contains the majority of all known asteroids. An estimated 1.2 ± 0.5 x 10^6 asteroids with a diameter larger than 1km have so far been identified representing an estimated total mass of ~4 % that of the Moon (Asphaug 2009; Raymond et al. 2014; Tedesco and Desert 2002). The MAB is located between the orbits of Mars and Jupiter, specifically between 1.78 AU and 3.28 AU, which correspond to the v6 secular resonance and the 2:1 mean-motion resonances of Jupiter, respectively (Malhotra 2012; Roig et al. 2002). The MAB is also compositionally stratified with its inner regions dominated by water-poor, S-type asteroids and its outer regions dominated by water-rich, C-type asteroids (Chapman et al. 1975; DeMeo et al. 2015; Walsh et al. 2012). An overview of asteroid classification follows in section 1.1.2.

The stratification of the MAB is thought to be a consequence of giant planet migration (especially Jupiter) during the early solar system. The Grand Tack model (illustrated in Figure 1.3) describes the events which likely took place during such a period to produce a stratified MAB (Walsh et al. 2011, 2012). The grand Tack model advocates for two initially seperate asteroid populations during the gas-rich phase of the solar nebula; one likely composed of volatile-poor material, inside the orbit of the giant planets (~0.7-3.0 AU), and one between and beyond the orbits of the giant planets within which material was more primitive and water-rich (Walsh et al. 2011, 2012). These two populations were initially disrupted by the inward migration of Jupiter and Saturn scattering ~15% of inner solar system ('S-type') asteroids into more distant orbits. The 'Tack' occurred when Jupiter and Saturn's migration reversed and they moved into more distant orbits. During this "Tack" the giant planets, first encountered the recently scattered 'S-type' material and following this the more distant and, as yet undisrupted, 'C-type' material. Both these populations were scattered inwards into stable orbits, in what is by the time of the gas-disk dissipated, the MAB (Walsh et al. 2011, 2012).

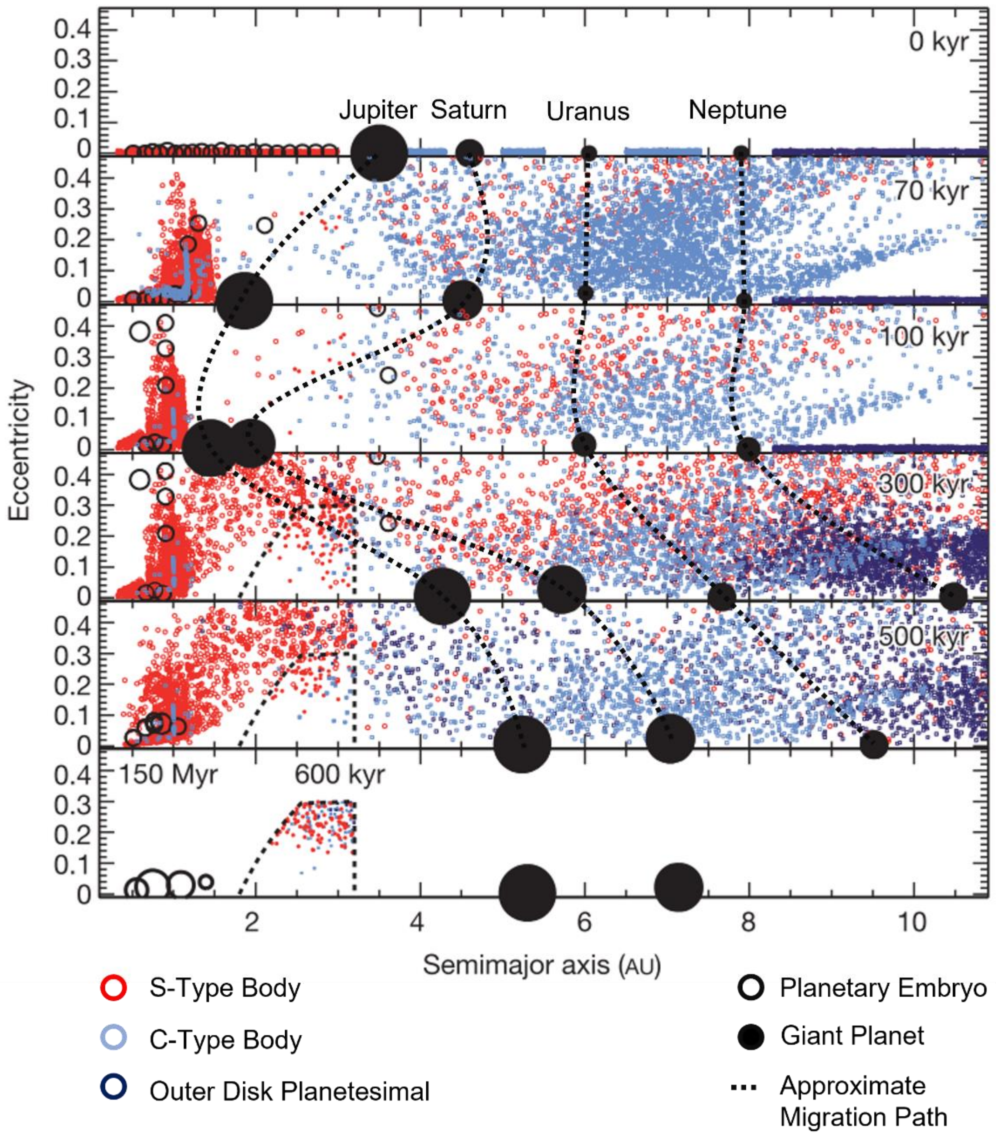

Figure 1.3. *Diagram illustrating the Grand Tack model for the migration of the giant planets and the effect this migration had on the originally separate populations of small bodies to form the stratified MAB. The model runs for 150 Myr from the point of giant planet migration beginning. It illustrates the S-type bodies being scattered outwards and the C-type bodies being scattered inwards. Image adapted from Walsh et al. (2011).*

1.1.2 Asteroid Classification

Alongside categorisation by their orbits and heliocentric distances, taxonomic classification schemes have also been developed for asteroids. These schemes use spectral data collected from Earth-based observatories. Taxonomic classification of asteroids has seen numerous changes over the past five decades. As each new iteration builds on the last, it is pertinent to briefly outline the taxonomic schemes and their evolution.

Chapman: Chapman et al. (1975) used Ultraviolet, Blue, Visual (UBV) photometry to explore the range of colours for a large sample of asteroids. Their studies revealed two distinct groups; dark 'carbonaceous' (C) – Type asteroids and brighter 'stony' (S) – Type asteroids. An additional group of 'unclassified' (U) – Type asteroids which did not fit into either S or C classification were also identified (Chapman et al. 1975). The simplicity of the Chapman et al., (1975) scheme has resulted in S- and C-type classifications being the basis on which many models of asteroid formation and migration (such as the Grand Tack) have been developed.

Tholen: One of the most widely used schemes, the Tholen taxonomy, was developed using data collected during the Eight-Color Asteroid Survey (ECAS) and identifies 14 asteroid classes (Tholen 1984; Zellner et al. 1985). In addition to the two previously identified spectral classes (S- and C-type) a further six spectrally distinct asteroid types were identified during this survey: A, B, D, F, G and T. Three additional, spectrally featureless types: E, M and P are identified based on albedo measurements. Where albedo data is not available to distinguish between the E-, M- and P-types they are grouped into the classification of X-class. Three final classes: Q, R and V were assigned to spectrally unusual objects which did not conform to previous classes (Bus and Binzel, 2002). A relationship between heliocentric distance and predominant compositional type (S - C – D) was also observed as a result of the ECAS (Zellner et al. 1985).

Bus: The Bus taxonomic scheme was developed in 2002 and was based on data from the second phase of the Small Main-Belt Asteroid Spectroscopic Survey (SMASSII) (Bus and Binzel, 2002a, 2002b). Bus and Binzel, (2002a) define three major groupings of spectrally similar asteroids. These groups, termed complexes: S, C and X, are consistent with the previous spectral definitions of S-, C- and X-type asteroids in addition to demonstrating similar heliocentric distributions as identified in other studies (Zellner et al. 1985). Within these 'complexes' a total of 26 asteroid classes are identified, with 12 (A, B, C, D, K, O, Q, R, S, T, V and X) carried over from the Tholen scheme and maintaining their single letter designations. A new class L is introduced and those asteroids with intermediate characteristics assigned multilettered designations based on which complex they most align with: Cb, Cg, Cgh, Ch, Ld, Sa, Sk, Sl, Sq, Sr, Xc, Xe and Xk (Bus and Binzel, 2002, 2002).

Bus-DeMeo: The Bus-DeMeo taxonomy was developed as a refinement of the Bus taxonomy, after improvements in telescopic instruments allowed for spectral measurements extending into the near-infrared to be collected and analysed (DeMeo et al. 2009). This taxonomy was composed originally of 24 classes which were identical to the Bus taxonomy except for: Sl, Sk and Ld classes which are eliminated and the class Sv which was added. The notation "w" was assigned to indicate objects which have similar spectral features but differing in having a higher spectral slope (DeMeo et al. 2009). After publication of the Bus-DeMeo scheme (DeMeo et al. 2009) an Xn classification was also added (Hasegawa et al. 2017). Typical spectra for each class of asteroid in the Bus-DeMeo scheme can be seen in Figure 1.4, which illustrates the significant differences between each asteroid complex and the subtle differences between each class. The Bus-DeMeo scheme shall be used when reference to asteroid classification is made during this work.

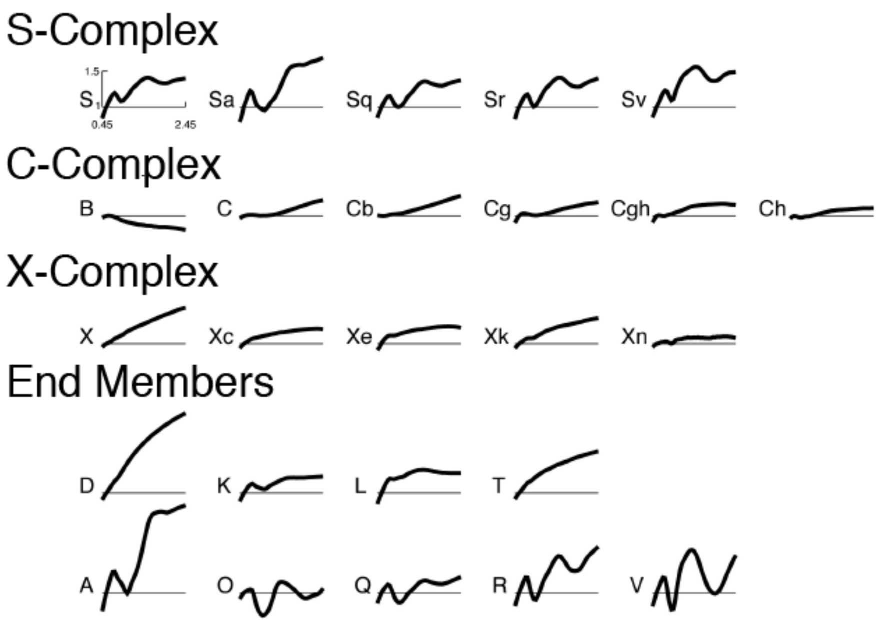

***Figure 1.4**. An overview of the Bus-DeMeo taxonomy for asteroid classification. Plotted are the average spectra for each asteroid class, separated into the major asteroid complexes. Spectra are plotted with constant horizontal and vertical scaling with the x-axis representing wavelength (μm) and the y-axis reflectance. Figure taken from DeMeo et al. (2009).*

1.2 Asteroids to Meteorites: The Link

In addition to being used for taxonomic classification, spectral characterisation of asteroids has been compared with meteoritic spectra allowing relationships between the different asteroid and meteorite classes to be suggested (Burbine 2000; Chapman 1976; Chapman and Salisbury 1973; DeMeo et al. 2022). The S-complex asteroids have spectral similarities with ordinary chondrites and the C-complex asteroids with carbonaceous chondrites (Burbine 2000; Chapman 1996). An example of the similarities observed between the C-complex asteroids and the carbonaceous chondrites is shown in Figure 1.5, created using the M4ast asteroid spectra database (Birlan et al. 2016) and the NASA RELAB meteorite database.

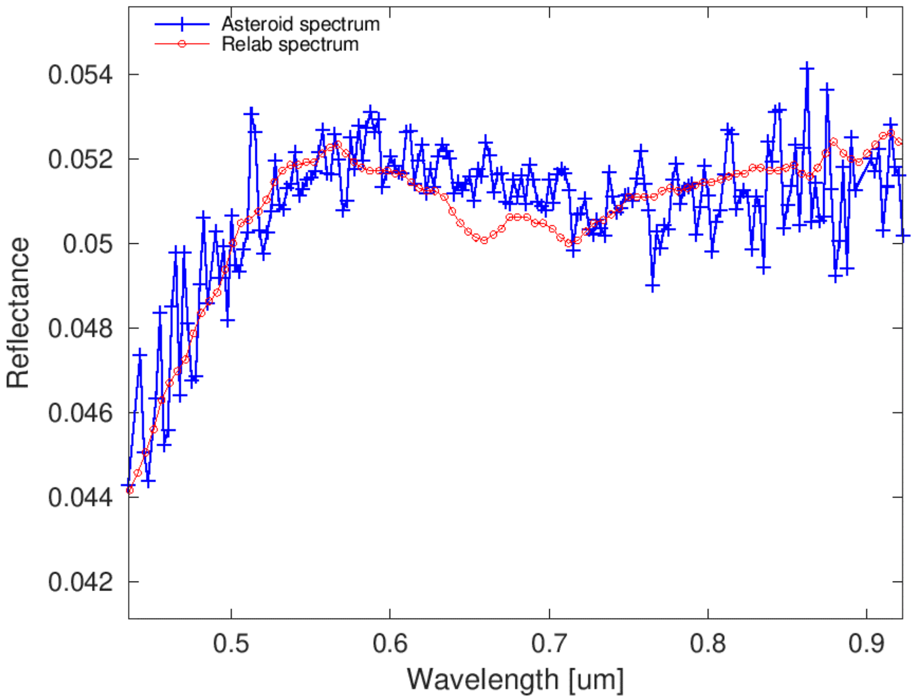

Figure 1.5. *Spectral comparison produced by the M4ast database illustrating similarities in the spectral properties of a C-complex asteroid and carbonaceous chondrite. Asteroid spectrum is that of a Cgh complex asteroid; spectrum ID: 6509, 1983 CQ3, collected by SMASS II* (Birlan et al. 2016). *NASA RELAB spectrum is of carbonaceous CM chondrite Murchison; spectrum ID: CGP 096 of sample MR-MJG-190 Murchison. To facilitate comparison the asteroid spectrum is normalised to its median value and then multiplied by the median value of the Relab spectrum.*

While it is possible to find similarities between the spectra of asteroids and meteorites, drawing conclusive links between individual meteoritic groups and asteroids is very challenging. The exception to this is the Howardite-Eucrite-Diogenite (HED) assemblage which is composed of achondrites from a differentiated source. The HED meteorites are characterised by spectra with a particularly strong affinity to 4 Vesta (Buratti et al. 2013; Mccord et al. 1970).

In some instances, observations and measurement made of meteorite falls can allow their orbits to be reconstructed allowing an origin within the MAB to be determined. Such orbital reconstructions have been applied to five carbonaceous chondrites: Tagish Lake (C2-ung), Suters Mill (CM2), Maribo (CM2), Flensburg (C1-ung), and Winchcombe (CM2 chondrite) (Borovička et al. 2019, 2021; Brown et al. 2000; Jenniskens et al. 2012; King et al. 2022). Orbital reconstructions such as these provide evidence to support the spectral observations and links between the different meteorite and asteroid classifications.

The only method for total certainty regarding a meteorite-asteroid link is direct sample return. In these cases, the returned sample's spectra can be compared to spectra collected from their parent body helping to ground-truth the links. Asteroid 25143 Itokawa was spectrally identified as an S-type asteroid (Fujiwara et al. 2006) and following sample return by the JAXA Hayabusa 1 mission, material was found to be LL5 ordinary chondrite-like (Nakamura et al. 2011).

Difficulty in linking meteorites and asteroids spectra arises from three primary factors: 1) Averaging of asteroid spectral measurements over very large areas, often on the km scale, results in macro-scale heterogeneities on the asteroid surface being included. Comparatively, meteoritic samples are analysed on significantly smaller scales, typically on the cm scale and heterogeneities are less prevalent (DeMeo et al. 2022). 2) Spectral analysis is not only dependant on composition; factors such as grain size, phase angle of observation and temperature can all produce variations in results (Reddy et al. 2015). 3) Space weathering of asteroid surfaces via impact and/or irradiation (Brunetto et al. 2015; Noguchi et al. 2011). Space weathering is described in more detail in section 1.3.5.

Whilst only material collected during sample return missions can be conclusively linked to a parent asteroid, improvements in spectral analysis and our understanding of the processes which effect their outputs, give more confidence than ever in the links between the different asteroid and meteorite populations. Meteorites do therefore remain an invaluable resource for the study of asteroid formation and evolution across the different spectral complexes.

1.3 Meteorites

Meteorites are extra-terrestrial solids which survive passage through Earth's atmosphere to reach the surface following ejection from their parent body and perturbation on to Earth intersecting orbits. It is thought impacts are likely responsible for ejection from their parent bodies. As introduced above, most meteorites are thought to derive from asteroid parent bodies and consequently meteorites have a wide range of compositional forms, reflecting the compositional diversity found in asteroids. Whilst the majority of meteorites are thought to have asteroidal origins, meteorites of Martian and Lunar origin also exist.

1.3.1 Meteorite Classification

Meteorites have an array of textures and mineralogies alongside a variety of chemical and isotopic compositions resulting in an expansive hierarchal taxonomic scheme to classify them into discrete populations (illustrated in Figure 1.6). Meteorites can be initially divided into one of three categories, achondrites, primitive achondrites and chondrites.

The achondrites are differentiated meteorites composed of melts, partial melts and melt residues, in some cases they can also take the form of a breccia, composed of the aforementioned components. The melting experienced by the achondrites classifies them as igneous rocks which likely formed as part of differentiated asteroids or planetary bodies (e.g. Moon, Mars) (Weisberg et al. 2006).

Primitive achondrites fit between the chondrites and achondrites; typically containing an igneous texture with evidence of melting and/or recrystallisation these meteorites share a primitive chemical signature similar with the chondrites (Weisberg et al. 2006).

Chondrites represent the largest group of meteorites which have been classified. As undifferentiated meteorites they have not been subjected to widespread melting and are composed of a sedimentary-like mixture of coarse- and fine-grained components which have become consolidated over time. Chondrites take their name from their principal components, chondrules, discussed in detail in section 1.3.2. Chondrules are present in abundances of 0-80 vol% between the chondritic groups; thus despite taking their name from the presence of chondrules, not all chondrites contain chondrules. A more accurate definition of chondritic meteorites would therefore be those meteorites with a solar-like compositions (Weisberg et al. 2006).

This research focuses on the carbonaceous chondritic meteorites which are noted for their affinity to the C-complex asteroids and so only they will be discussed further.

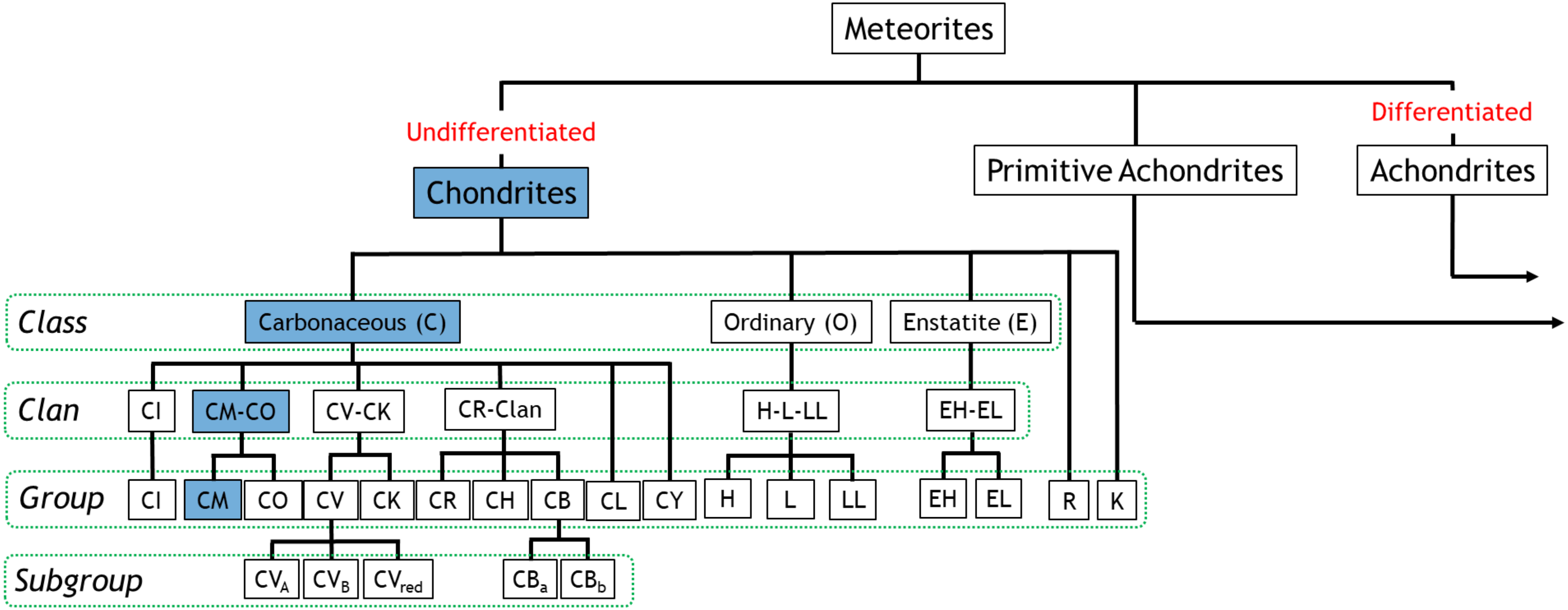

Figure 1.6. *Schematic illustration of the meteorite classification scheme focused on the undifferentiated, chondritic meteorites. The blue regions highlight the CM chondrite group, which is the focus of this thesis, and where it sits within the wider classification. The green dashed lines indicate hierarchal classification groups. Figure adapted from* (Weisberg et al. 2006).

1.3.2 Chondrules

Before introducing the carbonaceous chondritic class, it helpful to first understand and explore their principal components, chondrules; their types, textures and numerous suggested formation mechanisms.

Chondrules are roughly spherical particles, composed of the Mg-Fe silicates: Olivine [$(Mg,Fe)_2SiO_4$], low-Ca pyroxene [$(Mg,Fe)SiO_3$] and high-Ca pyroxene [$Ca(Mg,Fe)Si_2O_6$] (Hewins 1997; Zanda 2004). Minor amounts of glass, Fe,Ni metal and troilite can also be found in chondrules depending to the degree of post-accretion alteration (Hewins 1997). Representing the dominant components of the chondritic meteorites comprising 20-80 vol.%, chondrules were likely the most abundant objects within the early solar system and provided the building blocks for asteroids and the terrestrial planets (Connolly and Jones 2016; Jones et al. 2000; Weisberg et al. 2006).

Despite their abundance within the meteorite record no chondrules have yet been identified within any of the returned samples (Nakamura et al. 2011; Yada et al. 2022; Yokoyama et al. 2023). Despite this result, some authors have suggested potential evidence for chondrules. In a study of 38 Itokawa particles Nakamura et al., (2011) found six poorly equilibrated particles containing olivine and low-Ca pyroxene; three of these particles contain mesostasis composed of small diopside and troilite crystals embedded in albitic glass. Nakamura et al. (2011) concluded that the texture and composition of this mesostasis is akin to that found in chondrules and thus the three particles containing mesostasis are pieces of chondrules (Figure 1.7). Jaumann et al. (2019) reported what they believed to be chondrules on asteroid Ryugu's surface using the Hayabusa 2, MASCOT lander's MASCam (Figure 1.8). However, given the rubble-pile nature of Ryugu and classification as CI-like it is unlikely that the features they identified are chondrules.

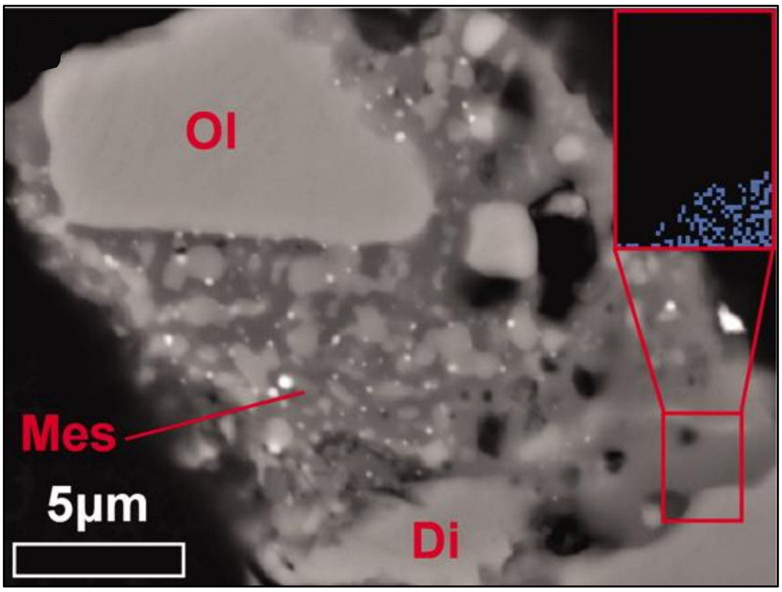

Figure 1.7. *BSE image of poorly equilibrated Ryugu particle RA-QD02-0011-1. Mesostasis (Mes) can be seen between coarse silicate crystals of Olivine (Ol) and Diopside (Di). Insert shows EBSD map indicating no diffraction in the mesostasis confirming it as glass. Figure adapted from* Nakamura et al. (2011).

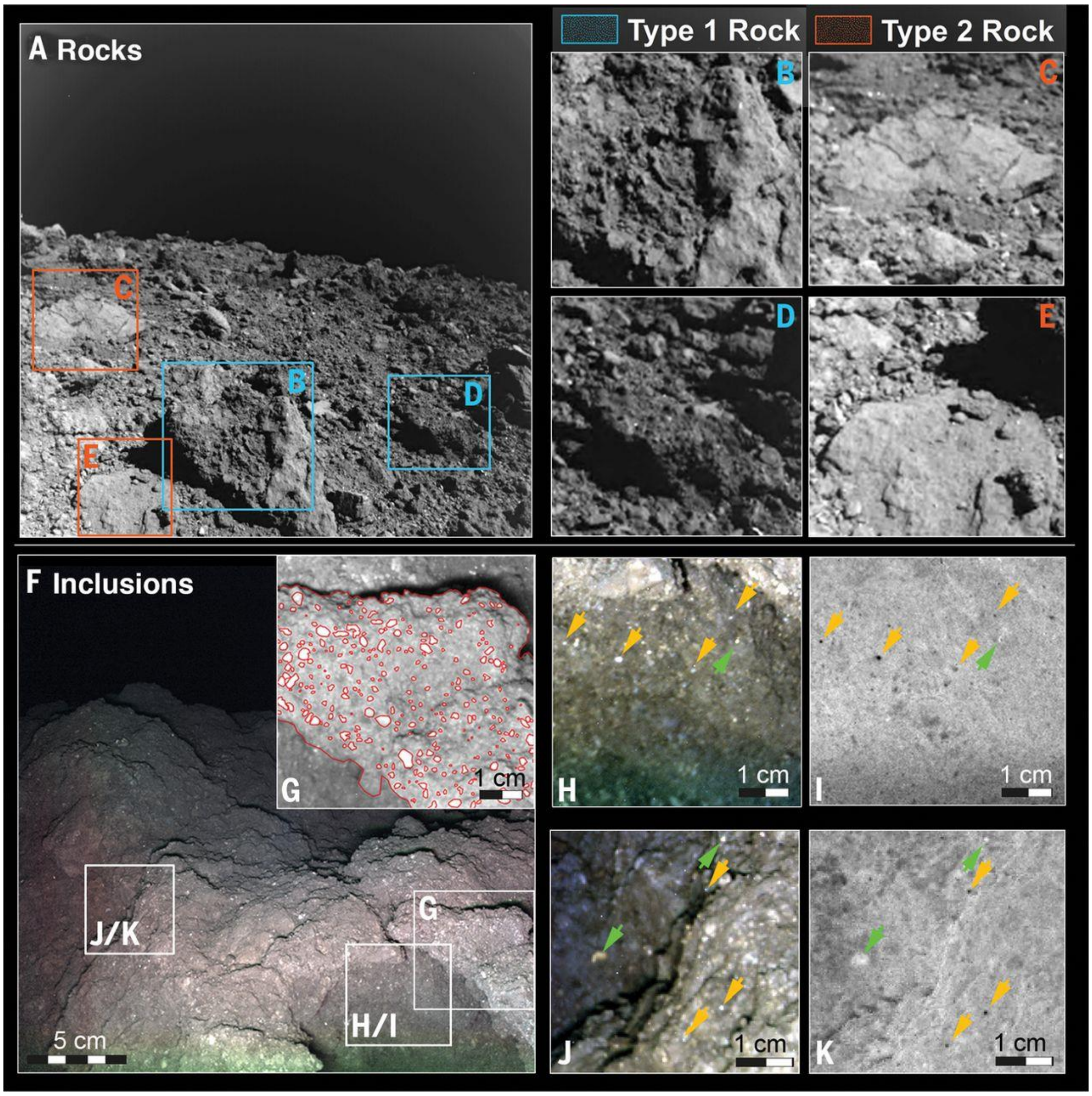

***Figure 1.8**. A-E) MASCam images from asteroid Ryugu showing two different textures of rock. A) A general overview of the surface area examined. B & D) The dark and rough textured type 1 rock. C & E) The brighter and smoother type 2 rock. F) Colour image of the Ryugu surface (type 1 rock) revealing bright inclusions (chondrule candidates). G) Magnified region showing the outlines of the inclusions highlighted in red. H and J) Magnified regions showing inclusions are either bluish (orange arrows) or reddish (bright green arrows). I and K) Infrared ratio images of H and J. Image taken from* Jaumann et al. (2019).

1.3.2.1 Chondrule Formation

As chondrules were likely the most abundant components within the early solar system and formed the building blocks of the asteroids and terrestrial planets, understanding their mechanisms of formation is of great significance. Despite their importance however, chondrule formation remains a conundrum, to the extent that Connolly and Jones, (2016) declared "They would not be predicted to exist if they did not exist". Our failure in being able to accurately predict the presence of chondrules within the early solar system is at the heart of the debate surrounding possibilities for their formation with no unifying theory predicting their petrology, geochemistry or astrophysical processes being forthcoming. A summary of the different formation mechanisms proposed is found in the following pages. What has been widely agreed is that chondrules display igneous textures and represent the solidified remains of a precursor material which underwent a melting, or at least a partial melting, event (Jones et al. 2000; Zanda 2004). Results from experimentally produced chondrules (which assume a single-stage thermal history) suggest melting occurred at peak temperatures of between 1550-2200°C, depending on the type of chondrule produced (Connolly and Jones 2016). Heating is thought to have been maintained on timescales of just minutes to hours, any longer would have resulted in the loss of volatile and moderately volatile elements such as Na, K and S, something that is not observed (Hewins et al. 2005). Following the heating events the droplets must have experienced cooling to allow crystallisation. It has been estimated that cooling was experienced at a rate of approximately 0.5-100°C/hr (Connolly and Jones, 2016).

A selection of the main chondrule formation theories discussed in the literature are outlined in the next section. These represent only a small fraction of the literature surrounding the complex, and often emotive subject of chondrule formation and any reader is encouraged to explore these different mechanism and theories for themselves.

X-Winds:

The X-Winds model for chondrule formation was developed by Shu et al. (1996, 1997, 2001). The model is built around understanding the gas-dynamics operating in the early solar system and the collimating outflows extending from protostars (Desch et al. 2010). In the X-wind model chondrules are heated as they are lofted upward from the disk by magnetocentrifugal outflows (Desch et al. 2012). While temperatures in the disk are thought to be much lower than the blackbody due to oblique light absorption it is radiated evenly over its entire surface. Shu et al., (1996) estimated that at 0.1 AU prior to lofting a temperature of 1160 K would be achieved. Following upward lofting and direct exposure to light temperature would increase to 1700 K (Shu et al. 1996). This model can also provide a natural mechanism for the aerodynamic size sorting of chondrules.

Collision Models and Impact Jetting:

An impact model for chondrule formation has been long discussed in the literature. Urey, (1952, 1967) suggested that collision between higher temperature materials could produce melt droplets, even suggesting the moon as a potential source of chondrules. Asphaug et al. (2011) proposed that during the dynamic stages of the early solar system planetesimals that were molten or partially molten could collide and produce sufficient chondrules to seed the chondritic meteorites.

Impact Jetting is an expanded impact origin model for chondrule formation (Johnson et al. 2014, 2015, 2018). In the impact jetting theory chondrule formation occurs very early in the collision process. As the two bodies are still colliding a small amount of material is squeezed out of the collision zone (Jetting) at velocities greater than the impact velocity (>2.5 km/s) (Johnson et al. 2015). During the jetting process some of the ejected material is shocked to high temperatures and pressures resulting in the formation of melt droplets which form chondrules. A schematic illustration of impact jetting is shown in Figure 1.9.

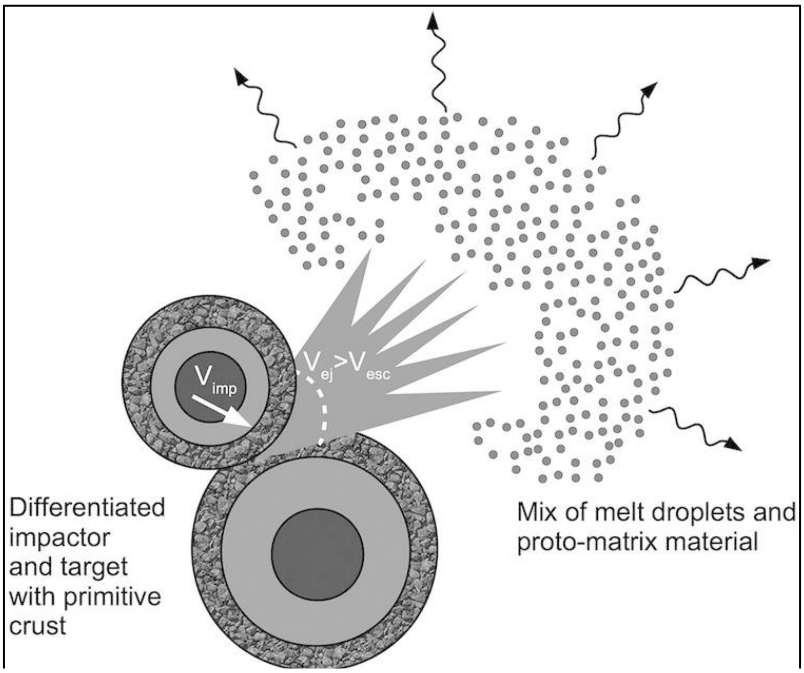

Figure 1.9*. Schematic illustration showing the proposed formation of chondrules and protomatrix by the impact jetting model. Shown is the small fraction of primitive crustal material being squeezed between the two colliding bodies and ejected at great velocity. Some of this material becomes shocked and experiences melting or partial melting. Illustration taken from* Johnson et al. (2018).

Lightning:

Whipple (1966) first proposed lightning as a potential formation mechanism for chondrules, with the observation that wherever there is a dust-laden circulating gas that is a poor electrical conductor, extreme electrical potentials can develop. Kaneko et al. (2023) nicely summarises the mechanics of the lightning model: Electrons within the circulating gas are accelerated by an electric field in the early disk, these accelerated electrons can then collide with neutral molecules and when this process occurs in a sufficiently strong electric field these collisions cause the ionisation of the neutral molecules. When ionisation occurs, there can be a rapid increase in electron density within the gas medium, improving the conductivity of the discharge current sufficiently that the energy store in the electric field is liberated (Kaneko et al. 2023). There are numerous studies investigating the complexities associated with this proposed process including those examining how the charging of particles occurs (Desch and Cuzzi 2000; Muranushi 2010; Johansen and Okuzumi 2018) and those examining how the lightning model fits in with the cooling history for chondrules (Kaneko et al. 2023).

Nebular Shock:

The nebular shock theory has developed the over years and decades with numerous sources for a nebular shock event proposed (see below). All nebular shock chondrule formation theories involve the passage of early solids through a shock wave which induced melting (Desch et al. 2005). Proposed sources of nebular shock include:

- Planetesimal bow shocks whereby planetesimals are excited onto eccentric orbits while gas remains in the protoplanetary disk (Hood 1998; Weidenschilling et al. 1998). The planetesimal on the more eccentric orbit travels at a significantly greater velocity when at perihelion relative to other solids and gases in the disk travelling in more circular orbits. The consequence of this velocity differential is a bow-shock around the planetesimal with gas surrounding it shocked and any entrained solids becoming heated (Desch et al. 2005).

- X-ray flare shock whereby an early sun would produce extensive high energy X-ray flares because of magnetic reconnection events in the solar magnetosphere (Desch et al. 2005; Nakamoto et al. 2005). As magnetic fields of opposite polarity combine, they merge or annihilate one another converting that energy into heat and kinetic energy as motion of gas along magnetic field lines (Nakamoto et al. 2005). This accelerated gas can produce shock and thus the heating of solids along its ejection plane(Desch et al. 2005).

- Gravitational Instabilities whereby the disk's own vertical self-gravity exceeds that due to the solar systems' central star (Boley and Durisen 2008; Boss and Durisen 2005; Desch et al. 2005). In such an event the disk gas begins to reorganise leading in bar or spiral patterns. The reorganised gas patterns are significantly denser than gas orbiting the disk which enters the spiral or bar patterns at highly supersonic speeds leading to shock and associated heating (Desch et al. 2005).

Chondrule age (at what point they solidified), is another important aspect of chondrule study which has garnered much attention. A significant aspect of determining chondrule age is understanding the chronology relative to calcium aluminium-rich inclusions (CAIs) which are thought to be the oldest solids in the solar system (Bouvier and Wadhwa 2010). Application of ^{26}Al, ^{53}Mn and ^{129}I isotopic systems suggested a formation age for chondrules several million years after that of the CAI's (Swindle et al. 1996). This was subsequently refined using Pb-Pb isochron ages of obtained from chondrules within a CR chondrite indicating formation 4564.7 ± 0.6 Ma, 2.5 ± 1.2 My after the CAIs (Amelin et al. 2002). However, such is the field of chondrule study that there are also findings to suggests a contemporaneous formation age for both the CAIs and chondrules (Connelly et al. 2012).

1.3.2.2 Chondrule Types

Chondrules have an array of textures and compositions, and they can be classified according to both. Compositionally, chondrules can first be categorised into two chemical groups: Type I (FeO-poor, olivine Fa < 10) and Type II (FeO-rich, olivine Fa > 10) (Hewins 1997). Following this, they can be further sub-divided into types A, B and AB, based on SiO_2 abundance: A = SiO_2-poor and thus olivine-rich, B = SiO_2-rich and therefore pyroxene-rich, AB = Intermediate (*Figure 1.10*) (Hewins 1997).

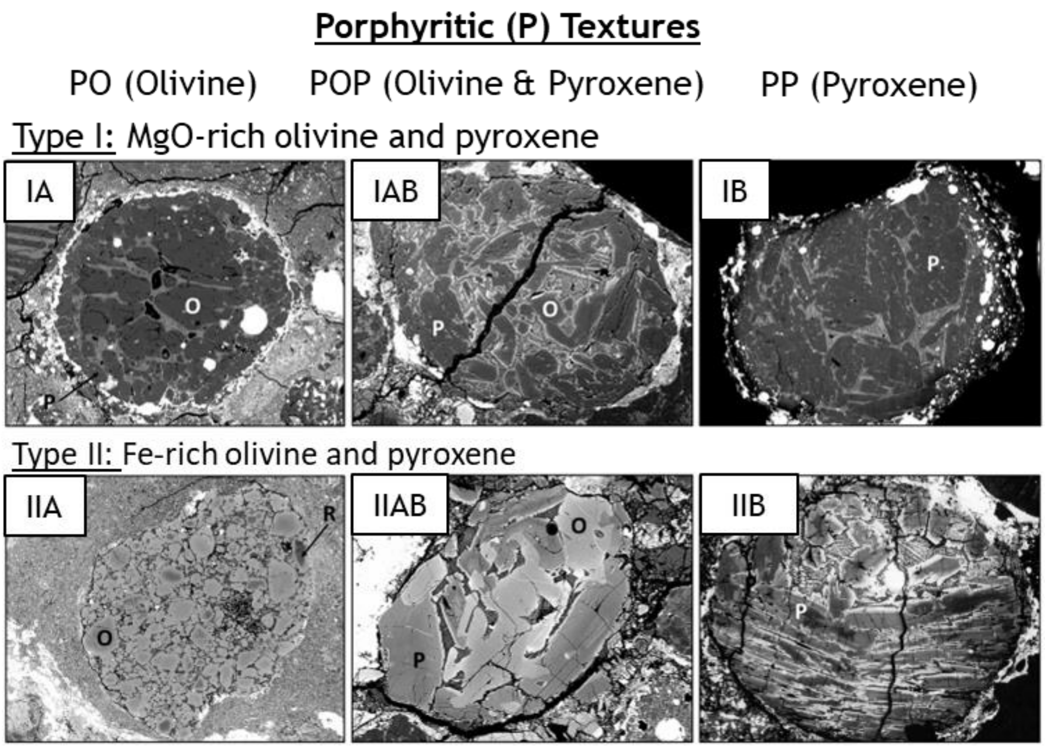

Figure 1.10. *Scanning electron microscopy (SEM) images of the six different chemical types of chondrules. Texturally these are identified as porphyritic chondrules (discussed in the following section). Figure adapted from* (Jones et al. 2018).

In addition to chemical classification a textural classification of chondrules was devised by Gooding and Keil, (1981). Textural classification is based on the dominant texture and/or mineralogy present, and the classification terms are often abbreviated (see parentheses below):

- *Porphyritic chondrules (PO, PP and POP)* – Porphyritic chondrules consist of large olivine and/or low Ca-pyroxene phenocrysts with accessory amounts of sulphides and Fe,Ni metal all set within a mesostasis of glassy or cryptocrystalline material. Porphyritic chondrules are further sub-divided based on the olivine/pyroxene modal ratio: Poryhritic Olivine (PO) and Porphyritic Pyroxene (PP) are defined based on a modal ratio of ≥ 10:1 of the dominant mineral. Porphyritic olivine-pyroxene (POP) chondrules are those with ratios between these limits.
- *Granular (GP & GOP)* – Granular chondrules contain fine-grained material and can be further sub-divided into Granular olivine (GO), Granular pyroxene (GP) and Granular olivine-pyroxene (GOP).

- *Barred Olivine (BO*) – BO chondrules consist of crystalographically aligned, prismatic olivine phenocrysts termed 'bars'. The space between bars is filled with mesostasis.
- *Radial Pyroxene (RP)* – RP chondrules have distinctive fan-like arrangements of low-Ca pyroxene which emanate from a point or points near the chondrule edge.
- *Crytocrystalline (C)* – C chondrules are dominated by glassy material and therefore have lack any systematic crystal structure.
- *Metallic (M)* – M chondrules are the most unique and least abundant type of chondrule. These consist almost entirely of Fe,Ni metal, usually accompanied by some accessory phases - sulphides and occasional silicate fragments.

An overview of chondrule classification and the relationships between the chemical and textural classifications is shown in Table 1.1. Examples of some of the more common chondrule types are in Figure 1.11.

It is also helpful to acknowledge the presence of compound chondrules. In these instances, chondrules are fused together; either along their boundaries or with one chondrule enveloping another (Hewins 1997; Wasson et al. 1995).

Table 1.1*. Chondrule classification setting out the two major chemical varieties, the three sub-types for each and the textural compositions of chondrules associated with each type/sub-type. Table sourced from* Hewins (1997).

Type	**Sub Type**		**Textural Varieties**
I (FeO-poor, olivine Fa < 10)	IA	ol > 80%	(BO, PO), MPO, GO, DZ
	IAB	Intermediate	RPO, POP, GOP, DZ
	IB	px > 80%	RP, PP, GP, DZ
II (FeO-rich, olivine Fa > 10)	IIA	ol > 80%	BO, PO, (MPO, GO) DZ
	IIAB	Intermediate	RPO, POP, GOP, DZ
	IIB	px > 80%	RP, PP, GP, DZ

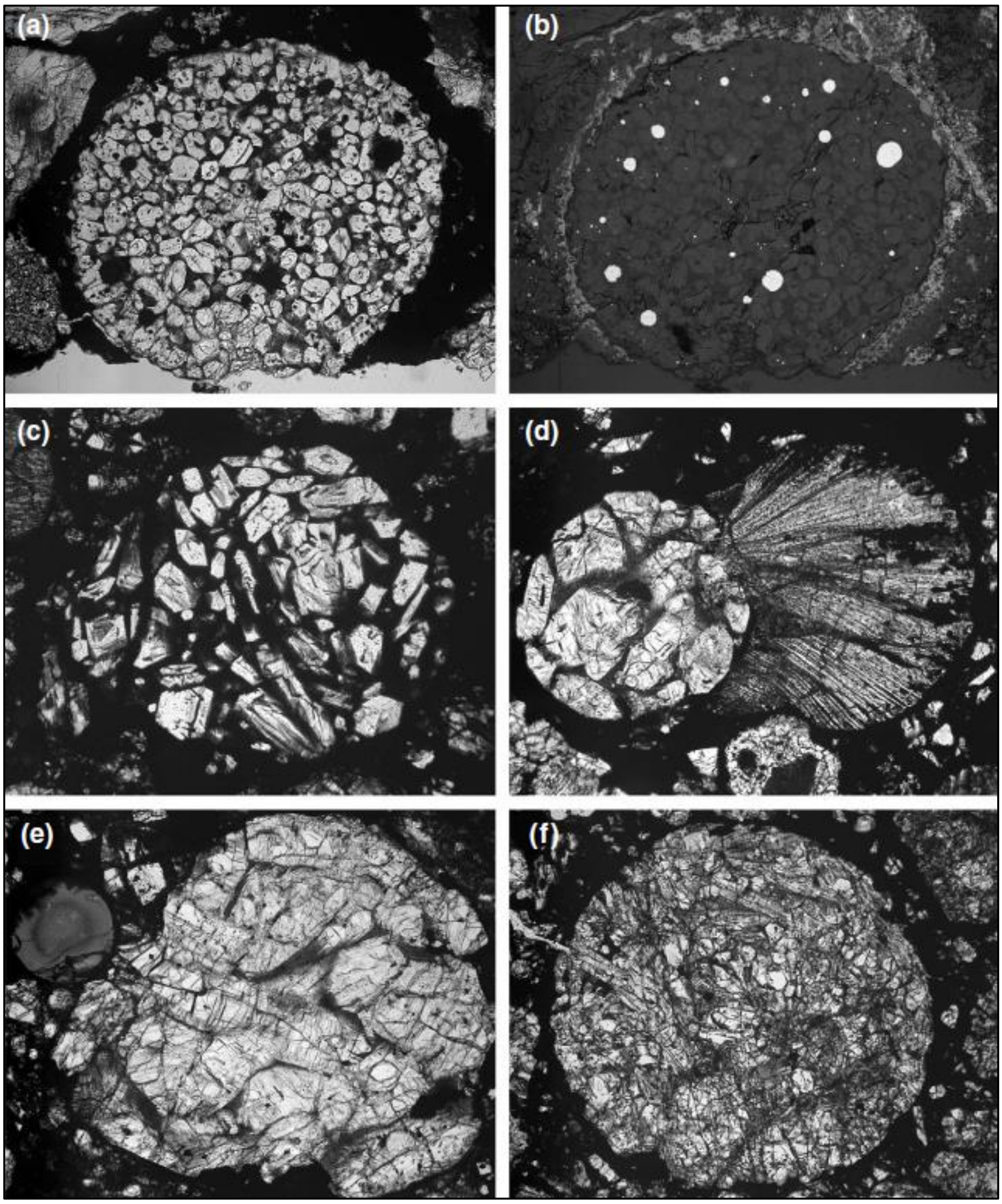

Figure 1.11. *Optical microscopy images showing a range of chondrule textures found in chondritic meteorites. The field of view for images a) - f) is 1.35 mm.* ***a)*** *PO chondrule from L chondrite QUE97008.* ***b)*** *Reflected light image of (a) showing metal droplets concentrated near the chondrule boundary.* ***C)*** *PO chondrule from H chondrite Clovis, in this instance the grains are significantly larger than those in (a).* ***d)*** *A PO-RP chondrule pair from L chondrite EET 90066.* ***e)*** *A PP chondrule and cryptocrystalline chondrule (upper left) within L chondrite ALH 78119.* ***f)*** *A POP chondrule from LL3 chondrule Bishunpur showing olivine crystal towards the chondrule centre and pyroxene crystals towards the margins. Images from* Lauretta et al. (2006).

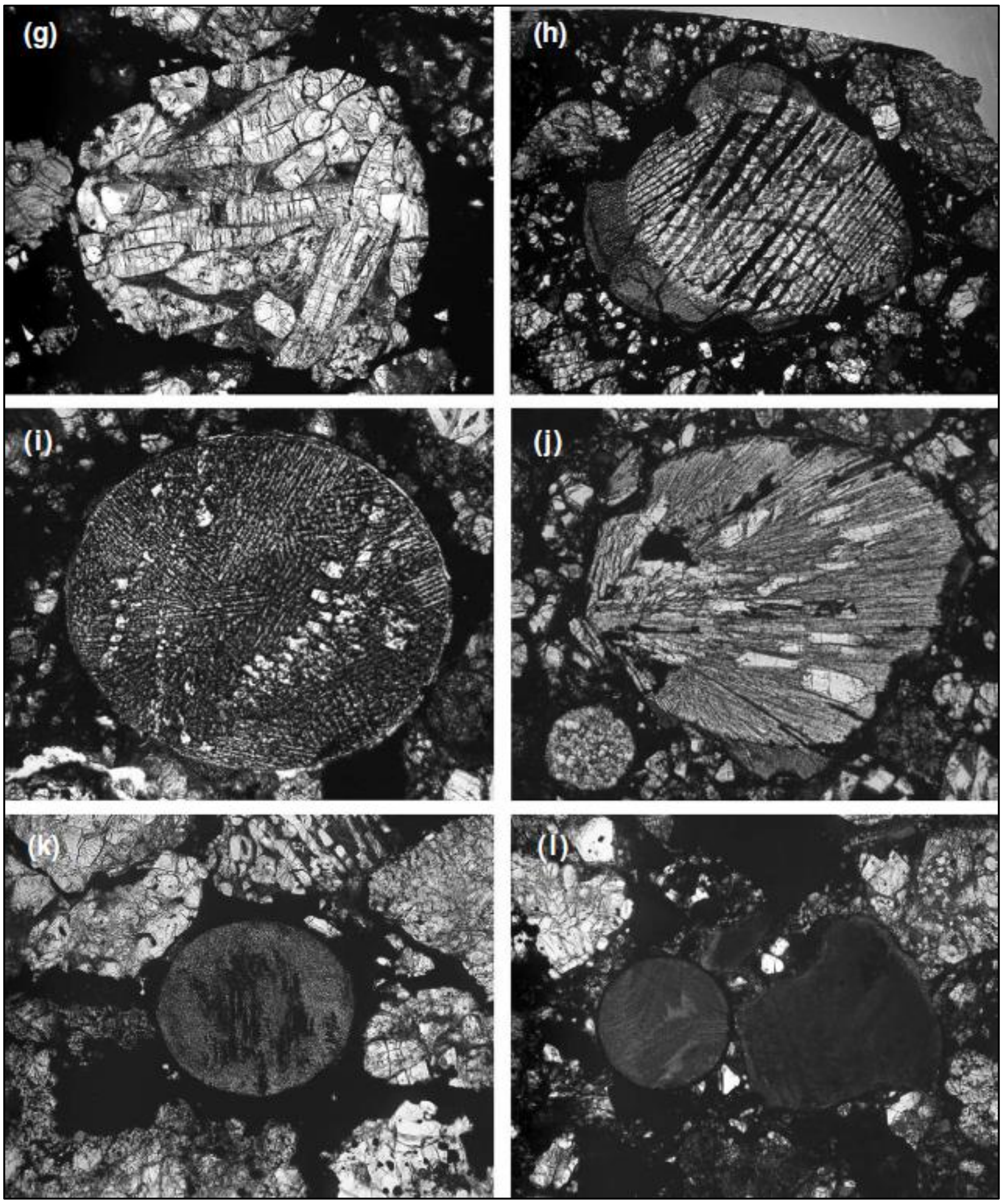

Figure 1.11. *(continued). **g)** Coarse-grained porphyritic pyroxene chondrule within L chondrite EET 90066. **h)** Barred olivine chondrule LL chondrite Bishunpur, in this instance field of view is 2.7 mm. **i)** Barred olivine chondrule with multiple barred units and some porphyritic olivine crystals which appear brighter, within L/LL chondrite Saratov. **j)** Radial pyroxene chondrule from L chondrite ALH 78119. **k)** Granular olivine chondrule from L chondrites QUE 97008. **l)** Two cryptocrystalline chondrules from L chondrites ALH 78119. Images from* Lauretta et al. (2006).

1.3.3 Carbonaceous Chondrites

Carbonaceous chondrites are the most chemically primitive meteoritic samples and take their name from the elevated carbon content found in some groups (1.5-6.0 % CM and CI groups) (Braukmüller et al. 2018). As part of the chondritic family of meteorites, carbonaceous chondrites are typically dominated by three components: chondrules, refractory inclusions and a silicate-rich fine-grained matrix. However, variations in the abundance and/or presence of these three components is observed within the carbonaceous chondrite groups and used for classification criteria (Table 1.2). Apart from the CV, CO and CK carbonaceous groups, which plot along the C-chondrite anhydrous mineral mixing line, carbonaceous chondrites also contain variable abundances of hydrated components (Weisberg et al. 2006). Chondrules and refractory inclusions represent high temperature components whilst the fine-grained matrix often has a low temperature origin. Well-defined fine-grained rims (FGRs) are present within the CM, CO, CV, CR and CY carbonaceous chondrite groups and surround chondrules, aggregates, inclusions, and in some cases, xenoliths, having accreted onto these objects whilst free-floating in the protoplanetary disk (King et al. 2019; Lee et al. 2023; Metzler 2004; Zanetta et al. 2022). FGRs are typically composed of an unequilibrated fine grained assemblage (≤1 µm) of Mg-Fe amorphous silicates, phyllosilicates embedding anhydrous silicates, sulphides, metals and organics. FGRs have similar compositions to the matrix however, differences in their texture and pre-solar grain abundances suggest they have been accreted and processed differently; making them the interface between the high and low temperature components with carbonaceous chondrites (Zanetta et al. 2021, 2022). The presence of these components, whilst indicative, do not represent a strict criterion for classification as a carbonaceous chondrite. Many of the aforementioned features are also commonplace within the ordinary and enstatite chondrites and variations in the abundance and presence of these components within the carbonaceous class also exist. Thus, to discriminate carbonaceous chondrites from other chondritic classes, whole chondrite (Mg-normalised) refractory-lithophile-element abundances ≥1x CI and/or O-isotopic compositions near or below the terrestrial fractionation line should be used (Weisberg et al. 2006).

Within the carbonaceous chondrite class, eight compositional groups can be identified. As shown in Table 1.2, each group can be identified by the abundances of refractory inclusions, chondrules, metallic Fe,Ni and matrix, alongside average chondrule size (Scott and Krot 2013; Weisberg et al. 2006). The groups are so named using a two-letter designation based on exemplar specimens: CM (Mighei-like), CI (Ivuna-like), CO (Ornans-like), CV (Vigarano-like), CR (Renazzo-like), CH (ALH85085-like), CB (Bencubbin-like), CK (Karoonda-like), CL (Loongana-like), and CY (Yamato-like).

Table 1.2. *The typical characteristics of refractory inclusions, chondrules, metal and matrix with the different carbonaceous chondrite groups. Modified from* (Scott and Krot 2013).

CC Group	CAI & AOA (vol. %)	Chondrule average diameter (mm)	Chondrules (Vol. %)	Metal (Vol. %)	Matrix (Vol. %)
CI	*<0.01*	*None*	*<5*	*<0.01*	*95*
CM	*5*	*0.30*	*20*	*0.1*	*70*
CO	*13*	*0.15*	*40*	*1 - 5*	*30*
CV	*10*	*1.00*	*45*	*0-5*	*40*
CR	*0.5*	*0.70*	*50 - 60*	*5 - 8*	*30 - 50*
CH	*0.1*	*0.02 - 0.09*	*~70*	*20*	*5*
CB	*<0.1*	*0.5 - 5*	*30 - 40*	*60 - 70*	*<5*
CK	*4*	*0.80*	*15*	*<0.01*	*75*
CL[†]	*1.4*	*0.457*	*67-79*	*14.4*	*17-21*
CY[‡]	*18**	*0.42*	*18**	*<2*	*20*

[†] Based on information from Metzler et al., (2021)

[‡] Based on information from Suttle et al., (2021a)

*Combined values for CAI and chondrule abundance

In addition to the differing sizes and abundances of their constituent components, the carbonaceous chondrite groups have evidence for varying degrees of secondary alteration. The alteration experienced can be defined on a petrologic scale; from petrologic type 1, significant aqueous processing; to petrologic type 6, significant thermal metamorphism (see Figure 1.12) (Van Schmus and Wood 1967). Where subjected to aqueous alteration (petrologic types 1 and 2) alteration occurs at low temperatures typically <~100°C (Brearley 2006). In chondrites subjected to thermal metamorphism (petrologic types 3-6) temperatures increase with increasing petrologic grade, typically from ~500 – 900 °C (Huss et al. 2006; Van Schmus and Wood 1967). Chondrites assigned a petrologic type of 3.0

represent those which have been least modified by secondary processing, having undergone neither significant aqueous alteration nor thermal metamorphism (Krot et al. 2013; Weisberg et al. 2006). Figure 1.12 illustrates the relative abundances of petrologic types within each of the carbonaceous groups.

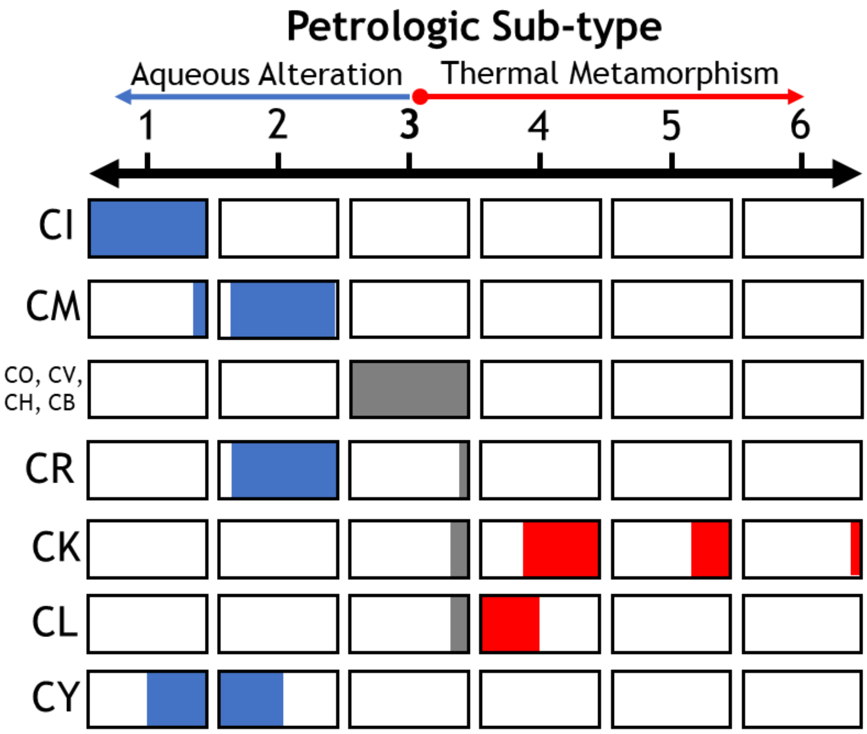

***Figure 1.12**. Petrologic classification and abundance of each carbonaceous chondrite group. Blue shaded regions indicate aqueous alteration, grey shaded region represent relatively unaltered material and red shaded regions represent those groups which have experienced thermal metamorphism. Figure adapted from* Lipschutz and Schultz (2014).

1.3.4 Carbonaceous CM Chondrites

The carbonaceous CM (Mighei-like) chondrites (an example illustrated in Figure 1.13) are the largest group of carbonaceous chondrites accounting for ~25.3% of all carbonaceous meteorites collected (The Meteoritical Society 2023). These primitive meteorites have spectral similarities to the B, C, F and G class asteroids and therefore provide important insights into the processes occurring during the formation and evolution of outer MAB objects (Chizmadia and Brearley 2008; Pieters and McFadden 1994; Vilas and Gaffey 1989). At the macro-scale these meteorites appear as dark, predominantly fine-grained rocks with some larger feature such as chondrules and clasts visible to the un-aided eye (Figure 1.13).

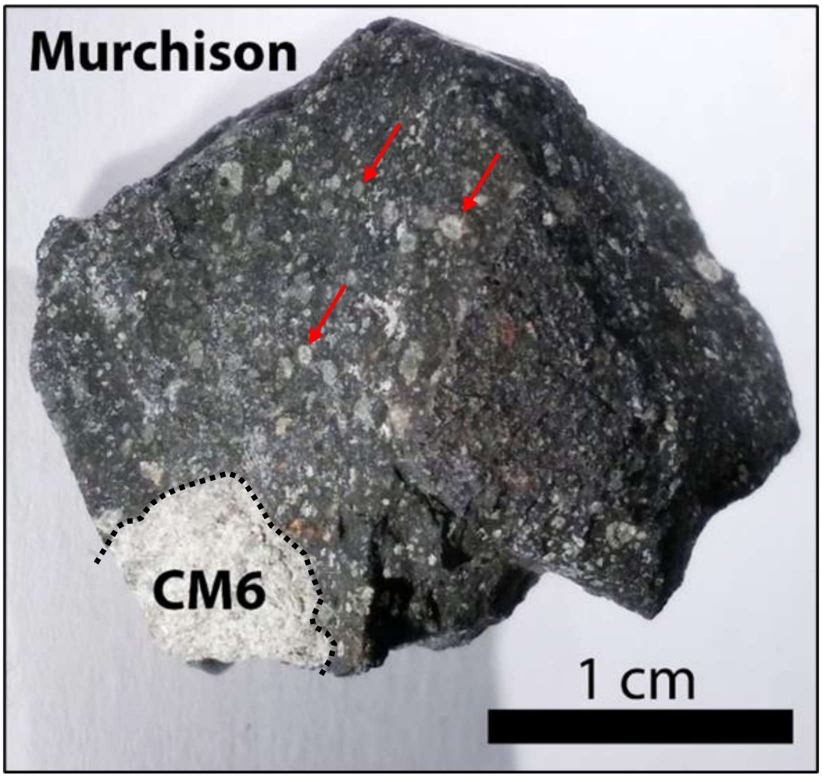

Figure 1.13. *An example carbonaceous CM chondrite (Murchison). Red arrows identify some of the chondrules which are observable to the naked eye. Additionally, this sample contains a small lithic clast, highlighted by the dashed line. This clast is identified as a CM6 and has therefore experienced metamorphism. Image adapted from* Bischoff et al. (2018) and Kerraouch et al. (2019).

1.3.4.1 Principle Components

The major components of the CM chondrites are: chondrules, FGRs, minor amounts of Fe,Ni metal, refractory calcium-aluminium rich inclusions (CAIs) and amoeboid olivine aggregates (AOAs), all of which are set within a fine-grained matrix (Weisberg et al. 2006). The approximate abundances of these components are listed in Table 1.2.

Chondrules: Chondrules within the CM chondrites are comparatively small when compared to those in other carbonaceous groups (as shown in Figure 1.14) with a reported average size of just 270-300 µm (Friedrich et al. 2015; Rubin and Wasson 1986; Weisberg et al. 2006). Compositionally, type I chondrules dominate and represent 60-90% of all chondrules (Figure 1.15B). Also, ~95% of CM chondrule textures are defined as porphyritic (Jones 2012). Chondrule and mineral fragments can also be observed within the CM chondrites (Figure 1.15C).

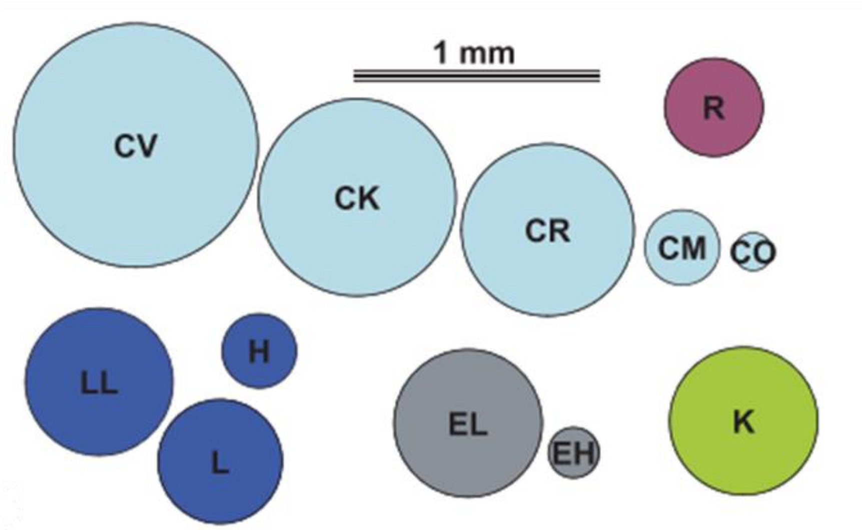

Figure 1.14*. Illustration of the mean chondrule sizes within the chondrule-bearing chondritic groups. Diagram taken from* Jones (2012).

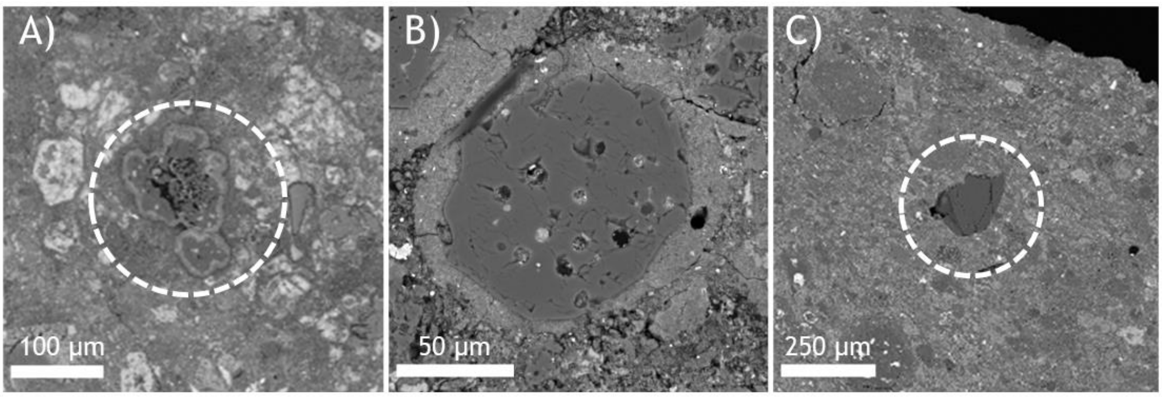

Figure 1.15*. BSE images showing some of the major components in CM chondrites. A) A CAI (circled) within CM chondrite Murchison. B) An intact type I chondrule with surrounding fine-grained rim within the CM chondrite LEW85311. C) A mineral fragment (circled) within the CM chondrite Cold Bokkeveld.*

FGRs: FGRs surround many of the chondrules and refractory inclusions within CM chondrites (Figure 1.15B). They are composed primarily of phyllosilicates and are Mg-enriched and Ca-poor compared to the matrix (Metzler et al. 1992). FGR thickness is observed to vary between objects, and outward coarsening has also been recorded (Zega and Buseck 2003). FGR fragments are fairly common within the CM chondrites and provide a key piece of evidence for regolith processing, having likely broken off from their host object during a disruption event. It is widely thought that FGRs accreted onto chondrules (and some refractory inclusions) whilst these objects were free-floating in the protoplanetary disk and passing through a cloud of dust (Metzler 2004; Metzler et al. 1992). There are however competing theories for the formation of FGRs including non-nebular origins (Trigo-Rodriguez et al. 2019).

Refractory Inclusions: Typically occurring as submillimetre sized objects, the highly refractory inclusions (AOAs and CAIs) represent minor components of the CM chondrites, occupying only ~1.2 area% (Hezel et al. 2008; Shen et al. 2022). Whilst the textures and mineralogies present within AOAs are very similar, CAIs show significant variation and have been classified by numerous authors in different ways including, texture, mineralogy, isotopic compositions and trace element chemical compositions (Krot 2019). The CM chondrites are known for their relative abundance of hibonite-rich CAIs (MacPherson 2007).

1.3.4.2 Mineralogy

The mineralogy of CM chondrites reflects the aqueous alteration they have been subjected to (aqueous alteration is discussed later). A high indigenous water content ~9 wt.% is found within the CMs (Jarosewich, 1990). Much of this water is structurally bound within the OH molecules of the phyllosilicate minerals composing the matrix and FGRs. Phyllosilicates constitute ~55-90 vol% of all CM chondrite minerals, primarily in the form of cronstedtite ($Fe^{(II)}_2Fe^{(III)}[Si,Fe^{(III)}O_5[OH]_4$) and Fe/Mg serpentine ($[Fe,Mg]_3Si_2O_5[OH]_4$) (Howard et al. 2009, 2011, 2015; Suttle et al. 2021b; Trigo-Rodríguez et al. 2019).

After phyllosilicates, anhydrous Fe,Mg silicates specifically olivine [$(Fe,Mg_2]SiO_4$] and pyroxene [$XY(Si,Al)_2O_6$] are the most abundant (Suttle et al. 2021b). Within pyroxene the X site is usually occupied by Mg, $Fe^{(II)}$, Ca or Na and the Y site by Mg,

$Fe^{(III)}$, Al or Cr (Suttle et al. 2021b). Anhydrous silicate abundances vary from 13-31 vol% and constitute the bulk components of chondrules, CAIs and AOAs (Howard et al. 2011; Suttle et al. 2021b).

The CM chondrites also contain abundant minor phases which typically constitute <5 vol% of the overall meteorite. Minor phases can include carbonates such as calcite, dolomite, aragonite and breunnerite, also Fe-sulphides and Fe,Ni metal (Lee et al. 2014). The CM chondrites are also enriched in organic molecules when compared to other chondritic groups (Schmitt-Kopplin et al. 2010).

1.3.4.3 Aqueous Alteration

Like many of the carbonaceous chondrites, the CMs have been the subject of secondary alteration processes, specifically post-accretion, low-temperature aqueous alteration. The CM chondrites are therefore described as belonging to either petrologic type 1 (CM1) if highly altered or more commonly, petrologic type 2 (CM2) if moderately altered (Brearley 2006; Rubin et al. 2007). The processes leading to aqueous alteration within the CM chondrites are not fully understood; however, it is widely thought that the alteration occurred on the CM parent asteroid, contemporaneously or shortly after CAI formation and lasted a minimum of 4Ma (Bunch and Chang 1980; de Leuw et al. 2009; Rubin et al. 2007; Tomeoka and Buseck 1985; Trigo-Rodriguez et al. 2019). The source of the water is thought to have been water ice which was accreted directly into the CM parent body (Grimm and Mcsween 1989). Suggested mechanisms to produce the melting of water ice include internal heating resulting from the decay of short-lived radioactive isotope Al^{26} (Grimm and Mcsween 1989) and impact derived heating (Rubin 2012).

The effects of aqueous alteration within the CMs are significant, producing a series of secondary phases which are diagnostic of the CM chondrite group. Arguably the most characteristic is the unusual iron-sulphide-hydrate mineral, tochilinite [$6Fe_{0.9}S\cdot5(Fe,Mg)(OH)_2$] which is often intergrown with Fe^{3+}-rich serpentine and cronstedtite (Brearley 2006; Tomeoka and Buseck 1985). These phases have a complex history within the literature and were initially designated as PCP (poorly characterised phases) due to challenges in identifying the constituent minerals (Fuchs et al. 1973; Mackinnon and Zolensky 1984; Tomeoka and Buseck 1985).

Following successful mineral identification and improved characterisation, PCPs were referred to as tochilinite and serpentine/cronstedtite intergrowths by Brearley, (2006) & Rubin et al., (2007). The term tochilinite and cronstedtite intergrowths was then abbreviated to TCIs by Palmer and Lauretta in 2011. TCIs occur within the matrix and FGRs of CM chondrites as well as being a replacement product surrounding Fe,Ni metal grains (both chondrule and matrix located) (Brearley 2006; Palmer and Lauretta 2011).

Carbonates are another alteration phase ubiquitous to the CM's despite only representing a few vol.% (Lee et al. 2014). Typically present as calcite but occasionally as aragonite, dolomite and breunnerite, the carbonates present reflect the degree to which a CM has experienced aqueous alteration (Lee et al. 2014). Isotopic analysis of carbonates using the $^{53}Mn/^{53}Cr$ system has been used to infer the timing for the onset of aqueous alteration. Results indicate aqueous alteration started contemporaneously or just after CAI formation and lasted for ~2-6 Ma (Fujiya et al. 2012; de Leuw et al. 2009; Visser et al. 2020).

1.3.4.4 Sub-classification

Whilst the petrologic descriptors CM2 (moderate aqueous alteration) and CM1 (highly aqueously altered) are helpful in describing the general extent of alteration, significant variations in the degree of alteration between CM samples has facilitated the development of sub-classification schemes. These schemes aim to more precisely describe the degree of aqueous alteration experienced. Bulk techniques such as X-ray diffraction (Howard et al. 2009) and light element analysis (Alexander et al. 2012, 2013) allow for samples to characterised according to their degree of alteration. However, these bulk methods do not accommodate intrasample variability originating from the brecciation experienced (see section 1.3.4.5) and rely on a single factor in determination of classification.

The more commonly used approach was developed by Alan Rubin and is based on multiple criteria (detailed in Table 1.3) (Rubin 2015; Rubin et al. 2007). The Rubin scheme assigns a classification between CM3.0, a hypothetical entirely unaltered sample and CM2.0, a completely altered/replaced sample (comparable to the CM1 designation). The criteria for classification using the Rubin scheme can be easily determined using readily available microanalysis techniques such as scanning electron microscopy (SEM) (Suttle et al. 2021b). To remain consistent throughout his thesis, the scheme developed by Rubin et al., 2007 and expanded by Rubin, (2015) will be used.

Table 1.3. *Rubin's diagnostic characteristics of progressive aqueous alteration in the CM chondrites. Table taken from* (Rubin 2015).

Petrologic Subtype	2.7	2.6	2.5	2.4	2.3	2.2	2.1	2.0
Chondrule mesostases	Phyllosilicate	Phyllosilicate	Phyllosilicate	Phyllosilicate	Phyllosilicate	Phyllosilicate	Phyllosilicate	Phyllosilicate
Matrix phyllosilicates	Abundant	Abundant	Abundant	Abundant	Abundant	Abundant	Abundant	Abundant
Matrix composition:								
MgO/ "Feo"	0.35-0.43	0.35-0.43	0.35-0.43	0.35-0.43	0.50-0.70	0.50-0.70	0.50-0.70	0.50-0.70
S/SiO	0.10-0.18	0.10-0.18	0.10-0.16	0.10-0.16	0.07-0.08	0.07-0.08	0.05-0.07	0.05-0.07
Metallic Fe-Ni (vol%)	1-2	~1	0.03-0.30	0.03-0.30	0.03-0.30	0.03-0.30	≤0.02	≤0.02
Mafic silicate phenocrysts in chondrules	Unaltered	Unaltered	Unaltered	Unaltered	2-15 % altered	15-85 % altered	85-99 % altered	Completely altered
Large TCI clumps (vol%)	5-20	15-40	15-40	15-40	15-40	15-40	2-5	2-5
TCI composition:								
FeO/SiO_2	4.0-7.0	2.0-3.3	2.0-3.3	1.5-2.0	1.5-2.0	1.0-1.7	1.0-1.7	1.0-1.7
S/SiO_2	0.40-0.60	0.18-0.35	0.18-0.35	0.14-0.20	0.14-0.20	0.05-0.09	0.05-0.09	0.05-0.09
Sulfide	po+pn	Mainly po+pn	Mainly po+pn	po+pn+int	po+pn+int	Mainly pn+int	Mainly pn+int	Mainly pn+int
Carbonate	Ca carbonate	Ca carbonate	Ca carbonate	Ca carbonate	Ca carbonate	Ca carbonate	Ca carbonate + complex carbonate	Ca carbonate + complex carbonate

1.3.4.5 Brecciation

The majority (if not all) CM chondrites have been identified as regolith breccias, composed of primarily subangular cognate clasts, and occasionally xenolithic clasts, set within a fine-grained matrix (Bischoff et al. 2006; Lee et al. 2023). Breccias can be distinguished within the CMs by differences in mineralogy, chemistry, texture, petrofabric and degree of aqueous alteration between individual clasts (Bischoff et al. 2006; King et al. 2022; Lentfort et al. 2020; Lindgren et al. 2013; Metzler et al. 1992). The degree to which a CM chondrite is brecciated is heterogenous and varies between sections of any given meteorite (Lindgren et al. 2013). Figure 1.16 shows two CM chondrite thin sections and demonstrates the variable degrees of brecciation which can be observed. The numerous different clasts and lithologies are distinguished by their differences in greyscale, representing variations in chemistry and degree of aqueous alteration.

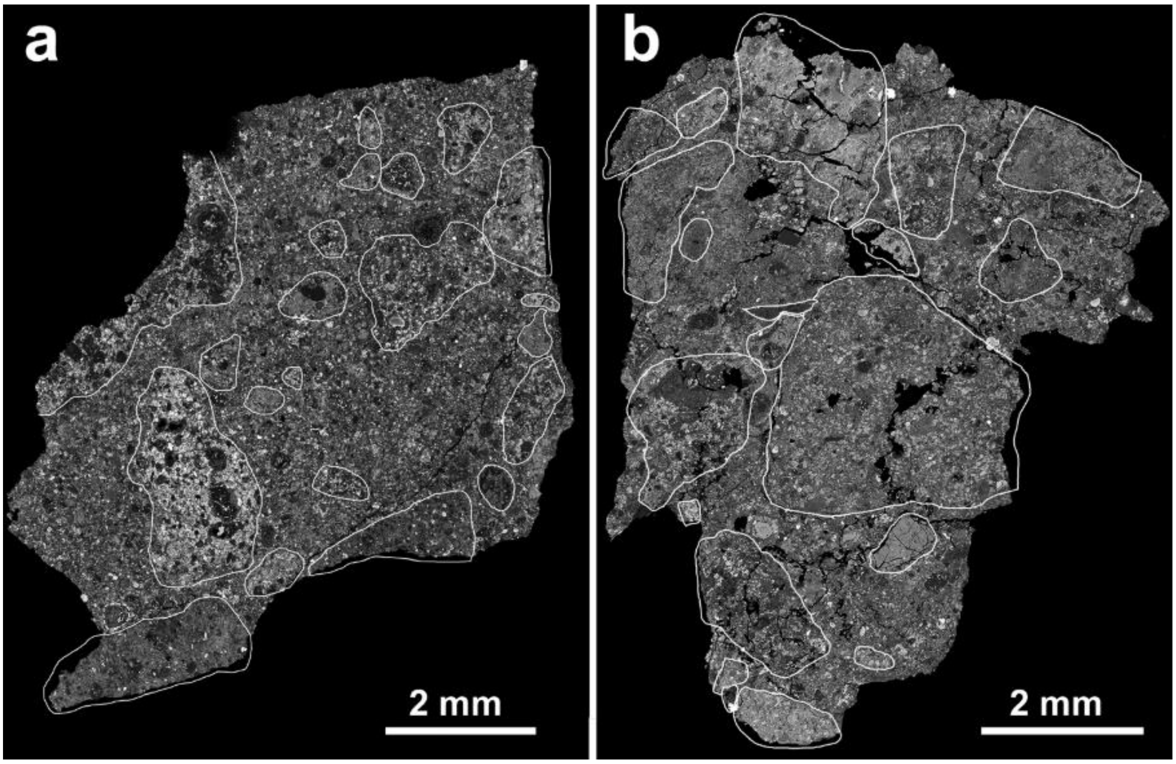

Figure 1.16*. BSE images of two CM chondrites demonstrating the appearance of brecciation within BSE images and the variable degrees of clast abundance between samples. A) a moderately brecciated thin section of ALH 58013. B) A heavily brecciated thin section of LON 94101. Image source from* Lentfort et al. (2020).

Breccias can be formed by the accretion of already fragmented material or by in situ brecciation, whereby material is fragmented and mixed on or within a parent body. The cause of brecciation within the CMs is believed to be impacts on the CM parent body leading to the fragmentation and mixing of material from different regions within the same parent body. In addition to the presence of brecciation, chondrule defined petrofabrics have also been identified by both 2D and 3D methods and provide further evidence for parent body impact processing (Hanna et al. 2015; Rubin 2012; Vacher et al. 2018). However, despite the evidence for parent body impact processing most CMs display little to no evidence of shock, with most being classified as shock stage S1 (Table 1.4) (Lindgren et al. 2015; Scott et al. 1992).

Differences in the degree of aqueous alteration between clasts, and the heterogenous nature of brecciation, have proved a challenge for attributing a single petrologic subtype (Table 1.3) to any given chondrite. Whilst some samples may exhibit a consistent degree of alteration across different clasts, others may exhibit significant differences between clasts, such as Cold Bokkeveld (Lentfort et al. 2020). Lentfort et al. (2020) therefore suggested that classifications should encompass the full range of subtypes exhibited by the clasts within a sample (e.g. CM2.2-2.7). The relationship between brecciation and aqueous alteration can be used to infer chronological information regarding the onset of both brecciation and aqueous alteration. Given that the majority of CM breccias contain clasts of different petrologic subtypes it can be concluded that aqueous alteration pre-dated the brecciation and subsequent re-accretion and consolidation of material (Lindgren et al. 2013).

Table 1.4*. Stages of shock metamorphism in ordinary chondrites with primary shock criteria highlighted in red. Table adapted from Stöffler et al. (1991).*

Shock Stage	Effects Resulting from Equilibration Peak Shock Pressure		Effects Resulting from Local P-T Excursions	Shock Pressure (GPa)	Post-shock Temperature increase (°C)	Estimated Minimum Temperature Increase (°C)
	Olivine	Plagioclase				
S1 - Unshocked	Sharp optical extinction, irregular fractures		None	< 4 - 5	10 - 20	10
S2 - Very Weakly Shocked	Undulatory extinction, irregular fractures		None	5 - 10	20 - 50	20
S3 - Weakly Shocked	Planar Fractures, undulatory extinction, irregular fractures	Undulatory extinction	Opaque shock veins, incipient formation of melt pockets, sometimes interconnected	15 - 20	100 - 150	100
S4 - Moderately Shocked	Mosaicism (weak), planar fractures	Undulatory extinction, partially isotropic, planar deformation features	Melt pockets, interconnecting melt veins, opaque shock veins	30 - 35	250 - 350	300
S5 - Strongly Shocked	Mosaicism (strong), planar fractures and planar deformation features	Maskelynite	Pervasive formation of melt pockets, veins and dykes; opaque shock veins	45 - 55	600 - 850	600
S6 - Very Strongly Shocked	Restricted to local regions in or near melt zones. Solid state recrystallisation and staining, ringwoodite, melting	Shock melted (normal glass)	As in S5	75 - 90	1500 - 1750	1500
Shock Melted	Whole rock melting (impact melt rocks and melt breccias)					

1.3.5 Space Weathering

Space weathering encompasses a diverse range of processes, all of which can alter the optical, physical, chemical, and mineralogical properties of airless solar system bodies (Clark et al. 2002). It is therefore important to consider the impacts of space weathering when trying to understand the evolutionary processes affecting solar system bodies.

Much of what is understood about space weathering has its origins in lunar science. Crating and a darker appearance in some regions of the lunar surface are perhaps the most obvious and well discussed examples of space weathering, with early authors suggesting these were the result of meteorite bombardment and solar X-ray irradiation (Daly 1946; Gold 1955; Kuiper 1954). The returned lunar soils from the Appollo missions were significant in developing our understanding of space weathering features. From the returned soils it was found that natural lunar soils were darker, with significantly weaker absorption bands for the diagnostic minerals than crushed materials from the same site (Adams and McCord, 1970; Pieters and Noble, 2016). Returned samples also revealed that up to 60 % of lunar soil is composed of amorphous glass-welded aggregates, termed agglutinates (Mckay et al. 1991). The discovery of nanophase Iron-Nickel grains (abbreviated to $npFe^0$) within the agglutinates and as inclusions within depositional rims surrounding individual mineral grains proved pivotal in our understanding what produces the darkening observed in the lunar soils, which is believed to be a consequence of the $npFe^0$ (Hapke 2001; Keller and MacKay 1993; Keller and McKay 1997). Amorphous solar-wind damaged rims containing no $npFe^0$ were also identified by (Keller and MacKay 1993; Keller and McKay 1997). An example of a $npFe^0$ bearing agglutinate is shown in Figure 1.17. It is generally agreed that micrometeorite bombardment and solar-wind irradiation are involved in the production of agglutinates, amorphous rims, and $npFe^0$ grains however, the relative contribution of each remains debated (Hapke 2001; Pieters and Noble 2016).

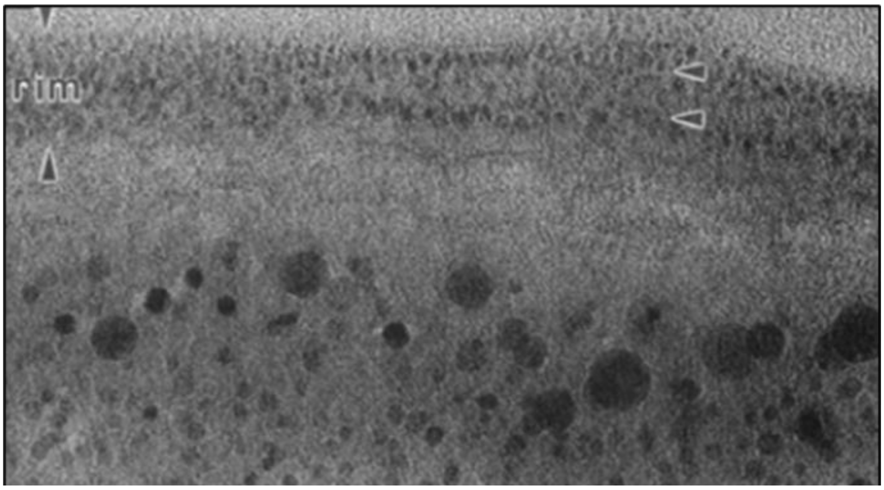

Figure 1.17*. Transmission electron microscope image through a lunar agglutinate with many npFe^0 particles within the rim labelled by the arrows. Metal particles in the interior (bottom of the image) are observed to be several orders of magnitude larger than those in the rim. Image adapted from* Pieters et al. (2000).

Understanding the space weathering processes affecting asteroids is considerably more challenging than the lunar case due to the lack of returned samples; just three sample return missions have so far taken place. Researchers therefore rely on the meteorite record to gain insights into the space weathering likely experienced by asteroids. Given the diversity of meteorite groups, lack of spatial context regarding their origin within a parent body, and sometimes significant secondary processing meteorites can prove complex specimens for space weathering studies. Understanding the space weathering processes in this context is important for drawing links between the different asteroid and meteorite classes, as discussed previously in section 1.2 (Brunetto et al. 2015).

Meteorite evidence for space weathering processes has long been noted within the literature with micrometeorite impact craters (Brownlee and Rajan 1973), irradiation damage tracks (Goswami and Lal 1979; Pellas et al. 1969; Price et al. 1975), gas-rich meteorites (Gerling and Levskii 1956; Goswami et al. 1984), brecciation (Bischoff et al. 2006; Partsch 1843), and shock (Stöffler et al. 1988) all reported.

As discussed previously space weathering can produce significant changes within airless bodies, all of which present challenges to obtaining an accurate understanding of solar system processes and early disk dynamics. Space weathering also presents challenges for correlating asteroids and meteorites with the need for a better understanding of asteroidal space weathering, and by extension that present in meteorites, highlighted by the recently returned Ryugu samples, courtesy of the JAXA Hayabusa 2 mission. Prior to arrival at the asteroid studies had suggested a CM-like composition for Ryugu (Le Corre et al. 2018; Sugita et al. 2013; Vilas 2008). However, following higher resolution orbital analysis and sample return analysis Ryugu was shown to be more akin to a CI chondrite (Yada et al. 2022). During subsequent attempts to understand what caused the initial mischaracterisation of asteroid Ryugu, it has been shown that the reflectance spectra of CI chondrites is severely affected by terrestrial weathering and that the surface of Ryugu is likely more significantly space weathered than initially thought (Amano et al. 2023; Matsuoka et al.).

Drawing on previous studies, space weathering processes can be broadly split into two categories, impact related processes and irradiation effects (Pieters and Noble 2016). Figure 1.18 illustrates the different space weathering processes believed to effect different solar system bodies.

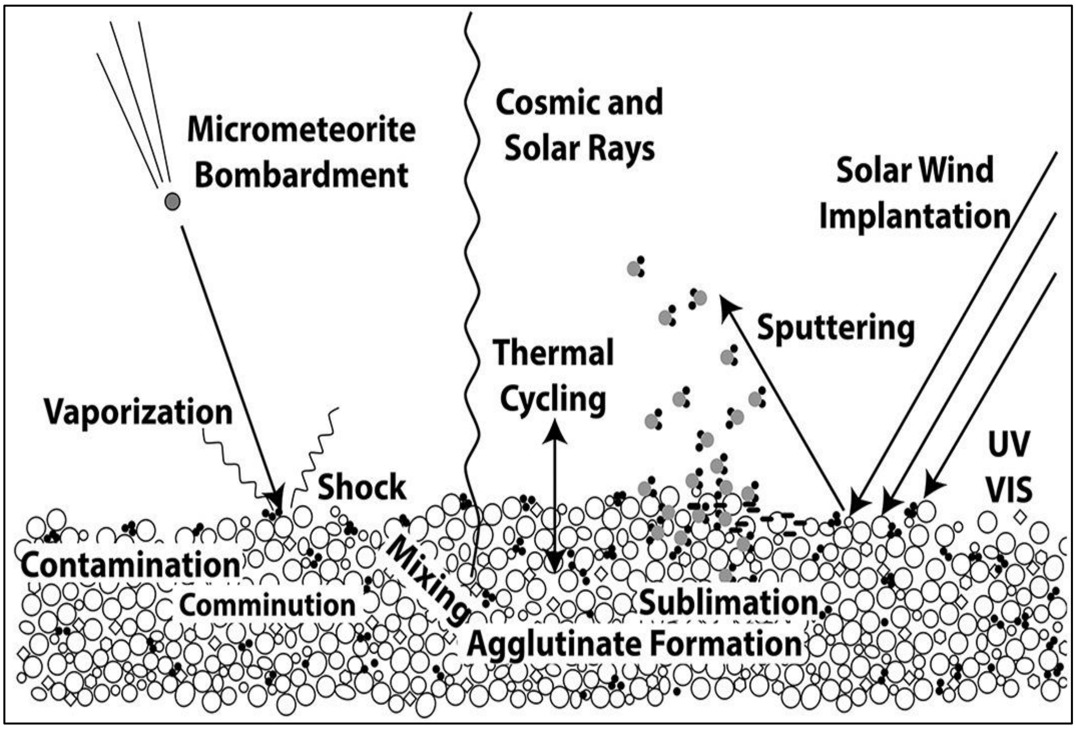

Figure 1.18*. Schematic illustration of the different space weathering processes believed to be acting on solar system bodies. The effect of each process illustrated varies between bodies and is poorly constrained. Illustration sourced from* Pieters and Noble (2016).

1.3.5.1 Impact Processes

Impact related space weathering includes impacts on all scales from the large events which produce catastrophic disruption of a parent body, smaller events producing brecciation and shock effects, and micrometeorite bombardment. This range of impactor sizes is clearly reflected by the cratering observed on the lunar surface where sizes range from ~1000 km to less than 1 um in diameter (Mckay et al. 1991). While all scales of impact are examples of space weathering, it is more typical within the literature for space weathering impacts to refer specifically to micrometeorite bombardment and its associated effects. Despite their small size the hypervelocity nature of the micrometeorites facilitates the production of vaporisation deposits and localised shock illustrated in Figure 1.18.

1.3.5.2 Irradiation

Irradiation can be the result of electromagnetic radiation or charged atomic particles. The precise nature of the irradiation depends on the source which could include the Sun, magnetosphere or other galactic origins. The different forms of irradiation and their effects will be discussed in Chapter 5.

1.4 Relevance of This Project

Accurate knowledge of the processes involved in the formation and evolution of C-type asteroids is crucial for our understanding of primitive material in the solar system. The CM chondrites represent the most readily available source of material analogous to the C-type asteroids and therefore the best material to use to try and answer these questions. Furthermore, the CM chondrites have long been hailed as potentially important carriers of water and organic components to the early Earth (Alexander et al. 2012; Johnson and Fanale 1973; Trigo-Rodríguez et al. 2019; Vacher et al.). A detailed understanding of the processing they experienced whilst incorporated into their asteroid parent bodies is therefore crucial for the accuracy of any conclusions regarding their role in bringing biologically significant components to Earth.

Fundamental to our understanding of the CM chondrites and their parent body/bodies are chondrules. Being one of the first formed and dominant components of CMs, chondrules record important information regarding the primary accretionary processes occurring during the early solar system and the subsequent secondary processes such as alteration and impact processing which have shaped the parent asteroids since their formation.

This work is also timely because at the time of writing NASA's ORSIRIS-REx mission has just returned material collected directly from uppermost few cm-mm's of asteroid Bennu. Bennu is spectrally identified as a B-type NEA and therefore shares spectral properties with the carbonaceous chondrites, including the CM's. Given the close spectral affinity to CM chondrites a thorough understanding of the physical properties such as chondrule size and orientation are vital for the correct interpretation of this material and its pre-collection history.

1.5 Overview of Chapters

1.5.1 Chapter 3

Chondrule size is an important classification criterion for chondritic meteorites and is used to distinguish between chondritic groups and as evidence for linking groups into clans (e.g. CM-CO clan). Chondrule sizes within the CM chondrites are frequently reported as averaging 270-300 μm however, recent published work has reported CM chondrule size averages significantly below this average with chondrule sizes far more alike to those observed in CO chondrites (~150 μm). Chapter 3 therefore aims to re-examine chondrule sizes within the CM chondrite group. Using a suite of CM chondrites across a range of petrologic subtypes chapter 3 sets out: 1) a new standardised measurement methodology for chondrules, 2) an updated analysis of average chondrule sizes within the CM group, and 3) an analysis of the CM-CO relationship through the lens of chondrule size and implications of this relationship on accretionary processes on the CM parent body.

The chapter 3 study utilises SEM and XCT analysis to collect 2D and 3D measurements of whole chondrules for size analysis. The collection of 2D and 3D data sets also allows the study to investigate and review numerous stereological correction methodologies, highlighting the importance of acknowledging the limitations of 2D size analysis.

1.5.2 Chapter 4

Petrofabrics characterised by chondrule alignment and deformation, fractures, and TCI structures are frequently reported within the CM chondrite group. However, despite their seemingly ubiquitous nature they remain poorly characterised, and their origins poorly understood. Within chapter 4 high-resolution 3D analysis is applied to a suite of CM chondrites, representing a range of petrologic subtypes and brecciation states, to examine evidence of chondrule-defined petrofabrics. The nature of the fabrics detected is used to investigate the post-accretionary processing which may have been experienced by the CM parent body/bodies and explore the true extent of chondrule deformation.

Additionally, by examining the relationships between detected fabric orientations and other post-accretionary processes such as brecciation and aqueous alteration, chapter 4 also assesses the relative chronology of alteration events and the implications for current models of alteration.

1.5.3 Chapter 5

Chapter five is a review style chapter examining the evidence for space weathering by heavy, high energy ion irradiation within CM chondrite olivine grains, using latent damage track analysis. The types of ion irradiation are explored, and mechanisms of damage track production and revelation discussed. A review of some of the most significant studies relating to this topic is provided outlining the methods and findings from previous studies and highlighting the lack of recent research in this field. Finally, it is suggested that there should be a renewed application of this technique, especially to some of the more recent and highly brecciated CM falls. Further study using this technique could provide fresh insights into the surface processes occurring on the CM parent body/bodies with implications for our understanding of other post-accretionary processes such as those discussed in chapter 4.

1.5.4 Chapter 6

Chapter six synthesises the previous chapters, setting out the key findings from this project and how they improve our understanding for the pre- and post-accretionary histories of CM chondrites and their parent body/bodies. Chapter six also summaries the usefulness of 3D analysis techniques such as XCT for the study of chondritic meteorites.

3.1.1 Chapter 7

Chapter seven outlines' avenues for future research including the application of the CIS methodology and high-resolution 3D analysis (size and orientation) to studies of other CM chondrites and other chondritic groups. Also discussed is the potential usefulness of future application of WN etchant to CM chondrite studies. Identification of track-rich grains could help improve our understanding of the accretionary and regolith turnover processes occurring on the CM parent body(ies).

Chapter 2 Methods, Techniques & Samples

2.1 Scanning Electron Microscopy (SEM)

2.1.1 Overview

Scanning electron microscopy (SEM) is a microscopic technique developed during the mid-20^{th} century. SEM uses the interaction of a focused electron beam with the outermost <~1 μm of a sample to produce a greyscale image allowing nano-meter sized details in surface topography to be resolved at magnifications of up to x300,000 (Abdullah and Mohammed 2018; Goldstein et al. 1992; Lee and Smith 2006).

Three main types of SEM exist: conventional SEM (CSEM, more often referred to just as SEM), environmental SEM (ESEM), and low vacuum SEM (LV SEM). The primary difference between the three SEM techniques is the pressure at which they operate (10^{-6} torr, 0.2-20 torr and 0.2-2 torr respectively) (Abdullah and Mohammed 2018). Some SEMs combine a conventional and low vacuum SEM to create a variable pressure SEM (VP SEM), such as the microscope used throughout this thesis, a Zeiss Sigma Field Emission Gun Variable Pressure SEM at the University of Glasgow's Geoanalytical Electron Microscopy & Spectroscopy Centre (GEMS) (Figure 2.1). A vacuum is necessary when conducting SEM analysis to minimise the effect of collisions between the returning electrons and atmospheric molecules, the result of which can disrupt the signal (Goldstein et al. 2017).

Most SEMs are fitted with two detectors, a secondary electron (SE) detector and a backscatter electron (BSE) detector. The SE detector can obtain topographic information from a sample while the BSE detector produces mean atomic number contrast images. Additional detectors for energy dispersive X-ray spectroscopy (EDS) and electron backscattered diffraction (EBSD) facilitate a wider range of analysis. Of the two EDS detectors are most commonly fitted to SEMs and discussed in more detail in section 2.2.

In this thesis SEM was used to collect BSE images and SE images and image mosaics of meteoritic thin sections. SEM was also used to collect elemental composition data by EDS mapping (discussed in section 2.2).

Figure 2.1. *Image of the Zeiss sigma field emission gun variable pressure (VP) SEM at the University of Glasgow's GEMs laboratory. This microscope was used for all imaging and mapping conducted during this thesis.*

2.1.2 How it Works

The process of generating an image using an SEM begins with the creation of an electron beam, produced by emission of electrons from an electron gun (typically made of tungsten). The electron beam is then accelerated to a higher energy, typically between 0.1-30 keV (Goldstein et al. 2017). A series of apertures, lenses and/or electromagnetic coils then modify, and compress the accelerated electron beam into a smaller diameter, before directing the beam to a discrete location known as the region of primary excitation. This process allows for a sharper image to be computed (Goldstein et al. 2017; Zhou et al. 2007). The final spot size of the electron beam is usually <10 nm and while a static spot is used for some types of analysis, during imaging the electrons are rastered over the incident area (Goldstein et al. 2017).

The resolution of surface-level details detected using SEM is dependent on the incident beam penetration depth, itself a function of beam energy and the atomic number of the sample being analysed. Penetration depths of around 1 μm are possible in some instances (Lee and Smith 2006; Zhou et al. 2007). Where the electron beam is accelerated to a higher energy, the electron beam is capable of deeper sample penetration. However, this effect can be offset by the atomic number of the material examined. If the region of interest has a high atomic number, then the incident electrons do not penetrate as deep; Figure 2.2 illustrates this relationship (Zhou et al. 2007).

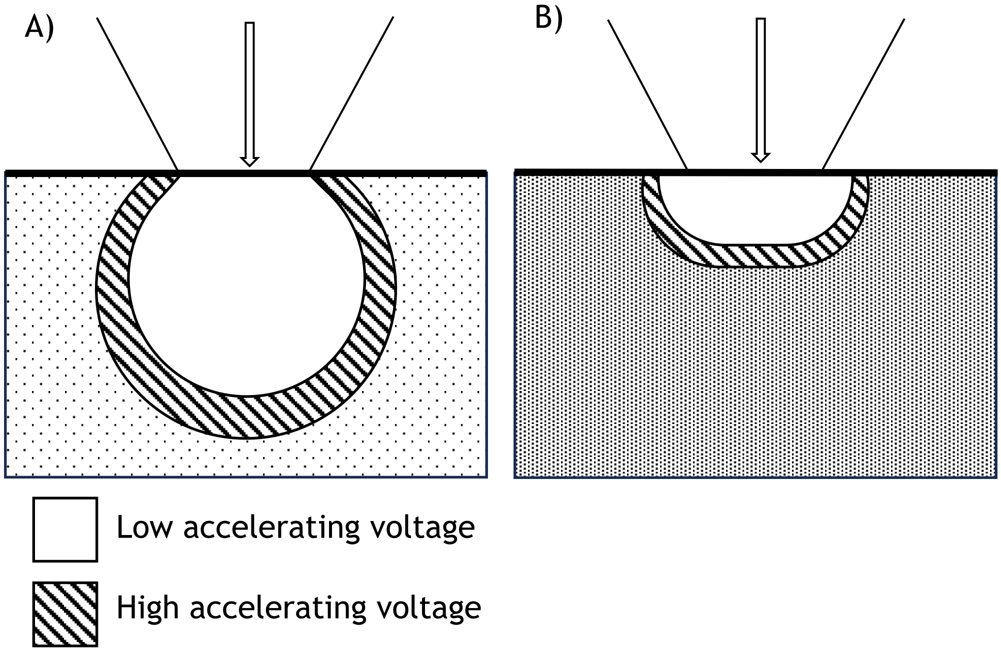

Figure 2.2. *Illustration showing the relationship between accelerating voltage and material atomic weight. Both illustrations are at the same scale with a total cross-sectional depth of a few micons. Accelerating voltage is the same. A) A lower atomic weight material facillitating deeper penetration with a 'teardrop' shaped interaction volume B) A higher atomic weight material allowing shallower penetration in a hemisphodial shaped interaction. Figure adapted from Zhou et al. (2007).*

Where the electron beam meets and interacts with the sample it produces backscattered electrons, secondary electrons, auger electrons, characteristic X-rays and cathodoluminescence as shown in Figure 2.3. BSEs and SEs are described below; X-rays will be discussed in section 2.3.

- BSEs are electrons emerging from the sample with a large proportion of the original incident beam energy (>50 eV) having experienced scattering and deflection by the atomic structure within the sample (Goldstein et al.

2017). 10-50% of the incident beam electrons are typically backscattered towards their source. The higher energy of the produced BSEs means they are less easily absorbed into the sample and consequently their generation occurs over a larger area of a sample. This process results in a significantly reduced lateral resolution when compared to SEs; ~1 µm compared to ~ 10 nm (Zhou et al. 2007). An example of a BSE image is shown in Figure 2.4A.

- SEs are electrons which are liberated from the atomic structure of the sample atom by ionization produced by the incident electrons. Because of the poor kinetic energy transfer between the beam electrons and the SEs, secondary electrons have very low energies typically around 3-5 eV (Goldstein et al. 2017; Zhou et al. 2007). The low energies of SEs mean that they can only escape from the uppermost few nm of a sample making them effective for high resolution topographic imaging and investigation (Zhou et al. 2007). An example SE image is shown in Figure 2.4B.

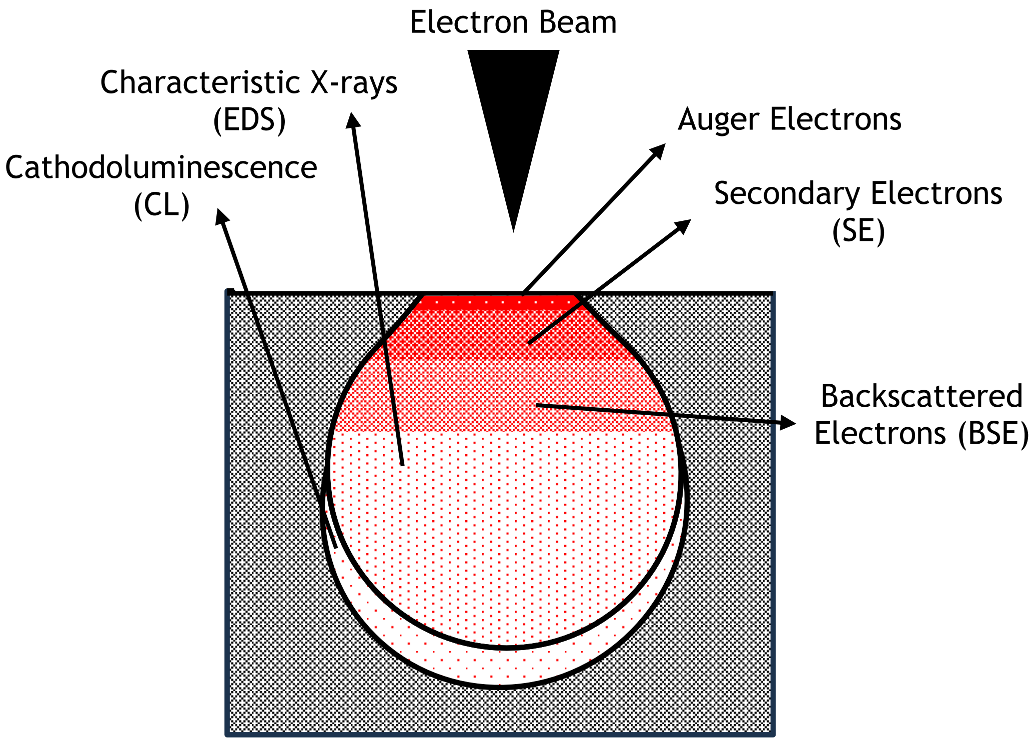

Figure 2.3. *Illustration showing the interaction of an electron beam with a specimen surface and the different signals generated from this interaction.*

The generated BSEs and SEs are detected and their signals digitised to computer greyscale values which can be assigned to a specific pixel on the monitor to produce an image (Goldstein et al. 2017).

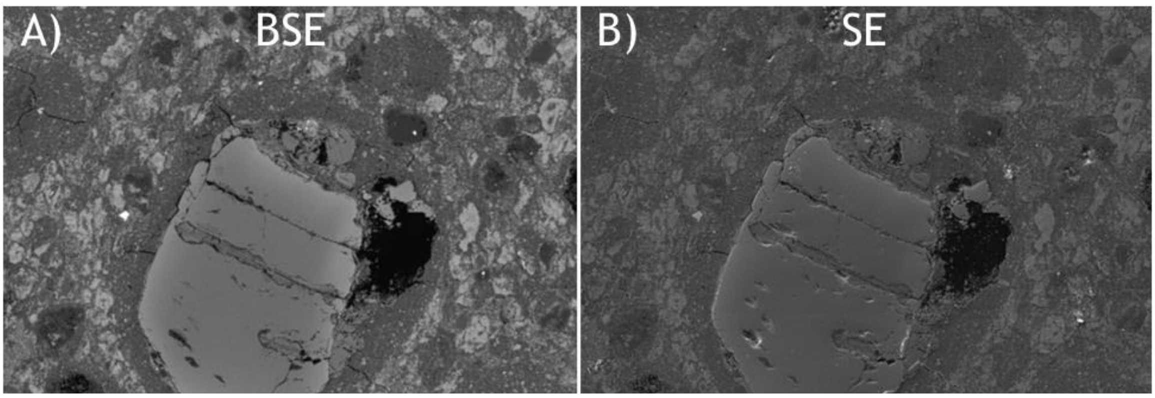

Figure 2.4. *Illustration showing the differences between BSE (A) and SE (B) images. Both images show an identical location within the CM2 chondrite Aguas Zarcas and were collected under the same conditions and at the same scale. The images clearly show the topographic differences picked up using SE compared to BSE.*

2.1.3 Sample Preparation

During the work presented in this thesis, thin sections and polished blocks to be analysed using SEM techniques were polished and carbon coated prior to data collection. Polishing was conducted using a Buehler Beta Grinder-Polisher with a 1 μm Al polishing pad initially, followed by a 0.3 μm Al pad. Al-Glycol solution was used as a polishing lubricant. A Quorum Q150T coater, was used to apply a 20 nm carbon coat to the thin sections and polished blocks after polishing. The machine used is a termolecular pumper coater which uses sharpened carbon rods to produce an even coating under high vacuum conditions. The purpose of the carbon coat is to minimise the charging experienced by the insulating sample material preventing sample surface deterioration and image aberration.

2.1.4 Data Collection and Processing

Data collection was conducted at the University of Glasgow's GEMS lab, located in the school of Geographical and Earth Sciences. Data collection was conducted using a Zeiss Sigma Field Emission Gun Variable Pressure SEM operated at an accelerating voltage of 20 kV and beam current of 1-2 nA. Zeiss image software was used for single area image collection, whereas proprietary processing software Aztec was used for large area montages where the images were stitched together with an overlap of 10%.

2.2 Energy Dispersive X-ray Spectroscopy (EDS)

2.2.1 Overview

EDS detectors allow the elemental composition of a sample to be assessed. The technique is generally thought of as being qualitative to semi-quantitative with data considered quantitative when known standards are used alongside the sample to calibrate the intensities of detected X-rays (Goldstein et al. 2017).

2.2.2 How it Works

EDS analysis uses a process known as photoelectric absorption. During this process an incident electron liberates an inner-shell electron which has a lower binding energy than the energy of the incident X-ray photon, leaving the sample atom ionized. To re-establish charge balance an outer shell electron transitions to fill the inner shell vacancy - for example, from the L_3 subshell to the K shell (Figure 2.5.) (Zhou et al. 2007). The relaxation of this ion causes the emission of an X-ray photon (Figure 2.3) with an energy equal to the differences in binding energies of the shells involved in the process (Figure 2.5) (Hodoroaba 2019). The newly liberated electron becomes a photoelectron while the original incident X-ray photon is absorbed. Incident X-ray photon energy and the atomic weight of the specimen are controlling factors in the probability of this effect which, can be approximately described by: $\sim Z^4$ (Als-Nielsen and McMorrow 2011; Hsieh 2022; Ketcham and Carlson 2001). Of the X-rays emitted during the ionization process only a small fraction are collected by the EDS detector, where they are displayed as peaks along the energy spectrum, as illustrated in Figure 2.6. The detected X-ray energies are characteristic of an atomic structure and thus the element from which they were emitted. Thus, using the detected X-ray energies, the different elements present can be determined. The signal amplitude for each X-ray peak can also be used to assess the relative abundance of elements providing a qualitative indication of a sample’s chemical composition, alongside major and minor element chemistry.

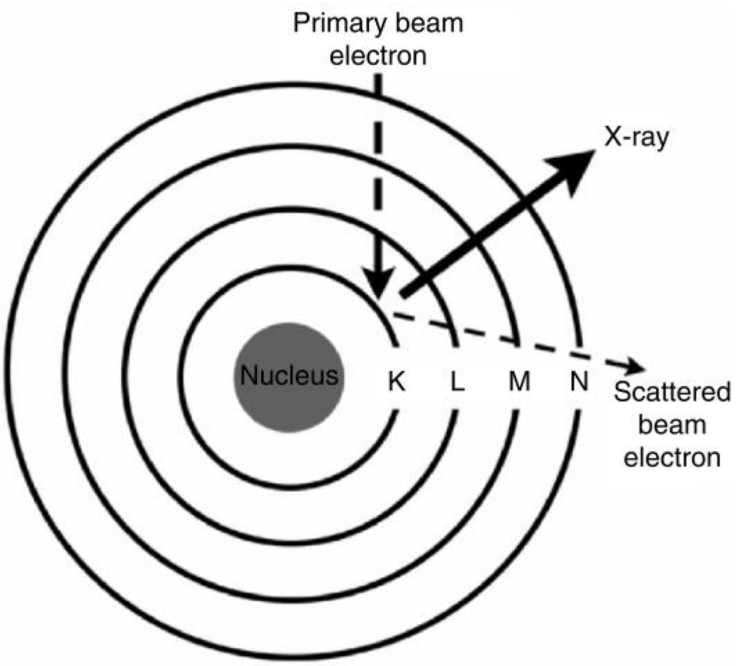

Figure 2.5*. A diagram illustrating the process of X-ray generation following beam interaction with a sample atom. In this example a K shell orbital electron is ejected and replaced by an electron from an outer orbital. Image taken from (Anderhalt, 2007).*

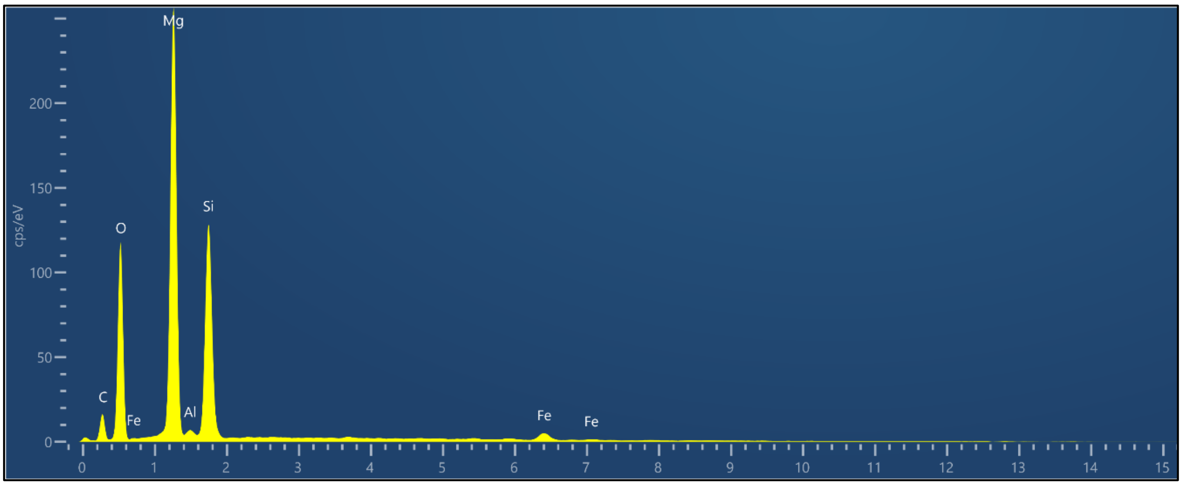

Figure 2.6. *Example EDS spectrum collected from the olivine fragment in Figure* ***2.4***. *Each of the major peaks is identified and labelled automatically in Aztec software.*

2.2.3 Data Collection and Processing

EDS analysis was carried out on thin sections and polished blocks following the polishing and carbon coating procedure mentioned in section 2.1.3. Data collection used an Oxford Instruments 170 mm^2 silicon-drift detector attached to the VP SEM at the GEMs lab. Proprietary processing software Aztec, from Oxford Instruments was used for collecting and analysing the EDS data. Where large area EDS maps were collected, montaging was conducted in Aztec software with an image overlap of 10%.

2.3 X-ray Computed Tomography

X-ray computed tomography (XCT) is a three-dimensional (3D) imaging technique. Originally developed during the 1970's it was initially applied to the field of medical study before being proven as a useful tool in Earth and Planetary science (Ambrose 1973; Hounsfield 1995; Vinegar and Wellington 1987; Wellington and Vinegar 1987). The first application of XCT on a meteoritic sample came in 1983 using Allende (CV3) (Arnold et al. 1983).

The primary benefit of XCT is its non-destructive nature, being able to visualise the internal structure of samples without the need for sectioning. This technique also allows for assessment of the internal structure of a meteorite sample to inform the region and orientation of a section to be made, thus maximising the scientific return (previously most sections were prepared from meteorite samples in a random orientation relative to their internal structure). XCT does not have any significant impact on potentially X-ray sensitive properties such as magnetism or astrobiologically significant amino acids and polycyclic aromatic hydrocarbons (PAHs) (Ebel et al. 2009; Friedrich et al. 2016; Hanna and Ketcham 2017).

The technique of XCT can be divided into four classes depending on the spatial resolution achieved, and the sizes of sample for which they are most suitable: Conventional CT (scale of observation: m, scale of resolution: mm), high-resolution CT (scale of observation: dm, scale of resolution: 100 μm), ultra-high-resolution CT (scale of observation: cm, scale of resolution: 10 μm) and microtomography, often abbreviated to μCT (scale of observation: mm, scale of resolution: μm) (Ketcham and Carlson 2001). The application of XCT to meteoritic studies has increased significantly over the past decade following improvements in computing power, data processing/analysis packages and the development of μCT instruments.

2.3.1 How it works

An X-ray source generates a beam of X-ray photons which are directed towards a sample. The X-ray photons penetrate the sample and are attenuated based on the sample composition and incident X-ray photon energy. During conventional X-ray imaging a single view is acquired. However, during XCT imaging multiple images across multiple sets of views are collected over a range of angular orientations. Such a result is achieved by rotating the sample through 360° during the imaging process to produce a series of sinograms (Kastner and Heinzl 2018; Ketcham and Carlson 2001).

Once collected the data must be processed to convert the sinograms collected over the 360° rotation into a series of 2D image slices which comprise the final 3D volume. This step is called reconstruction and typically involves applying a mathematical filtered backprojection reconstruction (Ketcham and Carlson 2001). During reconstruction the raw X-ray intensity data in each sinogram is converted to CT values, commonly based on a 12-bit format (thus 4096 possible values) (Ketcham and Carlson 2001). In most industrial systems these CT values correspond to the greyscale values in the image files produced and exported following reconstruction. Once reconstruction is complected the 3D volume can be viewed in any orientation with the 2D slice corresponding to what would be encountered if the sample were sectioned along the line of orientation (Ketcham and Carlson 2001).

Crucial to understanding XCT data is knowledge of the attenuation experienced by the incident X-rays during scanning. In a homogenous material, X-ray attenuation can be described simply by Lambert-Beer's Law (Equation 2.1) (Hanna and Ketcham 2017).

$$I = I_0 exp(-\mu\chi) \quad \text{(Equation 2.1)}$$

where I is the recorded X-ray intensity, I_0 the initial X-ray intensity, μ the linear attenuation coefficient of the material and χ is the path length of the X-ray, including its passage through the material. More typically however, materials are heterogeneous and therefore the linear attenuation of each material present must be accounted for (μ_i), as well as their linear extent (χ_i). The attenuation experienced by a heterogeneous sample is therefore express more accurately by Equation 2.2 (Hanna and Ketcham 2017).

$$I = I_0 exp[\sum(-\mu_i\chi_i)] \quad \text{(Equation 2.2)}$$

Three different absorption or scattering processes are responsible for attenuation of X-rays: Photoelectric absorption (described previously in Section 2.2.2), incoherent (Compton) scattering and coherent (Rayleigh) scattering.

1. Incoherent (Compton) scattering: Where the incident X-ray photon energy is considerably greater than the electron binding energy the incident X-ray photon ejects an outer shell electron while retaining some of its original energy. The reduction in the original photon's energy causes it to be deflected or scattered prior to being detected (Hsieh 2022; Ketcham and Carlson 2001). Scattered photons can be deflected between 0-180° (Figure 2.7A) (Hsieh 2022). The probability of this effect is dependent on the electron density of the material, causing Compton scattering to be

considered less sensitive to sample composition than the photoelectric effect, particularly at lower energies (Hsieh 2022).

2. Coherent (Rayleigh) scattering: During this interaction none of the initial photon energy is converted into kinetic energy and there is no ionization. Instead, the incoming X-ray photon produces a momentary vibration of the electrons within an atom. This vibration causes the release of an X-ray photon of the same energy. The overall effect is that the incident X-ray is scattered in the forward direction producing a slightly broadened X-ray beam (Figure 2.7B) (Hsieh 2022).

For geological materials the photoelectric effect is dominant at low X-ray energies (50-100 keV) whilst Compton scattering is dominant at higher energies (5-10MeV) (Ketcham and Carlson 2001).

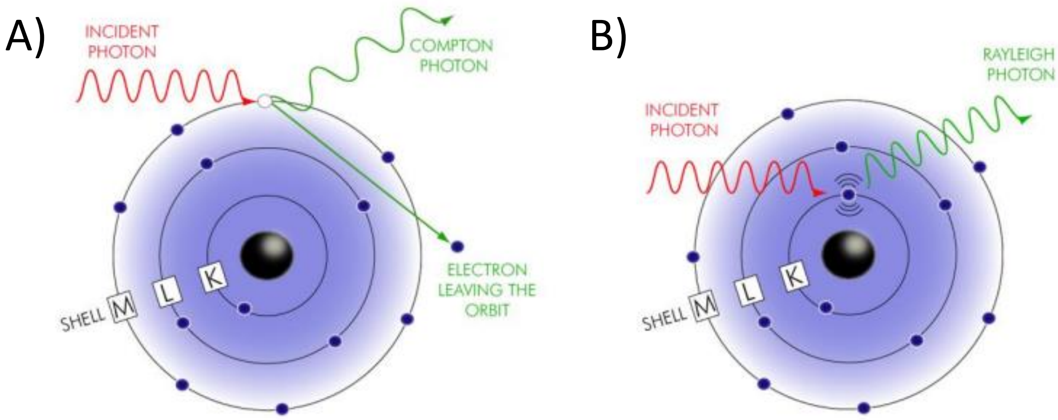

Figure 2.7. *A diagram illustrating the differences between Compton (incoherent) scattering (A) and Rayleigh (coherent) scattering (B). Illustration sourced from* Snickt, (2012).

2.3.2 XCT Analysis

Each chapter that uses XCT data describes the data collection location, scan parameters and analysis methodology employed. However, given the complexity and multi-stage nature of the analysis process for the XCT data presented in this thesis, a more thorough description of the analysis methodologies is provided in the following sections.

2.3.2.1 Volume Filtering

All XCT analysis conducted during this work was carried out using Thermo Fisher Scientific Avizo software. Following initial inspection of the data volume to ensure no errors had occurred during the backprojection and reconstruction process a ‘filter sandbox’ function was applied to the volume. The filter aims to reduce noise in the volume and allow better identification of object boundaries. The filter applied was a non-local means filter with the parameters: search window: 9, local neighbour: 4, similarity value: 0.4. The effect of the non-local means filter is illustrated in Figure 2.8.

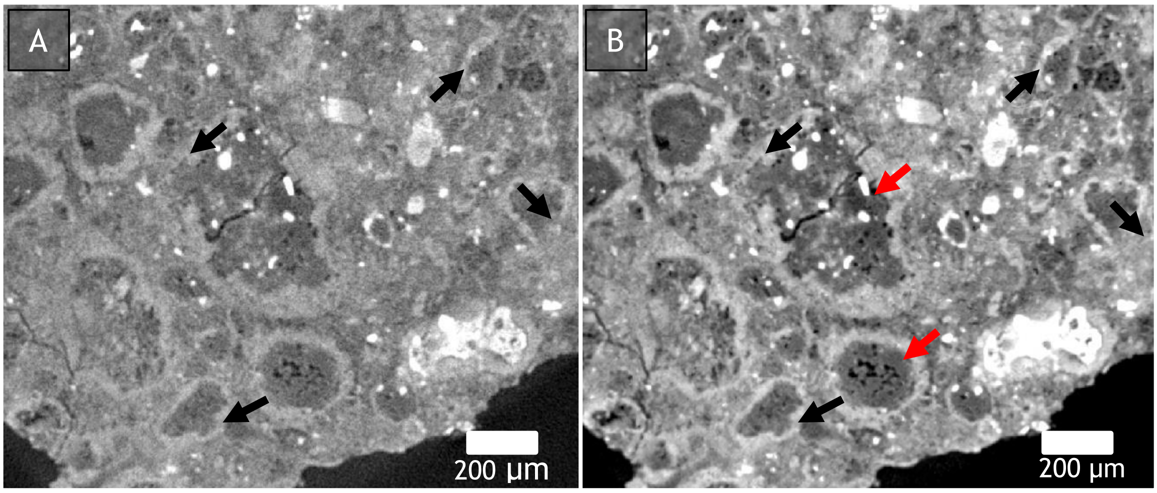

***Figure 2.8**. XCT slices from LEW 85311 illustrating the difference in appearance between the unfiltered data (A) and the data following application of a non-local means filter (B). The black arrows indicate example regions where application of the filter has produced a clearer boundary edge. The Red arrows indicate dark-toned objects identified as chondrules.*

2.3.2.2 Chondrule and Metal Grain Identification

Identification of the various phases within XCT data volumes is based on the different attenuation coefficients of the materials present, which in turn is reflected in their greyscale value displayed (as discussed previously). The work contained within this thesis focuses on chondrules and metal grains and so only the identification of those phases will be discussed here.

Chondrules are composed predominantly of the Mg-Fe silicates olivine and pyroxene and have a low X-ray attenuation coefficient and appear as dark grey objects within the brighter matrix of the host meteorite. Within the literature chondrules within XCT data sets are typically referred to as dark-toned objects (Friedrich et al. 2008; Hanna et al. 2012; Lindgren et al. 2015). In addition to their low greyscale intensity, their shape and the presence of FGRs can also be used to help identify chondrules in XCT volumes. Example chondrules and their appearance in XCT are shown in Figure 2.8.

Metal grains within the CM chondrites are typically composed of Fe and Ni with the relative abundances of each determining the exact mineralogy (kamacite: ~90 wt. % Fe, ~10 wt. % Ni; taenite >~12 wt.% Ni.). Given the high atomic weight of these minerals, incident X-rays are highly attenuated and thus have a greater greyscale intensity than surrounding material, appearing bright white within the XCT volume. Distinguishing between Fe,Ni metal grains and any Fe-sulphides (FeS) which may also be present is possible as FeS grains appear slightly darker (bright grey) when compared to the bright white Fe,Ni metal grains (Friedrich et al. 2008). Typical metal grain sizes within the CM chondrites vary and can range from 10’s to 100’s of micrometres with isolated metal grains typically observed to be larger (van Kooten et al. 2022). These sizes allow for high resolution XCT and SEM techniques to used in their analyses.

2.3.2.3 3D Segmentation

Segmentation in 3D is significantly more time-consuming than conventional 2D segmentation as to capture their full 3D shape each chondrule must be accurately traced multiple times. Chondrules within XCT data volumes are particularly complicated to segment due to their heterogeneity and their greyscale intensity (based on X-ray attenuation) which is similar to, and in some instances the same as, the surrounding matrix, as also noted by Hanna et al. (2015). Consequently, standard semi-automated & automated segmentation techniques such as thresholding and trainable segmentation programmes, are unable to accurately detect and distinguish chondrules from the data volume. A manual approach is therefore required to ensure reliable and accurate segmentation. Two forms of manual chondrule segmentation are used in the literature:

- Full segmentation involves segmenting the outline of chondrules in all the XCT slices in which they appear. For example, a 300 μm spherical chondrule in a scan volume with a resolution of 3 μm/voxel, would require ~100 segmentations.

- Partial segmentation developed by Hanna et al. (2015) involves segmenting a representative slice in each orthogonal view (XY, XZ and YZ) and fitting an ellipse to the outer margins of the intersecting planes. Using this method requires only three segmentations per chondrule.

A comparison of the output for full and partial segmentation methodologies is shown in Figure 2.9 Hanna et al. (2015) tested the partial segmentation approach and found it provided an accurate indicator of chondrule orientation compared to the full segmentation approach. The differences in chondrule size measured using the two techniques were tested using a chondrule within LEW 85311. Results revealed the partial segmentation produces a fractionally smaller measurement, with a 1.82 % difference recorded in the long axis. Given the range of chondrites investigated, the numbers of chondrules requiring segmentation, and the small difference between the techniques, the faster and simpler partial method is used for all 3D segmentation in this thesis.

Segmentation of each representative cross section was conducted using the ‘draw’ tool in the Avizo Segmentation Editor. The three intersecting planes produced by the partial segmentation were then fitted with an ellipsoid for the analysis phase using a specialized merit function in Blob3D software (Ketcham 2005a).

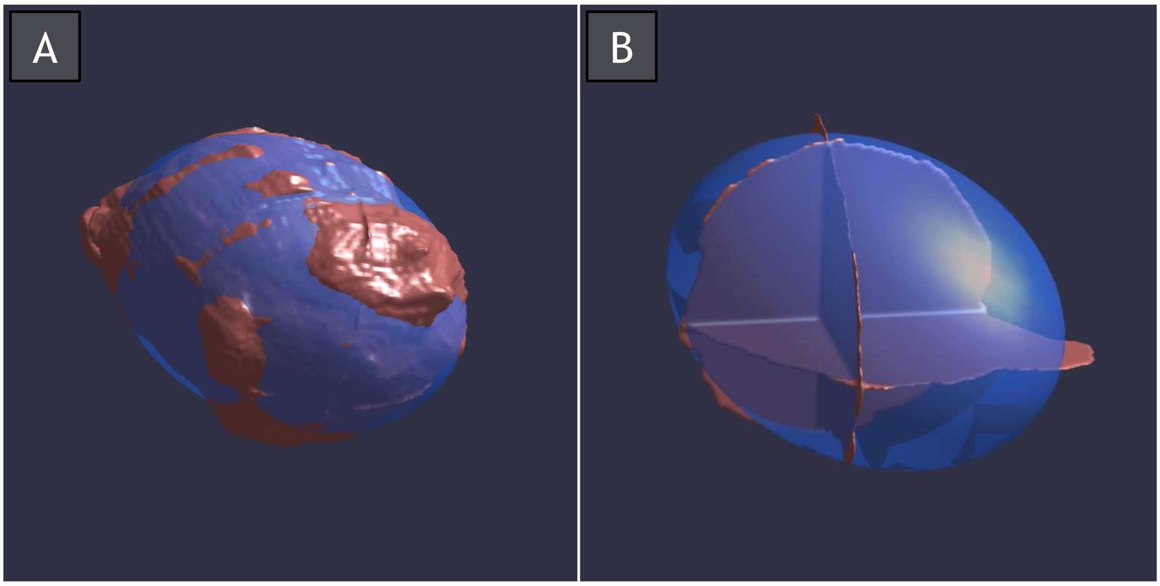

Figure 2.9*. A comparison between the full and partial segmentation methodologies A) The full segmentation method a chondrule segmented in every XCT slice it appears B) The partial segmentation method where a representative cross section for each orthogonal view has been segmented. In both cases best-fit ellipsoids have been fitted to the segmented chondrules.*

Size and Orientation Analysis

3D chondrule size analysis is carried out on the produced ellipsoids in Blob3D with the Primary (longest), Intermediate and Tertiary (shortest) axes measured perpendicular to one another. All length measurements reported by Blob3D are in mm and later converted to µm where appropriate.

Orientation analysis is also carried out on the ellipsoids in Blob3D with the orientation of each axis described by three directional cosines (e.g., X1, Y1 and Z1 for the primary axis). Directional cosines define a vector in Euclidean space based on Cartesian notation. The three directional cosines for each axis can be described as follows:

$$\alpha = cos\alpha = \frac{v \cdot e_\chi}{\|v\|} = \frac{v_\chi}{\sqrt{v_\chi^2+v_y^2+v_z^2}} \qquad \text{(Equation 2.3)}$$

$$\beta = cosb = \frac{v \cdot e_y}{\|v\|} = \frac{v_y}{\sqrt{v_\chi^2+v_y^2+v_z^2}} \qquad \text{(Equation 2.4)}$$

$$\gamma = cosb = \frac{v \cdot e_z}{\|v\|} = \frac{v_z}{\sqrt{v_\chi^2+v_y^2+v_z^2}} \quad \text{(Equation 2.5)}$$

Where v is a Euclidean vector in three-dimensional space, e_χ, e_y, and e_z are the standard basis in cartesian notation for each axis, and v_χ, v_y, and v_z are the x, y, and z components of the vector respectively.

For simplicity and useful visualisation, the directional cosines were subsequently converted into the more geologically useful parameters: trend and plunge. These were then plotted on equal area stereographic projections using Stereo32 software (Roeller and Trepmann 2010).

2.3.2.4 Porosity Loss Estimates

The degree of porosity loss resulting from post-accretion compaction processes can also be estimated by assuming an idealized spherical chondrule shape prior to any deformation, and the strain (ε) experienced during deformation is entirely uniaxial (Hanna et al. 2015). The equations to calculate porosity loss (Equations 2.9 & 2.12) were first set out by Hanna et al., (2015) and a full derivation is found below:

Strain: Firstly, the strain experienced is calculated based on the degree to which chondrules are no longer spherical. The tertiary axis (r_3) is related to strain (ε) by the radius (R) of the undeformed chondrule and strain as shown in Equation 2.6:

$$r_3 = R(1-\varepsilon) \quad \text{(Equation 2.6)}$$

Assuming the chondrule is incompressible and thus, the chondrule volume remains the same before and after deformation then Equation 2.7 is true, where r_1 represents the radius of the deformed ellipsoid r_1 long axis:

$$R^3 = r_3 r_1^2 \quad \text{(Equation 2.7)}$$

Aspect ratio (a) of the deformed ellipsoid can be defined by the ratio of the long (r_1) and short (r_3) axis as shown in Equation 2.8:

$$a = \frac{r_1}{r_3} \quad \text{(Equation 2.8)}$$

Rearranging Equations 2.6 & 2.8 and to substitute R and r_1 in Equation 2.7 leads to Equation 2.9 after simplification, allowing the strain experienced by a chondrule to be derived simply from just the aspect ratio of the deformed chondrule:

$$\varepsilon = 1 - a^{-2/3} \quad \text{(Equation 2.9)}$$

Porosity: To calculate the porosity (P) of a material requires grain volume (V_g) and bulk volume (V_b) as shown in Equation 2.10. Grain volume represents the volume of solid material excluding pore spaces and bulk volume is the total sample volume including pore spaces.

$$P = \left(1 - \frac{V_g}{V_b}\right) \times 100\% \quad \text{(Equation 2.10)}$$

It has been suggested that chondrule deformation is accompanied by porosity loss in the surrounding matrix (Hanna et al. 2015). As a result, the strain calculation in Equation 2.9 can be used to calculate the porosity lost in the matrix during deformation. Providing deformation of the matrix is accommodated entirely by pore space collapse, the grain volume would be constant, and the bulk volume reduces by a factor of (1- ε). Thus, post-deformation porosity (P_1) can be shown by Equation 2.11 and pre-deformation porosity (P_0) by Equation 2.12 (through the re-arrangement of Equation 2.6 and substitution for V_g into Equation 2.10.

$$P_1 = \left(1 - \frac{V_g}{(1-\varepsilon)V_b}\right) \times 100\% \quad \text{(Equation 2.11)}$$

$$P_0 = \left[1 - (1-\varepsilon)\left(1 - \frac{P_1}{100}\right)\right] \times 100\% \quad \text{(Equation 2.12)}$$

2.4 Samples

During this thesis a total of 10 different CM chondrites were analysed. A complete breakdown of the samples analysed is provide in Table 2.1 and Table 2.2.

The meteorites selected for study represent a range of petrologic subtypes allowing relationships between the characteristics explored in this thesis and the degree of aqueous alteration to be investigated. Additionally, all the samples selected have been identified as meteoritic breccia's and therefore contain evidence of impact related parent body processing which is relevant to this thesis.

The inclusion of the mildly altered CM chondrites Lewis Cliff (LEW) 85311 (CM2.7) (Lee et al. 2019) and Paris (2.7-2.9) (Rubin 2015) allows for expansion of the current literature regarding mildly altered CM chondrites and the ability to better extrapolate patterns towards the least altered end of the classification spectrum. Many of the samples selected for study are also considered fresh falls (Aguas Zarcas, Kolang, Shidian, and Winchcombe) these were selected due to their availability and relatively unstudied nature allowing this work to help build the literature database on these samples. Cold Bokkeveld and Murchison were selected for study as these represent arguably the most widely studies CM chondrites and form the foundation of much of our understanding of the CMs. Their inclusion allows importantly allows for comparison of this work with previous studies.

Table 2.1*. Information on the origins of all meteorites examined during this thesis.*

Meteorite	Fall/Find[†]	Year Collected	Fall/Find Location	Total Mass (g)[‡]	Weathering Grade[*]	Shock Effects
Aguas Zarcas	Fall	2019	Alajuela, Coasta Rica	2700	-	-
Cold Bokkeveld	Fall	1838	Western Cape, South Africa	5200	-	S1[1]
Kolang	Fall	2020	Sumatera Utara, Indonesia	2550	-	-
LaPaz Icefield (LAP) 02239	Find	2002	Antarctica	39.3	B	-
Lewis Cliff (LEW) 85311	Find	1985	Antarctica	199.5	B_e	S1[1]
Mighei	Fall	1889	Nikolayev, Ukraine	8000	-	S1[1]
Murchison	Fall	1969	Australia	100000	-	S1-S2[1]
Paris[3]	Find	2001	UNKNOWN	1370	W0	S1[2]
Shidian[4]	Fall	2017	Yunnan, China	1809	-	-
Winchcombe	Fall	2021	England, UK	602	-	-

[†]Falls are observed falling to Earth and are subsequently recovered, finds are merely found without being observed
[‡]The Meteoritical Society, (2023)
[*]Weathering grade reported for find meteorites only. In hand specimen: B – moderate rusting & B_e – moderate rusting with visible evaporite formation. In thin section: W0 – No visible oxidation of metal or sulfides (Wlotzka 1993).
[1]Scott et al., (1992)
[2]Rubin, (2015)

Table 2.2. *A breakdown of the CM thin sections and chips examined in this thesis and the literature classifications for petrologic type.*

Meteorite	2D Analysis	3D Analysis	Petrologic Type[a]	Petrologic Subtype[b]
	Section ID	Chip ID and Mass (g)		
Aguas Zarcas	AZ-P1[5] (PB) AZ-P2[5] (PB)	Aguas Zarcas (3.840)[5]	---	CM2.2-2.8[h]
Cold Bokkeveld	---	BM.1727 (2.154)[1]	1.4[d]	CM2.2[k], CM2.1-2.7[l]
Kolang[5]	(TS)	---	1.3[c]	CM2.2[c]
LaPaz Icefield (LAP) 02239	02239,5[2] (PB)	---	1.5[d]	CM2.4-2.5[i]
Lewis Cliff (LEW) 85311	85311,90[2] (TS)	LEW85311, 84[2]	1.7[e]	CM2.6-2.7[j]
Mighei	(TS)	---	1.4[f]	---
Murchison	3.864g TS1[5] (TS) BM1970.6 (P19258)[1] (PB) BM1988, M23 (P19261)[1] (PB)	Murchison (3.86)[5]	1.5[f]	CM2.5[k], CM2.9-CM2.7 (main lithology CM2.7[l])
Paris[3]	(PB)	---	---	CM2.7-2.9[m]
Shidian[4]	(PB)	---	---	CM2.1-2.6, mainly CM2.2[n]
Winchcombe	BM.2022, M9-14 (P30552)[1] (PB)	Bag4.17 (0.025)[1] Bag4.17 Crumbs & Frag[1] Bag1_Stone34 (0.238)[1] Bag6.2_Frag2[1] Bag6.2_Frag3[1]	1.1-1.2[g]	CM2.0-2.6[o]

PB = Polished resin block
TS = Thin section
[1]Natural History Museum (U.K)
[2]ANSMET
[3]Museum National d'Histoire Naturelle de Paris
[4]Chinese Academy of Sciences
[5]Commercially obtained (Skyfall Meteorites)
[a]Using the scheme of Howard et al. (2015)
[b]Using the scheme of Rubin et al. (2007)
[c]King et al. (2021)
[d]Howard et al. (2015). Value from LAP 02333, which is paired with LAP 02239
[e]Lee et al. (2019)
[f]Howard et al. (2015)
[g]King et al. (2022)
[h]Kerraouch et al. (2021)
[i]Lee et al. (2023)
[j]Choe et al. (2010)
[k]Rubin et al. (2007)
[l]Lentfort et al. (2020)
[m]Rubin (2015)
[n]Fan et al. (2022)
[o]Suttle et al. (2022)
--- denotes not measured

Chapter 3 Chondrule Sizes within the CM Carbonaceous Chondrites and Measurement Methodologies

C. J. Floyd[1*], S. Benito[2], P-E. Martin[1], L. E. Jenkins[1], E. Dunham[3], L. Daly[1,4,5], M. R. Lee[1]

[1]School of Geographical and Earth Sciences, University of Glasgow, Glasgow, G12 8QQ, UK.
[2]Ruhr-Universität Bochum, Chair of Materials Technology, Bochum 44780, Germany.
[3]Department of Earth, Planetary and Space Sciences, University of California, Los Angeles, PO Box 951567, 90095-1567, CA, USA.
[4]Australian Centre for microscopy and Microanalysis, The University of Sydney, 2006 NSW, Australia.
[5]Department of Materials, University of Oxford, Oxford, OX1 3AN, UK.

Key Points:

- CIS methodology provides a simple, accurate method for chondrule size measurements and analysis
- Disparity in measurements between 2D and 3D methodologies
- CM chondrite average chondrule sizes are smaller than previously recorded and more similar to those in the CO chondrites
- Adapted version on the Benito et al. (2019) stereological correction models provide the most reliable 2D-3D correction

Submitted: *Meteoritics and Planetary Science* (Accepted with minor revisions)
DOI: 10.5284/zenodo.10604567 (Preprint)
This chapter represents the pre-peer reviewed article

Data related to this paper can be found in the supplementary materials associated with this publication.

C.J.F and M. L designed research project
C.J.F undertook SEM and XCT analysis
C.J.F, S.B and E.D adjusted and applied stereological correction models
C.J.F wrote paper based on discussions with S.B, E.D, L.E.J, P-E.M, L.D and M.R.L
C.J.F, L.E.J, P-E.M, S.B, E.D, L.D and M.R.L contributed to editing the paper

3.1 Abstract

The sizes of chondrules are a valuable tool for understanding relationships between meteorite groups and the affinity of ungrouped chondrites, documenting temporal/spatial variability in the solar nebula, and exploring the effects of parent body processing. Many of the recently reported sizes of chondrules within the CM carbonaceous chondrites differ significantly from the established literature average and are more closely comparable to those of chondrules within CO chondrites. Here we report an updated analysis of chondrule dimensions within the CM group based on data from 1937 chondrules, obtained across a suite of CM lithologies ranging from petrologic subtypes CM2.2 – CM2.7. Our revised average CM chondrule size is 194 µm. Among the samples examined, a relationship was observed between petrologic subtype and chondrule size such that chondrule long axis lengths are greater in the more highly aqueously altered lithologies. These findings suggest a greater similarity between the CM and CO chondrites than previously thought, and support arguments for a genetic link between the two groups (i.e., the CM-CO clan). Using the 2D and 3D data gathered, we also apply numerous stereological corrections to examine their usefulness in correcting 2D chondrule measurements within the CM chondrites. Alongside this analysis we present details of a standardised methodology for 2D chondrule size measurement to facilitate more reliable inter-study comparisons.

3.2 Introduction

Chondritic meteorites (chondrites) are a class of primitive meteorites that are believed to have accreted during the first few million years of Solar System history and so provide valuable information on the nature of the solar nebula and planetary body formation (Scott & Krot, 2013). They are composed primarily of chondrules, refractory inclusions, and fine-grained matrix material (Krot et al. 2014). Chondrites can be divided into the ordinary, enstatite, R, K, and carbonaceous classes, and further divided into 15 groups (H, L, LL, EH, EL, CI, CM, CO, CV, CK, CR, CH, CB, R, K; Weisberg et al., 2006).

Chondrules are a major component of most chondritic meteorites, with abundances ranging from 20 to 80 vol.% and sizes from ~100 μm to more than 2000 mm (Jones et al. 2000; Weisberg et al. 2006; Zanda 2004). Chondrules are typically dominated by the Fe,Mg silicates olivine and pyroxene, with minor amounts of Fe,Ni metal and glass. Chondrule formation theories are numerous, though most agree that chondrules formed by rapid heating and subsequent rapid cooling of a silicate precursor material (Hewins, 1997; Connolly & Jones, 2016).

Chondrite classification into class and group is based upon distinct chemical and isotopic signatures alongside physical properties (Krot et al. 2007). Average chondrule dimensions are one aspect of this classification, with distinct group-level size distributions well established (Friedrich et al. 2015; Weisberg et al. 2006). Distinct size differences of chondrules have been used to inform astrophysical theories of chondrule origin, distribution, migration and alteration during Solar System history (Cuzzi et al. 2001; Teitler et al. 2011; Wurm et al. 2010). While most chondrite groups have specific chondrule size ranges, there are some similarities between groups that have been used as evidence for potential genetic links between them (Weisberg et al. 2006). The CM (Mighei-like) and CO (Ornans-like) chondrites have been found in numerous studies to have similarly sized chondrules when compared to other chondritic groups, with reported averages of 270-300 μm (CM) and ~148 μm (CO) (Friedrich et al. 2015; Rubin & Wasson 1986a; Weisberg et al. 2006). These similarities, alongside affinities in refractory lithophile abundances and

O isotopic compositions, has led to the idea of a CM-CO clan (Kallemeyn & Wasson 1979, 1982).

The CM chondrites are a group of primitive and commonly brecciated meteorites characterised by high indigenous water contents (~9 wt.% H_2O^+) acquired from their aqueously altered parent body/bodies (Jarosewich, 1990; Bischoff et al., 2006; Hamilton et al., 2019; Lentfort et al., 2021). Chondrules (including lithic clasts and mineral fragments) constitute ~20 vol.% of CM chondrites, although this figure is highly variable between meteorites, and whilst the CM chondrule size average of 270-300 mm is well established in the literature, recent studies have reported significant deviations from this value (Table 3.1) (Weisberg et al. 2006). Given the absence of recent detailed investigations of CM chondrule sizes and the recent range in reported averages, we present an updated analysis of CM chondrite chondrule sizes and investigate the similarities with the CO chondrite chondrules.

Table 3.1. *Examples of average chondrule sizes reported for CM carbonaceous chondrites arranged in order of decreasing mean diameter.*

Chondrite	Mean Chondrule Diameter (μm)	*n*	Method	Study
Murchison	558	61	XCT	Hanna & Ketcham, (2018)
Asuka 12085	310	-	X-ray maps	Kimura et al. 2020
Pollen	284	77	TLM	Kerraouch et al. (2021)
Aguas Zarcas	275	40	SEM	
Murray	270	100	TLM	Rubin & Wasson, (1986)
Maribo	268	88	TLM	Kerraouch et al. (2021)
Askuka 12169	260	-	X-ray maps	Kimura et al. (2020)
Boriskino	249	61	XCT	Kerraouch et al. (2021)
Murchison	196	-	X-ray Maps	Fendrich & Ebel, (2021)
	184	-	X-ray Maps	
Jbilet Winselwan	149	321	SEM	Friend et al. (2018)
	141	187	SEM	
Reported Average	270-300			

TLM = Transmitted Light Microscopy
SEM = Scanning Electron Microscopy
XCT = X-ray Computed Tomography

3.3 Materials and Methods

During this study 10 meteorites were examined, nine using 2D techniques such as scanning electron microscopy (SEM) and Energy Dispersive X-ray Spectroscopy (EDS) mapping, and four with the 3D technique of X-ray Computed Tomography (XCT). The samples analysed and techniques used are listed in Table 3.2 alongside literature reported petrologic subtypes (i.e., degree of aqueous alteration), according to two classification schemes (Rubin et al. 2007, and Howard et al. 2015).

***Table 3.2**. List of meteorite thin sections and chips investigated and their reported petrologic types and subtypes.*

Meteorite	2D Analysis	3D Analysis	Petrologic Type[a]	Petrologic subtype[b]
	Section ID	Chip ID and Mass (g)		
Aguas Zarcas	AZ-P1[5] (PB) AZ-P2[5] (PB)	Aguas Zarcas (3.840)[5]	---	CM2.2-2.8[h]
Cold Bokkeveld	---	BM.1727 (2.154)[1]	1.4[d]	CM2.2[k], CM2.1–2.7[l]
Kolang[5]	(TS)	---	1.3[c]	CM2.2[c]
LAP 02239	02239,5[2] (PB)	---	1.5[d]	CM2.4–2.5[i]
Lewis Cliff (LEW) 85311	85311,90[2] (TS)	LEW85311, 84[2]	1.7[e]	CM2.6–2.7[j]
Mighei	(TS)	---	1.4[f]	---
Murchison	3.864g TS1[5] (TS) BM1970.6 (P19258)[1] (PB) BM1988, M23 (P19261)[1] (PB)	Murchison (3.86)[5]	1.5[f]	CM2.5[k,] CM2.9–CM2.7 (main lithology CM2.7[l])
Paris[3]	(PB)	---	---	CM2.7–2.9[m]
Shidian[4]	(PB)	---	---	CM2.1–2.6, mainly CM2.2[n]
Winchcombe	BM.2022, M9-14 (P30552)[1] (PB)	Bag4.17 (0.025)[1] Bag4.17 Crumbs & Frag[1] Bag1_Stone34 (0.238)[1] Bag6.2_Frag2[1] Bag6.2_Frag3[1]	1.1–1.2[g]	CM2.0-2.6[o]

PB = Polished resin block
TS = Thin section
[1]Natural History Museum (U.K)
[2]ANSMET
[3]Museum National d'Histoire Naturelle de Paris
[4]Chinese Academy of Sciences

[g]King et al. (2022)
[h]Kerraouch et al. (2021)
[i]Lee et al. (2023)
[j]Choe et al. (2010)
[k]Rubin et al. (2007)
[l]Lentfort et al. (2020)

[5]Commercially obtained
[a]Using the scheme of Howard et al. (2015)
[b]Using the scheme of Rubin et al. (2007)
[c]King et al. (2021)
[d]Howard et al. (2015):value from LAP 02333, which is paired with LAP 02239
[e]Lee et al. (2019)
[f]Howard et al. (2015)
[m]Rubin (2015)
[n]Fan et al. (2022)
[o]Suttle et al. (2022)
--- denotes not measured

3.3.1 2D Chondrule Size Measurements

SEM analysis was carried out on 12 thin sections representing nine CM chondrites at the University of Glasgow's GEMS facility. A Zeiss Sigma field-emission SEM was used, with an Oxford Instruments Energy Dispersive X-ray Spectrometer (EDS) detector operated through Oxford Instruments AZtec software. An accelerating voltage of 20 kV was used for all samples. Samples were polished and coated in 20 nm of carbon prior to analysis. A total area of 750.2 mm^2 was investigated, and the sections examined are listed alongside their individual section areas and mosaic resolutions in Table 3.3. Backscattered electron image (BSE) mosaics and EDS maps of entire section areas were used in this study. 2D apparent chondrule sizes were measured using the CIS method (Floyd & Lee 2022) as outlined below. Samples analysed using SEM and EDS had their petrologic subtypes determined using the Rubin et al. (2015) classification scheme for comparison with the literature reported values. Where multiple clasts or lithologies were present, each was classified individually.

***Table 3.3**. CM chondrite sections analysed during this study alongside their resulting image mosaic resolution.*

Meteorite	Section ID	Area (mm^2)	Resolution (µm/pixel)
Aguas	AZ-P1	8.29	0.731
Zarcas	AZ-P2	24.94	1.003
Kolang	Kolang	164.99	2.558
LAP 02239	02239,5	79.72	1.721
LEW 85311	85311,90	52.17	1.672
Mighei	Mighei	59.52	2.008
Murchison	3.864g_TS1	57.45	1.202
	P19258	19.39	1.203
	P19261	31.14	1.203
Paris	Paris	167.72	2.320
Shidian	Shidian	78.22	2.410
Winchcombe	P30552[†]	9.68	0.601

[†]BSE mosaic and EDS maps collected by Suttle et al. (2022).

3.3.1.1 The CIS Method

The Chondrule Image Segmentation Method (CIS Method) is a simple, four-step, standardised process for 2D chondrule size measurement and analysis taking advantage of freely available image processing and analysis software. The four steps are outlined below and illustrated in Figure 3.1.

1) *Chondrule Identification*: Whole chondrules (defined for this study later) are identified in image mosaics (in this case BSE and EDS mosaics).
2) *Chondrules Segmentation:* Mosaics are loaded into an image processing package; our preference was GNU Image Manipulation Program (GIMP™), where chondrules are manually segmented using the free select tool.
3) *Chondrule Measurement*: Segmented chondrules are then exported (maintaining original resolution) and imported into ImageJ, an open-source image processing package (Schindelin et al. 2012), where the scale, defined by the original resolution of the image mosaic, is set. The analyse particle function is then used to produce and measure best-fit ellipses of each whole chondrule. Fitting an ellipse to each chondrule smooths out their often-irregular perimeter and allows ImageJ to measure maximum and minimum axes lengths perpendicular to one another (this is not possible with ferret diameter measurements). Fitting ellipses also facilitates improved comparison with XCT data analysis where fitted ellipsoids are produced.
4) *Size Analysis:* The resulting long (R_1) and short (R_3) axes lengths (mm) should subsequently be logarithmically transformed into Phi-units (φ) defined by (Equation 3.1) where *d* is in mm (W. C. Krumbein 1936):

$$\varphi = -\log_2(d) \qquad \text{(Equation 3.1)}$$

The transformed data in Phi-units provides equal weighting to smaller particles and allows the data to be more reliably subjected to statistical analysis such as mean, median and standard deviation. Calculation of the mean chondrule diameter is done graphically, using Equation 3.2 as set out by Folk and Ward (1957) where φ_{16} represents the average of the finest third of particles, φ_{50} the middle third and φ_{84} the coarsest third:

$$\mathrm{M}_C = \frac{\varphi_{16} + \varphi_{50} + \varphi_{84}}{3} \qquad \text{(Equation 3.2)}$$

Statistical analysis can be easily undertaken using GRADISTAT software (Blott and Pye 2001) using the quarter phi interval binning. GRADISTAT also provides outputs for standard deviation, skewness and kurtosis using the Folk and Ward (1957) graphical methods. To ensure data can be easily understood and to allow comparison to previous studies, results are reported in both φ-units and either mm or mm e.g., 2.306 φ (202 μm).

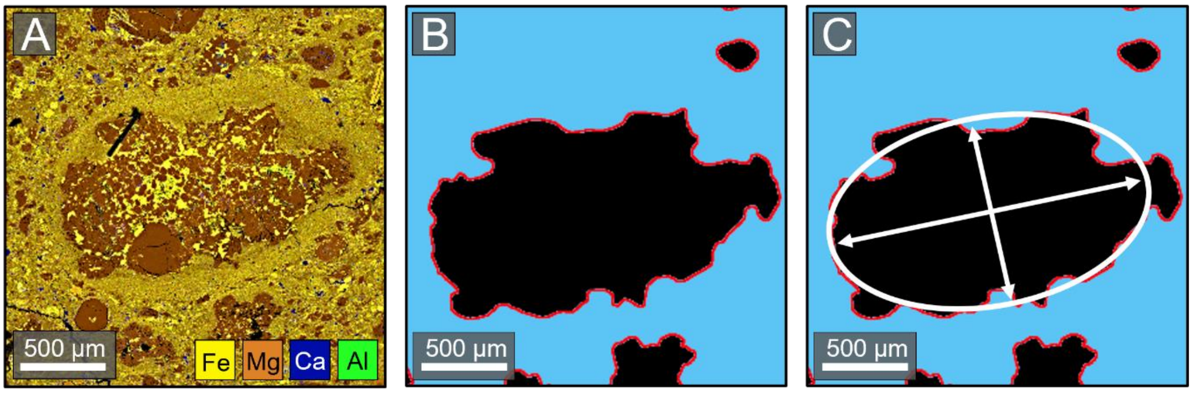

Figure 3.1*. Images showing the first three steps involved in the CIS method. A) Identification of whole chondrules by examining BSE and EDS mosaics. B) Chondrule segmentation, involving tracing each whole chondrule in an image processor and copying it to a new image layer. C) Chondrule measuring, involving exporting the image file containing all the segmented chondrules to ImageJ and using the 'set scale' and 'analyse' particles function to fit and measure ellipse dimensions.*

3.3.2 3D Chondrule Size Measurements

Chips of five CM chondrites spanning a range of petrologic subtypes as listed in Table 3.4 were subjected to X-ray computed tomography (XCT) at the University of Strathclyde, UK, using a Nikon XT H 320 LC equipped with a 180 kV transmission source. Data was corrected for beam hardening and a non-local means filter was applied post-acquisition to reduce noise. Non-local means filter settings; search window: 9, local neighbour: 4, similarity value: 0.4. Data parameters and the reconstructed voxel sizes are listed in Table 3.4.

Table 3.4. *CM chondrite chips analysed in 3D using XCT, their scan parameters and resulting reconstructed volume voxel resolutions.*

Meteorite	Sample ID	Accelerating Voltage (kV)	Current (mA)	Number of Slices	Resolution (mm/voxel)
Aguas Zarcas	Aguas Zarcas	80	140	1627	12.13
Cold Bokkeveld	Cold Bokkeveld	70	153	2000	11.15
LEW 85311	LEW85311	65	43	2000	3.026
Murchison	Murchison_3.1864g	90	124	2000	12.13
Winchcombe	Bag4.17_0.0253g	80	87.5	998	3.936
	Bag4.17_Crumbs & Frag	70	85.7	996	2.130
	Bag_1_Stone34	130	76.9	3214	4.057
	Bag6.2_Frag2	70	85.7	995	2.238
	Bag6.2_Frag3	70	85.7	995	2.457

Chondrules were identified within the reconstructed volume by their distinctive X-ray attenuation, appearing as dark grey objects relative to fine-grained rims and matrix (Hanna & Ketcham 2018; Hanna et al. 2015). Identified chondrules were segmented in Avizo software using the method set out by Hanna et al. (2015) with chondrules manually segmented in their largest profile for each orthogonal plane (XY, XZ, & YZ). Segmented planes were subsequently exported to Blob3D, where a specialised merit function was used to fit ellipsoids to the outer margins of the segmented planes (Ketcham 2005a). Measurements of the primary and tertiary axis of each ellipsoid were recorded in Blob3D with the resulting data subjected to step 4 of the CIS method.

3.3.3 Whole Chondrule Definition and Criteria

Only whole chondrules were measured in this study. For the CMs investigated they are defined as: polymineralic, rounded edge appearance over >50% of total perimeter, surrounded by an intact fine-grained rim, not more than 50% internally eroded from polishing and not cut by a fracture or the edge of the sample. The criteria for whole chondrules have been developed based upon the characteristics described in previous studies (Dodd 1982; King & King 1978; Metzler 2004; Metzler et al. 1992; Weisberg et al. 2006; Wlotzka 1983). Whilst this definition is appropriate for defining CM chondrules for the present study, it may not be appropriate for studies of chondrules within other chondrite classes and groups.

3.4 Results

3.4.1 2D Analysis

A total of 983 whole chondrules were identified and measured in 2D across 12 CM chondrite sections. Three of the sections were composed of a single lithology, whilst the other nine contained multiple clasts that could be distinguished by differences in elemental abundance using EDS or contrast in BSE mosaics (Figure 3.2) (Lentfort et al., 2020). Owing to random sectioning effects, the 2D measurements represent 'apparent' chondrule size (Eisenhour 1996) and the measurements referred to hereafter reference the lengths of either the major (R_1) or minor (R_3) axes of the best-fit ellipses produced.

3.4.1.1 Chondrule Types and Abundances

During chondrule characterisation, the relative abundances of Type I (FeO-poor and volatile poor) and Type II (FeO-rich) chondrules (Hewins, 1997) was noted alongside the areal. % of whole chondrules (Table 3.5). Results indicate that the relative abundance of type I and II chondrules is broadly consistent with previous studies with Type I chondrules predominant (Hewins et al. 2014; Jones 2012). These findings differ from previous studies by showing the abundance of Type II chondrules to be significantly lower than the 10-40% abundance range suggested by Jones (2012). The areal % of whole chondrules is highly variable between the whole polished sections examined supporting the findings of Weisberg et al. (2006); there is no relationship between areal. % of chondrules and average R_1 diameter within each polished section. Chondrule abundances differ between the clasts and lithologies as can be observed in Figure 3.2B supporting previous observations of chondrule rich and chondrule poor lithologies (Suttle et al. 2022).

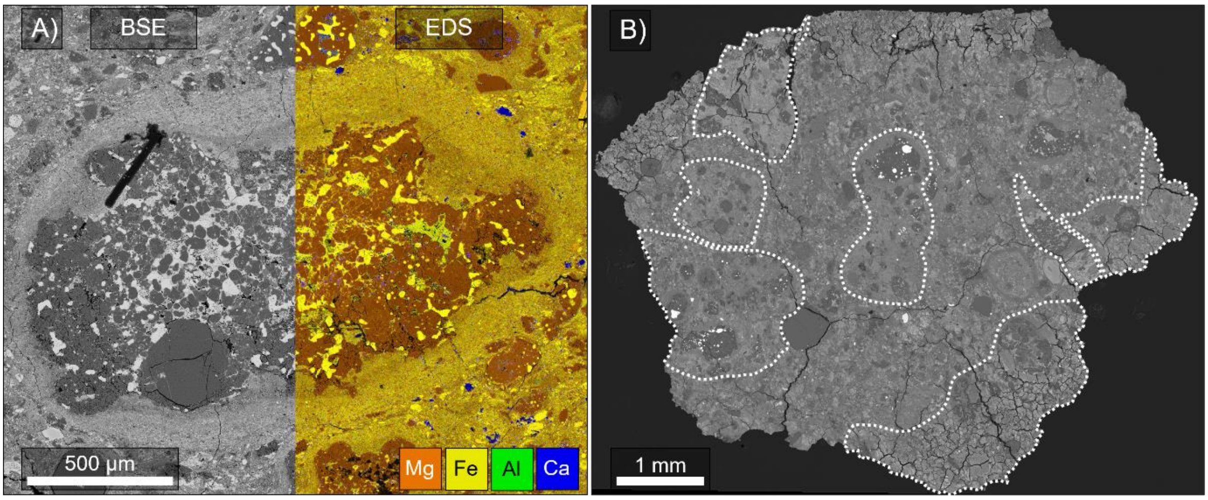

Figure 3.2. *A) A large type I chondrule, surrounded by a FGR in Paris. B) BSE mosaic of Aguas Zarcas section AZ_P2. The seven clasts identified within the main lithology are outlined in white.*

3.4.1.2 2D Size Distributions

Prior to logarithmic transformation, the 2D size data exhibited a significant positive skew that could be approximately characterised as log-normal, supporting the approximately log-normal distribution found by Friend et al. (2018). Following conversion into Phi-units, chondrule size histograms were produced for each section and are reported alongside associated skewness and kurtosis values (Figure 3.3). After logarithmic transformation, chondrules exhibit approximately normal distributions. Inter-clast variations in size are observed, with notable differences between the clasts of Paris, Aguas Zarcas AZ-P2, and Kolang.

The host clasts or lithologies of chondrules were assigned a petrologic subtype (Table 3.6), and results reveal size distributions generally symmetrical within lithologies of subtypes CM2.2, 2.4 and 2.5. A marginal coarse skew (0.113) was observed in size distributions of CM2.7 lithologies. Kurtosis values indicate mesokurtic distributions for CM2.2, 2.4, and 2.7 and a leptokurtic distribution for CM2.5. A Kolmogorov-Smirnov two sample one-tailed statistical test was conducted to investigate the differences in average chondrule size between petrologic subtypes. This non-parametric test compares two distributions and does not assume normality. Clasts or lithologies with a small sample size (n < 10 chondrules) were removed from this analysis as it was judged these could introduce error by being unrepresentative. The results of the Kolmogorov-Smirnov test indicate that, at a 97% confidence interval (CI), chondrules from the CM2.7 population are smaller than those in the CM2.2 population. Additionally, CM2.7 chondrules are smaller than chondrules in CM2.4 with 90% confidence interval. No relationship was observed between chondrule aspect ratio and petrologic subtype or axis size. To account for the presence of chondrule-rich lithologies within some samples and the spread of data within the CM2.2 classification, weighted averages were calculated for clasts or lithologies with *n* > 10 chondrules. Weighted averages indicate a negative correlation between chondrule R_1 length and the extent of aqueous processing (Table 3.7).

Table 3.5. *List of investigated meteorites and sections examined in 2D using SEM. For each section the number of clasts present, whole chondrule abundance and chondrule type is reported.*

	Section ID	Clasts (*n*)	Whole chondrules (*n*)	Whole chondrule Area %	Type I		Type II	
					n	(%)	*n*	(%)
Aguas Zarcas	AZ-P1	4	9	1.23	9	100	0	0.0
	AZ-P2	8	38	6.90	36	94.7	2	5.3
Kolang	Kolang	13	80	3.59	79	98.8	1	1.3
LAP 02239	02239,5	5	150	10.25	144	96.0	6	4.0
LEW85311	85311,90	3	133	10.38	127	95.5	6	4.5
Mighei	Mighei	1	30	4.65	30	100	0	0.0
Murchison	3.864g_TS1	1	140	6.98	132	94.3	8	5.7
	P19258	7	10	2.80	9	90.0	1	10.0
	P19261	4	50	4.06	48	96.0	2	4.0
Paris	Paris	5	215	7.80	207	96.3	8	3.7
Shidian	Shidian	1	90	8.30	89	98.9	1	1.1
Winchcombe	P30552	1	38	7.21	38	100	0	0.0
TOTAL		53	983		948	96.4	35	3.6

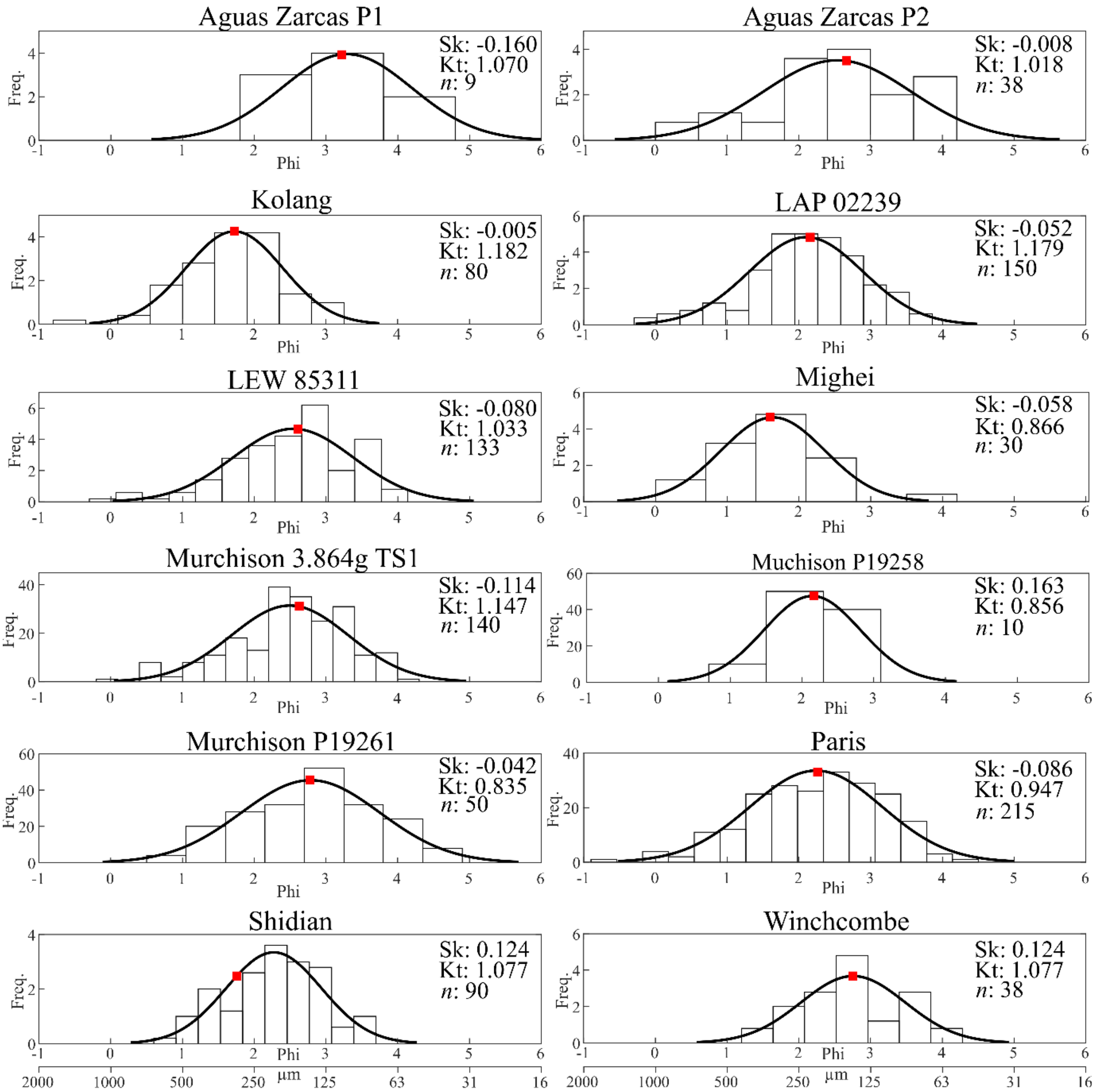

***Figure 3.3**. Histograms for chondrule size in Phi-units for each of the polished sections examined. Black lines indicate fitted normal distribution curves and the red squares indicate the average chondrules sizes for the sections as calculated using the CIS method. Values for kurtosis (Kt), skewness (Sk), and number of chondrules (n) are stated in the top right of each histogram.*

Table 3.6. *2D 'apparent' chondrule sizes and statistics for major and minor axis of all chondrule-bearing clasts and lithologies within each section.*

Polished Section	Clast (C_x)	*n*	Petrological subtype	Average R_1 ϕ (μm)	σ	Median R_1 ϕ (μm)	*Average* R_3 ϕ (μm)	σ	Average Aspect Ratio
Aguas Zarcas AGZ_P1	C_1	7	2.2	3.214 (107.8)	0.62	3.415 (93.8)	3.531 (86.52)	0.55	1.24
	C_2	2	2.2	2.917 (132.4)	1.27	2.000 (250.0)	3.493 (88.81)	1.07	1.42
	TOTAL	9	2.2	3.216 (107.6)	0.97	3.415 (93.8)	3.528 (86.70)	0.88	1.28
Aguas Zarcas AGZ_P2	C_1	2	2.3	2.576 (167.7)	0.86	2.000 (250.0)	2.982 (126.6)	0.76	1.23
	C_2	6	2.3	3.487 (89.31)	0.46	3.474 (90.0)	3.831 (70.25)	0.66	1.29
	C_3	8	2.3	2.510 (175.6)	0.81	2.395 (190.1)	2.787 (144.9)	0.62	1.34
	C_4	5	2.3	2.092 (234.5)	0.78	2.540 (171.9)	2.562 (169.3)	0.91	1.37
	C_5	2	2.2	1.155 (449.1)	0.96	1.468 (3615)	1.661 (316.2)	0.96	1.46
	C_6	1	2.2	3.899 (0.067)	-	-	4.083 (0.059)	-	1.14
	C_7	14	2.2	2.452 (182.8)	1.07	2.159 (223.9)	2.866 (137.3)	1.01	1.36
	TOTAL	38	-	2.666 (157.5)	1.07	2.579 (167.4)	1.031 (122.3)	0.98	1.34
Kolang	C_1	26	2.2	1.812 (284.9)	0.74	1.850 (277.5)	2.343 (197.1)	0.56	1.48
	C_2	15	2.2	1.861 (275.4)	0.61	1.868 (273.9)	2.282 (205.6)	0.45	1.42
	C_3	1	2.2	1.577 (335.0)	-	-	1.756 (296.0)	-	1.13
	C_4	22	2.2	1.536 (345.0)	0.69	1.456 (364.5)	2.126 (229.1)	0.75	1.46
	C_5	1	2.2	1.296 (407.0)	-	-	1.34 (395.0)	-	1.03
	C_6	6	2.2	1.536 (344.9)	0.49	1.494 (355.0)	1.862 (275.1)	0.49	1.32
	C_7	1	2.2	1.442 (368.0)	-	-	1.595 (331.0)	-	1.11
	C_8	1	2.2	3.070 (119.0)	-	-	3.293 (102.0)	-	1.17
	C_9	7	2.2	1.720 (303.5)	0.32	1.676 (312.9)	2.304 (202.4)	0.41	1.58
	TOTAL	80	2.2	1.722 (303.0)	0.67	1.737 (300.0)	2.221 (214.5)	0.60	1.44
LAP02239	C_1	1	2.5	1.847 (0.278)	-	-	2.139 (0.227)	-	1.22
	C_2	92	2.4	2.267 (207.8)	0.80	2.238 (212.0)	2.708 (153.0)	0.82	1.45
	C_3	4	2.5	1.909 (266.2)	0.91	1.737 (300.0)	2.323 (199.8)	0.91	1.53
	C_4	53	2.5	2.001 (249.8)	0.75	2.020 (246.6)	2.443 (183.9)	0.68	1.42

	TOTAL	150	-	2.157 (224.2)	0.81	2.140 (226.9)	2.603 (164.6)	0.78	1.44
LEW 85311,90	C_1	118	2.7	2.623 (162.4)	0.84	2.605 (164.3)	3.001 (124.9)	0.82	1.36
	C_2	12	2.7	2.584 (166.8)	0.74	2.737 (150.0)	2.912 (132.8)	0.76	1.27
	C_3	3	2.7	2.605 (164.3)	0.08	2.605 (164.3)	2.953 (129.2)	0.15	1.19
	TOTAL	133	2.7	2.606 (164.2)	0.82	2.605 (164.3)	2.994 (125.6)	0.80	1.35
Mighei	-	30	2.2	1.599 (330.2)	0.66	1.640 (320.9)	2.020 (246.6)	0.72	1.34
Murchison 3.864g TS1	-	140	2.2	2.628 (161.8)	0.79	2.657 (158.5)	3.178 (110.5)	0.77	1.43
Murchison P19258	C_1	9	2.5	2.144 (226.3)	0.64	1.956 (257.7)	2.465 (181.2)	0.71	1.23
	C_2	1	2.2	2.204 (217.0)	-	-	2.900 (134.0)	-	1.62
	TOTAL	10	-	2.752 (222.7)	0.62	2.000 (250.0)	2.515 (175.3)	0.70	1.27
Murchison P19261	C_1	27	2.5	2.461 (181.6)	0.94	2.415 (187.5)	2.826 (141.0)	0.90	1.47
	C_2	17	2.2	3.419 (93.51)	0.85	3.540 (85.99)	3.685 (77.74)	0.87	1.27
	C_3	4	2.2	3.324 (99.89)	0.41	3.238 (106.0)	3.530 (86.59)	0.51	1.27
	C_4	2	2.5	2.158 (224.1)	0.35	2.247 (210.1)	2.650 (159.4)	0.36	1.50
	TOTAL	50	-	2.779 (145.6)	1.00	2.825 (141.2)	3.276 (103.2)	0.93	1.39
Paris	C_1	165	2.7	2.293 (204.1)	0.93	2.336 (198.1)	2.777 (145.9)	0.96	1.45
	C_2	25	2.7	2.327 (199.3)	0.93	2.415 (187.5)	2.660 (158.2)	0.91	1.46
	C_3	9	2.7	2.368 (193.8)	0.86	1.967 (255.8)	3.115 (115.5)	0.76	1.71
	C_4	9	2.7	1.968 (255.6)	094	1.616 (326.2)	2.449 (183.2)	0.95	1.40
	C_5	7	2.7	2.262 (208.5)	0.97	2.415 (187.5)	2.869 (136.9)	0.97	1.49
	TOTAL	215	2.7	2.259 (209.0)	0.93	2.311 (201.5)	2.757 (148.0)	0.96	1.46
Shidian	-	90	2.2	1.758 (295.6)	0.73	1.685 (311.0)	2.243 (211.3)	0.71	1.46
Winchcombe	-	38	2.2	2.752 (148.5)	0.81	2.662 (158.0)	3.257 (104.6)	0.70	1.45

σ is one standard deviation.
n = number of chondrules measured.

Table 3.7*. Chondrule size statistics for lithologies classified by petrologic sub-type (where n > 10). Graphical statistical analysis based on* Folk and Ward (1957).

Petrologic subtype	Weighted Average R_1 ϕ (µm)	Graphical Skewness (ϕ)	Graphical Kurtosis (ϕ)
CM2.2	2.154 (224.69)	0.001	1.001
CM2.4	2.267 (207.80)	-0.033	1.085
CM2.5	2.454 (182.40)	-0.027	1.147
CM2.7	2.419 (186.95)	-0.113	1.032

3.4.2 3D Analysis

A total of 954 chondrules were identified and measured in 3D within nine CM chondrite chips (Table 3.8). Where possible all identifiable chondrules within a clast or lithology were segmented. However, given the time-consuming nature of 3D segmentation, for larger volumes where segmentation of all chondrules would have been impractical, a minimum of 100 chondrules were segmented per chip/clast. Within some volumes multiple clasts could be clearly distinguished by differences in X-ray attenuation. However, due to the often-small sizes and similarities in attenuation coefficients, constraining lithological boundaries was challenging. Consequently, the study of lithological variations was limited to Aguas Zarcas and Winchcombe Bag 1 Stone 34; in those samples the different clasts could be confidently identified by their contrasts in attenuation coefficients and were large enough to obtain a significant number of chondrule measurements. For all other meteorites, chondrules were segmented from the dominant lithology present. The appearance of chondrules within the different scan volumes was heavily dependent on scan resolution. Scan resolutions greater than 3-4 µm/voxel allowed greater distinction of more finely crystalline materials such as fine-grained rims and inter-chondrule Fe,Ni metal (Figure 3.4). The 3D measurements collected represent 'true' chondrule size and the chondrule sizes referred to hereafter reference the lengths of the long or short axes of best-fit ellipsoids.

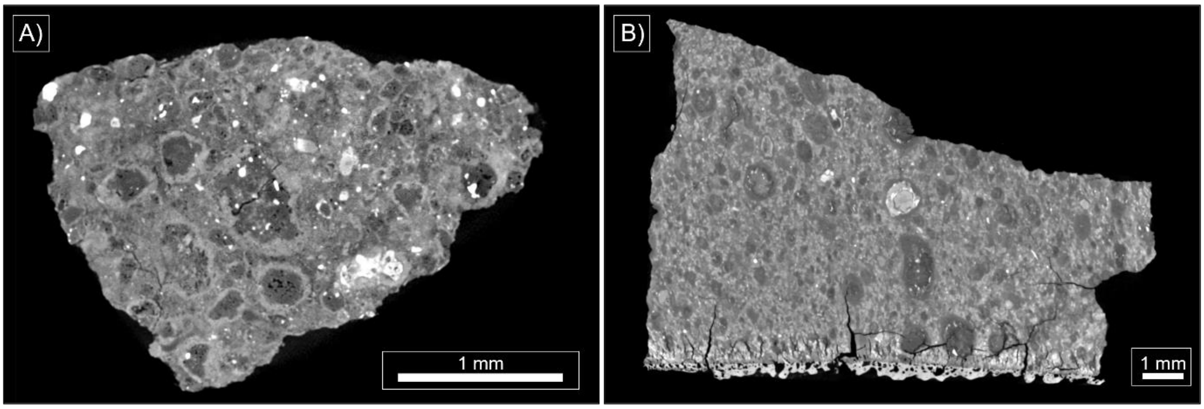

***Figure 3.4**. Example XCT slices showing dark objects identified as chondrules and the differences in resolution between some volumes. A) XCT slice of LEW 85311 (resolution: 3.026 µm/voxel). Within this volume fine grained rims and intra-chondrule Fe,Ni metal grains can be easily identified. B) XCT Slice of Murchison 3.864g within which the fine-grained rims and Fe,Ni metal grains are less well resolved even accounting for its lower magnification (resolution: 12.13 µm/voxel).*

3.4.2.1 3D Size Distributions

Size distribution histograms are in Figure 3.5 alongside fitted normal distribution curves and skewness and kurtosis values with statistical data in Table 8. In common with the 2D datasets, the 3D skewness and kurtosis values have a generally symmetrical distribution once logarithmically transformed. Average sizes are generally larger than those recorded in 2D with a greater range of values documented. There are subtle contrasts in sizes between clasts, although the extent of these differences appears less pronounced compared to 2D. Average chondrule aspect ratios were strikingly similar between all 3D analyses, with values ranging from 1.57 to 1.77

Table 3.8. *3D 'true' chondrule sizes and statistics for major and minor axis of chondrule-bearing clasts and lithologies examined within each chip.*

Sample	Clast (C_x)	*n*	Average R_1 ϕ (µm)	σ	Median R_1 ϕ (µm)	*Average* R_3 ϕ *(µm)*	σ	Average Aspect Ratio
Aguas Zarcas	C_1	102	1.449 (366.3)	0.62	1.494 (355.0)	2.175 (221.5)	0.55	1.72
	C_2	104	1.545 (342.8)	0.40	1.552 (341.1)	2.201 (217.4)	0.41	1.57
	C_3	107	1.410 (376.3)	0.46	1.399 (379.1)	2.196 (218.2)	0.42	1.77
	TOTAL	313	1.474 (360.1)	0.49	1.476 (259.5)	2.206 (216.7)	0.46	1.69
Cold Bokkeveld	-	103	1.164 (446.1)	0.47	2.507 (175.9)	1.780 (291.1)	0.48	1.57
LEW 85311	-	154	2.565 (169.0)	0.59	2.575 (167.8)	3.184 (110.0)	0.51	1.60
Murchison 3.864g	-	180	1.106 (464.5)	0.58	1.163 (446.6)	1.811 (285.1)	0.52	1.69
Winchcombe								
Bag 1 Stone 34	C_1	30	2.427 (186.0)	0.57	2.427 (186.0)	3.093 (117.2)	0.51	1.62
	C_2	50	2.170 (222.1)	0.51	2.143 (226.5)	2.857 (138.1)	0.45	1.68
Bag 4.17 0.0253g	-	40	2.320 (200.3)	0.59	2.435 (185.0)	2.962 (128.4)	0.60	1.62
Bag 4.17 Crumbs & Frags	-	30	3.159 (111.9)	0.62	3.102 (116.5)	3.811 (71.26)	0.56	1.70
Bag 6.2 Frag 2	-	31	2.706 (153.3)	0.71	2.803 (143.3)	3.487 (89.16)	0.64	1.68
Bag 6.2 Frag 3	-	23	2.712 (152.6)	0.57	2.793 (144.3)	3.361 (97.30)	0.56	1.61
Total	-	204	2.501 (176.7)	0.69	2.507 (175.9)	3.201 (108.7)	0.66	1.66

σ is one standard deviation.
n = number of chondrules measured).

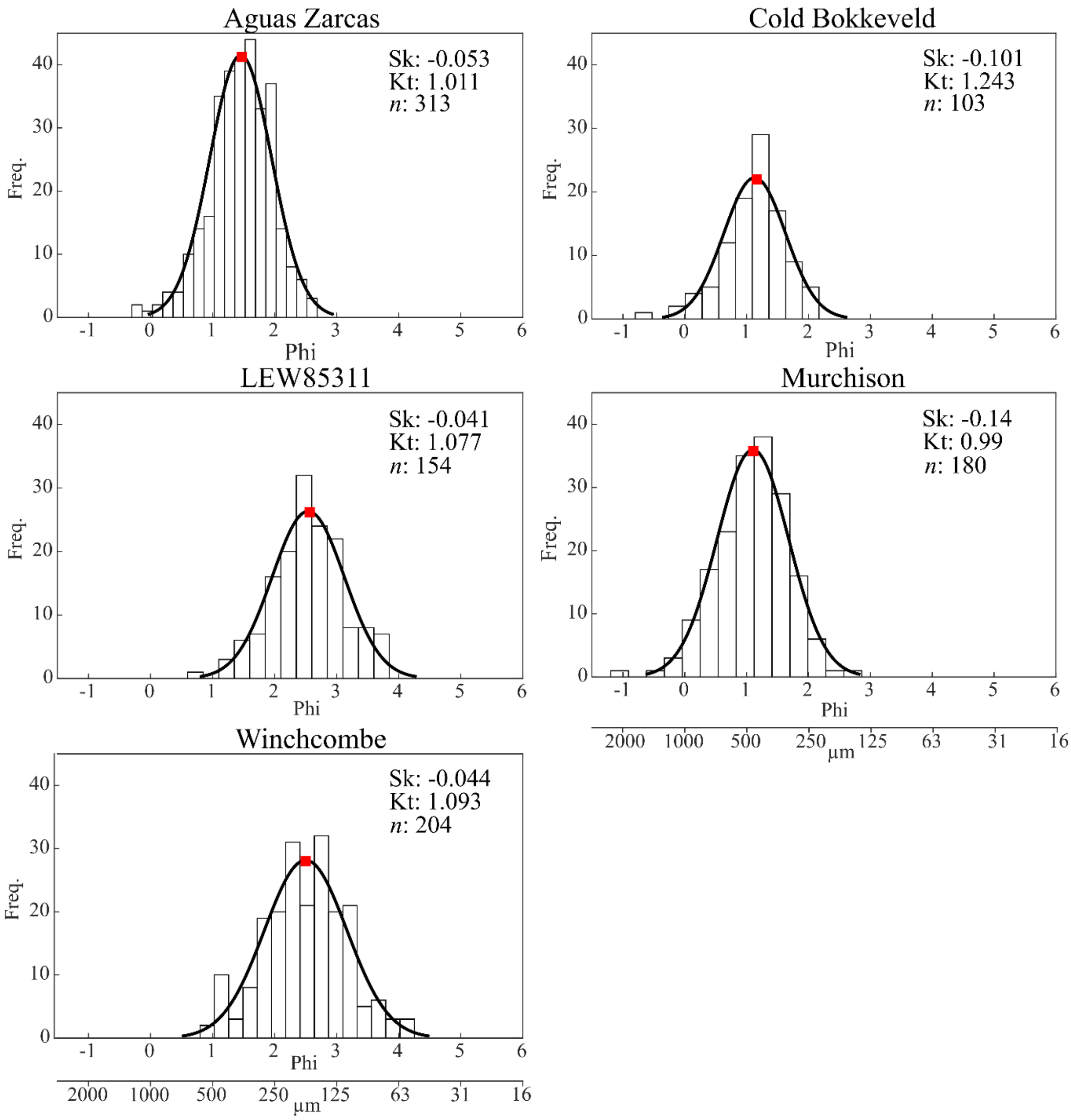

***Figure 3.5**. Histograms of major axis chondrule sizes in Phi-units for chondrules in each of the meteorites examined by XCT. Black lines indicate fitted normal distribution curves and the red squares indicate the graphical average chondrules sizes as calculated using the analysis component of the CIS method. Values for kurtosis (Kt), skewness (Sk) and number of chondrules (n) are in the top right of each histogram.*

3.4.3 2D-3D Size Corrections

Reconciling the effects of random sectioning and the relationship between 2D 'apparent' and 3D 'true' particle size has been previously explored in numerous previous studies encompassing terrestrial and extra-terrestrial geology (Benito et al. 2019; Cuzzi & Olson 2017; Eisenhour 1996; Metzler 2018; Sahagian & Proussevitch 1998). Many of these authors have developed or modified stereological correction models to allow them to predict 3D particle size distributions based on 2D apparent diameters, such as those measured in petrographic then sections. In terrestrial geology stereological corrections have been applied widely to a range of subject including, vesicles in volcanic rocks (Sahagian and Proussevitch 1998– discussed in more detail later), grain size distributions in pyroclastic rocks (Jutzeler et al. 2012), and ice pore analysis in glaciology (Eicken 1993). In addition to the terrestrial functionality of stereological corrections some corrections have also been developed and applied to the study of chondrule sizes within chondritic meteorites (Benito et al. 2019; Cuzzi & Olson 2017; Eisenhour 1996).

Many of the stereological corrections applied are based on the assumption that particles can be approximated by spheres and that reconciling their 3D size can be reduced to four effects (Benito et al. 2019):

i) A randomly cut sphere is likely to be non-diametrical and therefore not represent a cross-section through the widest point of a sphere.

ii) Larger spheres will be more frequently sectioned and measured in 2D due to their larger diameters.

iii) Thin sections themselves have a dedicated thickness (in the case of petrographic thin sections typically 30 μm).

iv) Sections cutting a sphere in a plane slightly smaller than that of the sphere radius may be missed due to the resolution of the measuring method.

It should also be considered that cognitive bias will likely factor into choosing the orientation of a sectioning plane within a rock chip, perhaps leading to preferential sectioning alongside pre-existing planes of weakness. This bias may influence the sectioning of any internal features to be examined using stereological models and should be considered during chip sectioning.

Four stereological corrections, outlined briefly below, were applied to the 2D dataset Murchison 3.864g TS1 and compared with the XCT dataset Murchison 3.864g, from which the thin section was made. Although the datasets are not precisely correlated, they provide an opportunity to compare, for the first time, the outcomes of such stereology models with real 2D and 3D data from a meteorite. The outcomes of the corrections are shown in Figure 6.

Eisenhour (1996): The first model developed and applied specifically to chondrule size analysis (developed using CO chondrite chondrules) is based on effects i), ii) & iii) listed above and assumes chondrules as undeformed spheres. The original findings of this model indicated that the corrected chondrule sizes have mean/median values smaller than those of the apparent diameters measured in 2D, there is an increase in the number of minimum diameter chondrules recorded, and the data are transformed from having a nearly log-normal distribution to conforming to a Weibull probability function.

Sahagian & Proussevitch, (1998): Originally developed to examine vesicles sizes in basalts, this model addresses the assumption of particle sphericity. Three systems are defined within this model to help users understand this issue: a) monodispersal systems, where particles are the same size and shape; b) polydispersal systems, where particles are the same shape but different sizes; c) multidispersal systems, where particles have different sizes and shapes. The Sahagain and Proussevitch model uses individual particle areas and aspect ratios to produce a size correction based on the assumption of a multidispersal system.

Cuzzi & Olson (2017): This is the second dedicated model developed to investigate particle size corrections in chondrites. In common with Eisenhour (1996), this model assumes particle sphericity (therefore categorising itself as a polydispersal model) and zero-thickness slicing. The presented algorithms are based on an inversion technique which “unfolds” arithmetically or geometrically binned histograms of particle apparent diameters in 2D sections. Due to the discrete nature of the recovery process, the model requires a minimum of 100-300 apparent diameter measurements to produce a good recovery.

Benito et al. (2019): This is a refinement on the Cuzzi and Olson (2017) model. To address the main shortcomings of the original method, namely scatter in the recovered distribution and negative-valued histogram bins, Benito et al. proposed a fitting step and the inclusion of numerical optimization tools to solve the inverse problem. An additional benefit of this model is a reduction in the minimum number of measurements required (50–100) to produce a good reconstruction.

Examining a cumulative distribution function (CDF) plot of the four models (Figure 3.6) reveals subtle differences between model outcomes. The Eisenhour model plots almost entirely to the right of the 2D data indicating a model outcome predicting smaller chondrule sizes. The Sahagian & Proussevitch and Cuzzi & Olson models are similar to one another, although the former predicts a median reconstructed diameter smaller than the apparent measured diameter whilst the Cuzzi & Olson model matches closely with the 2D measured data. Finally, the Benito model predicts a reconstructed chondrule diameter which is generally to the left of the 2D plotted data and indicates a larger reconstructed diameter than the measured apparent diameters.

It is worth noting that the Cuzzi & Olson and the Benito reconstructions were performed on the original log-normally distributed measurements as opposed to the Phi-transformed data. These models predict the 3D size distribution that would produce the observed 2D distribution by assessing the cumulative contributions of all measured cross-sectional areas. The transformation proposed in Equation 1, crucially interferes with this recovery process. As a result, the Phi transformation was performed on the reconstructed PDFs.

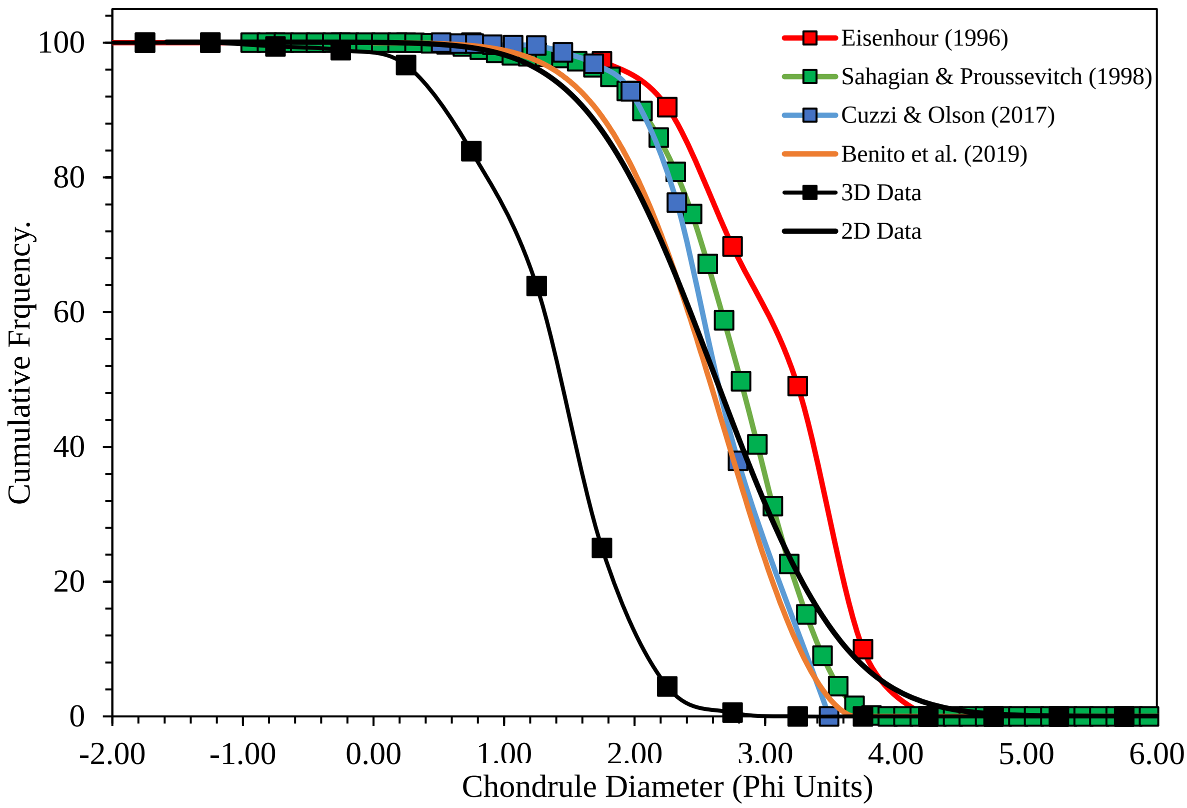

Figure 3.6*. Cumulative frequency diagram comparing the outcomes of the Eisenhour (1996), Sahagian & Proussevitch (1998), Cuzzi & Olson (2017) and Benito (2019) particle size correction models. Corrections were carried out on the 2D data collected from Murchison 3.864g TS1. Also shown is the 3D data collected from chip Murchison 3.864g, which is plotted at half-ϕ intervals.*

3.5 Discussion

Measurement of 1,937 CM chondrules suggests a significant discrepancy between results from 2D and 3D measuring methods alongside variations in model outcomes when applying different stereological corrections. Below we evaluate these measuring methodologies, stereological corrections, provide an updated summary of the CM chondrule sizes, and discuss the implications for the putative CM-CO clan.

3.5.1 2D vs 3D Methodologies

The data reported here illustrate the complexities accompanying what initially appears to be a simple task of determining average chondrule size. The reported average values show significant differences between the two measurement techniques used, with 3D 'true' chondrule diameters spanning a far greater range of average values than the 2D 'apparent' measurements Figure 3.7. This discrepancy is best illustrated by comparing the measurements recorded for Murchison and Aguas Zarcas, which both report 3D average R_1 values of more than 1.515 ϕ (350 μm), far in excess of the maximum total R_1 averages reported for these chondrites using 2D methods (2.752 ϕ (222.7 μm) and 2.666 ϕ (157.5 μm), respectively). The larger R_1 values recorded in 3D are similar to those observed by (Hanna et al. 2015) from a different Murchison chip and taken together could suggest 2D measurements are significantly underestimating the 'true' chondrule size. However, the XCT scan resolutions used in these studies are more than 10 μm/voxel, making identification and accurate segmentation of smaller chondrules (<~100 μm) challenging. The positive skew towards finer particles within all the chondrule size datasets indicates a significant portion of smaller chondrules are being overlooked in 3D studies due to insufficient scan resolutions. The 3D datasets for Winchcombe and LEW 85311 highlights this bias. In these scans, a reconstructed voxel size of <4 μm was achieved, and the average 3D values recorded are much more comparable to those collected using the 2D methods with a resolution of ~2-4 mm/pixel (Tables 3.4, 3.6, & 3.8).

The use of XCT to accurately measure the sizes of objects within CM chondrites therefore appears to be highly resolution dependent, with the potential for resolution-induced bias towards larger chondrules. From the results presented here, it is proposed that scan resolutions equal to or better than ~4 μm/voxel are required for accurate determination of 3D 'true' chondrule sizes by XCT. Thus, XCT data sets with resolutions >4 μm/voxel are excluded from determination of CM averages in this study.

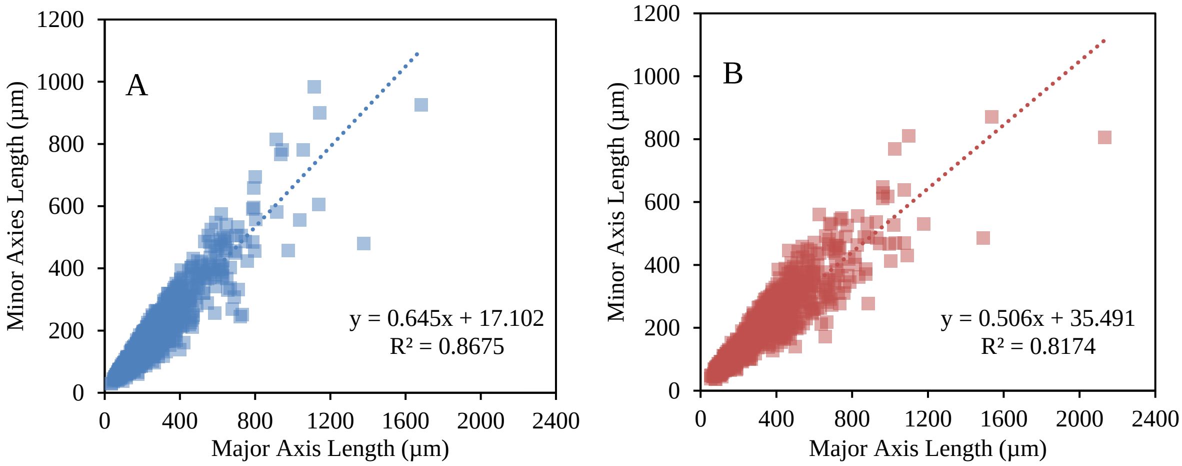

Figure 3.7. *Major/Minor axis relationships for all 2D measurements n = 983 (A) and all 3D measurements n = 954 (B).*

3.5.2 Stereology Corrections

The different stereological corrections illustrated in Figure 3.6 demonstrate the range in outcomes that can be achieved by applying different models. The most significant difference was observed when the Eisenhour (1996) model was applied. The outcome of the Eisenhour (1996) model predicts 3D chondrule sizes smaller than those measured in 2D, implying that random 2D sectioning is producing an overestimate of the 'true' chondrule size. Whilst this finding is consistent with the outcome of the model when published, it disagrees with the 3D measured data and the logical expected result given the probability of randomly sectioning only the largest diameters of chondrules.

The Sahagian & Proussevitch model fared slightly better, producing a model outcome more akin to the 2D data. Despite a median value below that of the 2D measured data, the Sahagian & Proussevitch model did predict ~20% of chondrules were likely to be larger than measured in 2D. Given the model's focus on dealing with non-spherical components and multidispersal systems it perhaps surprising that this model does not better reflect the larger chondrule sizes indicated by the 3D analysis.

The Cuzzi & Olson model has similarities to both the Sahagian & Proussevitch and Benito et al. models. Its similarities to the Benito model are unsurprising given their comparable methodology. The deviation from the Benito model can likely be explained by the improvements in the Benito reconstruction. Figure 3.8 illustrates the differences between the Cuzzi & Olson and Benito models in more detail by comparing the outcomes as both probability density functions (PDFs) and CDFs. This comparison highlights the smoothing effect the Benito model has as a result of the underlying data fitting step. Further, the Benito model is the only one to produce a reconstructed median size larger than that measured in 2D, and therefore agrees with the general findings of the 3D 'true' measured diameters.
There remains a significant discrepancy between the four model outcomes and the 2D/3D data collected. We suggest two possible factors that may be responsible for this:

1. With the exception of Sahagian & Proussevitch, all models have assumed chondrule sphericity. The chondrule dimensions and aspect ratios measured in 2D and 3D demonstrate that CM chondrite chondrules are inherently non-

spherical and therefore any assumption of sphericity is misplaced. It is thought a combination of pre-accretionary and post-accretionary processes are responsible for their shape (Charles et al. 2018; Miura et al. 2008; Tsuchiyama et al. 2003) with post-accretionary processes being particularly important for CM chondrites (Lindgren et al. 2015; Rubin 2012; Vacher et al. 2018). Whilst it is difficult to quantify the effects of this assumption on the model outcomes, the consequences of non-sphericity on stereological models which assume sphericity has been widely discussed within the stereological literature and is likely to be having some effect on the model outcomes (Cuzzi & Olson 2017; Oakeshott & Edwards 1992; Sahagian & Proussevitch 1998).

2. The relatively poor resolution of the 3D Murchison data used here (12.13 μm/voxel) compared to the 2D Murchison data (1.202 μm/pixel). Such disparity between the 2D and 3D data resolutions is likely leading to an exaggerated difference between the 3D and 2D data curves. It is unlikely that using a similar resolution for 2D and 3D analysis will produce a 3D ‘true’ diameter smaller than that recorded in 2D diameters however, it may significantly reduce the difference between the two and allow for better comparison with the models.

None of the models used produced a correction which aligns with the 3D measured true diameters, and this is likely a consequence of both factors listed above. However, given the Benito model is the only one to produce a reconstruction suggesting an increase in the number of larger chondrules, we propose the Benito model is likely the most accurate model currently available for reconstructing 3D chondrule diameters. An updated version of the Benito et al. (2019) code, designed to produce outcomes in Phi-units, is provided in the supplementary materials (Supplementary Materials 1, available with the manuscript version of this chapter). Future analysis should seek to use higher resolution XCT data to help build further understanding of the accuracy of the Benito model relative to true chondrule diameters, alongside attempts to better quantify the errors involved with this type of manual measurement. Efforts should also be made to apply the model to other chondritic groups to investigate the effects of differently sized chondrules on the model and if larger or smaller average sizes have a marked impact on the model’s outcome.

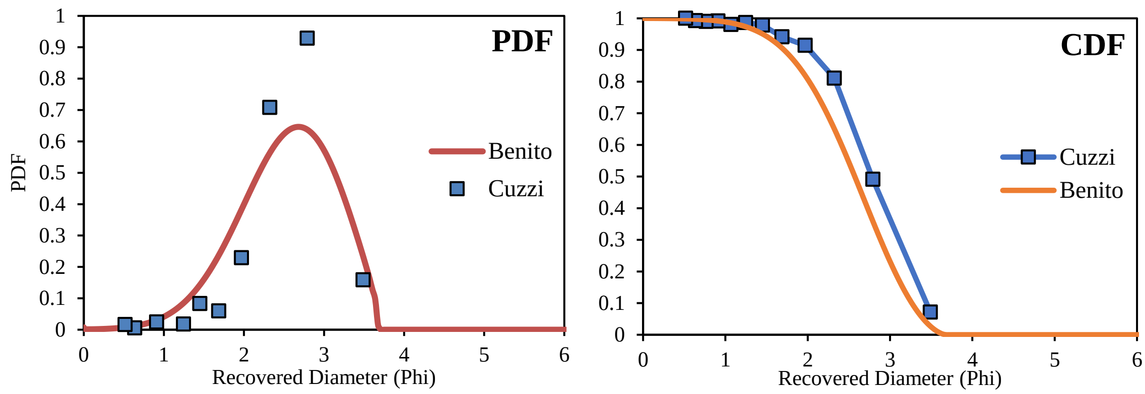

***Figure 3.8**. PDF and CDF plots comparing the Cuzzi & Olson (2017) and Benito et al. (2019) models shown in blue and orange, respectively. The PDF plot reveals the extent to which the Benito et al. model produces a smoother fit compared to the Cuzzi & Olson model; this significant smoothing is not noticeable in the CDF diagram.*

3.5.3 Comparison with chondrule size data in the literature

A comparison of the data presented here (Figure 3.9) with literature values indicates that the stated 270-300 µm average for CM chondrules (Rubin & Wasson, 1986; Weisberg et al., 2006; Friedrich et al., 2015) is an overestimate. This conclusion supports other recent findings of individual CM chondrites, where methodologies similar to those used here, have yielded smaller than reported chondrule sizes (Fendrich & Ebel 2021; Friend et al. 2018). An average CM chondrule size of 2.363ϕ (194 µm) is likely a more appropriate estimate when analysis involves SEM and higher-resolution XCT techniques (i.e., a 28 % reduction compared to 270 µm). The high-resolution imaging and segmentation techniques, alongside the improved statistical methodology, are likely responsible for this reduction in average. A comparison of the CIS methodology with simple arithmetic averaging of non-logarithmically transformed (and thus non-gaussian data) shows that average values are 8.3-28 % smaller when analysed using the CIS methodology.

Comparing average values across the literature is inherently challenging given the variety of methodologies used. Given the ease and effectiveness of CIS methodology, we suggest it could be adopted as a standardised approach for chondrule measurement. Such standardisation would allow for effective and reliable inter-study size comparisons alongside the development of a large-scale repository of chondrule size data.

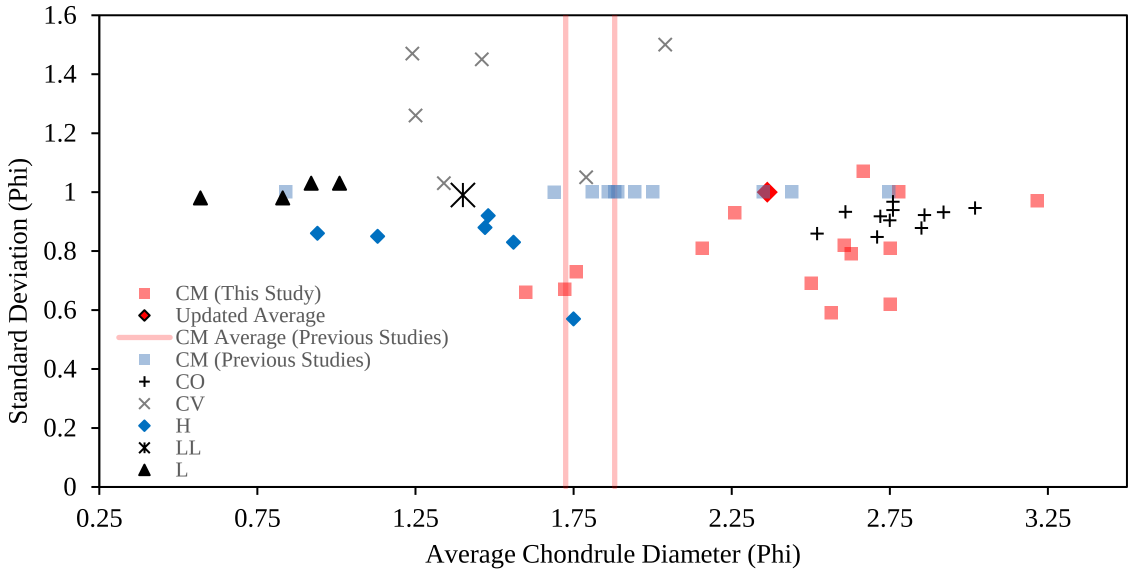

***Figure 3.9**. Chondrule diameters within the major chondritic groups alongside data from the present study. Data not published with graphic standard deviation were given an arbitrary standard deviation of 1 to allow useful visualisation. Chondrule size averages were sourced from the following previous studies. CM chondrites:* Fendrich & Ebel (2021), Friend et al. (2018), Hanna & Ketcham (2018), Kerraouch et al. (2021), Kimura et al. (2020), Rubin & Wasson (1986a), Vacher et al. (2018), *CO chondrites:* Rubin, (1989)*, CV chondrites:* King & King (1978)*, H, L and LL chondrites:* King & King (1979).

3.5.4 Chondrule size/petrologic subtype relationship

Relationships between the size of chondrules and the extent of alteration experienced by their host meteorite/lithology have been described for other carbonaceous groups including the COs where average chondrule size increases with petrologic type (Pinto et al. 2021; Rubin 1989).

Brecciation within the CM chondrites is well recorded and considered ubiquitous within the group (Metzler et al. 1992) with clasts representing highly variable fractions of any CM chondrite volume. Differences in petrologic subtype between clasts are recorded here and within other studies (Bischoff et al. 2017; Lentfort et al. 2020; Suttle et al. 2022). The effects of brecciation and intra-meteorite lithological differences have made identifying any relationship between alteration extent and chondrule size extremely challenging within the CMs. Analysis of any correlation between chondrule size and the petrologic subtype of its host lithology is complicated further by the wide-ranging and often overlapping parameters within the Rubin (2007) and Rubin (2015) classification scheme. These overlapping parameters result in identical subtype classifications for clasts and lithologies which may appear very different in BSE images and EDS maps. The extent of this issue for chondrule size analysis is highlighted by the large spread of chondrule sizes recorded within CM2.2 lithologies identified here (Average R_1: 93.51 µm to 449.1 µm).

By studying a relatively large number of samples and classifying each clast, we have been able to assign a petrologic subtype to each lithology from which chondrules were measured (in 2D). Doing so has facilitating analysis of chondrule size variations between host lithological subtypes (Figure 3.10A). Clasts and lithologies with n < 10 chondrules were excluded from this analysis to avoid introducing noise from small and possibly unrepresentative samples. The results (Figure 3.10B) illustrate a negative correlation between the calculated average sizes and petrologic subtype, with smaller average chondrule sizes towards the more pristine end of the alteration spectrum.

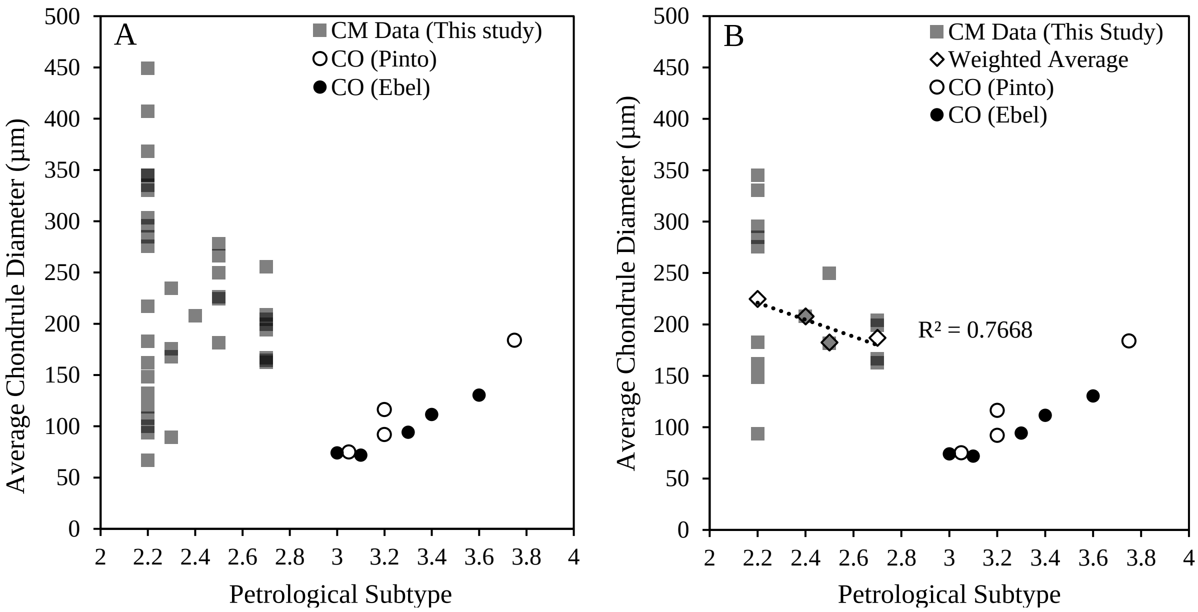

Figure 3.10*. Plots showing the relationship between average chondrule size and petrologic subtype alongside data for CO chondrule size and petrologic type. A) All Clasts/lithologies B) Clasts or lithologies with >10 chondrules with weighted average size for each subtype.*

Potential explanations for a chondrule size/petrological subtype relationship within the CM's include:

1. Aqueous alteration selectively destroying smaller chondrules, resulting in a bias towards larger particles within more altered samples.
2. A size sorting process occurring during parent body accretion such as the contraction of a self-gravitating clump of chondrules of various sizes (Pinto et al. 2021). Such a process would produce a size gradation of chondrules within the original parent body, with larger chondrules towards its centre. Subsequent aqueous alteration may then have been more intense at greater depths within the parent body as a result of proximity to decaying ^{26}Al (Kerraouch et al. 2019; Visser et al. 2020).

Of the two explanations outlined above we favour explanation 2, outlined in Figure 3.11, due to a lack of evidence for total alteration or destruction of smaller chondrules within the moderately altered CM chondrites.

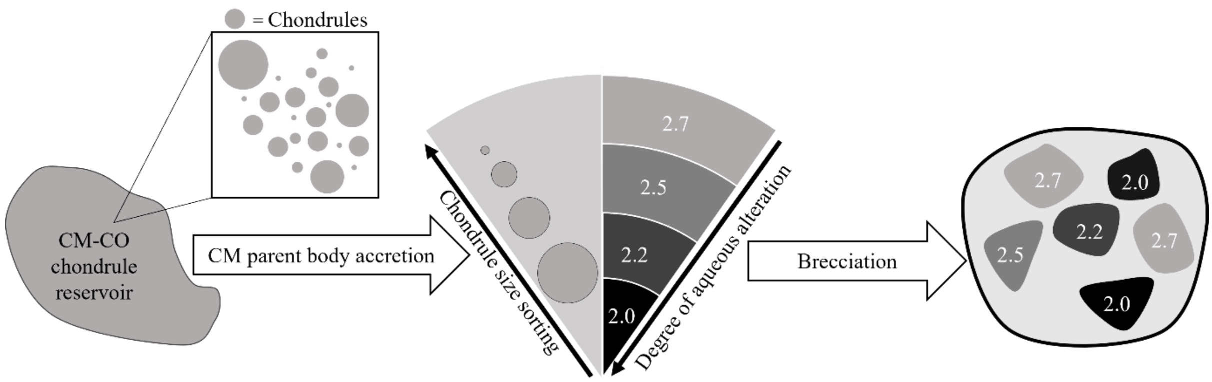

Figure 3.11*. Schematic diagram outlining the series of events which could have led to the relationship between chondrule size and petrological subtype as observed within the CM chondrites.*

3.5.5 Implications for the CM-CO clan

The revised sizes of the CM chondrite chondrules presented here has implications for the widely discussed CM-CO clan. Similarities in chondrule sizes between the two groups (CO average: 148 +132/ -70 μm (Rubin 1989) have been used by some authors (Kallemeyn & Wasson, 1982; Rubin & Wasson, 1986) as a key piece of evidence linking the two groups, whilst others (Schrader and Davidson, 2017) have argued that the subtle differences in chondrule size is evidence for distinct origins. The lower average chondrule size of the less altered meteorites/lithologies reported here, further supports a link between the CM and CO groups. When the CM petrological trend identified here is compared with recent, high resolution analyses of the CO group (Pinto et al. 2021) (Figure 3.10A & 10B) chondrules appear to converge towards a common size at a 3.0 classification. This convergence provides yet further evidence for a deeply intertwined history between the CM and CO chondrites. Whilst differences between the two groups remian (e.g., chondrule abundances) the findings here indicate that differences in chondrules sizes should not be used as evidence against the CM-CO clan and that similarity in chondrule sizes further indicate the strong affinity between the CM-CO chondrites and their likely similar early histories.

3.6 Conclusions

The findings presented here show that the commonly cited literature value for the CM chondrite chondrule size is overstated, likely as a consequence of the measurement methods used. An updated average chondrule size based on our results, and which aligns better with other recent CM studies, of 2.363ϕ (194 μm) is proposed. It is also recommended that the CIS methodology be adopted as a standardised approach to chondrule size measurements to help improve inter-study comparisons of chondrule size. We also support the recommendations of other authors that undigested (raw) chondrule size data should be presented alongside average chondrule size values, and data from this study can be found in Supplementary Materials (Supplementary Materials 2, available with the manuscript version of this chapter) (Friedrich et al. 2015).

Additionally, the methods used here have demonstrated the significance of resolution when quantifying particle size. This is most important when using 3D techniques such as XCT where resolutions may be poorer owing to limitations in scanning large chips. The application of robust stereological corrections to CM chondrules remains a challenge due to their non-spherical form, however the results here indicate that application of the model developed by Benito et al. (2019) provide the best estimate for a 3D particle size distribution.

3.7 Acknowledgements

We thank the STFC for support through grants ST/T002328/1 and ST/W001128/1. We thank the Scottish Alliance for Geoscience, Environment and Society Small Grants Scheme for contributions towards conducting XCT analysis. We thank the Natural History Museum, London, for the loan of Cold Bokkeveld, Murchison (BM1970.6 and BM1988, M23) and Winchcombe samples, Shijie Li for loan of the Shidian sample, Skyfall Meteorites for providing the Aguas Zarcas, Murchison and Kolang samples, Museum National d'Histoire Naturelle de Paris for loan of the Paris sample and to ANSMET for the loan of LAP 02239, LEW 85311 and Mighei. US Antarctic meteorite samples are recovered by the Antarctic Search for Meteorites (ANSMET) program, which has been funded by NSF and NASA, and characterized and curated by the Department of Mineral Sciences of the Smithsonian Institution and Astromaterials Acquisition and Curation Office at NASA Johnson Space Centre. Additional thanks go to Peter Chung for assistance in collecting BSE mosaics and EDS maps and Romy Hanna and Alice Macente for assistance with XCT data acquisition and processing.

Chapter 4 CM Carbonaceous Chondrite Petrofabrics and their Implications for Understanding the Relative Chronologies of Parent Body Deformation and Aqueous Alteration

C. J. Floyd[1*], L. E. Jenkins[1], P-E. Martin[1], L. Daly[1,2,3], M. R. Lee[1]

[1]School of Geographical and Earth Sciences, University of Glasgow, Glasgow, G12 8QQ, UK.
[2]Australian Centre for microscopy and Microanalysis, The University of Sydney, 2006 NSW, Australia.
[3]Department of Materials, University of Oxford, Oxford, OX1 3AN, UK.

Key Points:

- Chondrule-defined petrofabrics are identified in CM chondrites using 2D and 3D techniques
- Comparison of chondrule-defined fabrics within different clasts reveals a complex and variable chronology of alteration and deformation events within and between different CM chondrites
- Chondrules are shown to have a prolate original shape with implications for deformation shock pressures and thus the paradox of low shock stages within the CM chondrites

***Submitted**: Meteoritics and Planetary Science (Accepted with minor revisions)*
DOI: 10.5281/zenodo.10604656 (Preprint)
This chapter represents the pre-peer reviewed article

Data related to this paper can be found in the supplementary materials associated with this publication.

C.J.F and M. L designed research project
C.J.F undertook XCT analysis
C.J.F wrote paper based on discussions with L.E.J, P-E.M, L.D and M.R.L
C.J.F, L.E.J, P-E.M, L.D and L.R.L contributed to editing the paper

4.1 Abstract

CM chondrites have been subjected to numerous alteration processes including brecciation and ductile deformation. Here we present the results of 2D and 3D petrofabric analysis across a suite of meteorites: Aguas Zarcas, Cold Bokkeveld, Lewis Cliff (LEW) 85311, Murchison and Winchcombe. We find that chondrule-defined petrofabrics are commonplace, but not ubiquitous, and where present chondrule long axes typically define foliation fabrics. Interpolation of the shock pressures required to generate these fabrics initially suggests that between 27.8 - 41.8 GPa are needed. Such impacts should ordinarily produce shock microstructures in olivine, but the high pre-compaction porosities calculated in this work and predicted for C-type asteroids may have significantly attenuated energy transfer during collisions. Additionally, we show that the assumption of initial chondrule sphericity is likely inaccurate, and significantly lower shock pressures may be required to produce the deformation and alignment observed. We also show that the relative timings of aqueous alteration, brecciation and deformation vary between CMs. Within Aguas Zarcas we find multiple lithic clasts interpreted as having experienced different degrees of aqueous alteration, with opposing fabrics that formed after water/rock interaction but before brecciation. Within Cold Bokkeveld we find a consistent fabric between clasts suggesting they were deformed after both aqueous alteration and brecciation.

4.2 Introduction

The CM carbonaceous chondrites are a chemically primitive group of meteorites with spectral affinities to the C-complex asteroids (Clark et al. 2010; Pieters and McFadden 1994; Vilas and Gaffey 1989). Despite their primitive composition, the CM chondrites have experienced significant secondary processing within their parent body including aqueous alteration, brecciation, and deformation (Bischoff et al. 2006; Dodd 1965; Hanna et al. 2015; Lindgren et al. 2015; Metzler et al. 1992; Rubin 2012; Rubin et al. 2007). While aqueous processing is discussed at great length within the literature, far less attention has been paid to understanding the origins and evolution of the brecciation and deformation experienced by the CMs.

Despite the lack of attention within the literature, evidence for brittle deformation is abundant within the CM chondrite group with the majority of meteorites being defined as regolith breccias (Bischoff et al. 2006; Hanna et al. 2015). They comprise angular lithic clasts set within a fine-grained matrix of variable abundance, typically constituting 70% (Bischoff et al. 2006; Suttle et al. 2022; Weisberg et al. 2006). The lithic clasts contain abundant solar-wind gases and solar flare tracks indicating that they spent a period close to the parent bodies outer surface (Bischoff and Schultz 2004; Bischoff et al. 2006). Brecciation is readily identified in the CMs using scanning electron microscopy (SEM) techniques such as backscattered electron (BSE) imaging and energy dispersive X-ray spectroscopy (EDS). These techniques reveal mineralogical, chemical, and textural contrasts between clasts reflecting different formation environments and their varying degrees of aqueous alteration (Bischoff et al. 2006; Lentfort et al. 2020; Rubin et al. 2007).

Deformation within the CMs has been identified by numerous previous studies using both 2D and 3D techniques (Hanna et al. 2015; Lindgren et al. 2015; Rubin 2012; Vacher et al. 2018; Yang et al. 2022). Typically, deformation is described by assessing the alignment or 'flattening' of constituent chondrules that are assumed to have once been spherical (Hanna et al. 2015; Rubin 2012; Vacher et al. 2018; Zolensky et al. 1997). Other deformation features such as parallel fractures (King et al. 2022), deformed veins (Lee et al. 2019) and the alignment of phyllosilicate mineral serpentine (Fujimura et al. 1983) have also been observed within CM chondrites and discussed in the context of deformation.

Deformation and alignment of chondrules is not restricted to the CM chondrites, and many other chondritic groups (e.g., CV3, L, LL and H) also preserve evidence of deformation occurring in this way (Cain et al. 1986; Dodd 1965; Forman et al. 2016; Martin and Mills 1980; Ruzicka and Hugo 2018; Scott et al. 1992; Sneyd et al. 1988). Where the CM chondrites differ from the other deformed chondrite groups is their lack microstructural shock effects. The CM chondrites are almost exclusively characterised as shock stage S1 interpreted as having experienced <5 GPa shock pressure (Scott et al. 1992; Stöffler et al. 1991; Stöffler et al. 2018).

The common observation of features typically associated with deformation and mineral and chondrule alignment within the CM group has promoted significant debate as to its likely causes and timing relative to aqueous processing (Rubin 2012; Vacher et al. 2018). Proposed mechanisms for the deformation observed include:

- A nebular accretionary process, such as deposition within a flowing medium on a body capable of sustaining an atmosphere and liquisphere (i.e., a body larger than asteroidal size). Such deposition in turn caused the differential segregation and sedimentation of chondrules based on their degree of flattening (Dodd 1965). Alternatively, alignment could be produced by the process of convection in an unlithified mud (Bland and Travis 2017).
- Lithostatic compaction/overburden from burial on the parent asteroid (Cain et al. 1986; Fujimura et al. 1983; Martin and Mills 1980; Stacey et al. 1961)
- Impacts, sometimes referred to as dynamic processing, ranging from single hypervelocity impacts to multiple low-intensity impacts (Lindgren et al. 2015; Sneyd et al. 1988; Vacher et al. 2018)

Reconciling the lack of shock features, extent of brecciation, and degree of deformation observed within the CMs with a mechanism to produce these effects remains challenging, despite the numerous theories. This work sets to build on previous studies by examining chondrule defined petrofabrics within a suite of CM chondrites in 2D and 3D to better understand the degree of deformation experienced, the potential mechanisms to produce deformation and the likely relative chronology of alteration events on the CM parent body(ies).

4.3 Methods

4.3.1 Materials and Methods

Five CM chondrite chips were examined using the non-destructive 3D technique of X-ray computed tomography (XCT). Additionally, two chips were subjected to random sectioning and their petrofabrics examined in 2D for comparison with the 3D datasets. The meteorites selected for analysis represent a range of petrologic subtypes, comprise several notably brecciated examples and include Murchison, one of the few CMs recorded as shock stage S1/2. The samples analysed are listed in Table 4.1.

Table 4.1. *List of CM chondrite chips investigated during this work alongside their reported petrologic subtype and evidence of fabric.*

Meteorite	**Chip ID and mass (g)**	**Previously reported petrofabric**	**Shock Stage**	**Petrologic subtype[e]**
Aguas Zarcas	Aguas Zarcas (3.840)[a]	Yang et al. (2022)	---	CM2.2-2.8[e]
Cold Bokkeveld	BM.1727 (2.154)[b]	Rubin (2012) Suttle et al. (2017)	S1[d]	CM2.2[f] CM2.1-2.7[g]
Lewis Cliff (LEW) 85311[†]	LEW85311, 84[c]	Lee et al. (2019)	S1[d]	CM2.6-2.7[h]
Murchison[†]	Murchison (3.86)[a]	Rubin (2012) Hanna et al. (2015) Lindgren et al. (2015)	S1/2[d]	CM2.5[f] CM2.9-CM2.7 (main lithology CM2.7)[g]
Winchcombe	BM.2022, M2-34 (0.238)[b]	King, Daly et al. (2022)	---	CM2.0-2.6[i]

[†]Randomly sectioned for 2D analysis

[a] Commercially obtained

[b] Natural History Museum (U.K.)

[c] ANSMET

[d]Scott et al., (1992)

[e] Kerraouch et al., (2021)

[f] Rubin et al., (2007)

[g] Lentfort et al., (2020)

[h] Choe et al., (2010)

[i] Suttle et al., (2022)

--- Not Available

4.3.2 X-ray Computed Tomography:

XCT was conducted on five carbonaceous CM chondrites (Table 4.1) to produce three-dimensional (3D) datasets. Each acquisition collected a series of 2D projections (tomographs) over a 360° rotation of the sample and these projections were subsequently reconstructed as a 'stack' by filtered back-projection (Ketcham and Carlson 2001). Each 2D slice records variations in the grey scale intensity, corresponding to X-ray attenuation, which in turn is dependent on the density and atomic number (Z) of the material (Hanna and Ketcham 2017; Ketcham and Carlson 2001). The components represented by the lowest grey scale intensity (darkest pixels) represent the least attenuating or lowest density materials (Hanna and Ketcham 2017, 2018). Within CM chondrites the least attenuating materials include matrix, type I chondrules and pore space (Vacher et al. 2018). Components with the greatest grey scale intensity (brightest pixels) are composed of the most attenuating or highest density material (Hanna and Ketcham 2017, 2018). These highly attenuating materials in the CMs include metal and sulphide grains, with the latter distinguished by having a slightly lower grey scale intensity (Friedrich et al. 2008; Vacher et al. 2018).

XCT analysis was undertaken in the UK at both the University of Strathclyde (UoS) and the Natural History Museum (NHM) London, UK. Analysis at the UoS used a Nikon XT H320 LC CT system equipped with a 180 kV transmission source. Reconstruction was achieved using Nikon proprietary software. Analysis carried out at the NHM's Imaging and Analysis Centre used a Zeiss Xradia Versa 520 CT system equipped with a 160 kV source. In both cases X-rays were generated from a tungsten source using the conditions outlined in Table 4.2. Data collected using the NHM XCT instrument were reconstructed using Zeiss reconstructor software with an appropriate X-ray source filtration used to reduce the effect of beam hardening. The final reconstructed voxel sizes and number of 2D slices within each stack set varied as a function of sample size (Table 4.2).

Table 4.2*. Table outlining the XCT scan parameters and resulting voxel sizes for each of the CM chips.*

Meteorite	**Facility**	**Voltage (kV)**	**Current (μA)**	**Voxel Size (μm)**	**Number of Slices**
Aguas Zarcas	UoS	80	140	12.13	1627
Murchison	UoS	90	124	12.13	2000
LEW 85311	UoS	70	76	3.026	2000
Cold Bokkeveld	UoS	70	153	11.15	2000
Winchcombe	NHM	130	76.9	4.057	3214

4.3.3 3D Petrofabric Analysis:

Within the 3D volumes an abundance of sub-angular to rounded dark-toned objects (low X-ray attenuation) were observed and interpreted as type I chondrules, while light-toned objects were identified as either metallic components or sulphides. Segmentation of chondrules was carried out in Avizo^{TM} software following the partial segmentation techniques described by (Hanna et al. 2015). Prior to segmentation a non-local means filter was applied to the volume to reduce noise in the dataset and simplify the boundaries between the chondrules and the matrix as both have low attenuation coefficients. Non-local mean filter parameters were as follows: search window = 9, local neighbour = 4, similarity value = 0.4. The partial segmentation outlined by (Hanna et al. 2015) involved manually segmenting the largest cross-sectional area of each chondrule in each of the three orientations (XY, XZ and YZ). Following segmentation, data were then exported to Blob3D (Ketcham 2005a, 2005b) where a specialised merit function was used to fit an ellipsoid to the three orthogonal sections collected for each chondrule. Blob3D subsequently measured the size, shape, and orientation of each ellipsoid. Directional cosines were produced by Blob3D to describe ellipsoid orientations, and these were converted to trend and plunge before being plotted onto stereonets using OpenStereo software (Grohmann and Campanha 2010). Eigenvalues (λ_1, λ_2 & λ_3) were also computed and used to assess the randomness of any orientation detected (Woodcock and Naylor 1983). Petrofabric shape is assessed by the shape parameter *K* (Equation 4.1):

$$K = ln\left(\frac{\lambda_1}{\lambda_2}\right)/ln\left(\frac{\lambda_2}{\lambda_3}\right) \quad \text{(Equation 4.1)}$$

K ranges from 0 to ∞, with $K<1$ indicating a girdle distribution and $K>1$ a cluster distribution (Woodcock and Naylor 1983). The strength of a given fabric can also be characterised by strength parameter *C* (Equation 4.2):

$$C = \ln\left(\frac{\lambda_1}{\lambda_3}\right) \quad \text{(Equation 4.2)}$$

A value for *C* that is close to 0 indicates a weak fabric, $C \geq \sim 1$ a weak to moderate fabric, $C \geq 2.0$ a moderate to strong fabric, and $C \geq 4$ a strong fabric (Woodcock and Naylor 1983). The orientation of any fabric detected can be described by the pole to the primary axis girdle which can be described most simply by the primary axis third eigenvector (λ_3). Where comparisons between fabric orientations are made between lithologies, the long axis λ_3 is used to quantify the orientation differences.

Within Cold Bokkeveld metal grain orientation analysis was also conducted. In this instance the lightest-toned objects, identified as Fe,Ni metal given the chondritic composition (Rubin et al. 2007) were segmented and analysed using the aforementioned technique.

Axial length measurements of ellipsoids allow for shape assessment of each chondrule using Sneed and Folk, (1958) ternary plots. Chondrule shape was determined using the ratios of the primary (a), intermediate (b) and tertiary (c) axes and defined quantitatively by 10 categories (Figure 4.1).

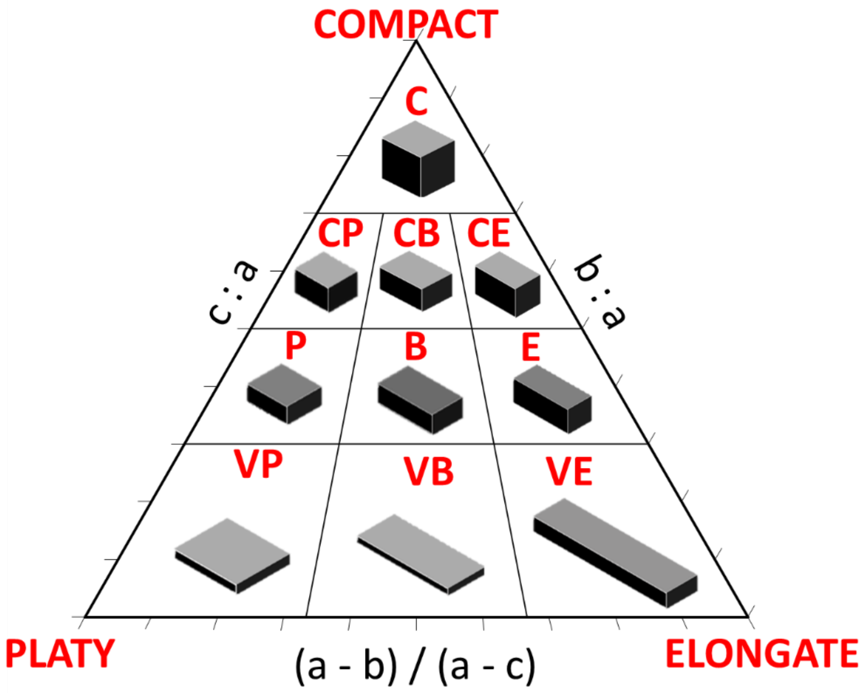

Figure 4.1. *Adapted figure from Sneed and Folk, (1958) showing a particle shape ternary plot with the 10 different shape classifications and three end members. Each shape is described according to C: compact, P: platy, B: bladed, E: elongate, V: very. Also shown are the equations for calculating a given shape descriptor (a: primary axis length, b: intermediate axis length, and c: tertiary axis length).*

4.3.4 2D Chondrule Petrofabric Analysis:

2D chondrule petrofabric analysis was conducted on thin sections that were prepared from the Murchison and LEW 85311 chips and were not oriented relative to any petrofabric. Following polishing, the sections were coated in 20 nm of carbon before SEM work was carried out at the University of Glasgow's GEMS facility. A Zeiss Sigma field-emission SEM was used with an Oxford Instruments EDS detector operated through Oxford Instruments Aztec software. BSE and EDS mosaics of whole section areas were collected at resolutions of 1.20 µm/pixel and

1.67 µm/pixel for Murchison and LEW 85311, respectively. An accelerating voltage of 20 kV was used for both samples. Chondrule defined petrofabrics were subsequently investigated by segmenting the chondrules according to the CIS methodology (Floyd et al., Forthcoming) and fitting an ellipse to segmented outlines. Chondrule ellipse orientations were determined using ImageJ software. Ellipse long axis orientations were measured relative to the x-axis of the image.

4.3.5 Strain and Porosity Loss Estimates:

Estimates of the strain experienced, and the sample's pre-deformation porosity, were calculated using equations 4.3 & 4.4, first derived by Hanna et al. (2015) (see Hanna et al. 2015 for full derivation). Equation 4.3 calculates strain (ε) using aspect ratio (α) assuming an initially spherical chondrule shape, incompressibility, and uniaxial strain. Equation 4.4 calculates pre-deformation porosity (P_0), using the post-deformation porosity measured (P_1) and assuming that porosity loss occurred entirely within the matrix.

$$\varepsilon = 1 - a^{-2/3} \quad \text{(Equation 4.3)}$$

$$P_0 = \left[1 - (1 - \varepsilon)\left(1 - \frac{P_1}{100}\right)\right] \times 100\% \quad \text{(Equation 4.4)}$$

4.4 Results

Three of the five 3D meteorite volumes examined in this study were breccias. The various clasts and lithologies were distinguished by contrasts in X-ray attenuation, differences in the abundance or presence of dark- and light-toned objects and occasionally, fracture defined lithological boundaries (Figure 4.2). In common with other studies, we identified dark-toned objects within our XCT volumes as chondrules, light-toned (bright) objects as Fe,Ni metal, and bright grey material as FeS (Friedrich et al. 2008; Hanna and Ketcham 2018; Vacher et al. 2018). To confirm this assumption, image registration was carried out by correlating regions within the Murchison XCT volume with the BSE and EDS mosaics produced from thin sections of the same sample (Figure 4.2C/D).

Due to the large size (> 1 cm^2) of the Murchison, Aguas Zarcas and Cold Bokkeveld chips, and the high resolution of the XCT scans of the LEW 85311 and Winchcombe chips, analysis of complete volumes was not practical (Table 4.3). Consequently, where only one lithology was present a representative sub-volume was extracted for analysis. Where multiple lithologies were observed, analysis was carried out within only the most well-defined lithologies to avoid trying to constrain poorly defined lithological boundaries, an example of which is shown in Figure 4.2B. Details regarding the number of chondrules and lithologies examined and an estimated total number of lithologies for each chip are outlined in Table 4.3.

Table 4.3*. The number of lithologies within each chip, estimated using XCT analysis, the number of lithologies examined within each chip and the total number of chondrules segmented for orientation analysis.*

Sample	**Est. total no. Lithologies**	**No. lithologies examined†**	**Chondrules segmented (*n*)**
Aguas Zarcas	9	3	311
Cold Bokkeveld	>8	3	199
LEW 85311	1	1	155
Murchison	1	1	180
Winchcombe	7	2	139

†Where only one lithology was identified within the volume a representative sub-volume was extracted for analysis

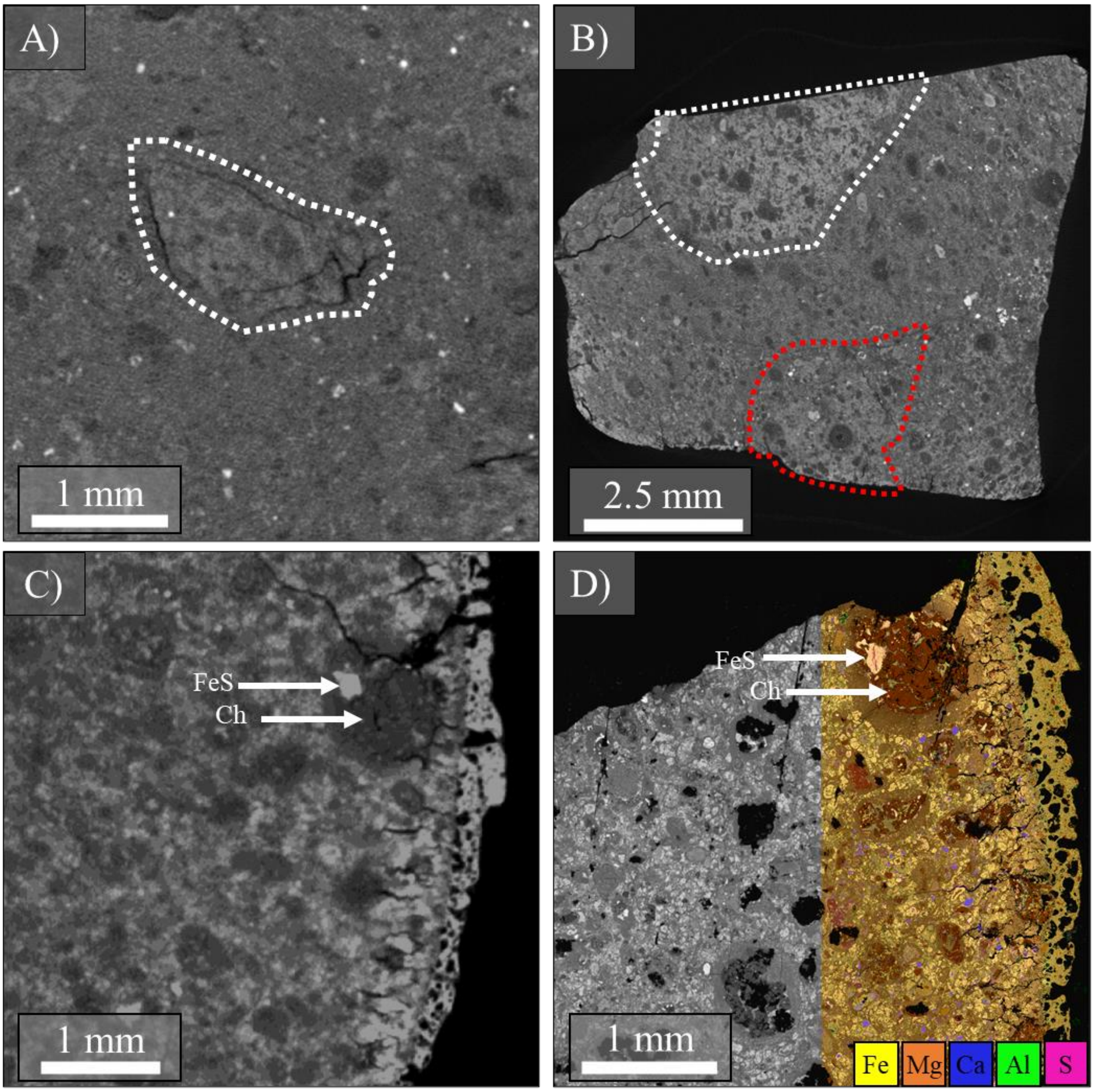

Figure 4.2. *A) X-ray tomograph slice 920/2000 from Cold Bokkeveld showing a fracture defined clast (outlined in white). B) X-ray tomograph 961/1627 from Aguas Zarcas illustrating the subtle differences in attenuation coefficients between lithologies. Highlighted in white is a higher attenuating lithology with clearly defined boundaries, and highlighted in red is a lower attenuating lithology with poorly defined boundaries. C) X-ray tomograph 656/2000 from Murchison. Dark-toned objects are clearly distinguishable throughout the slice and interpreted to be chondrules. White arrows indicate an example chondrule (Ch) and FeS grain. D) Composite BSE and EDS image of a thin section used for image registration. The view shows the same region as shown in C) and provides confirmation of the interpretation of the dark and light-toned objects.*

4.4.1 Chondrule-defined Petrofabrics and Chondrule Shapes

4.4.1.1 Aguas Zarcas:

Three lithologies (L_1, L_2 & L_3) were clearly distinguishable within Aguas Zarcas from differences in X-ray attenuation. L_1 and L_3 appeared as small bright lithologies within the larger and darker lithology L_2, which is the dominant lithology within the volume (as shown in Figure 4.2B). Chondrule-defined fabrics were detected in all three lithologies (Figure 4.3A) with shape factor (K-values) for the ellipsoid long axes (r_1) <1 indicating the presence of a foliation fabric. A foliation fabric is further evidenced by the clustering of the short axes (r_3) with K values > 1. The strength of these fabrics was variable, with a strength factor (C-value) range of 0.78-1.34, representing weak-moderate fabrics. In all three lithologies chondrule orientations were found to be non-random at the 99% confidence interval.

The L_1 and L_2 lithologies have similar foliation orientations ($L_1\lambda_3$: 260.9°, $L_2\lambda_3$: 257.1°). However, a difference is observed within lithology L_3 where a foliation orientation of: $L_3\lambda_3$: 55.4° is recorded, representing a deviation from the L_1 - L_2 average orientation by 156.4°.

Shape analysis of chondrules within the Aguas Zarcas lithologies is shown in Figure 4.3B. Chondrules are predominantly defined as either compact (C), compact bladed (CB), or compact elongate (CE). Within both L_1 and L_3 the average chondrule aspect ratio (AR) is calculated as 1.77, and both sets of chondrules plot as more elongate in shape with >10 % of chondrules defined as elongate (E). L_2 chondrules have an average AR of 1.57 and are mostly defined as compact (32.69%) with fewer than 3% of chondrules defined as elongate. A full breakdown of the shape classes is provided in the Supplementary Materials.

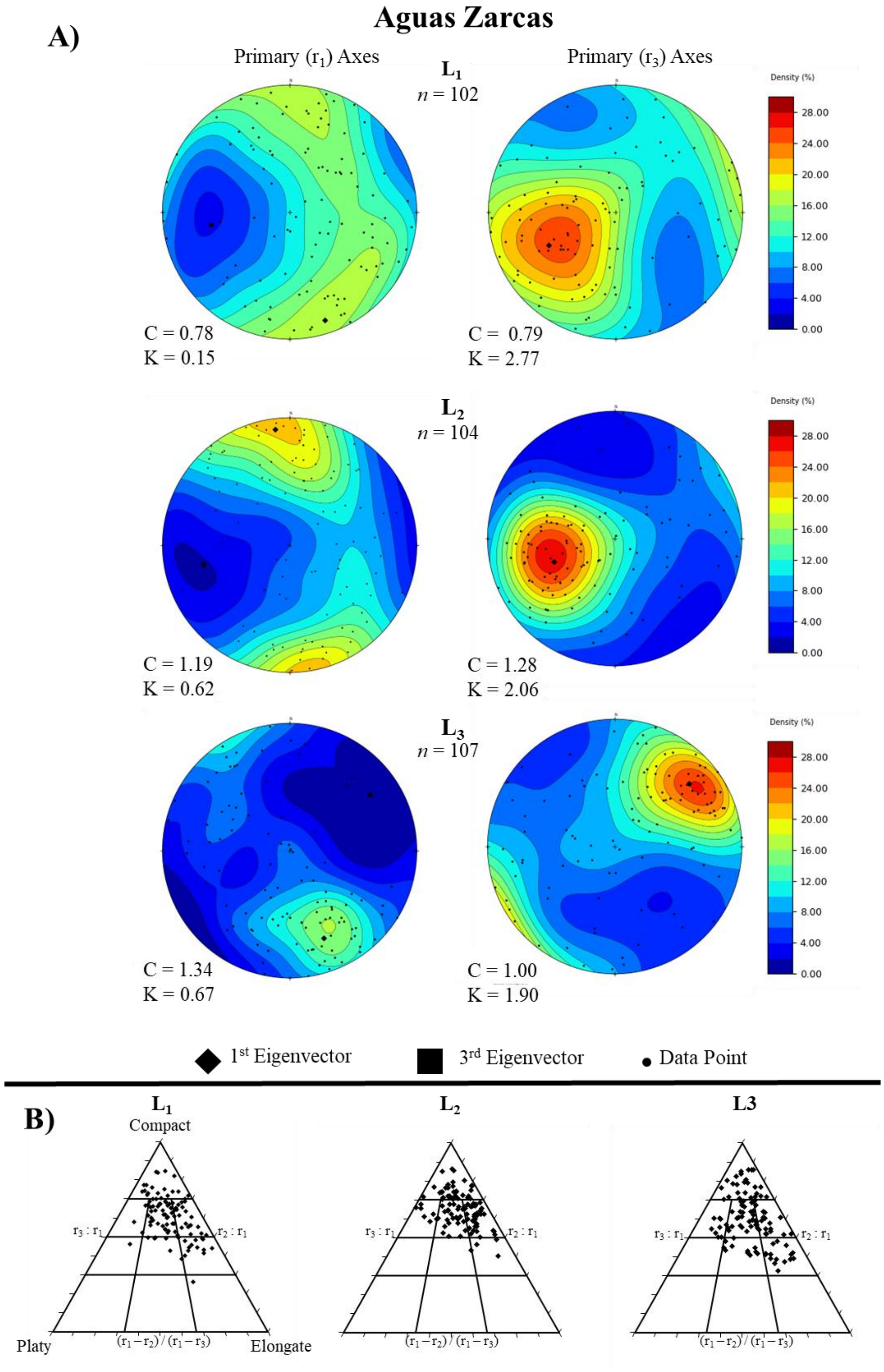

Figure 4.3. *A) Lower hemisphere equal-area projections showing the orientations of chondrule primary and tertiary axes within the three Aguas Zarcas lithologies (L_1, L_2 & L_3). Strength parameter (C) and shape parameter (K) are provided beneath each projection. B) Tri-plot diagrams based on Sneed and Folk (1989) illustrating chondrule shapes. The number of datapoints in each plot is the same as for each lithology in A.*

4.4.1.2 Cold Bokkeveld:

Three lithologies (L_1, L_2 & L_3) were selected for analysis from the Cold Bokkeveld volume. Each lithology was distinguished by differences in X-ray attenuation, and in the case of L_1, by abundant highly attenuating light-toned objects, interpreted as Fe,Ni metal.

K-value analysis reveals that all three lithologies have chondrule defined foliation fabrics with r_1 orientations defining girdle distributions and r_3 orientations clustering (Figure 4.4A). In all lithologies slight clustering along the foliation girdle suggests a minor stretching lineation accompanies the foliation. C-values in L_1 and L_2 indicate a weak-moderate fabric strength whilst L_3 has a weak fabric. In all three lithologies orientations are non-random at the 99% confidence interval. Fabric orientations within each lithology are broadly consistent: $L_1\lambda_3$: 174.3°, $L_2\lambda_3$: 187.6° and $L_3\lambda_3$: 159.3 with a maximum orientation deviation of 28.3° recorded between L_2 and L_3.
Shape analysis of the Cold Bokkeveld chondrules reveals similarities with Aguas Zarcas in that chondrule shapes generally vary between C, CB and CE (Figure 4.4B). Chondrule average aspect ratios show some variation between lithologies (L_1: 1.79, L_2: 1.75, L_3: 1.92). Compact chondrules represent the most abundant shape class within L_1 (32.6%). Shapes differ significantly in L_2 with compact chondrules representing only 9.52%. Despite the higher aspect ratio of L_3 it contains equal percentages of C and CB chondrule shapes (27.42%). The high aspect ratio recorded in L_3 appears to be a consequence of a single chondrule defined as very elongate.

4.4.1.3 Cold Bokkeveld L_1 Metal Grains:

Due to the abundant Fe,Ni grains identified within the L_1 lithology of Cold Bokkeveld, additional orientation analysis was conducted to investigate evidence for a discernible fabric defined by the grains. A total of 95 metal grains were segmented with the resulting stereonet (Figure 4.5) showing their orientations. K-values calculated indicate that r_3 orientations define a foliation whilst r_1 orientations cluster, C-values indicate a weak fabric strength. The orientation distribution is found to be non-random at the 99% confidence interval. The foliation orientation for the short axis is $L_1MG\lambda_3$: 68.7°, approximately perpendicular to the foliation direction defined by the chondrules.

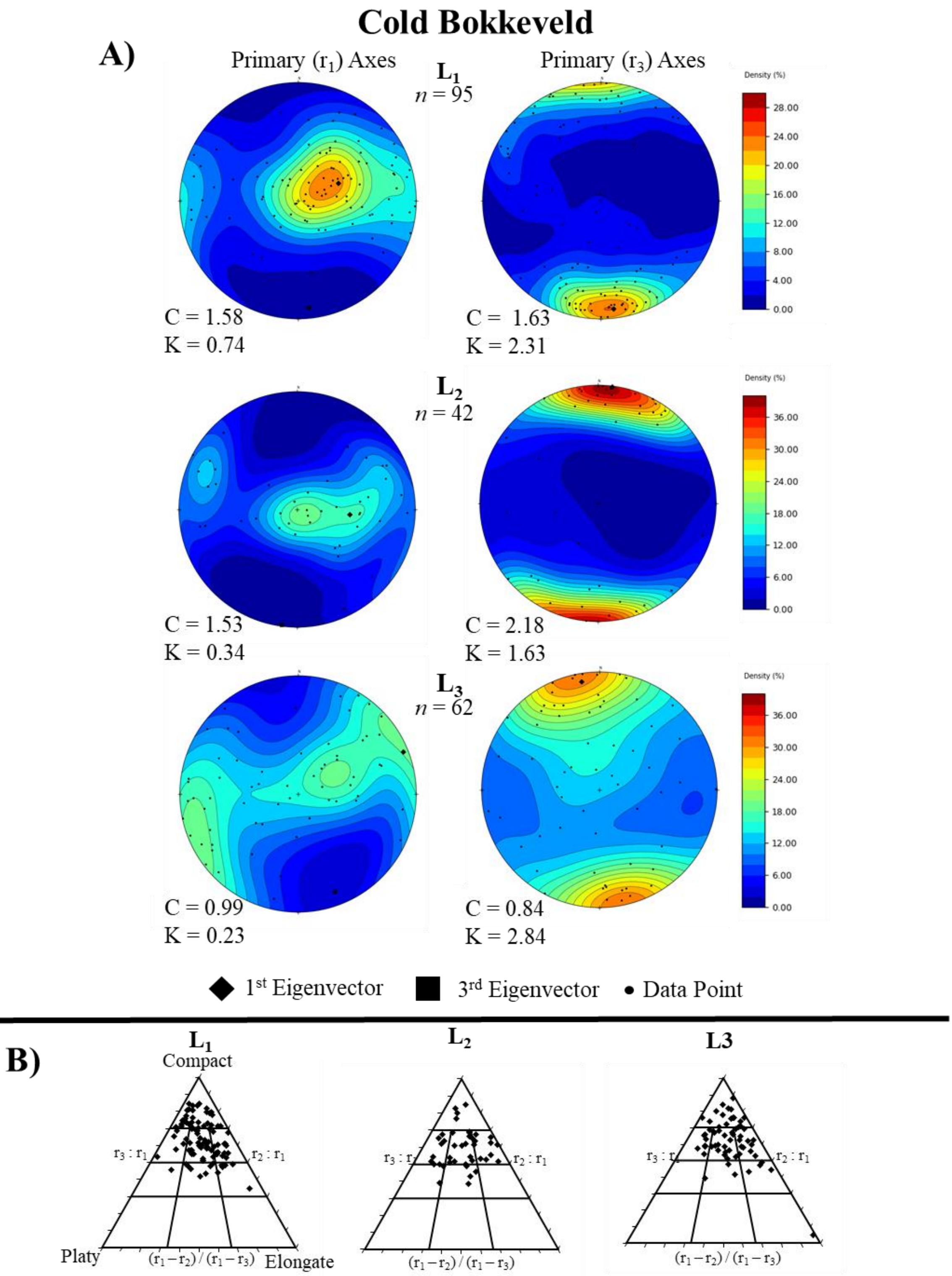

Figure 4.4. *A) Lower hemisphere equal-area projections showing the orientations of chondrule primary and tertiary axes within the Cold Bokkeveld lithologies (L_1, L_2 & L_3). Strength parameter (C) and shape parameter (K) are provided beneath each projection. B) Tri-plot diagrams based on Sneed and Folk (1989) illustrating chondrule shapes. The number of datapoints in each plot is the same as for each lithology in A.*

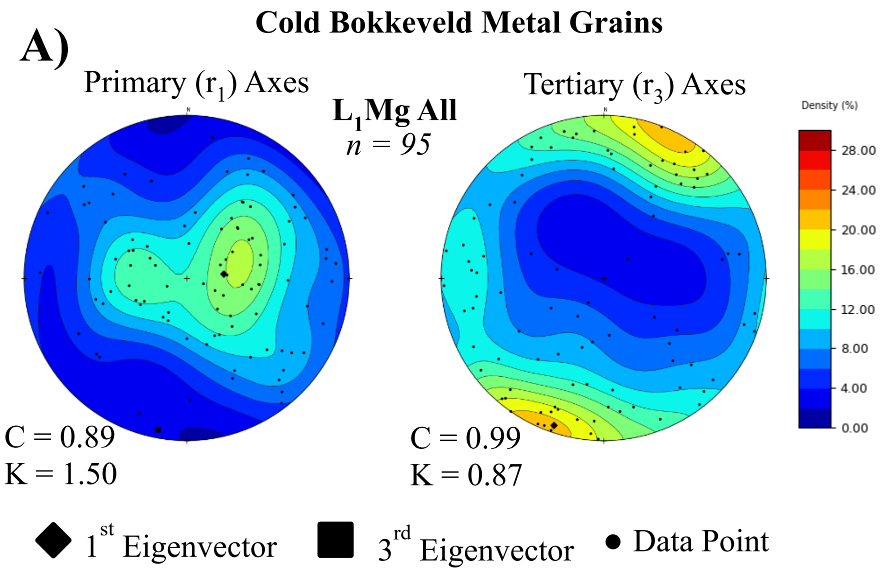

***Figure 4.5**. Lower hemisphere equal-area projections showing the orientations of segmented metal grains primary and tertiary axes within the Cold Bokkeveld lithology L_1.*

4.4.1.4 LEW85311 3D Petrofabric Analysis:

A single lithology was identified within LEW85311 which we interpret as the main lithology. A sub-volume was extracted from this lithology and a total of 155 chondrules were segmented for orientation analysis. K-value analysis indicates r_1 orientations define a lineation whilst the r_3 orientations sit on the on the lineation/foliation transition (Figure 4.6A). The C-values associated with this fabric indicate this is very weakly defined with the r_1 orientation non-random at the 90% confidence interval and the r_3 fabric non-random at the 99% confidence interval. The orientation of the foliation defined by the short axes is $L_1\lambda_3$: 47.2°.

An average AR of 1.61 was determined with chondrule shapes predominantly compact (33%); CB and CE chondrules account for 23% and 25 %, respectively (Figure 4.6B).

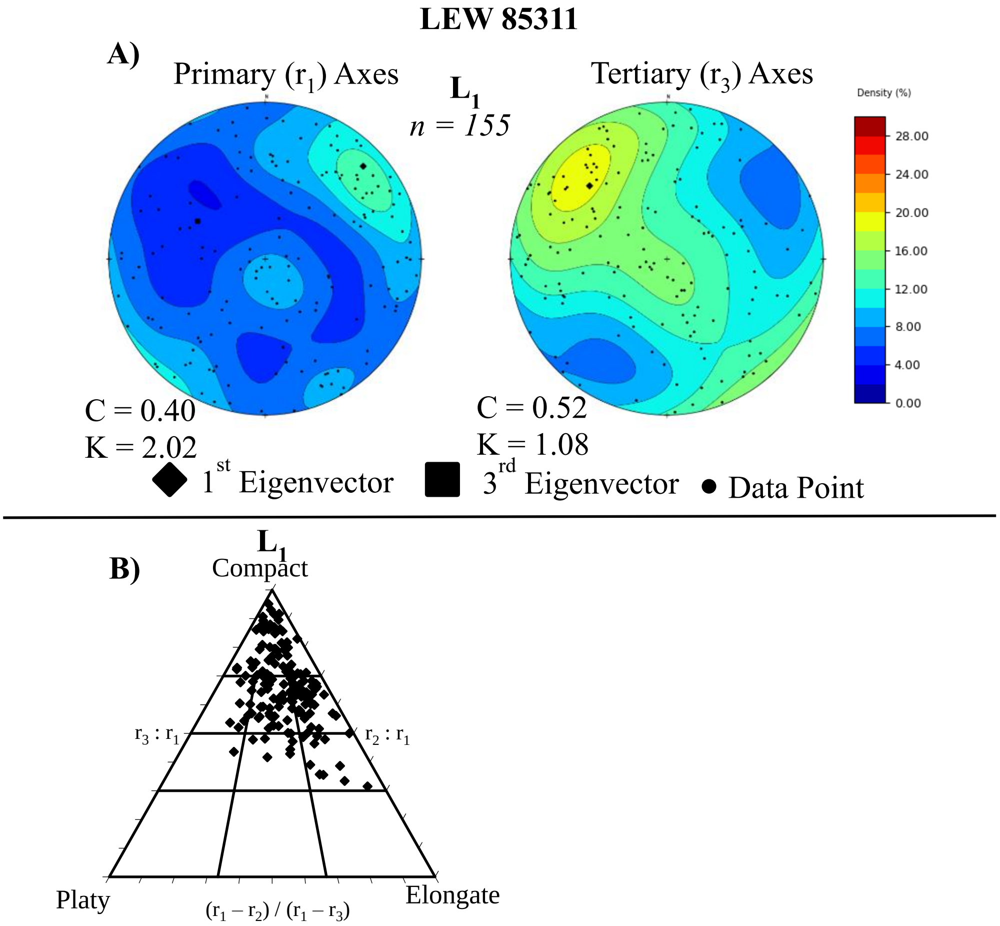

Figure 4.6. A) Lower hemisphere equal-area projections showing the orientations of chondrule primary and tertiary axes within LEW85311. Strength parameter (C) and shape parameter (K) are provided beneath each projection. B) Tri-plot diagrams based on Sneed and Folk (1989) illustrating chondrule shapes. The number of datapoints in the plot is the same as for A.

4.4.1.5 LEW 85311 2D Petrofabric Analysis:

2D petrofabric analysis was conducted following random sectioning of the LEW 85311 chip used for XCT analysis (thin section LEW 85311, 90). A total of 133 chondrules were identified and segmented. A rose diagram shown in Figure 4.7 illustrates no significant chondrule alignment is present within the 2D section with just 15% of all chondrules sitting within 10% of the median azimuth angle (AA): 85.28° and 25% within 20% of the median. An Average AR of 1.35 ± 0.27 is calculated in 2D (reported previously in Floyd et al., (Forthcoming)) and is 17.6% lower than the 3D obtained AR. The low degree of fit with the median AA and low aspect ratio support the 3D findings of only a weak-very weak petrofabric being present within LEW 85311.

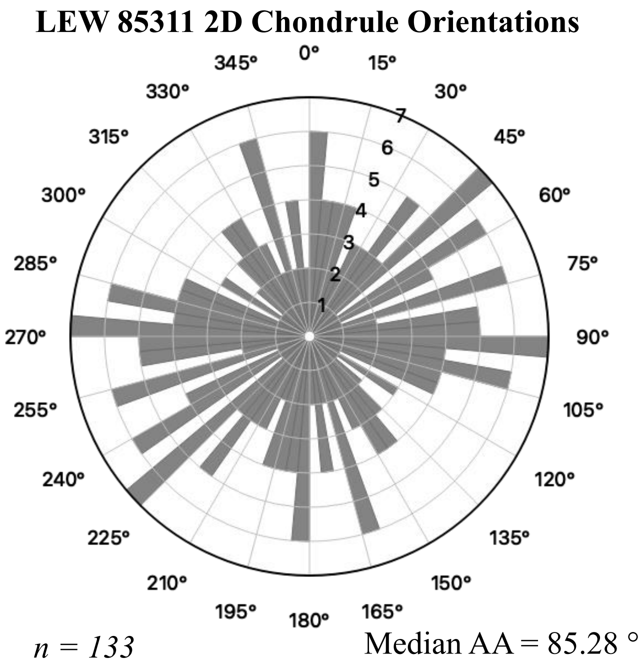

Figure 4.7*. Rose diagram binned at 5° intervals showing no significant, 2D measured, chondrule alignment in the LEW 85311 thin section.*

4.4.1.6 Murchison 3D Petrofabric Analysis:

A single lithology was identified within the Murchison chip from which a sub-volume was extracted and 180 chondrules segmented and analysed. A very clear chondrule defined fabric was detected with a calculated r_1 K-value defining a foliation fabric and strong clustering of the r_3 axes. Some clustering along the foliation girdle suggests a minor element of stretching lineation. The calculated C-value is the highest observed in this study, despite still classifying as a weak-moderate fabric (Figure 4.8A). The r_1 and r_3 distributions are non-random at the 99% confidence interval. The foliation orientation defined by the long axes is $L_1\lambda_3$: 76.2° relative to the volume orientation.

Results of chondrule shape analysis in Murchison are shown in Figure 4.8B. Compact chondrule shapes represent the most abundant classification (30.56%) while a notable 16.6% are classified non-spherical (P, B or E) classes. This variation in chondrule shape is reflected in the average AR: 1.72.

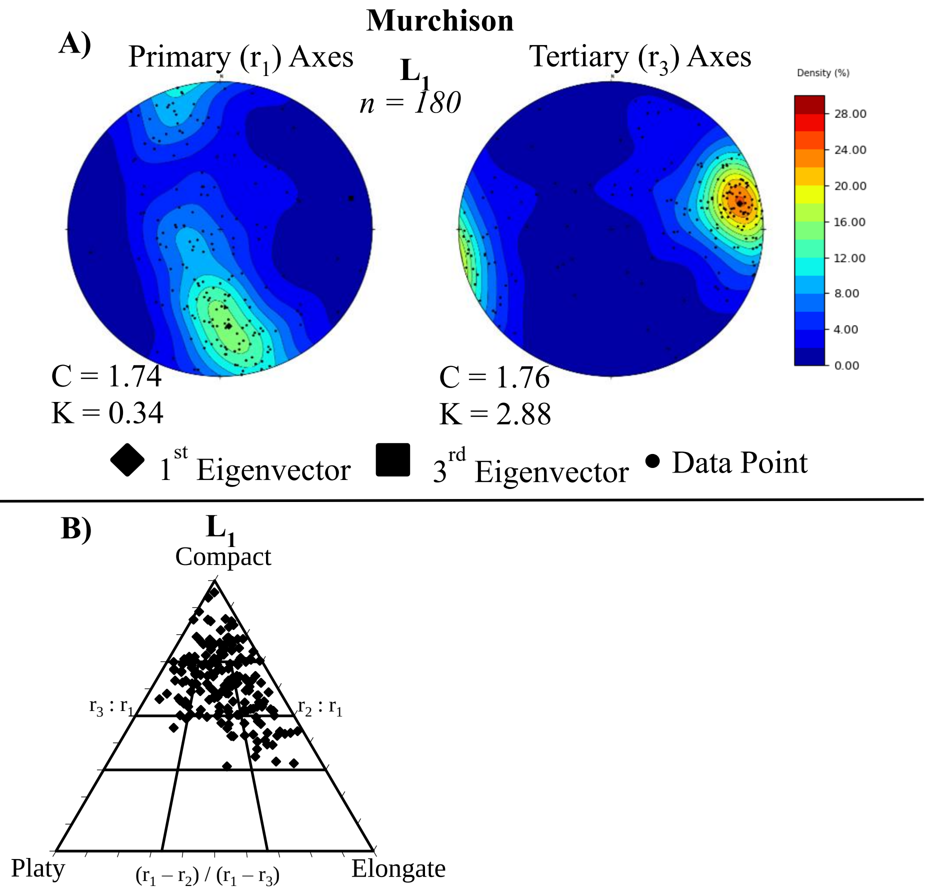

***Figure 4.8**. A) Lower hemisphere equal-area projections showing the orientations of chondrule primary and tertiary axes within Murchison. Strength parameter (C) and shape parameter (K) are provided beneath each projection. B) Tri-plot diagrams based on Sneed and Folk (1989) illustrating chondrule shapes. The number of datapoints in the plot is the same as for A.*

4.4.1.7 Murchison 2D Petrofabric Analysis:

2D petrofabric analysis conducted following random sectioning of Murchison chip used for XCT analysis. A total of 140 chondrules were identified and segmented. A rose diagram showing the orientations of the segmented chondrules is shown in Figure 4.9. 26% of the chondrules examined sit within 10% of the median azimuth angle (AA): 87.44°, and 44% sit within 20% of the median. The high degree of fit with the median AA is suggestive of a strong petrofabric. An average AR of 1.43 ± 0.29 is calculated from the 2D data, 18.4% lower than the 3D obtained AR.

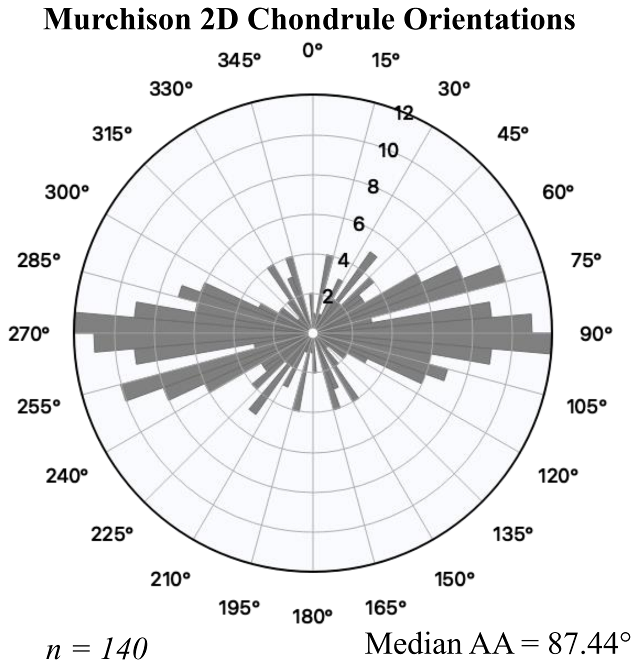

Figure 4.9*. Rose diagram binned at 5° intervals showing significant alignment of chondrules in the Murchison thin section.*

4.4.1.8 Winchcombe:

Two lithologies (L_1 & L_2) distinguished by differences in X-ray attenuation were analysed within the Winchcombe chip. Within L_1, K and C values indicate r_1 orientations weakly define a foliation fabric with r_3 clustering. The fabric observed within L_2 is weaker and similarly indicates a weak foliation fabric (Figure 4.10A). The orientations of L_1, r_1 & r_3 are non-random at the 99% confidence interval, within L_2 and r_3 non-random at the 99% confidence interval and r_1 non-random at the 97.5% confidence interval. The orientations of the recorded fabrics vary: $L_1\lambda_3$: 283.4°& $L_2\lambda_3$: 203.1° resulting in an orientation deviation of 80.3° between the two lithologies.

Chondrule shapes within Winchcombe are less compact when compared to the other CMs examined; in L_1 and L_2 compact chondrules account for just 28% and 21%, respectively. Within L_1 compact-bladed chondrules represent the largest shape (29.69%) with ~11% identified as either P, B or E. L_2 chondrules are even less spherical in shape with 29.33% defined as compact bladed and ~20% defined as being wither bladed or elongate (Figure 4.10B). Average ARs recorded in Winchcombe are: L_1: 1.64 ± 0.32 & L_2: 1.67 ± 0.35.

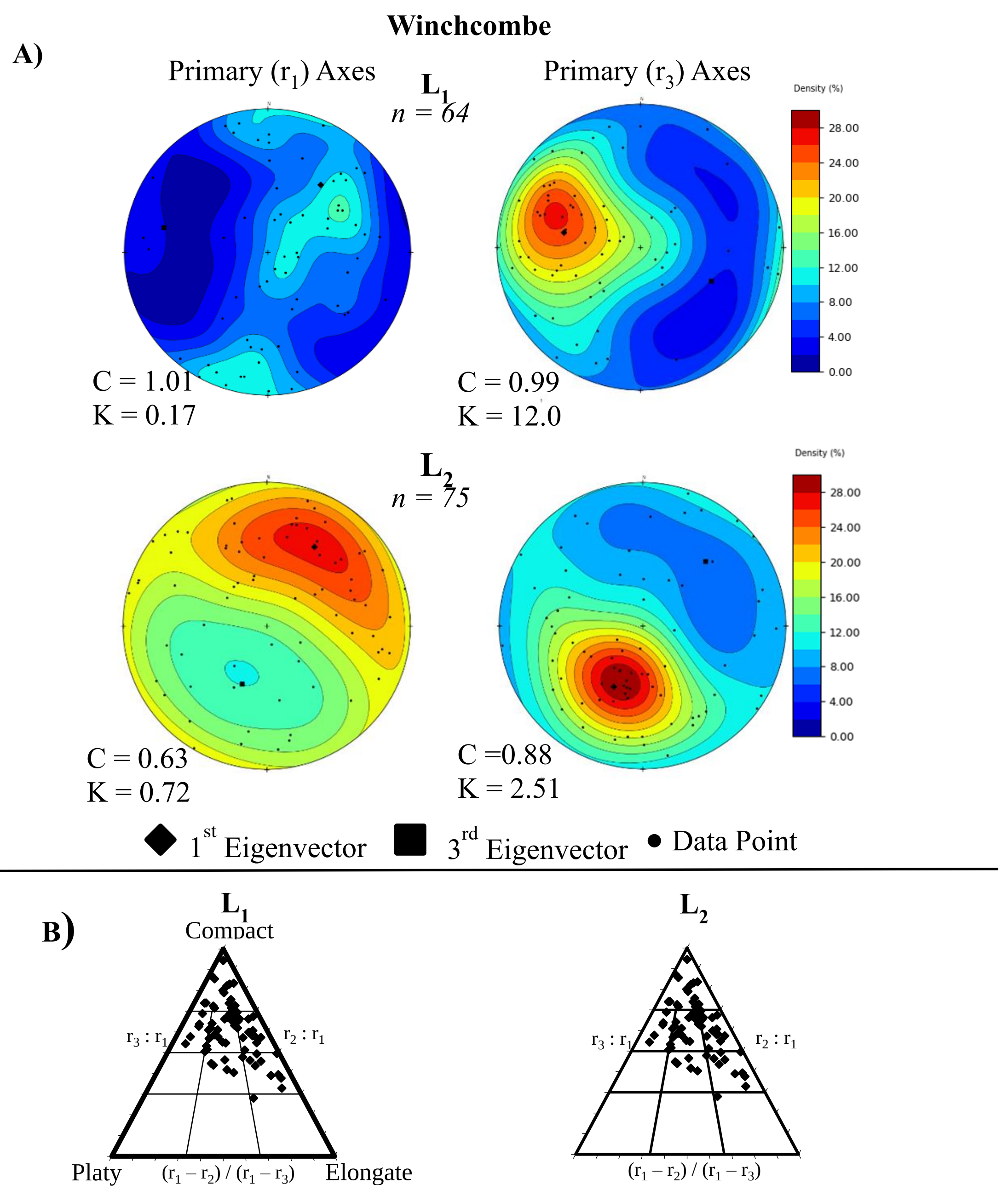

Figure 4.10*. A) Lower hemisphere equal-area projections showing the orientations of chondrule primary and tertiary axes within Winchcombe. Strength parameter (C) and shape parameter (K) are provided beneath each projection. B) Tri-plot diagrams based on Sneed and Folk (1989) illustrating chondrule shapes. The number of datapoints in each plot is the same as for each lithology in A.*

4.4.2 Estimating Porosity Loss:

Using the average ARs collected during this study we have calculated an approximate value for the strain experienced by each lithology, based on the following assumptions: (i) the initial chondrules were spherical and incompressible; (ii) that strain was entirely uniaxial (Hanna et al. 2015). Using this technique, it is possible to estimate the original porosity of the lithology prior to deformation. The assumption of chondrule sphericity in these estimates is idealised and allows for calculation simplicity and comparison with other calculations in the literature where sphericity is assumed. Uniaxial strain is assumed given the likelihood that deformation or alignment was the result of impact related processes acting along a single axis. The assumption of uniaxial strain is supported by the presence of foliation fabrics within the samples as pure uniaxial compression would result in uniform flattening (Hanna et al. 2015).

Determination of the approximate original porosity requires a value for the present porosity. However, there have been few studies of CM chondrite porosity and the average reported porosity (23-25%) is based on limited previous studies (Consolmagno et al. 2008; Corrigan et al. 1997; Hanna et al. 2022; Macke et al. 2011). Where measured porosity values are available, they range from 15 - 34% (Hanna et al. 2022; Leroux et al. 2015; Macke et al. 2011).

Where no reference porosity was available for our samples (Aguas Zarcas, LEW 85311 and Winchcombe) we have inferred a reference porosity based on published data for samples with a similar degree of aqueous alteration. This was done as porosity is expected to decrease with increasing alteration as more pore-filling secondary phases form, such as tochilinite-cronstedtite intergrowths (Leroux et al. 2015). The results of this analysis are outlined in Table 4.4 and suggest pre-compaction porosities ranging from 37.1% to 49.0%.

Table 4.4. *Table outlining the findings of the strain estimations and porosity loss calculations. Where multiple lithologies were examined within a volume, estimations for each lithology are given followed by an estimation for the total, where all chondrules analysed within a volume are included.*

Sample		Average AR	Strain (ε)	Reference Porosity	Est. Pre-Compaction Porosity (%)	Est. Pre-Compaction Porosity Range (%)†	
						+1σ	-1σ
Aguas Zarcas	L_1	1.72	0.30	15.0[1]	40.8	48.17	30.07
	L_2	1.57	0.26		37.1	45.54	24.31
	L_3	1.77	0.32		41.9	48.97	31.75
	Total	**1.69**	**0.30**		**40.1**	**47.67**	**29.00**
Cold Bokkeveld	L_1	1.64	0.28	15.0[2]	39.0	45.82	29.47
	L_2	1.75	0.31		41.5	47.84	32.72
	L_3	1.92	0.35		45.0	50.08	38.33
	Total	**1.66**	**0.29**		**39.4**	**46.11**	**30.03**
LEW85311	**Total**	**1.61**	**0.27**	30.0[3]	**49.0**	**55.74**	**39.06**
Murchison	**Total**	**1.69**	**0.30**	22.1[2]	**45.10**	**52.19**	**34.60**
Winchcombe	L_1	1.64	0.28	15.0[1]	38.9	46.79	27.18
	L_2	1.67	0.29		39.6	47.31	28.31
	Total	**1.66**	**0.29**		**39.4**	**47.14**	**27.94**

†Range of pre-compaction porosities calculated using standard deviation (±1σ) of aspect ratio as a proxy for measurement error. Calculations produce an expanded range of uniaxial shortening and thus a range of estimated pre-compaction porosities.

[1]Basedon the similarly altered sample Cold Bokkeveld (CM2.2) (Macke et al. 2011)

[2]Based on (Macke et al., 2011)

[3]Based on the similarly unaltered sample Paris (CM2.7-2.9) (Leroux et al. 2015)

4.5 Discussion

4.5.1 Chondrule Shapes and Petrofabrics within CM Chondrites

Our results show that all of the CM chondrites examined in 3D display some evidence of chondrule defined petrofabrics indicating deformation of their CM parent body(ies). These fabrics were typically characterised by a primary axis defined foliation, accompanied by strong clustering of the tertiary axes. In some cases, clustering along the primary axis girdle plane was indicative of accompanying lineation. These results are in keeping with previous descriptions of foliation fabrics within CM chondrites (Hanna et al. 2015; Lindgren et al. 2015; Rubin 2012; Vacher et al. 2018).

Figure 4.11A illustrates the fabric shapes and strengths identified in the meteorites examined. Murchison had the strongest fabric within our study, with a calculated r_1 C-value >1.7. This finding is consistent with previous studies where Murchison's fabric is noted as being particularly strong relative to other CM chondrites (Hanna et al. 2015; Lindgren et al. 2015). The relative strength of Murchison's fabric is consistent with a hypothesis suggesting a greater degree of impact processing. Increased processing may also be responsible for developing the shock features in Murchison leading to its classification as shock stage S1-S2 (Scott et al. 1992).

Analysis of the abundant metal grains within Cold Bokkeveld's L_1 lithology revealed them to be foliated along in their r_3 axis, with the foliation plane approximately perpendicular to that of the chondrules. Similar perpendicular relationships have previously been observed in the CM chondrite Winchcombe, where matrix grain and porosity alignment was observed to be perpendicular to chondrule alignment (King et al. 2022), and within CV chondrite Allende with matrix olivine aligned perpendicular to the chondrule fabric (Forman et al. 2023). Forman et al., (2023) proposed a multiple impact origin for this phenomenon with an initial impact aligning the chondrules and a second subsequent impact to align the matrix. Although we do not dispute this mechanism, we propose the alternative hypothesis that the difference between the metal grain alignment and chondrule fabric may be a result of metal grain deformation around the chondrules in response to uniaxial stress. If this is the case, metal grains adjacent to chondrules should display a significant deviation from the chondrule fabric whilst those isolated in the matrix should display a fabric consistent with the chondrules. Further XCT analysis investigating differences in metal grain and chondrule alignment is planned.

Chondrule shape analysis within our samples has revealed predominantly non-compact morphologies with average 3D aspect ratios of 1.57-1.92. Comparing chondrule shape with fabric strength suggests that 3D chondrule shapes are not a reliable indicator for the presence or relative strength of chondrule defined fabrics (Figure 4.11B). LEW 85311 and Winchcombe illustrate this contradictory relationship, with average chondrule aspect ratios exceeding those recorded in

Aguas Zarcas L_2, despite the chondrule defined fabric strengths in Winchcombe being significantly weaker.

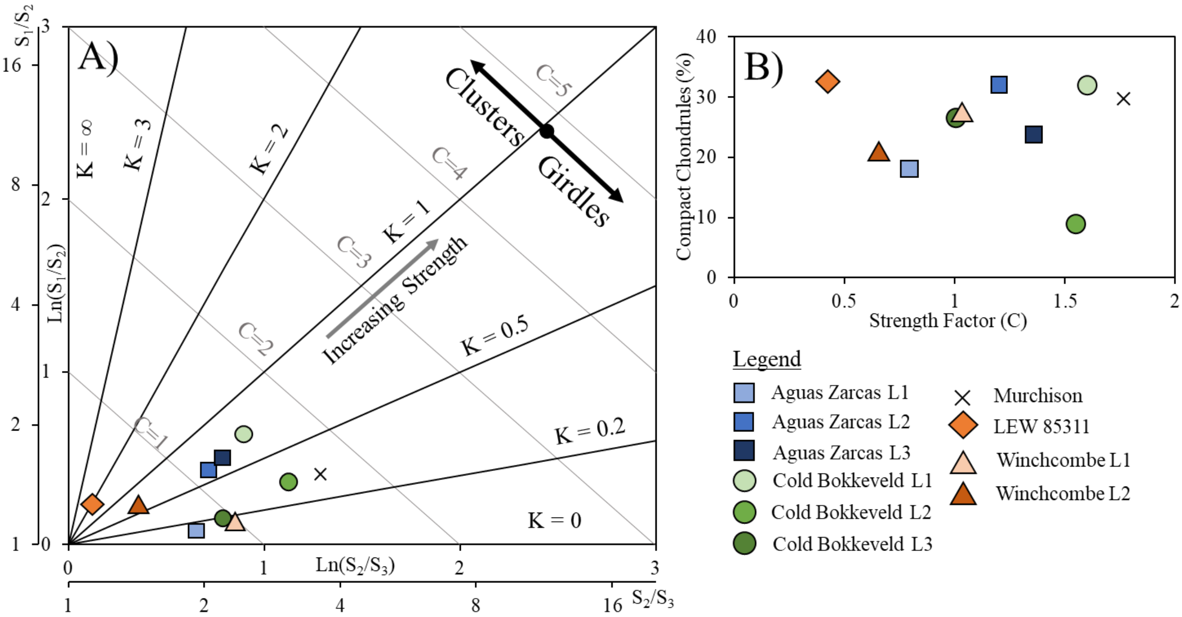

Figure 4.11. *A) An eigenvalue ratio graph illustrating the shape and strength factors (K and C factors respectively) for the chondrule long axes measured in 3D. B) Plot illustrating the lack of relationship between chondrule long axis fabric strength (C) and the percentage of compact shaped chondrules. The same legend applies to both figures.*

4.5.2 2D Thin Section vs 3D Chip Measurements

The effects of random sectioning on the accurate measurement of chondritic components are well documented (Eisenhour, 1996; Cuzzi and Olson, 2017; Benito et al., 2019; Floyd et al., Forthcoming). We have therefore sought to compare the results of 2D and 3D fabric analyses to determine if 2D derived fabric identification provides a reliable indication as to a 'true' 3D fabric. Murchison and LEW 85311 represented the strongest and weakest 3D fabrics observed, respectively, and were subjected to the additional 2D analysis.

Our 2D findings were generally in agreement with the 3D collected data. Murchison's 2D measurements showed a significant chondrule alignment with 26% of ellipse long axes within 10% of the median azimuth angle. Meanwhile LEW 85311 showed a significantly weaker alignment with just 15% of long axes within 10% of the median azimuth angle. While 2D techniques were successful in this instance in distinguishing the relative strength of a fabric compared to the 3D dataset, they remain unable to determine the true nature or strength of any fabric present. Furthermore, the 2D calculated aspect ratios show significant disparity to the 3D data, with an ~17.9% decrease observed in the 2D data for LEW 85311 and Murchison.

Despite our 2D results showing general agreement with our 3D data we suggest this is merely coincidence. Random sectioning along a foliation plane will result in higher chondrule aspect ratios and a weaker or supposedly random fabric orientation, while sectioning perpendicular to a foliation plane will reveal a stronger fabric with reduced chondrule aspect ratios. The effects of random sectioning of a sample should therefore not be overlooked with regards to interpreting 2D orientation data.

It is also worth noting that all the 3D data presented here demonstrates some degree of girdle and/or stretching lineation and therefore any lack of a fabric reported in 2D is unlikely to indicate the complete absence of fabric within the sample. Future interpretations made using 2D orientation data, collected from randomly orientated thin sections, should be mindful of these limitations and the possibility of under-reporting the true extent of deformation and alignment present within meteorites.

4.5.3 Porosity Loss Calculations

Porosity within CM chondrites is manifest in two forms: microporosity and macroporosity. Microporosity occurs at the grain or sub-grain scale typically as small cracks and voids within the fine-grained components such as the FGRs and matrix. Macroporosity is observed at scales larger than typical grains and is often identified as significant voids or fractures resulting from impact processing or diurnal thermal stress (Flynn et al., 1999; Rozitis et al., 2020; Hanna et al., 2022). It is believed that the porosity observed in the CM chondrites is primary and reflects the porosity of the original parent body (Rozitis et al., 2020).

Using the average chondrule aspect ratio for each lithology examined, we have estimated the strain that it experienced and calculated an estimated original pre-compaction porosity. Our calculations show that within the CM chondrites studied, original porosities were between 37.1 % and 49.0%.

Comparison of the pre-compaction porosity calculated for Murchison in the present study (45.1% ±1σ giving a range of 34.6-52.19%) with that determined for the same meteorite by Hanna et al., (2015) of 41.6% (±1σ gives a range of 35.3-46.6%) shows general agreement. The values calculated in the present study (Table 4) are also within 1 standard deviation of the total porosity estimated for C-type asteroids; 35-40% (Britt et al. 2002) and are consistent with porosities estimated for the rubble pile asteroids Ryugu (50-60%; (Okada et al. 2020) and Bennu (up to ~55%; (Rozitis et al., 2020).

Porosity has significant mechanical implications for the CM parent body. Laboratory experiments have shown that for lithological units with increasing porosity a greater energy per-unit mass is required to break them apart. This relationship is a consequence of energy dissipation by pore-space collapse and compaction (Bruck Syal et al. 2016; Flynn et al. 1999; Housen et al. 2018; Love et al. 1993). The results of hypervelocity impact experiments reinforce these findings with highly porous terrestrial analogues (60-85% porosity) showing significant resilience to catastrophic disruption when compared to a non-porous analogue of equal mass (Flynn et al. 2015; Jourdan et al. 2023). Taking our findings of high pre-compaction porosity together with those of Kieffer (1971), Love et al. (1993) and Flynn et al. (1999, 2015) suggests that impact energy within the CM parent body may be significantly attenuated. Attenuation would reduce the propagation of energy, and potentially limiting the development of clear shock effects, even in non-void areas, all while allowing chondrule alignment. In the event of rapid pore space collapse, it has been shown that significant heating and strain are produced and preferentially affect the matrix (Bland et al. 2014). Anhydrous silicates act as heat sinks during the heating and prevent prolonged thermal alteration, limiting the development of any heating effects within the matrix and thus the usefulness of heating products as evidence for impact intensity (Bland et al. 2014). Evidence within the CM matrix for significant strain and/or shock effects is also absent and thus either the impacts involved were of a low intensity nature or any effects were overprinted by later alteration.

The findings presented here are based on the limited amount of bulk porosity data available for the CM chondrites. Further analysis of bulk porosities in a greater range of CM chondrites is urgently needed to help refine these calculations and improve our understand of the role porosity plays in controlling deformation, brecciation and shock effects within the CM parent body.

4.5.4 Chondrule determined Shock Pressure

There have been several experimental investigations of the shock pressures required to deform and flatten chondrules (Miyahara et al. 2021; Nakamura et al. 1993; Tomeoka et al. 1999). Tomeoka et al., (1999) conducted shock experiments on CM chondrite Murchison at 5-55 GPa with intervals corresponding to the highest-pressure estimates for shock stages S1-S5 (Stöffler et al. 1991). They found that chondrule flattening and preferred orientations can be experimentally reproduced. Chondrule flattening was observed to begin between 4-10 GPa, with chondrule alignment beginning to develop beyond 10 GPa (Tomeoka et al. 1999). The most significant changes in aspect ratio and chondrule alignment were observed at 21-30 GPa (Tomeoka et al. 1999). These findings were consistent with those of Nakamura et al., (1993) in an experimental study of CV3 chondrites.

Using results of the Tomeoka et al., (1999) shock experiments, and the calculated average chondrule aspect ratios from our study, we predict the shock pressures that our samples may have been subjected to in order to induce the degree of chondrule flattening observed. While the experiments by Tomeoka et al. (1999) are imperfect analogues in that they are not capable of recreating the precise conditions on the parent asteroid and assume deformation resulted from a single impact, they do provide an indication of the maximum shock pressure which may have been experienced (Figure 4.12).

The results of our 2D analysis plot well within the range of the Tomeoka et al., (1999) dataset. LEW 85311 and Murchison indicate maximum shock pressures of 14.3 and 19.2 GPa, respectively. However, when considering all the 3D derived aspect ratios calculated during this study and applying these to the data series, the estimated shock pressures are significantly higher, with a minimum of 27.8 GPa and a maximum of 41.8 GPa. The shock pressure inferred from the 3D data are higher than those calculated in similar studies by Lindgren et al., (2015) and Vacher et al., (2018).

Tomeoka et al., (1999) found that shock pressures of 25-30 GPa did not produce a proportional change in mean aspect ratio, with preferred orientations beginning to degrade. Beyond 30 GPa Tomeoka et al., (1999) observed extensive disruption within the chondrule populations with most olivine and pyroxene grains displaying significant irregular fracturing. Further to this at 20-30 GPa localised melt veins and pockets were observed with pervasive melting of the matrix at ~35 GPa. At these higher shock pressures, you would also expect diagnostic shock indicators such as mechanical twins in pyroxene and diaplectic glass to be visible, these are not observed in the CMs. Despite the high shock pressures calculated for our samples from chondrule flattening, no evidence of melting or significant fracturing is observed in our 2D sections. Previously fracturing has been noted to have a systematic relationship with foliation plane and lineation direction with fractures commonly parallel to foliation plane (Hanna et al. 2015).

A significant dichotomy therefore exists between the shock pressures calculated for our samples and the features associated with those pressures observed by Tomeoka et al., (1999). A possible cause for this discrepancy is the application of our 3D measurements to the Tomeoka et al., study which was based on 2D measurements of thin and thick sections produced to intersect the sample centre and shock compression axis. Future shock experiments in the CM chondrites with samples being studied in 3D may help reconcile some of these differences.

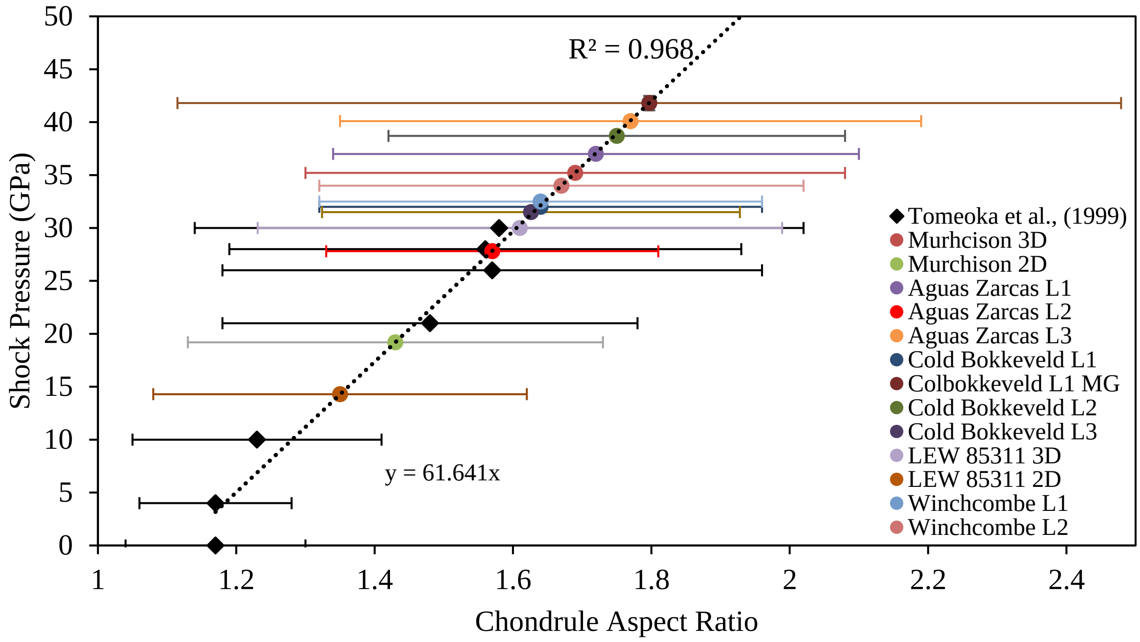

Figure 4.12*. Plot showing the inferred shock pressures experienced by the meteorites and clasts examined in this study using the experimentally determined relationship between shock pressure and chondrule aspect ratio from Tomeoka et al. (1999). Also plotted are the aspect ratios of chondrules in Murchison that were shocked to different pressures in the experiments by Tomeoka et al. (1999). The equation of the trendline (y = 61.641x) suggests that chondrule aspect ratio changes by 0.1 for every ~6.2 GPa increase in shock pressure. The standard deviations of the aspect ratios are shown by the error bars.*

4.5.5 Chondrule Sphericity

Calculations of porosity loss and shock pressure are limited by our assumption that chondrules were initially spherical. Any deviation from this assumption would result in shock pressures and pre-deformation porosities significantly lower than reported here and elsewhere.

Hanna et al. (2015) applied an ellipticity plot described by Ramsay et al., (1983) and originally developed to study ooid deformation to test for original sphericity. This approach involves plotting the primary and tertiary axis lengths for each deformed chondrule to test for a linear fit. If the chondrules were originally spherical and had the same response to the uniaxial compression then the resulting trendline should have a slope equal to the aspect ratio (Hanna et al. 2015; Ramsay et al. 1983). We have applied this technique to our 3D dataset with a total of 985 chondrules included in this analysis. Figure 4.13 shows a zero-intercept linear regression with a high correlation (R^2 = 0.95) and a slope of 1.65. The average aspect ratio for all chondrules is 1.67 which alludes to an almost spherical shape for the original undeformed chondrules which were subsequently deformed by a uniaxial compression mechanism. Whilst the ellipticity plot suggests a typically spherical pre-deformation chondrule shape, our data does not endorse this result and we suggest that the approach is too simplistic.

Evidence supporting a non-spherical original chondrule shape is found in least deformed chondrite examined (LEW 85311) (Lee et al. 2019). This meteorite shows a very weak 3D chondrule defined fabric, indicating very limited impact processing on the parent body. In spite of this weak fabric, LEW 85311 chondrules have a high average aspect ratio of 1.61 and shape analysis identifies 66.45% of these chondrules as non-spherical.

Within each clast examined chondrules have all been subjected to the same force to produce their prolate shape however, to reconcile the paradox of highly deformed chondrules with no substantive evidence of shock, or in some cases (e.g., LEW 85311) no fabric, it is more likely chondrules were accreted with their prolate aspect ratios already established. Miura et al., (2008) showed that prolate chondrules can develop whilst spinning during their molten phase, elongating along their rotation axis and flattening along the plane perpendicular to rotation this allowing chondrule elongation to occur prior to accretion. Charles et al., (2018) also sought to investigate original chondrule shape by retro-deforming chondrules within CR2 chondrite NWA 801. They found that after retro-deformation the number of chondrules defined as spherical did increase; however, there remained a significant proportion which remained highly deformed and did not retro-deform to spheres further supporting a predominantly prolate pre-accretionary chondrule shape.

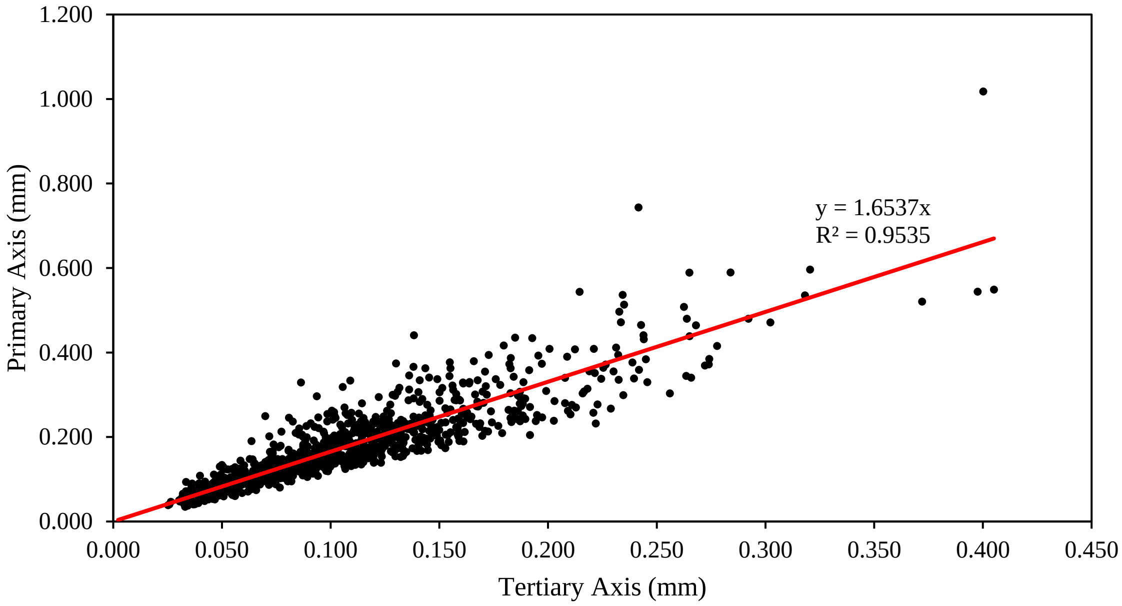

***Figure 4.13.** Primary (r_1) and tertiary (r_3) axis lengths for best fit ellipsoids produced by XCT analysis. A strong correlation (R^2 = 0.95) is observed between two axes as shown by a linear regression line (red), which goes through the zero-intercept. Similarities between the line slope and average aspect ratio suggest a nearly spherical original chondrules. However, spread around the regression line, especially at larger sizes indicates that not all chondrules conform to this relationship.*

4.5.6 Origin of Deformation and Alignment

As shown in the previous sections, understanding the mechanism by which CM chondrules were deformed and aligned despite the host meteorites having little to no observable shock effects is challenging. We suggest that three major obstacles remain to better understanding the origins and magnitude of deformation and alignment within the CMs: shock pressures, initial porosity, and chondrule sphericity.

An impact origin for deformation and alignment would produce the uniaxial compression required to generate the foliation fabrics observed within our samples. The subtle lineations observed can be explained by the compaction of regions not directly below an impactor through pure shear flow. Tomeoka et al., (1999) provides a constraint for the maximum shock pressures which may be experienced in an impact origin regime, estimated from chondrule AR. The lack of associated shock features observed in the Tomeoka et al., (1999) indicates their experiments were an imperfect analogue. Our calculations of a high initial porosity on the CM parent body(ies), alongside previous studies, suggest porosity and subsequent pore space collapse had a significant role in attenuating impact energy. However, calculations of maximum shock pressure and pre-compaction porosity assume chondrule sphericity, which our data indicates is unlikely to be an accurate representation of the original, undeformed chondrule shape. The effects of non-spherical chondrules on impact-driven petrofabric development, the shock pressures required and interaction with pre-compaction porosity remain unknown and require further investigation and modelling to ascertain the extent of the relationship.

An alternative model for chondrule alignment could be the flow of an unlithified mud (Bland and Travis 2017). Given the prolate pre-accretion shape of chondrules indicated by our data such a process would be capable of producing the chondrule alignment and occasional lineation observed. However, reconciling the S1/2 shock stage classification of Murchison and perpendicular relationship between the Cold Bokkeveld metal grains and chondrules is challenging in this scenario without some degree of impact processing.

Given the results reported here we support an impact origin for the chondrule alignment whereby, initially prolate chondrules, their shape developed whilst molten and spinning, were accreted to the CM parent body. Low energy impacts subsequently produced rotation of the chondrules to define a foliation fabric, with chondrule rotation accommodated by pore space collapse. Collisions between chondrules during their molten and/or semi-molten stage may also be partly responsible for the development of the lobate shapes altering chondrules from the ideal prolate form, a concept suggested and discussed by Jacquet (2021) in reference to compound chondrules. Further analysis to investigate the role of high pre-compaction porosities within the CMs and to understand the effects of prolate chondrule shapes on the shock pressure required to produce chondrule alignment is planned.

4.5.7 Relative Timing of Deformation, Brecciation and Aqueous Alteration:

Irrespective of the nature of the deformation events, assessing the relative timing of deformation and aqueous alteration events is important for a comprehensive understanding of parent body evolution. Analysis of the brecciated samples Aguas Zarcas and Cold Bokkeveld have revealed two different chronologies for aqueous alteration and chondrule fabric development.

4.5.7.1 Aguas Zarcas:

Within Aguas Zarcas we observe a relatively consistent 3D fabric throughout lithologies L_1 and L_2 although the eigenvector orientation for the L_3 fabric is displaced 156.4° relative to $L_{1/2}$. L_1 and L_2 are the host lithology (L_2) and a prominent clast (L_1) and so must have been brought together by an initial brecciation event. Given their differences in X-ray attenuation and thus implied differences in mineralogy and chemical composition, we interpret these lithologies as having been aqueously altered prior to this initial brecciation event. Once juxtaposed, both L_1 and L_2 were deformed to produce the similarly orientated chondrule defined fabrics.

Conversely, L_3 was subjected to alteration and deformation prior to its incorporation into the region of the parent body that already contained L_1 and L_2. It is conceivable that L_1 and L_2 were deformed during incorporation of L_3. No subsequent deformation has occurred since to homogenise the fabrics of the three lithologies. Additionally, given the implied differences in aqueous alteration it is unlikely any further aqueous processing has occurred to overprint previous alteration. Thus, the sample of Aguas Zarcas examined evidences two events of sufficient intensity to deform chondrules and two episodes of clast incorporation. This series of events is illustrated in Figure 4.14.

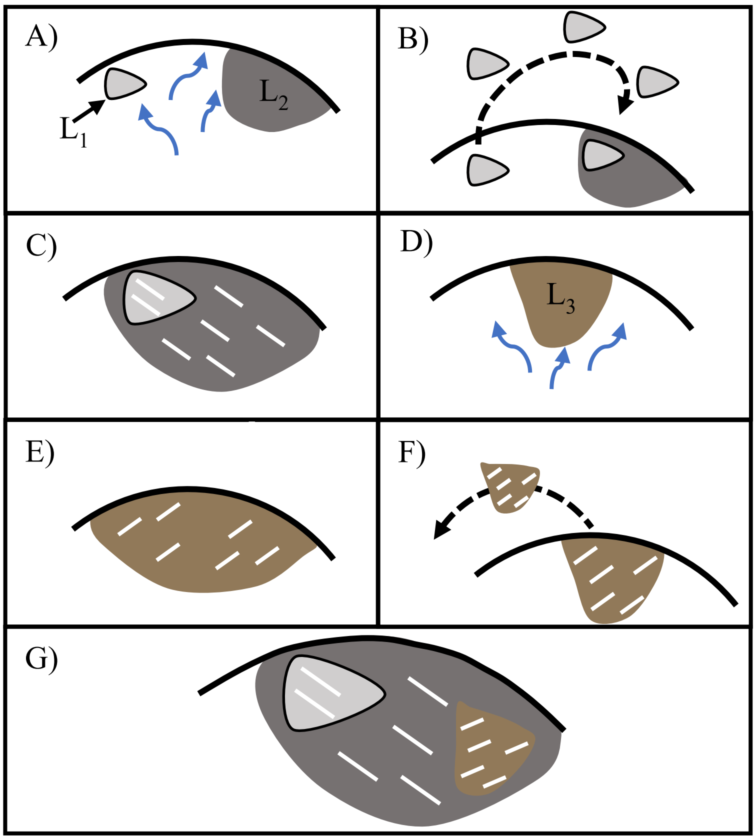

Figure 4.14. *Schematic illustration of the events producing the variety of petrofabrics observed in Aguas Zarcas. A-C outline the processes affecting L_1 and L_2. D-F outline the processes affecting L_3 A) L_1 and L_2 were aqueously altered to contrasting degrees in different regions of the parent body. B) The L_1 lithology was dislodged from its original position and mixed into L_2 following an impact event. C) Once L_1 was mixed with L_2 both lithologies were subjected to a deformation event which flattened and aligned their chondrules. D) The L_3 lithology experiencing aqueous alteration. E) The L_3 lithology experienced deformation to flatten and align its chondrules. F) L_3 was dislodged from its original setting and emplaced within the L_2 lithology so that its foliation fabric not aligned parallel to L_1 or L_2. G) The final result was a part of what would be the Aguas Zarcas meteorite consisting of three lithologies, two of which with the same foliation fabric and one misaligned. For simplicity we have illustrated these events occurring on the same parent body however, it is possible that the water/rock interactions and deformation events occurred on different parent bodies and lithologies $L_{1/2}$ and L_3 were later juxtaposed.*

4.5.7.2 Cold Bokkeveld:

Within Cold Bokkeveld all three lithologies examined are spatially distinct with none being the host lithology. In this instance all three lithologies have broadly similar fabric orientations with a maximum deviation of just 28.3°. It is therefore likely that all three lithologies were subjected to the same deformation event after being juxtaposed. The differences in X-ray attenuation between lithologies again likely reflect contrasts in mineralogy as a result of different degrees of aqueous alteration and indicate that water/rock interaction likely occurred prior to deformation. The presence of abundant Fe,Ni metal grains within L_1 indicates that the lithology is significantly less aqueously altered than L_2 and L_3. The minor variations observed in foliation orientation between lithologies (particularly L_2) may reflect inter-lithology contrasts in response to deformation. It is also possible that the subtle orientation differences between clasts may record a remnant signature from a previous deformation event which was only partially overprinted by the compaction experienced by all the clasts. This series of events is illustrated in Figure 4.15.

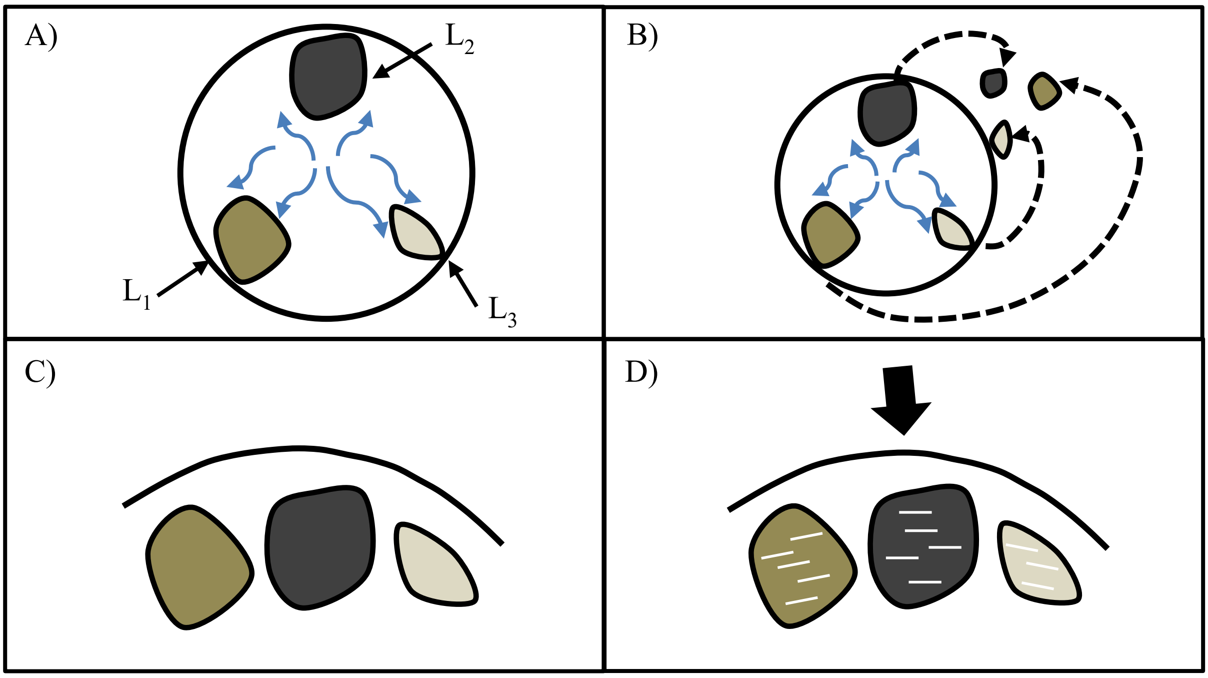

Figure 4.15. *Schematic illustration of the events producing the variety of petrofabrics observed in Cold Bokkeveld. A) L_1, L_2, and L_3 are subjected to aqueous alteration, likely at different locations within the parent body. B) All three lithologies are dislodged from their original positions by an impact event. C) L_1, L_2, and L_3 are redeposited on the parent body in close proximity to one another. D) An impact event deforms the region containing all three lithologies resulting in near-identical fabric orientations. For simplicity we have illustrated these events occurring on the same parent body however, it is possible that the water/rock interactions occurred on different parent bodies with lithologies subsequently juxtaposed and deformed.*

4.5.8 Fabric and Degree of Aqueous Alteration:

Rubin (2012) proposed a relationship between the strength of chondrule defined fabrics within the CMs and petrologic subtype. It was suggested that impacts on the CM parent body form fractures and promote the mobilization of water through phyllosilicate dehydration and/or ice melting, thus allowing fracture-controlled fluid flow in regions subjected to a greater intensity of impacts. Petrographic support for the Rubin (2012) model can be found by the presence sub-parallel dolomite veins in CM2 meteorites QUE 93005 and SCO 06043 (Lee et al. 2014; Lindgren et al. 2015), serpentine veins parallel to foliation orientation in Murchison (Hanna et al. 2015), and aragonite crystals which are observed to be aligned to compactional fabrics in the matrix of the CM2 Murray (Lee and Ellen 2008).

Our results present an alternative to the Rubin (2012) model. Whilst we do find the least altered sample examined (LEW 85311) to have the weakest disenable fabric, the strongest fabric is within the mildly altered CM Murchison, and not the more highly aqueously altered CMs examined (Aguas Zarcas, Cold Bokkeveld, and Winchcombe). Given the higher recorded shock stage of Murchison and the similarity in the fabric strengths detected here compared to other studies (Hanna et al. 2015; Lindgren et al. 2015), it may be the case that Murchison is an exceptional case which defies the Rubin (2012) model. However, when examining the relative timings of deformation, outlined in the previous section, we find additional evidence contrary to the Rubin model. Within Cold Bokkeveld we observe post-aqueous alteration deformation, with near identical fabric orientations in three contrasting lithologies. We interpret this fabric to have formed during a single deformation event occurring after aqueous alteration and a period of brecciation juxtaposing all three lithologies. Furthermore, the metal-rich L_1 lithology has likely experienced significantly less aqueous alteration compared to L_2 and L_3 given its high Fe,Ni content (Rubin et al. 2007) thus, to remain consistent with the Rubin (2012) model should display a weaker fabric than the two other lithologies. This is not observed. Vacher et al., (2018) conducted similar analysis on CM Boriskino and similarly found evidence of post-aqueous alteration deformation.

It is likely that a plethora of different scenarios and chronologies exist for aqueous alteration, brecciation and deformation within and between the CM parent bodies. It is therefore not our intention to dispute or challenge the theory put forward in Rubin (2012), instead we aim to highlight the range of possible relationships between the pre- and post-deformational processes in the CMs.

4.6 Conclusions

This work has illustrated that chondrule defined petrofabrics are almost ubiquitous within the CM chondrites, with fabrics typically represented by long axis foliation and short axis clustering. We have shown that 2D analysis can provide a good initial indication of the existence of a fabric, but 3D analysis is needed to provide detailed information regarding the shape and strength of any fabric present. Our data show that many chondrules were not spherical at the point of accretion to the CM parent body reconciling the disparity observed between the high shock pressures inferred from chondrule aspect ratio and the low shock pressures from the microstructure. Further work is required to understand the implications of porosity and prolate original chondrule shapes on the impact processing. Doing so will help constrain a more accurate shock pressure range. It is also shown here that individual CM volumes can have lithological variations in fabric strength and orientation. Similarities and/or differences in these orientations can be used to infer a relative chronology of alteration events with implications for models correlating petrologic subtype and fabric strength.

4.7 Acknowledgements

We gratefully acknowledge funding from the UK Science and Technology Facilities Council through grants ST/W001128/1 and ST/T506096/1. We thank the Scottish Alliance for Geoscience, Environment and Society Small Grants Scheme for contributions towards XCT analysis.We thank the Natural History Museum, London, for the loan of the Cold Bokkeveld and Winchcombe samples, and to ANSMET for the loan of LEW 85311. US Antarctic meteorite samples are recovered by the Antarctic Search for Meteorites (ANSMET) program, which has been funded by NSF and NASA, and characterized and curated by the Department of Mineral Sciences of the Smithsonian Institution and Astromaterials Acquisition and Curation Office at NASA Johnson Space Center. The samples of Aguas Zarcas were obtained from Mendy Ouzillo, Skyfall Meteorites. Additional thanks go to Romy Hanna for her assistance with XCT processing, Alice Macente for assistance with XCT data acquisition and Peter Chung for assistance in collecting BSE and EDS mosaics and EDS maps. For the purpose of open access, the author(s) has applied a Creative Commons Attribution (CC BY) licence to any Author Accepted Manuscript version arising from this submission.

Chapter 5 Irradiation Damage Track Analysis

Chapter 5 represents a review of space weathering on the carbonaceous CM chondrites, through the lens of damage track development and analysis. The contents of the chapter were originally planned to be the focus of this thesis and form part of a research chapter however, as a result of the COVID pandemic and associated facility closures this work was unable to take place. This review sets out the fundamental principles, processes and methodologies for damage track analysis in the CM chondrites alongside discussing some of the previous works in the field and suggested avenues for future work.

5.1 Space Weathering

As discussed previously in thesis section 1.3.5 the effects of space weathering have been observed and widely recorded in numerous chondritic meteorites (Bennett et al. 2013; Bischoff et al. 2006; Goswami and Macdougall 1983; Lantz et al. 2017; Pieters and Noble 2016; Riebe 2012). Within the CM chondrites space weathering is most frequently observed and interpreted as impact-related processes leading to brecciation, fabric imposition (such as chondrule-defined fabrics discussed in Chapter 4), and occasionally microstructural shock effects (Bischoff et al. 2006, 2017; Hanna et al. 2015; Lindgren et al. 2015; Scott et al. 1992). Space weathering by irradiation of the CM parent body(ies) and its implications receive far less attention. In this chapter irradiation processes affecting the CM chondrites are explored, focusing on the development of nuclear damage tracks and their potential usefulness for understanding the evolution of the CM chondrites and their parent asteroid(s).

5.1.1 Space Weathering via Irradiation

There are three primary types of radiation which can affect solar system bodies such as asteroids: Galactic Cosmic Rays (GCRs), Solar Cosmic Rays (SCRs), and the Solar Wind (SW). Each radiation type has a distinct origin, associated energy and flux which allow for the effects of each type to be investigated. In the section below each type of irradiation is introduced and briefly described.

5.1.1.1 Solar Wind:

The solar wind refers to the continuous radial flow of ionised particles from the sun's outer corona into space (Fleischer et al. 1975). It is believed to be produced by the continuing expansion of the solar corona due to heating by the sun to temperatures of ~3 $x10^6$ K. Under such conditions charged particles within the corona are no longer contained by the sun's gravity and flow outwards into the solar system (Fleischer et al. 1975).

The solar wind is composed primarily of protons and electrons with associated energies of ~1.3 $x10^3$ eV which when combined with a particle flux of, 4.1 $x10^8$ $cm^{-2}s^{-1}$ produces a total energy flux of 6.7 $x10^{11}$ eV $cm^{-2}s^{-1}$ at 1AU when measured at solar minimum (Table 5.1) (Bennett et al. 2013).

5.1.1.2 Solar Cosmic Rays (SCRs)/Solar Energetic Particles (SEP):

The terms Solar Cosmic Rays (SCRs) and Solar Energetic Particles (SEPs) are used interchangeably within the literature; hereafter I refer to them as solar energetic particles (SEPs). SEPs have been accelerated by solar flare activity and coronal mass ejections (CMEs) within the sun's corona (Bazilevskaya et al. 2008; Bennett et al. 2013; Forbush 1946; Hassler et al. 2014). The frequency of flare activity and CMEs increases during periods of increased solar activity (during solar maximum), when an approximately twelvefold increase in the frequency of these events can be observed relative to periods of reduced solar activity (solar minimum) (Bennett et al. 2013). Solar flares and CMEs are thought to be a result of random reconnection events occurring within the sun's magnetic field (Shanmugaraju et al. 2023). These reconnection events occur when magnetic field lines of opposite directions merge and subsequently 'snap apart' in an explosive event that releases an enormous amount of energy (Shanmugaraju et al. 2023).

Compositionally, SEP events are dominated by protons with a variable abundance of other particles, including heavy and ultra-heavy ions (Cane et al. 2010). The heavy ion abundance of SEP events can exceed ~10-10^4 times that observed in the solar wind (Cane et al. 2010; Hassler et al. 2014). The particle energies associated with SEP range from 10 – 100 $x10^6$ eV (MeV) for protons during a typical SEP event although energies can exceed this during larger events (Biswas 2000).

It should be recognised that while SEP events are described separately to the solar wind, due to their differences in particle generation mechanism, particle energy, and particle flux, the particles comprising the SEPs are not separate from the solar wind. SEPs are similarly produced in the outflowing solar corona just under more specific condition and contribute a higher energy component to the solar wind.

5.1.1.3 Galactic Cosmic Rays (GCRs):

Galactic cosmic rays (GRCs) are charged particles which are not emitted from the Sun, and have their origins outside the solar system, but within our galaxy (Bennett et al. 2013). The galactic cosmic ray flux is ~99% composed of atomic nuclei representing with <~1% of the total flux composed of electrons/positrons (Simpson 1983). The nuclei component of GCRs is dominated (~85-90%) by protons, with ~10-13% composed of alpha particles, and ~<1% composed of heavier nuclei (Durante and Cucinotta 2011; Hassler et al. 2014; Simpson 1983).

Isotope analysis indicates a mixed source for GCR particles, with ~20% of particles thought to represent supernova ejecta, and ~80% representing normal interstellar material (Bennett et al. 2013; Blandford and Eichler 1987; Hillas 2005; Wolfendale and Erlykin 2014). The flux of GCRs is relatively constant in interplanetary space with a typical value of 4 protons $cm^{-2}s^{-1}$ (Bennett et al. 2013). However, GCR's are strongly anticorrelated with solar activity due to heliospheric modulation and therefore GCR flux can be reduced to ~2 protons $cm^{-2}s^{-1}$ during times of solar maxima, when the solar wind is at its strongest (Bennett et al. 2013; Gleeson and Axford 1968; Nordheim et al. 2019). Due to the strong anti-correlation between the SW and GCRs it is presumed that in the outer solar system (~80 AU) where the SW input is more limited GCR likely have a higher flux, perhaps by an order of magnitude (Bennett et al. 2013). It is therefore thought that GCRs in this region likely have a more significant irradiation effect than that experienced at 1 AU (Bennett et al. 2013).

Despite their low flux, GCRs are very high energy when compared to the other forms of irradiation in the solar system. GCR energies can reach up to 10^{11} eV (Durante and Cucinotta 2011). Figure 5.1 shows a comparison between the spectra for SEPs and GCRs. The combination of low particle flux and very high particle energy results in a roughly comparable total energy flux (eV cm^{-2} s^{-1}) with that produced by SEPs and the SW.

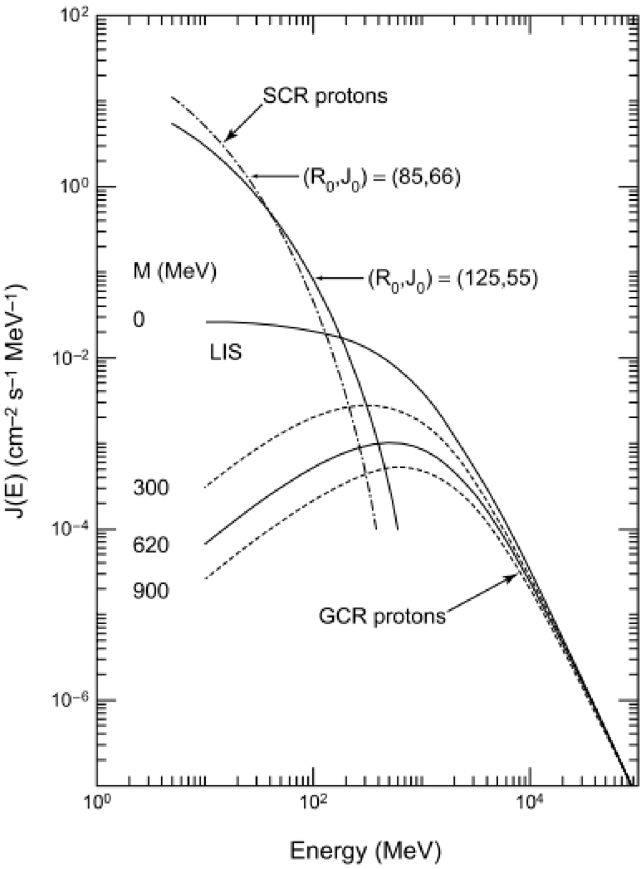

Figure 5.1*. Spectra of solar energetic particle (SEP) protons (referred to as SCR protons in figure) and galactic cosmic-ray (GCR) protons at 1 AU. The modulation parameter, M, is shown vs. proton energy. GCR spectra are plotted for times of an active (M = 900 MeV) and a quiet (M = 300 MeV) Sun, as well as for the average GCR spectrum during the last 10 m.y. and for the local interstellar spectrum (LIS, M = 0). Illustration sourced from* Michel et al. (1996).

Table 5.1*. Table outlining the energies and fluxes associated with the different types of radiation. Data collated from* Bennett et al. (2013) and Biswas (2000).

Radiation Source	**Associated Energy (eV amu^{-1})**	**Flux (cm^{-2} s^{-1})**	
		Solar Min	**Solar Max**
Solar Wind	1.3 x10^3	4.1 x10^8	6.4 x10^8
SEP	10 - 100 x10^6	1.1 x10^8	3.4 x10^8
GCR	10 x10^6 - >10 x10^9	4.0 x10^0	2.0 x10^0

5.1.2 Effects of Charged Particles on Extraterrestrial Matter

As mentioned in section 5.1.1 and above, each radiation type has a specific composition of charged particles, with a range of associated energies and fluxes. When each of the different types of energetic particles interact with solar system matter, they have contrasting effects. Here the different types of charged particles are discussed in the context of their effects on a meteoritic parent bodies.

5.1.2.1 The Solar Wind Effects

Despite the high flux of solar wind ions, their low energy (~1 keV) means that they lack sufficient energy to penetrate any significant depth into planetary materials such as asteroids. It has been calculated that solar wind ions have a potential penetration depth of just ~50 nm (Eugster et al. 2006).

In these instances, the particles do not produce any nuclear reaction or lattice defect and are instead simply implanted into exposed surface (Eugster et al. 2006). However, due to their high particle flux, grains exposed to the solar wind can suffer some radiation damage, becoming saturated in lighter elements such as He. As discussed in Chapter 1, solar wind ions are also thought to be responsible for the development of amorphization and $npFe_0$ observed surrounding some mineral grains and interpreted as evidence of exposure at the parent body surface.

5.1.2.2 Solar Energetic Particles Effects

The higher energies associated with SEPs allow deeper penetration within airless bodies compared to the solar wind, with penetration depths of a few mm possible (Goswami et al. 1984). Additionally, the higher energies and more variable composition of SEPs, which can include heavier nuclei, means SEPs can produce ionisation and lattice defects manifesting as damage tracks within the uppermost cms of a meteoritic parent body (discussed further in section 1.2). (Goswami et al. 1984)

5.1.2.3 Galactic Cosmic Ray Effects

GCR's have the highest associated energies of all incident particles in the solar system and this allows for the deepest penetration into planetary materials. Penetration depths on the m scale are possible for GCR's (Hassler et al. 2014; Metzler 2004; Nordheim et al. 2019; Vogt et al. 1990).

Similarly, to SEPs the high energy and variable atomic mass of the charged particles comprising GCRs mean both lattice defects and nuclear reactions are possible.

5.2 Development of Damage Tracks

Damage tracks can be produced by the fission of fissionable elements (for example U^{238}) or from the interaction of incident charged particles. This work focuses on the latter type of irradiation and the damage tracks produced; these are discussed in the following sections.

When energetic charged particles collide with a mineral or inorganic solid, they can either: (i) escape the mineral without incident; (ii) stop without causing a nuclear reaction; (iii) or begin a nuclear reaction through ionisation of the surrounding matter (Eugster et al. 2006; Fleischer et al. 1975). When a charged particle causes a nuclear reaction, the ionisation associated with the reaction produces a permanent lattice defect within the incident matter, in this instance a crystal or grain. These lattice defects manifest as a sub-micron scale tracks with radii < 50 Å (Fleischer et al. 1975). Tracks such as these have a diverse range of names in the literature including ion tracks, nuclear tracks, latent damage tracks and particle damage tracks. To remain consistent throughout this thesis, only the term particle damage track will be used hereafter. An example of a crystal containing particle damage tracks is shown in Figure 5.2.

Particle damage tracks are not formed in crystalline material by light elements but instead require the interaction of energised heavier nuclei, typically with an atomic number (Z) > 20 (Eugster et al. 2006; Keller et al. 2021; Lal 1972). These heavy nuclei can be divided into Very Heavy (VH) nuclei with $18 \leq Z \leq 30$ and Very Very Heavy (VVH) nuclei with $Z \geq 31$ (Fleischer et al. 1975).

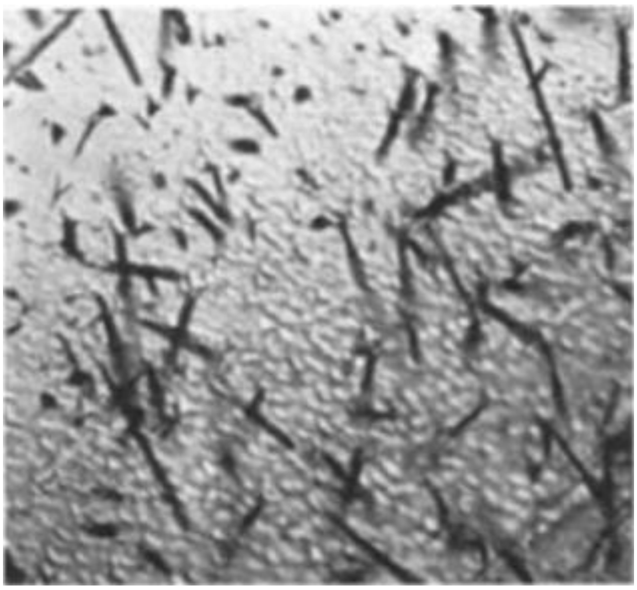

Figure 5.2*. Image showing particle damage tracks from within a bytownite crystal from the stoney-iron meteorite Crab Orchard. The length of the tracks indicates they were produced by very heavy primary cosmic rays. Image taken from* Fleischer et al. (1965b).

Whilst the atomic weight of an incident particle is one constraint on the formation of damage tracks, its energy also plays a role (Eugster et al. 2006). Low energy particles are least likely to induce an energy loss via nuclear reaction and are therefore least likely to produce damage tracks within solids. Approximately 300 MeV/nucleon is the 'crossover energy' at which the probability of a nuclear reaction is equal to that of particle survival via passage straight through the solid (Eugster et al. 2006). This is a consequence of the ionization potential of a particle being dependent on charge (Z) and velocity (energy) (v) such that Z^2/v^2 (Friedlander 2000). Due to Z^2 being proportional to the ionisation loss, this 'crossover' energy increases with increasing Z. Incident particle energy and mass are therefore the characteristics which control the probabilities of track development and resulting damage track length (Eugster et al. 2006). Typical observed track lengths for iron nuclei are ~10-12 μm (Pellas et al. 1969). As a result of these features analysis of damage tracks can reveal important information about a material's irradiation record.

Both GCRs and SEPs contain VH particles at high enough energies to produce damage tracks. However, given the differences in particle energy and consequently penetration depth, contrasts in the depths of track formation are observed between the two irradiation types.

SEP damage tracks are produced in the upper few mm-cm of material. The shallow depth profile of SEP tracks is therefore indicative of a surface position for a mineral during the period of irradiation. Due to the higher flux of SEP particles, damage track densities >10^6 tracks/cm^2 are recorded (Harries and Wild 2017a; Metzler 2004). It should be noted that during a meteor's transit to Earth any SEP damage tracks produced in minerals on the meteoroid surface are lost due to melting and ablation as the meteoroid enters the Earth's atmosphere (Bhattacharya et al. 1973).

GCR damage tracks can be produced in the top few m of regolith. The low flux and deep penetration of GCR particles means that GCR produced particle damage tracks are usually responsible for background track densities. GCR produced background damage tracks were likely produced during a meteoroid's transit to Earth when material is on the meter scale, allowing total irradiation of the meteoroid (Caffee et al., 1988; Vogt et al., 1990). Evidence for an Earth transit origin for background track densities is supported by densities approximately corresponding to the exposure ages for meteorites calculated using ^{21}Ne production rates (Nishiizumi et al. 1980). Previous studies of CM chondrites Nogoya and Mighei found typical background track densities of 3.6 x10^4 and 5.1 x10^5 tracks/cm^2 respectively (Metzler 2004). Variations in background track density are likely a result of varying degrees of shielding (depth) within the meteoroid. The effect of increasing regolith depth on particle track density gradient is illustrated in Figure 5.3.

The contribution of fission tracks to any analysis of the irradiation record described above is minor (Crozaz et al. 1989; Riebe 2012). The minor contribution is a result of the low total abundance of fissionable elements within the olivine crystals being examined in this work (Crozaz et al. 1989; Lal and Rajan 1969). The relative contribution of fission tracks can also be determined by the strongly anisotropic nature of the damage tracks discussed above, as fission tracks would produce an isotropic track distribution which is not observed (Riebe 2012).

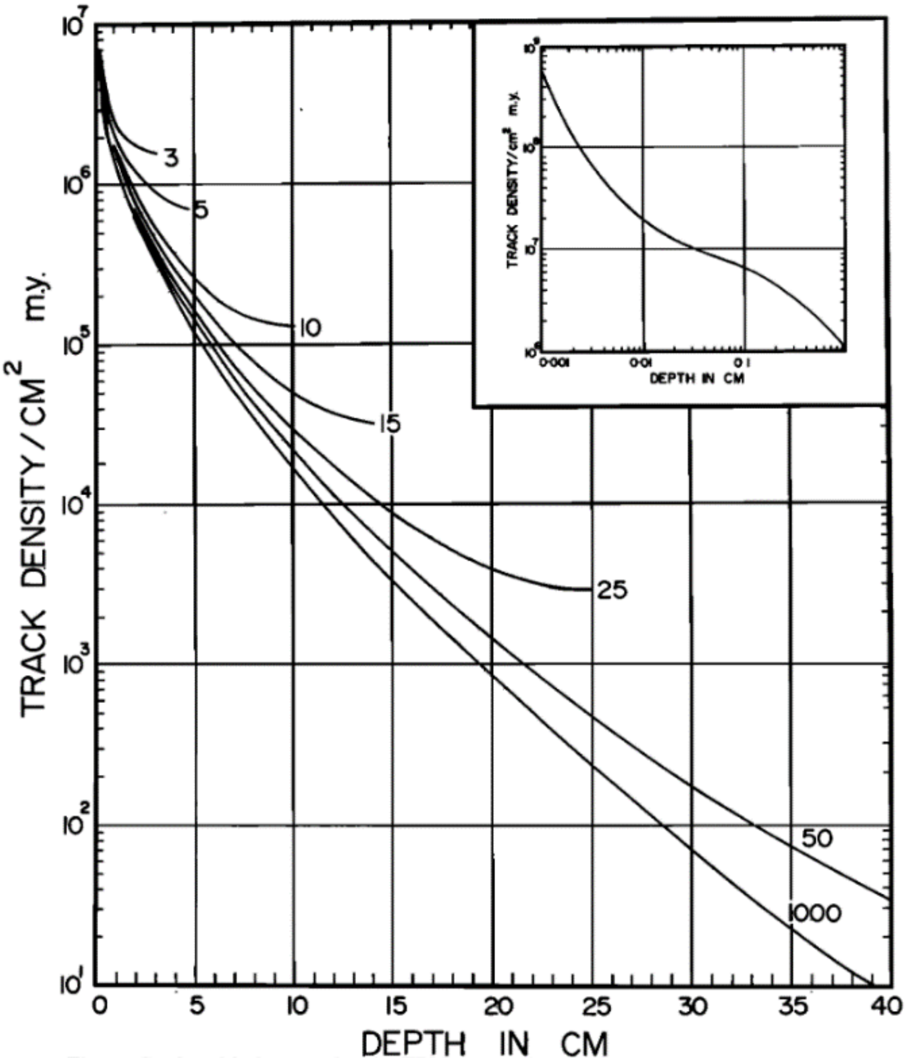

Figure 5.3. *Track productions rates (tracks/cm*^{2} *my) as a function of depth in chondritic material. Curves based on long-term averaged spectra of cosmic ray VH nuclei. Insert shows track production rates for depths <1 cm. Track production rates are given for chondrites with radii between 3 and 1000 cm. Figure sourced from Lal (1972).*

5.2.1 Ion Explosion Spike Model

There have been several models proposed to explain the development of damage tracks within solids. These models include direct atomic displacement, a thermal spike model, total energy loss during ionisation, primary ionisation and excitation, energy deposited by delta rays in track cores, total energy loss in track cores and restricted energy loss. For a complete breakdown of these proposed mechanisms and the associated evidence for and against see Fleischer et al., (1975) – particularly Table 1.5.

The ion explosion spike model was developed by Fleischer et al. (1965) and is the accepted model to explain the production of lattice defects and the resulting particle damage tracks produced by incident charged particles. Within the ion explosion spike model tracks only develop when the rate of ionisation along a given particles trajectory exceeds a critical ionization rate (J_c) (Riebe 2012). Consequently, the depth at which a damage track is formed is dependent on the energy of the inbound particle (as mentioned in the previous section) (Riebe 2012). For example, fast, high-energy particles (such as GCRs) have an ionisation rate lower than J_c and therefore particle damage tracks are not produced until an inbound particle has been slowed down by its passage through a material, such that the rate of ionisation exceeds J_c.

The ion explosion spike model can be described in three phases outlined below and illustrated in Figure 5.4:

- Step 1: As a charged particle passes through a solid, atoms along the particle's trajectory are ionised. During this ionisation atoms along the incident particle's path are stripped of their electrons, producing a series of electrostatically unstable ions adjacent to the charged particle's path, as shown in Figure 5.4A.

- Step 2: The unstable ions eject one another from their normal positions into interstitial positions, leaving behind vacant lattice sites. This process is termed electrostatic displacement and produces an acute stress on the localised region as the unstable ions pull away from the incident particle path. Electrostatic displacement is illustrated in Figure 5.4B.

- Step 3: Following the initial stress, elastic relaxation occurs, and the acute stress experienced in the immediate area of ionisation is spread more widely. The spreading of this stress results in the straining of previously undamaged matrix in a process termed elastic strain. This is processes is illustrated in Figure 5.4C.

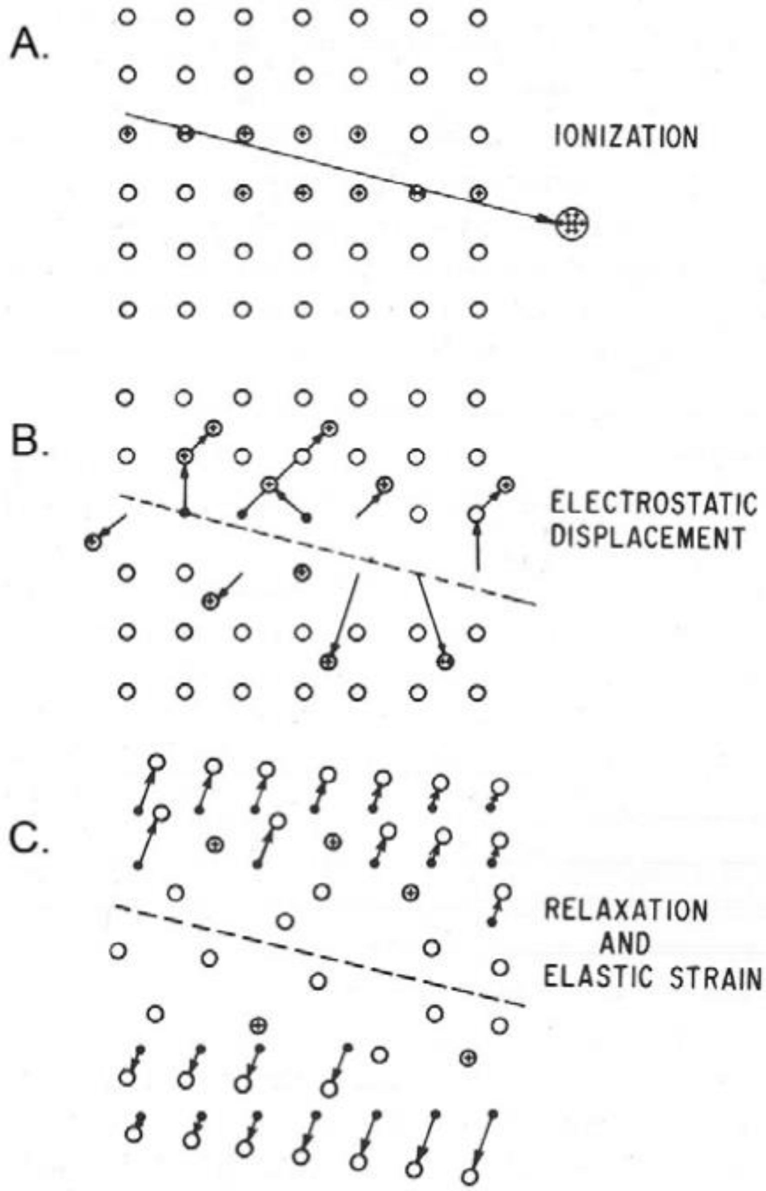

Figure 5.4*. The ion explosion spike model for damage track formation first proposed by* Fleischer et al. (1965). *Illustrated are the three step of the ion explosive spike model: A) Ionisation along the charged particles' path, B) Electrostatic displacement due to unstable ions occurs along the incident particles' path C) Elastic relaxation of the acutely stressed region produces a wider elastic strain damaged region in the previously unaffected matrix. Illustration taken from Fleischer et al. (1975).*

5.3 Observing Damage Tracks

Following irradiation that produces damage tracks within a mineral or other solid, the tracks can be analysed to explore a sample's exposure history. Analysis can involve examining track features such as length, orientation of the damage track surface opening, and track density (tracks per unit area, typically expressed as tracks cm^{-2}). However, due to the sub-microscopic nature of damage tracks, analysis requires either transmission electron microscopy (TEM) (Figure 5.5) or a chemical etchant to allow damage tracks to be viewed using lower resolution techniques (Price and Walker 1962).

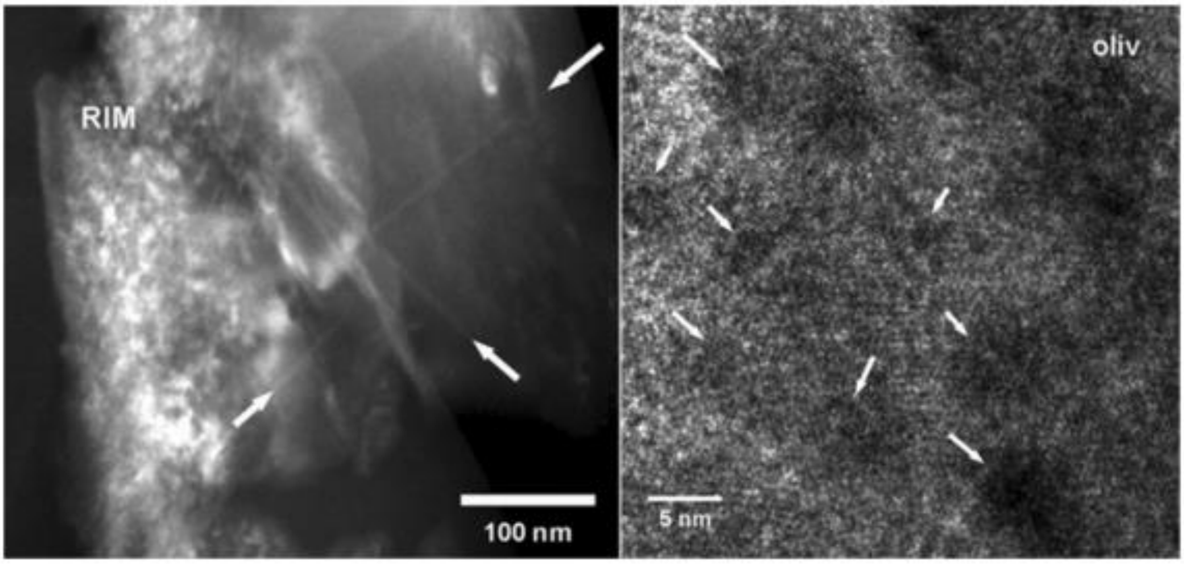

Figure 5.5. *Dark-field STEM image (left) and high-resolution TEM image (right) of solar flare tracks within Itokawa particle RA-QD02-0211. Image taken from* (Keller and Berger 2014).

Chemical etchants exploit a zone of increased chemical reactivity produced by the production of particle damage tracks. When an etchant is applied to this more reactive region it acts as a chemical 'amplifier' to preferentially dissolve the already damaged region (Fischer and Spohr 1983). This amplification process produces an 'etch pit' which is an enlargement of the damaged track opening and allows conventional optical microscopy to be used to view and analyse tracks. Chemical etching also makes damage tracks a permanent feature and prevents loss from any possible future annealing (the removal or reduction in track length and width under certain environmental conditions) (Fischer and Spohr 1983).

Chemical etching is the more typical method applied to particle damage track studies within meteoritic and geological materials. Etching is preferred due to its ability to be applied over large areas with relative ease and requirement for only optical microscopy for analysis. Conversely TEM analysis can only be conducted on small regions after significant sample preparation and analysis that is often costly.

There are a number of different chemical etchants which are used to reveal damage tracks. Depending on the material of interest the etchant used will differ, as will the concentration of the etchant, etchant temperature and total etch time (Fischer and Spohr 1983). Table 5.2 outlines some of the typical etchants used for various geological materials.

Table 5.2. *Exemplar etchants and their associated etching conditions for a variety of geologic materials.*

Material	Etchant	Temperature (°C)	Etch Time	Reference
Muscovite mica	48% HF	20	20 mins	Price and Walker (1962)
Quartz	a) KOH (aq) b) 48% HF	150 23	3hrs 24 hrs	Fleischer et al. (1965b)
Zircon	KOH NaOH	200-220	28-30	Garver (2003)
Olivine†	WN	100	2-4 hrs	Krishnaswami et al., (1971)

† Discussed in more detail in section 1.3.1

5.3.1 WN Etching

Olivine is one of the dominant minerals of CM chondrites, occurring in chondrules and as relict grains within the matrix. Track studies within the CMs therefore focus on damage tracks analysis within these olivine grains. As indicated in Table 5.2 WN etchant is used for modern olivine track studies. The term WN is a symbolic designation and not indicative of any feature or constituent component of the technique, contrary to most of the other chemical etchants (Krishnaswami et al. 1971).

WN etchant is produced by combining 1g oxalic acid, 1 mL of orthophosphoric acid (85%), 40g of disodium salt of ethylenediaminetetraacetic acid (EDTA), and 100 mL of distilled water. NaOH is added to the solution to achieve a pH of 8.0 ± 0.3 (Krishnaswami et al. 1971). Once the components are combined, the solution will remain cloudy until brought to the boil. To maintain the solution concentration and a pH of 8.0 ± 0.3 during boiling, a reflux system is used to capture and recondense evaporated solution (this is illustrated in Figure 5.7). Once the solution is fully mixed (appearing clear) and held at a steady boil, the olivine grains to be examined can be added to the solution. Olivine should be etched for 2-4 hours depending on the microscopy method being used (Krishnaswami et al. 1971). Where SEM techniques are being used for damage track analysis a 2 hour etch time is typically sufficient reveal damage tracks. Where optical microscopy techniques are being used an etch time of 4 hours is required.

A major challenge of etching meteoritic olivine is exposing enough olivine grains to the WN etchant to detect an irradiated grain. As will be discussed in section 1.4, not all meteoritic olivine grains contain damage tracks and thus a large number of grains are required for etching. Two approaches, disaggregation and thin sectioning have been used for meteoritic olivine track studies and the benefits and drawbacks of each are explained below.

Disaggregation: Meteoritic chips are either crushed or subjected to repeated freeze-thaw cycles to break them into a powder. Any olivine grains present are then handpicked from this powder and mounted on stubs or points for pre-etching examination. The grains are then suspended in the WN etchant and subsequently examined for damage tracks (Harries and Wild 2017a; Lal and Rajan 1969; Lal et al. 1968; Metzler 2004). Disaggregation is effective in extracting many olivine grains for analysis and so increasing the likelihood of locating damage tracks. However, due to disaggregation the spatial or contextual assessment of irradiated grains is not possible. Furthermore, a significant amount of meteoritic material is powdered during this process significantly limiting any future analysis.

Thin Sectioning: Polished thin sections are produced from a meteoritic chip using standard techniques. The thin sections can then be examined using optical microscopy and/or SEM prior to WN etching. Once examined the entire thin section is immersed within the etchant and subsequently examined (Lal and Rajan 1969; Metzler 2004; Riebe 2012). Thin sectioning is effective in allowing spatial and contextual information for irradiated grains to be assessed. However, analysis is limited to the number of olivine grains within the thin section and therefore multiple thin sections may be required to locate a sufficient number of irradiated grains. Furthermore, the etching process has an adverse effect on the thin section. As described by Metzler, (2004) WN etching changes the visual appearance of the sections from opaque to translucent, making textural features such as brecciation visible to the naked eye (Figure 5.6). Metzler, (2004) also noted that fine-grained materials such as clastic matrix and FGRs surrounding chondrules are mostly removed during the etching process with only material directly bonded to the glass section preserved.

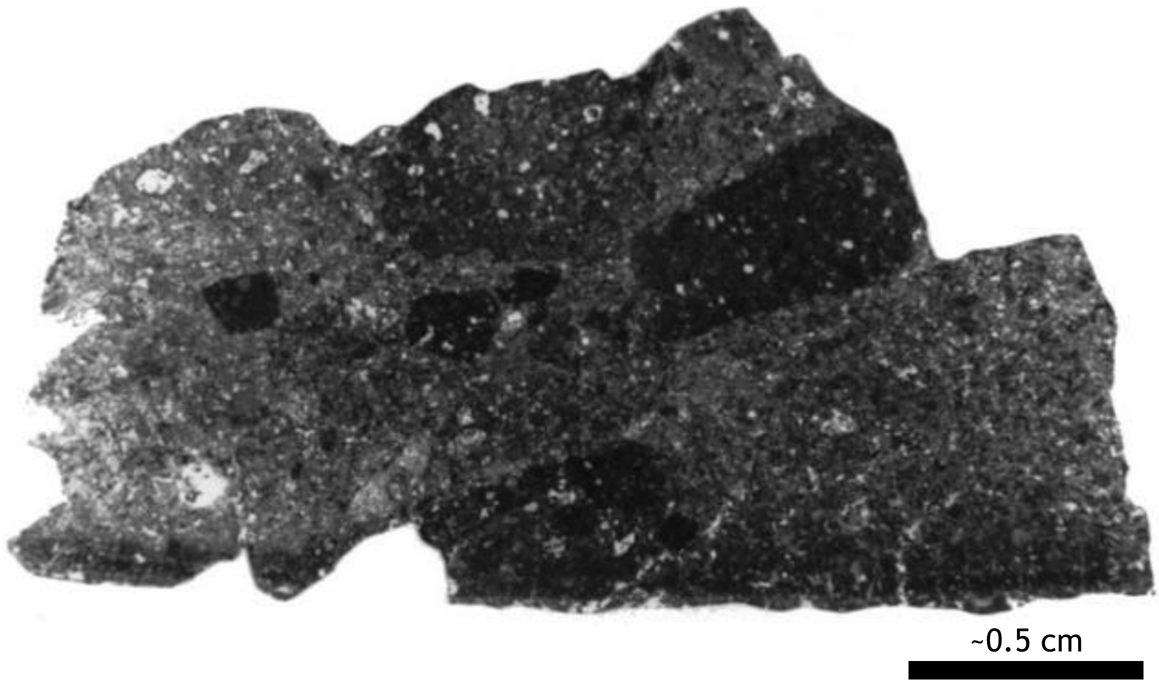

Figure 5.6. *Transmitted light image of a polished thin section of CM chondrite Nogoya following WN etching. The etching process has revealed several lithic clasts embedded within a fine-grained matrix that are all discernible without SEM techniques. Image taken from Metzler, (2004).*

Both techniques facilitate damage track analysis of olivine grain and despite the challenges associated with exposing enough olivine grains, the thin section approach is likely to be the more scientifically useful and ethical approach for future damage track analysis. Thin sectioning allows samples to be examined and catalogued pre-etching, maximising the science output and maintaining a record of samples before destructive etching. Thin sectioning also provides important spatial context to the irradiated grains. A diagram of the equipment set up for WN etching of a meteoritic thin section is shown below in Figure 5.7.

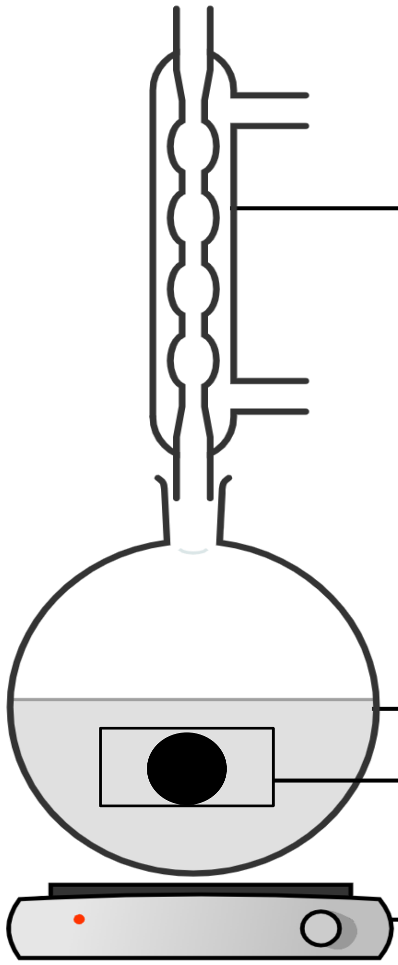

Figure 5.7*. Etching setup for WN treatment of a meteoritic thin section. Shown is a boiling flask atop a heating plate. Within the flask is the WN etchant and the thin section to be etched. The system is capped by a reflux system to condense evaporation, maintaining the pH of the solution.*

5.4 Previous Meteoritic Track Studies

To help understand the applications and usefulness of damage track studies in meteoritics, a brief overview of some of the most notable and relevant meteorite damage track studies follows. It should be noted that many of the seminal nuclear track studies were conducted in the 1960s and while these provide the foundation for knowledge on damage track studies there have been significant improvements in our understanding of space irradiation, the development of damage tracks, and meteorite composition and classification since these studies were conducted. The following reviews are not limited to carbonaceous or CM chondrites due to the limited literature on the topic.

5.4.1 Maurette et al. (1964)

The Maurette et al. (1964) study was the first to report damage tracks within meteorites – in this instance pallasites (stony-iron meteorites). Maurette et al., (1964) uncovered these damage tracks using a primitive olivine etchant requiring multiple etching cycles (usually at least two cycles required). Each cycle consisted of exposing olivine grains to potassium hydroxide (29g KOH; 9g H_20) at 160 °C for 4 minutes, followed by a 5% hydrofluoric acid (HF) solution at ambient temperature for 30 seconds.

The tracks identified by Maurette et al. (1964) had an average length of ~3 μm with track densities of ~ 5 x10^5 tracks cm^{-2} detected. The track densities measured are consistent with what has come to be acknowledged as a background track density. A marked anisotropy was also observed and interpreted as potentially indicating an 'up' and 'down' orientation for the olivine grain (Figure 5.8).

From these findings six different mechanisms were discussed as being potentially responsible for these damage tracks – these are also discussed in Fleischer et al., 1965. Maurette et al. (1964) concluded that the likely cause of was either heavy primary ion irradiation or spallation recoils. This conclusion was reached due to difficulties reconciling the other potential causes with the observations of overall track length, track distribution, track density, and results of olivine annealing experiments. For a complete description of the damage track production mechanisms discussed a reader is encouraged to see Maurette et al., (1964).

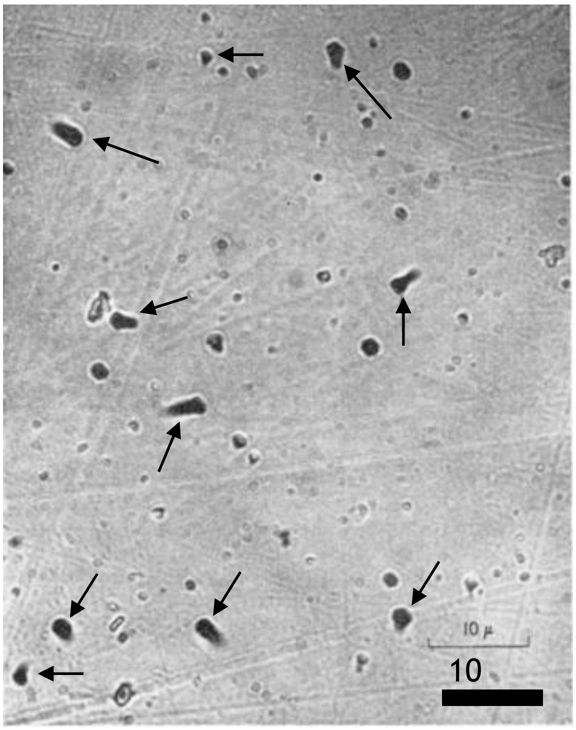

Figure 5.8*. Damage track etch pits revealed in meteoritic olivine from pallasite Pavlodar. The black arrows indicate etch pits interpreted as being produced by cosmic ray interaction with the meteorite. Image adapted from Maurette et al. (1964).*

5.4.2 Fleischer et al. (Assorted 1964-1965)

Fleicher and collaborators built on the work of Maurette et al. (1964) describing damage tracks in both terrestrial and extra-terrestrial rocks. Fleischer's work also explored the mechanisms by which track formation can occur, most notably developing the ion explosion spike model in 1965 (see Section 5.2.1) (Fleischer et al. 1964, 1965a, 1965c).

Fleischer's work established several key principles with regards to meteoritic track-studies. Most importantly Fleischer et al. (1964) noted that etchable track formation only begins when the rate of energy loss per unit length for an incident particle exceeds a critical value: $(dE/dx)_c$ which is a characteristic quantity of the irradiated material. Olivine is calculated to have a critical rate of energy loss of ~20 MeV/mg/cm^2 (Fleischer et al. 1965c). As a result of this finding, it was also determined that incident heavier particles produce longer the damage tracks, and therefore a particle damage tracks maximum length can be used as an indicator for incident particle mass (Fleischer et al. 1965a). It was also observed that track density can change as a function of depth therefore making meteoritic particle track studies a useful tool for studying erosion and ablation occurring in extra-terrestrial materials (Fleischer et al. 1965a).

As introduced earlier, provided the right environmental conditions, usually sufficient heating, un-etched tracks can be annealed, removing evidence of the internal stress produced by ionisation. Fleischer et al., (1965a) showed that refractory materials such as mica and olivine experience little effect from environmental conditions during their formation or retention period. The results of track annealing experiments to determine the potential for track removal in olivine are shown in Table 5.3 (Fleischer et al. 1965a). The exception to this is SEP tracks produced on a meteoroid surface, these likely experience the required conditions to be annealed during Earth atmospheric entry.

Table 5.3*. Track annealing conditions for olivine and for comparison zircon. Table adapted from* Fleischer et al. (1965c).

Material	Track fading temp. (1 hr heating time (± 25°C)	Time before track fading (years) [kT in units of eV]	Valid temp. range (°C)	Extrapolated temp. for a life of 4.5x10^9 year (°K)	Extrapolated life at 300°K (years)
Olivine	500°C	2.4 x10^{-27} exp (3.3/kT)	450-550	473	5 x10^{30}
Zircon	700°C 675° at 80 kb	8.5 x10^{-24} exp (3.6/kT)	25-125	205	1

Much of Fleischer's work is summarised in Fleischer et al., (1975) which is widely considered a fundamental review of track studies in both terrestrial and extra-terrestrial materials and should be considered an essential read prior to any track study experiments.

5.4.3 Goswami et al. (Assorted 1976-83)

Goswami et al. published significantly on olivine damage tracks in the CM chondrites during the 1970's and 1980's (Goswami and Lal 1979; Goswami and Macdougall 1983; Goswami et al. 1976). Much of this work was focused on understanding the environment in which damage tracks were formed and from this interpreting the evolution of the CM chondrite parent body.

Within all studies the WN etchant described in Section 1.3.1 was used for olivine etching. Goswami et al. (1976) and Goswami and Lal, (1979), used disaggregation methods to separate olivine from meteoritic chips prior to etching while Goswami and Macdougall, (1983) applied WN etchant to petrographic thick sections, handpicked olivines from the clastic matrix, and olivines collected using bulk crushing. Goswami and Macdougall, (1983) cited the benefits of understanding the spatial and contextual setting of olivine grains being analysed.

Goswami et al. (1976) sets out three findings which are broadly consistent within all of Goswami's work:

i) Damage track geometries are nearly always anisotropic

ii) Track densities observed can span four orders of magnitude

iii) The fraction of irradiated grains can vary significantly inter- and intra-sample.

Within their works Goswami and collaborators identified background track densities of ~10^4 tracks cm^{-2} and interpreted these densities as being the result of recent cosmic irradiation likely during transit to Earth as a meteoroid. Olivine grains with track densities >10^5 tracks cm^{-2} were interpreted as being track-rich and having experienced irradiation prior to incorporation into the parent. Goswami and Macdougall, (1983) found that ~2-3% of the isolated matrix grains handpicked from CM chondrites had track densities consistent with pre-incorporation irradiation by GCRs. Of these pre-irradiated grains ~30-50% were observed to have either detectable track gradients or track densities >10^8 cm^{-2}; these were interpreted as evidence of surface exposure with grains displaying particle track densities likely irradiated by SEP events.

Track azimuth angles revealed the anisotropic nature of the incident irradiation with distributions showing ~80% of grains had track geometries showing either a single peak or slightly bimodal distribution (Goswami and Macdougall 1983). Such a distribution was interpreted as being indicative of a single exposure history. The remaining ~20% of the irradiated grains were observed to have isotropic track geometries suggestive of a multi-stage exposure history.

One of the most significant points of discussion within Goswami and collaborator's work was the understanding of when track-rich grains were being irradiated. Earlier theories proposed by Lal and Rajan, (1969) and Pellas et al. (1969) suggest either isotropic irradiation of individual olivine grains whilst not incorporated into a parent body or irradiation whilst incorporated in the regolith of the meteorite parent body. The findings of Goswami and collaborators supported irradiation prior to compaction for the origin of track-rich grains, with Goswami and Lal, (1979) eventually suggested that irradiation likely occurred early in the solar nebula, prior to parent body compaction ~4.2 Ga when constituents were part of cm-m sized clumps of material.

5.4.4 Metzler, 2004

Metzler, (2004) set out to examine pre-irradiated (track-rich) olivines in CM chondrites to try and establish if FGRs were produced by accretionary processes in the solar nebula or regolith processes acting on the CM parent body. Relevant to this chapter is that Metzler, (2004) examined a total of 6220 olivine grains using the WN thin section etching procedure outlined in section 1.3.1. Thin sections from CM chondrites, Cold Bokkeveld, Mighei, Murchison, and Nogoya were examined as part of this study. As previously discussed, background track densities referred to by Metzler represent GCR produced tracks which were formed during meteoroid transit to Earth. Metzler (2004) measured background track densities between a of 3.6 $x10^4$ cm^{-2} (Nogoya) and 5.1 $x10^5$ cm^{-2} (Mighei) (Table 5.4).

Metzler (2004) like others describes preirradiated or track-rich grains as those exposed to irradiation prior to Earth transit within a meteoroid and therefore having track densities greater than the background density. These tracks were either produced whilst free-floating in the solar nebula prior to parent body accretion or whilst incorporated into the surface regolith of CM chondrite parent body.

115 of the analysed olivine grains examined had track densities > 10^6 tracks cm^{-2} and were classified as track-rich and preirradiated. These represented 2.1-2.3% of olivine grains in each respective thin section (Table 5.4). Examining the spatial context of the track-rich grains shows all were located within the clastic matrix and had an inhomogeneous distribution (as illustrated in Figure 5.9). Mean track densities within the track-rich grains ranged from 1.1-2.5 $x10^7 cm^{-2}$ within the preirradiated grains, additionally 17% - 29% of the preirradiated grains were observed to have track gradients indicative of SEP irradiation right at the parent body surface (Table 5.4).

None of the regions identified by Metzler as Primary Accretionary Rock (PAR) were observed to contain track-rick olivines with all grains having a background track density consistent only with single stage of GCR irradiation during Earth transit. Metzler therefore interpreted the PAR as representing an unbrecciated bedrock which was excavated from depths on the CM parent body which were not reachable by SEPs or GCRs. These fragments of PAR were then admixed with the pre-irradiated components in the upper regolith regions of the parent body, and the preirradiated grains with track gradients indicative of exposure in the upper few mm of parent body regolith.

Table 5.4. *Summarised table outline the track data obtained by Metzler, (2004)*

Meteorite	Thin section area (cm^2)	Number of analyzable olivines	Background track density (tracks/cm^2)	Percentage of irradiated olivine grains	Percentage of preirradiated olivines with track gradient	Mean track density in preirradiated olivines (tracks/$cm^{2)}$
Cold Bokkeveld	4.6	2400	2.6 $x10^5$	2.2	17	1.8 $x10^7$
Mighei	2.6	810	5.1 $x10^5$	-	-	-
Murchison	5.3	2700	7.1 $x10^4$	2.1	25	2.5 $x10^7$
Nogoya	1.8	310	3.6 $x10^4$	2.3	29	1.1 $x10^7$

Figure 5.9. *Sketch illustrations showing the locations and distributions of the lithologies and preirradiated olivines (black dots) within the thin sections investigated by Metzler (2004). Illustrations show the inhomogenous nature of the track-rich crystals and their confinement to the clastic matrix. Shaded areas represent fragments of what Metzler identified as primary rock. Faint-dashed lined in Cold Bokkeveld indicated the preirradiated breccica-in-breccia clast which Metzler (2004) identified. Illustration taken from Metzler (2004).*

5.4.5 Harries and Wild (2017)

Harries and Wild, (2017) provide the most recent study of damage tracks within CM chondrites. Harries and wild, (2017) set out to investigate the potential for the degree of space weathering to inform insights into regolith processing occurring on the CM parent body and thus helping to understand the parent asteroid's evolution.

To investigate this Harries and Wild, (2017) used randomly orientated petrographic thin sections from the moderately heated (<~500°C) CM chondrite Jbilet Winselwan. Petrographic thin sections were examined using SEM to investigate the sample chemistry and textures whilst the chips were subjected to repeated freeze-thaw action to disaggregate material and facilitate the handpicking of any olivine grains present. The grains were subsequently mounted and imaged using SEM before etching using the WN etchant described in section 5.3.1.

Analysis of the petrographic thin sections revealed no obvious brecciation within Jbilet Winselwan as is seen in many other CM2 chondrites with the textures conforming to what Metzler et al. (1992) described as PAR. From the disaggregated chips a total of 82 olivine grains were extracted and analysed for particle damage tracks. 65 of the olivine's examined (~79 %) were observed to contain tracks. In all cases track densities were <10^5 tracks cm^{-2}, consistent with the background track densities produced by GCR's during Earth transit noted by other authors (Metzler, 2004).

The absence of obvious brecciation within the petrographic thin sections and the lack of track-rich olivine grains, with track densities >10^6 tracks cm^{-2} leads Harries and Wild, (2017) to suggest that Jbilet Winselwan was never exposed in the upper few mm's or m's of the CM parent body. Based on the description of Jbilet Winselwan as being dominated by PAR these findings are support those of Metzler (2004) with regards to PAR representing unbrecciated bed rock excavated from depth and shielded from irradiation prior to Earth transit as a meteoroid.

One notable finding by (Harries and Wild 2017a) is that the background track densities detected (median ~9400 tracks cm^{-2}) were significantly below those reported by previous authors (Goswami and Macdougall 1983; Metzler 2004) (Figure 5.10). Given the unusually long exposure age of Jbilet Winselwan's, 6.6 ± 1.7 Ma (Meier et al. 2016), the low background track count is surprising and lead (Harries and Wild 2017b) to suggest that the damage tracks may have experienced partial annealing. The data presented in Table 5.3 supports the potential for track annealing at temperatures believed to have been experienced by Jbilet Winselwan (400-500°C) (King et al. 2018).

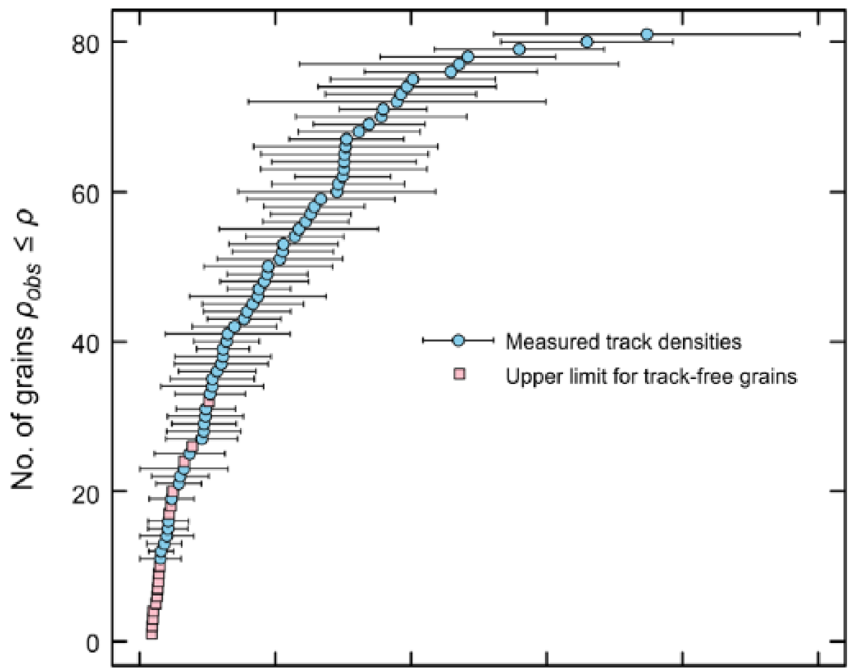

Figure 5.10*. Cumulative plot of the particle track densities in the disaggregated Jbilet Winselwan olivine grains. Figure taken from* (Harries and Wild 2017b).

Reconciling a heating event and the potential annealing of damage tracks within Jbilet Winselwan is challenging, as it is assumed that any heating event would have occurred whilst incorporated deep within the parent body. Meanwhile background track imposition should have occurred during the meteoroid phase following exhumation from the parent body. Whilst further analysis and track studies are required to ascertain if annealing has occurred within Jbilet Winselwan this paradox highlights the potential usefulness of track studies in understanding the evolution of the CM parent body.

5.5 Future Applications

Damage track analysis of CM chondrite olivine grains remains poorly studied despite the potential to yield significant information regarding parent body processes. The absence of track-rich grains within clasts is surprising especially given the almost ubiquitous brecciated nature of the CMs. If such a trend holds true amongst all CMs then it could support Metzler (2004) suggestion that the clasts and clastic matrix were sourced from different regions of the parent body which experienced different processes. Such a finding could have implications for our understanding of event chronology and the relationship between matrix and clasts. The inhomogeneous distribution of track-rich grains is also very interesting and to date no hypothesis has been presented to explain this unusual distribution. Further examination of the distribution of track-rich grains could help improve our understanding of the accretionary, impact and regolith processes occurring on the CM parent body and explain this distribution.

It is therefore suggested that significant further investigation is required in the field of particle damage track analysis within the CM chondrites. Of particular interest for future analysis should be those grains defined as track-rich (>10^8cm^{-2}) and having a track gradient as these grains have likely been irradiated by SEP events within the uppermost few mm of the parent body regolith. Future studies of damage tracks should seek to mimic the methodology set out in Metzler, (2004) using thin sections to provide contextual information regarding the locations of irradiated grains. It is also suggested that some of the highly brecciated recent CM falls such as Winchcombe (CM2.0-2.4) (King et al. 2022) and Aguas Zarcas (CM2.2-2.8) (Kerraouch et al. 2021) would be good candidates for future track analysis. It is further suggested that examining the relationships between track-rich grains and other parent body processes such as aqueous alteration would be beneficial and the recently classified and little altered samples such as Paris (CM2.7) (Rubin 2015) and Asuka (CM3.0-2.8) (Kimura et al. 2020) would be particularly useful for analysis of any relationship.

Further studies of damage tracks could prove highly significant for developing our understanding of the dynamic processes and regolith gardening occurring on the CM parent body and have potential implications for our understanding of impact and accretionary processes acting on the CM parent body.

Chapter 6 Final Summary

Chapter six draws together each of the previous chapters and presents the key findings and conclusions resulting from this project.

6.1 Conclusions

This project has sought to explore the pre- and post-accretionary processes occurring on the C-type asteroids by examining the spectrally linked CM chondrites (Burbine 2000).

Utilising a combination of high-resolution 2D and 3D imaging techniques, BSE and XCT respectively, alongside detailed chemical mapping, the CM chondrites Aguas Zarcas, Cold Bokkeveld, Kolang, LaPaz Icefield (LAP) 02239, Lewis Cliff (LEW) 85311, Mighei, Murchison, Paris, Shidian, and Winchcombe were examined. All were subjected to chondrule size analysis with a selection also used for chondrule orientation analysis.

Both analyses have highlighted the dynamic nature of the processing occurring on C-type asteroids and improved our understanding of how these processes manifest in the CM chondrites. The findings of this project include evidence for a pre-accretionary formation process resulting in prolate chondrule shapes prior to accretion, and a size sorting process operating during initial chondrule accretion. Furthermore, variations observed in chondrule sizes, abundance and orientations between clasts within the CM's has significant implications for interpreting post-accretionary deformation and alteration processes such as impact compaction and aqueous alteration. The inter-clast variability in chondrule characteristics reported here also highlights the importance of identifying and accounting for the effects of brecciation during CM chondrite studies.

During this project it has also been shown that damage track analysis of CM chondrite olivine grains using WN etchant could be a powerful technique to further improve our understanding of parent body(ies) accretion. Damage track analysis also has the potential to help further reveal the impact processing histories of the CM chondrites.

6.2 Key Findings

- Chondrule size measurement methods vary significantly between studies making inter-study comparisons of size unreliable. This project sets out a proposed standardised approach to enable accurate inter-study comparison of chondrule size
- CM chondrule sizes are smaller than the commonly reported average of 270-300 µm (Friedrich et al. 2015; Rubin and Wasson 1986; Weisberg et al. 2006). An updated average size of 2.363ϕ (194 µm) is reported and its similarity to the CO chondrule size average strengthens support for the proposed CM-CO clan
- Chondrule-defined fabrics are commonplace within the CM chondrites when examined in 3D with relative fabric strengths observed to vary between CM's
- The relative timings of deformation, aqueous alteration and brecciation have been inferred from similarities and/or differences in the chondrule defined fabrics within clasts. Variations in the chronology of events has implications for models of aqueous alteration being driven by impact facilitated fluid flow.
- Chondrules likely had a non-spherical original shape at the time of accretion to the CM parent body(ies). This finding reconciles a longstanding paradox within the CM chondrite literature between evidence for fabrics, alignment and deformation and no evidence of shock features in the microstructure
- Brecciation is highlighted as being a significant feature of the CM chondrites with variations in chondrule size, abundance, fabric strength, and fabric orientation observed between clasts
- This project has identified WN etching of CM olivine grains as a potentially useful technique for understanding the accretionary and regolith turnover processes occurring on the CM parent body(ies).

Chapter 7 Future Work

In the following sections future work related to each chapter is discussed. However, in addition to these individual points, this project has also demonstrated the benefits and usefulness of 3D analysis and utilising XCT studies within chondritic meteorites. While the work presented in this project represents the largest 3D study of CM chondrites so far conducted (the most CM chondrites examined in a single study) these represent only a fraction of all CM chondrites and expansion of the technique to more CM chondrite studies is proposed. The limited use of XCT with studies of other chondritic meteorites is something which should also be addressed. Further research and data collection using XCT will help develop a literature repository of 3D data allowing improved understanding of the pre- and post-accretionary processes which have affected chondrites.

7.1 Chondrule Size Analysis

The application of the CIS method for chondrule size measurements has, in this study, shown that the previous value overstated the average chondrule size. Applying the CIS method to other chondritic groups would identify other cases of such inaccuracy and facilitate reliable inter-group and inter-study comparison of chondrule size. The CO chondrites, which from this study have a close affinity to the CM chondrites, should be a priority in this regard. CIS studies with correlated high resolution XCT would also further improve stereological correction models allowing for more accurate reconstructions.

Furthermore, to improve the comparison of chondrule size data between chondritic groups large scale data collection of chondrule sizes should be pursued. Utilising citizen science and crowd sourcing could aid in gathering the large data sets required for analysis. In such an event the well-defined measurement methodology set out here as the CIS method would provide a clear and simple guide to measurement methods.

7.2 Chondrule Orientation and Impact Processing

While this project has reinforced the findings of previous authors regarding the almost ubiquitous nature of chondrule-defined fabrics, there remains significant scope for further 3D analysis of other CM chondrites. Further examination of inter-clast variability in fabric orientations and strength would help further demonstrate the complexity of alteration and deformation event chronology and potentially identify patterns in such chronologies between samples.

The degree to which metal grains are being deflected around chondrules is a further point for future analysis which could involve both XCT and correlated SEM and EBSD analysis.

Additional analysis investigating the effects non-spherical original chondrule shapes on the shock pressures required to produce deformation can help to further reconcile the disparity between fabric strengths and a lack of microstructures.

7.3 CM Damage Track Analysis

Although detailed analysis of CM chondrite olivine damage tracks was not possible during this project due to time and equipment constraints it remains a potentially significant avenue for future research. To date there has been only limited use of this technique within the literature and any future study would greatly add to the available literature employing this technique. Future studies using WN etching on the CM chondrites would be best suited to thin section studies, allowing the inhomogeneous distribution of pre-irradiated grains observed by Metzler (2004) to be further examined. It is further suggested that future studies concentrate on highly brecciated CM chondrites, as these have the greatest likelihood of revealing a pre-irradiated olivine within non-matrix lithologies.

Chapter 8 Appendices

8.1 Chapter 3 Specific Appendices

This section contains data and supplementary materials related to Chapter 3.

8.1.1 RAW 2D Chondrule Size Data

Table 8.1. *Table showing RAW 3D chondrule size data for long (R1) and short (R3) axes.*

R_1			R_3		
Sample	R_1 (mm)	R_1 (phi)	Sample	R_3 (mm)	R_3 (phi)
Paris	0.085	3.556	Paris	0.063	3.989
Paris	1.058	-0.081	Paris	0.780	0.358
Paris	0.136	2.878	Paris	0.067	3.900
Paris	0.113	3.146	Paris	0.083	3.591
Paris	0.300	1.737	Paris	0.161	2.635
Paris	0.262	1.932	Paris	0.228	2.133
Paris	0.081	3.626	Paris	0.062	4.012
Paris	0.236	2.083	Paris	0.130	2.943
Paris	0.286	1.806	Paris	0.203	2.300
Paris	0.242	2.047	Paris	0.235	2.089
Paris	0.110	3.184	Paris	0.092	3.442
Paris	0.126	2.989	Paris	0.072	3.796
Paris	0.087	3.523	Paris	0.057	4.133
Paris	0.290	1.786	Paris	0.162	2.626
Paris	0.439	1.188	Paris	0.328	1.608
Paris	0.157	2.671	Paris	0.127	2.977
Paris	0.287	1.801	Paris	0.116	3.108
Paris	0.976	0.035	Paris	0.457	1.130
Paris	0.220	2.184	Paris	0.087	3.523
Paris	0.648	0.626	Paris	0.457	1.130
Paris	0.046	4.442	Paris	0.044	4.506
Paris	0.121	3.047	Paris	0.117	3.095
Paris	0.182	2.458	Paris	0.121	3.047
Paris	0.105	3.252	Paris	0.068	3.878
Paris	0.282	1.826	Paris	0.200	2.322
Paris	0.193	2.373	Paris	0.170	2.556
Paris	0.161	2.635	Paris	0.152	2.718
Paris	0.073	3.776	Paris	0.064	3.966
Paris	0.793	0.335	Paris	0.658	0.604
Paris	0.129	2.955	Paris	0.081	3.626
Paris	0.268	1.900	Paris	0.153	2.708
Paris	0.063	3.989	Paris	0.048	4.381
Paris	0.215	2.218	Paris	0.163	2.617
Paris	0.259	1.949	Paris	0.147	2.766
Paris	0.109	3.198	Paris	0.073	3.776
Paris	0.361	1.470	Paris	0.297	1.751
Paris	0.370	1.434	Paris	0.325	1.621
Paris	0.222	2.171	Paris	0.200	2.322
Paris	0.157	2.671	Paris	0.108	3.211
Paris	0.142	2.816	Paris	0.126	2.989
Paris	0.259	1.949	Paris	0.117	3.095
Paris	0.200	2.322	Paris	0.131	2.932
Paris	0.232	2.108	Paris	0.137	2.868
Paris	0.330	1.599	Paris	0.209	2.258
Paris	0.601	0.735	Paris	0.470	1.089
Paris	0.182	2.458	Paris	0.084	3.573
Paris	0.525	0.930	Paris	0.321	1.639
Paris	0.453	1.142	Paris	0.245	2.029
Paris	0.110	3.184	Paris	0.107	3.224
Paris	0.373	1.423	Paris	0.339	1.561
Paris	0.460	1.120	Paris	0.402	1.315
Paris	0.308	1.699	Paris	0.195	2.358
Paris	0.182	2.458	Paris	0.094	3.411

Table continued

R1			R3		
Sample	**R_1 (mm)**	**R_1 (phi)**	**Sample**	**R_3 (mm)**	**R_3 (phi)**
Paris	0.114	3.133	Paris	0.096	3.381
Paris	0.181	2.466	Paris	0.154	2.699
Paris	0.075	3.737	Paris	0.062	4.012
Paris	0.291	1.781	Paris	0.247	2.017
Paris	0.596	0.747	Paris	0.443	1.175
Paris	0.317	1.657	Paris	0.164	2.608
Paris	0.346	1.531	Paris	0.154	2.699
Paris	0.289	1.791	Paris	0.206	2.279
Paris	0.212	2.238	Paris	0.133	2.911
Paris	0.387	1.370	Paris	0.234	2.095
Paris	0.129	2.955	Paris	0.088	3.506
Paris	0.073	3.776	Paris	0.052	4.265
Paris	0.548	0.868	Paris	0.411	1.283
Paris	0.075	3.737	Paris	0.073	3.776
Paris	0.227	2.139	Paris	0.198	2.336
Paris	0.276	1.857	Paris	0.167	2.582
Paris	0.119	3.071	Paris	0.080	3.644
Paris	0.070	3.837	Paris	0.051	4.293
Paris	0.349	1.519	Paris	0.320	1.644
Paris	0.260	1.943	Paris	0.154	2.699
Paris	0.230	2.120	Paris	0.195	2.358
Paris	0.937	0.094	Paris	0.767	0.383
Paris	0.411	1.283	Paris	0.336	1.573
Paris	0.143	2.806	Paris	0.109	3.198
Paris	0.150	2.737	Paris	0.102	3.293
Paris	0.120	3.059	Paris	0.081	3.626
Paris	0.108	3.211	Paris	0.079	3.662
Paris	0.175	2.515	Paris	0.138	2.857
Paris	0.399	1.326	Paris	0.334	1.582
Paris	0.279	1.842	Paris	0.248	2.012
Paris	0.182	2.458	Paris	0.129	2.955
Paris	0.167	2.582	Paris	0.117	3.095
Paris	0.332	1.591	Paris	0.264	1.921
Paris	0.226	2.146	Paris	0.141	2.826
Paris	0.099	3.336	Paris	0.085	3.556
Paris	1.684	-0.752	Paris	0.925	0.112
Paris	0.642	0.639	Paris	0.466	1.102
Paris	0.152	2.718	Paris	0.107	3.224
Paris	0.254	1.977	Paris	0.152	2.718
Paris	0.331	1.595	Paris	0.187	2.419
Paris	0.256	1.966	Paris	0.116	3.108
Paris	0.083	3.591	Paris	0.074	3.756
Paris	0.461	1.117	Paris	0.234	2.095
Paris	0.623	0.683	Paris	0.371	1.431
Paris	0.139	2.847	Paris	0.099	3.336
Paris	0.123	3.023	Paris	0.104	3.265
Paris	0.118	3.083	Paris	0.073	3.776
Paris	0.168	2.573	Paris	0.123	3.023
Paris	0.567	0.819	Paris	0.471	1.086
Paris	0.110	3.184	Paris	0.080	3.644
Paris	0.394	1.344	Paris	0.345	1.535
Paris	0.181	2.466	Paris	0.121	3.047
Paris	0.251	1.994	Paris	0.186	2.427
Paris	0.106	3.238	Paris	0.075	3.737
Paris	0.083	3.591	Paris	0.073	3.776
Paris	0.127	2.977	Paris	0.090	3.474
Paris	0.267	1.905	Paris	0.188	2.411
Paris	0.405	1.304	Paris	0.286	1.806
Paris	0.470	1.089	Paris	0.262	1.932
Paris	0.099	3.336	Paris	0.062	4.012
Paris	0.175	2.515	Paris	0.157	2.671
Paris	0.257	1.960	Paris	0.245	2.029
Paris	0.175	2.515	Paris	0.121	3.047
Paris	0.308	1.699	Paris	0.257	1.960
Paris	0.130	2.943	Paris	0.094	3.411
Paris	0.353	1.502	Paris	0.205	2.286
Paris	0.263	1.927	Paris	0.200	2.322
Paris	0.188	2.411	Paris	0.097	3.366
Paris	0.085	3.556	Paris	0.060	4.059

Table continued

R₁			R₃		
Sample	R_1 (mm)	R_1 (phi)	Sample	R_3 (mm)	R_3 (phi)
Paris	0.146	2.776	Paris	0.076	3.718
Paris	0.656	0.608	Paris	0.330	1.599
Paris	0.163	2.617	Paris	0.113	3.146
Paris	0.297	1.751	Paris	0.175	2.515
Paris	0.104	3.265	Paris	0.087	3.523
Paris	0.121	3.047	Paris	0.113	3.146
Paris	0.357	1.486	Paris	0.236	2.083
Paris	0.456	1.133	Paris	0.225	2.152
Paris	0.495	1.014	Paris	0.423	1.241
Paris	0.338	1.565	Paris	0.320	1.644
Paris	0.207	2.272	Paris	0.101	3.308
Paris	0.253	1.983	Paris	0.175	2.515
Paris	0.078	3.680	Paris	0.054	4.211
Paris	0.095	3.396	Paris	0.074	3.756
Paris	0.146	2.776	Paris	0.143	2.806
Paris	0.106	3.238	Paris	0.059	4.083
Paris	0.198	2.336	Paris	0.115	3.120
Paris	0.107	3.224	Paris	0.083	3.591
Paris	0.083	3.591	Paris	0.061	4.035
Paris	0.315	1.667	Paris	0.295	1.761
Paris	0.141	2.826	Paris	0.099	3.336
Paris	0.137	2.868	Paris	0.116	3.108
Paris	0.305	1.713	Paris	0.259	1.949
Paris	0.628	0.671	Paris	0.426	1.231
Paris	0.202	2.308	Paris	0.175	2.515
Paris	0.246	2.023	Paris	0.201	2.315
Paris	0.181	2.466	Paris	0.145	2.786
Paris	0.357	1.486	Paris	0.230	2.120
Paris	0.462	1.114	Paris	0.402	1.315
Paris	0.068	3.878	Paris	0.057	4.133
Paris	0.165	2.599	Paris	0.113	3.146
Paris	0.412	1.279	Paris	0.352	1.506
Paris	0.305	1.713	Paris	0.267	1.905
Paris	0.192	2.381	Paris	0.132	2.921
Paris	0.218	2.198	Paris	0.201	2.315
Paris	0.708	0.498	Paris	0.533	0.908
Paris	0.331	1.595	Paris	0.203	2.300
Paris	0.405	1.304	Paris	0.363	1.462
Paris	0.118	3.083	Paris	0.103	3.279
Paris	0.239	2.065	Paris	0.198	2.336
Paris	0.163	2.617	Paris	0.142	2.816
Paris	0.294	1.766	Paris	0.186	2.427
Paris	0.621	0.687	Paris	0.477	1.068
Paris	0.136	2.878	Paris	0.113	3.146
Paris	0.171	2.548	Paris	0.127	2.977
Paris	0.196	2.351	Paris	0.123	3.023
Paris	0.489	1.032	Paris	0.375	1.415
Paris	0.122	3.035	Paris	0.114	3.133
Paris	0.202	2.308	Paris	0.097	3.366
Paris	0.630	0.667	Paris	0.376	1.411
Paris	0.224	2.158	Paris	0.134	2.900
Paris	0.459	1.123	Paris	0.345	1.535
Paris	0.190	2.396	Paris	0.174	2.523
Paris	0.127	2.977	Paris	0.112	3.158
Paris	0.201	2.315	Paris	0.156	2.680
Paris	0.184	2.442	Paris	0.131	2.932
Paris	0.225	2.152	Paris	0.122	3.035
Paris	0.402	1.315	Paris	0.306	1.708
Paris	0.145	2.786	Paris	0.132	2.921
Paris	0.172	2.540	Paris	0.158	2.662
Paris	0.472	1.083	Paris	0.250	2.000
Paris	0.172	2.540	Paris	0.156	2.680
Paris	0.196	2.351	Paris	0.097	3.366
Paris	0.316	1.662	Paris	0.165	2.599
Paris	0.327	1.613	Paris	0.182	2.458
Paris	0.077	3.699	Paris	0.053	4.238
Paris	0.238	2.071	Paris	0.148	2.756
Paris	0.176	2.506	Paris	0.060	4.059
Paris	0.143	2.806	Paris	0.132	2.921
Paris	0.397	1.333	Paris	0.306	1.708

Table continued

R1			R3		
Sample	R_1 (mm)	R_1 (phi)	Sample	R_3 (mm)	R_3 (phi)
Paris	0.152	2.718	Paris	0.086	3.540
Paris	0.169	2.565	Paris	0.111	3.171
Paris	0.152	2.718	Paris	0.092	3.442
Paris	0.359	1.478	Paris	0.285	1.811
Paris	0.214	2.224	Paris	0.188	2.411
Paris	0.094	3.411	Paris	0.072	3.796
Paris	1.114	-0.156	Paris	0.984	0.023
Paris	0.108	3.211	Paris	0.088	3.506
Paris	0.119	3.071	Paris	0.088	3.506
Paris	0.199	2.329	Paris	0.140	2.837
Paris	0.107	3.224	Paris	0.061	4.035
Paris	0.116	3.108	Paris	0.048	4.381
Paris	0.403	1.311	Paris	0.217	2.204
Paris	0.153	2.708	Paris	0.083	3.591
Paris	0.118	3.083	Paris	0.094	3.411
Paris	0.097	3.366	Paris	0.037	4.756
Paris	0.093	3.427	Paris	0.060	4.059
Paris	0.167	2.582	Paris	0.114	3.133
Paris	0.164	2.608	Paris	0.117	3.095
Paris	0.197	2.344	Paris	0.105	3.252
Paris	0.074	3.756	Paris	0.049	4.351
Paris	0.139	2.847	Paris	0.106	3.238
Paris	0.146	2.776	Paris	0.085	3.556
Murchison	0.072	3.796	Murchison	0.059	4.083
Murchison	0.108	3.211	Murchison	0.059	4.083
Murchison	0.204	2.293	Murchison	0.148	2.756
Murchison	0.107	3.224	Murchison	0.080	3.644
Murchison	0.310	1.690	Murchison	0.250	2.000
Murchison	0.328	1.608	Murchison	0.225	2.152
Murchison	0.076	3.718	Murchison	0.068	3.878
Murchison	0.632	0.662	Murchison	0.498	1.006
Murchison	0.377	1.407	Murchison	0.223	2.165
Murchison	0.118	3.083	Murchison	0.097	3.366
Murchison	0.321	1.639	Murchison	0.285	1.811
Murchison	0.174	2.523	Murchison	0.085	3.556
Murchison	0.071	3.816	Murchison	0.066	3.921
Murchison	0.196	2.351	Murchison	0.095	3.396
Murchison	0.114	3.133	Murchison	0.081	3.626
Murchison	0.104	3.265	Murchison	0.090	3.474
Murchison	0.124	3.012	Murchison	0.102	3.293
Murchison	0.111	3.171	Murchison	0.061	4.035
Murchison	0.177	2.498	Murchison	0.117	3.095
Murchison	0.532	0.911	Murchison	0.380	1.396
Murchison	0.307	1.704	Murchison	0.138	2.857
Murchison	0.102	3.293	Murchison	0.076	3.718
Murchison	0.198	2.336	Murchison	0.122	3.035
Murchison	0.208	2.265	Murchison	0.175	2.515
Murchison	0.174	2.523	Murchison	0.102	3.293
Murchison	0.295	1.761	Murchison	0.187	2.419
Murchison	0.192	2.381	Murchison	0.089	3.490
Murchison	0.221	2.178	Murchison	0.148	2.756
Murchison	0.099	3.336	Murchison	0.070	3.837
Murchison	0.224	2.158	Murchison	0.108	3.211
Murchison	0.159	2.653	Murchison	0.105	3.252
Murchison	0.109	3.198	Murchison	0.099	3.336
Murchison	0.108	3.211	Murchison	0.088	3.506
Murchison	0.154	2.699	Murchison	0.087	3.523
Murchison	0.692	0.531	Murchison	0.456	1.133
Murchison	0.187	2.419	Murchison	0.125	3.000
Murchison	0.168	2.573	Murchison	0.147	2.766
Murchison	0.335	1.578	Murchison	0.167	2.582
Murchison	0.186	2.427	Murchison	0.155	2.690
Murchison	0.157	2.671	Murchison	0.124	3.012
Murchison	0.217	2.204	Murchison	0.187	2.419
Murchison	0.187	2.419	Murchison	0.098	3.351
Murchison	0.091	3.458	Murchison	0.074	3.756
Murchison	0.653	0.615	Murchison	0.498	1.006
Murchison	0.122	3.035	Murchison	0.096	3.381
Murchison	0.130	2.943	Murchison	0.105	3.252
Murchison	0.194	2.366	Murchison	0.168	2.573

Table continued

R1			R3		
Sample	R_1 (mm)	R_1 (phi)	Sample	R_3 (mm)	R_3 (phi)
Murchison	0.235	2.089	Murchison	0.107	3.224
Murchison	0.292	1.776	Murchison	0.261	1.938
Murchison	0.176	2.506	Murchison	0.161	2.635
Murchison	0.074	3.756	Murchison	0.042	4.573
Murchison	0.165	2.599	Murchison	0.107	3.224
Murchison	0.110	3.184	Murchison	0.092	3.442
Murchison	0.071	3.816	Murchison	0.059	4.083
Murchison	0.199	2.329	Murchison	0.174	2.523
Murchison	0.095	3.396	Murchison	0.073	3.776
Murchison	0.106	3.238	Murchison	0.073	3.776
Murchison	0.292	1.776	Murchison	0.186	2.427
Murchison	0.162	2.626	Murchison	0.093	3.427
Murchison	0.498	1.006	Murchison	0.337	1.569
Murchison	0.208	2.265	Murchison	0.169	2.565
Murchison	0.180	2.474	Murchison	0.145	2.786
Murchison	0.202	2.308	Murchison	0.188	2.411
Murchison	0.292	1.776	Murchison	0.223	2.165
Murchison	0.135	2.889	Murchison	0.103	3.279
Murchison	0.101	3.308	Murchison	0.067	3.900
Murchison	0.118	3.083	Murchison	0.105	3.252
Murchison	0.067	3.900	Murchison	0.055	4.184
Murchison	0.171	2.548	Murchison	0.110	3.184
Murchison	0.247	2.017	Murchison	0.191	2.388
Murchison	0.178	2.490	Murchison	0.144	2.796
Murchison	0.193	2.373	Murchison	0.130	2.943
Murchison	0.197	2.344	Murchison	0.119	3.071
Murchison	0.076	3.718	Murchison	0.070	3.837
Murchison	0.154	2.699	Murchison	0.126	2.989
Murchison	0.105	3.252	Murchison	0.074	3.756
Murchison	0.155	2.690	Murchison	0.119	3.071
Murchison	0.111	3.171	Murchison	0.055	4.184
Murchison	0.154	2.699	Murchison	0.146	2.776
Murchison	0.072	3.796	Murchison	0.064	3.966
Murchison	0.130	2.943	Murchison	0.064	3.966
Murchison	0.075	3.737	Murchison	0.062	4.012
Murchison	0.112	3.158	Murchison	0.082	3.608
Murchison	0.347	1.527	Murchison	0.179	2.482
Murchison	0.095	3.396	Murchison	0.062	4.012
Murchison	0.144	2.796	Murchison	0.121	3.047
Murchison	0.076	3.718	Murchison	0.056	4.158
Murchison	0.185	2.434	Murchison	0.172	2.540
Murchison	0.055	4.184	Murchison	0.049	4.351
Murchison	0.138	2.857	Murchison	0.080	3.644
Murchison	0.091	3.458	Murchison	0.073	3.776
Murchison	0.118	3.083	Murchison	0.061	4.035
Murchison	0.107	3.224	Murchison	0.080	3.644
Murchison	0.099	3.336	Murchison	0.091	3.458
Murchison	0.494	1.017	Murchison	0.381	1.392
Murchison	0.096	3.381	Murchison	0.080	3.644
Murchison	0.103	3.279	Murchison	0.088	3.506
Murchison	0.081	3.626	Murchison	0.046	4.442
Murchison	0.137	2.868	Murchison	0.077	3.699
Murchison	0.637	0.651	Murchison	0.504	0.989
Murchison	0.503	0.991	Murchison	0.363	1.462
Murchison	0.324	1.626	Murchison	0.203	2.300
Murchison	0.139	2.847	Murchison	0.072	3.796
Murchison	0.177	2.498	Murchison	0.130	2.943
Murchison	0.173	2.531	Murchison	0.155	2.690
Murchison	0.082	3.608	Murchison	0.065	3.943
Murchison	0.078	3.680	Murchison	0.073	3.776
Murchison	0.170	2.556	Murchison	0.130	2.943
Murchison	0.211	2.245	Murchison	0.118	3.083
Murchison	0.201	2.315	Murchison	0.145	2.786
Murchison	0.082	3.608	Murchison	0.075	3.737
Murchison	0.108	3.211	Murchison	0.098	3.351
Murchison	0.456	1.133	Murchison	0.310	1.690
Murchison	0.179	2.482	Murchison	0.090	3.474
Murchison	0.096	3.381	Murchison	0.071	3.816
Murchison	0.262	1.932	Murchison	0.172	2.540
Murchison	0.220	2.184	Murchison	0.173	2.531

Table continued

R1			R3		
Sample	R_1 (mm)	R_1 (phi)	Sample	R_3 (mm)	R_3 (phi)
Murchison	0.167	2.582	Murchison	0.147	2.766
Murchison	0.118	3.083	Murchison	0.061	4.035
Murchison	0.225	2.152	Murchison	0.159	2.653
Murchison	0.118	3.083	Murchison	0.086	3.540
Murchison	0.132	2.921	Murchison	0.096	3.381
Murchison	0.402	1.315	Murchison	0.252	1.989
Murchison	0.103	3.279	Murchison	0.070	3.837
Murchison	0.154	2.699	Murchison	0.110	3.184
Murchison	0.132	2.921	Murchison	0.099	3.336
Murchison	0.208	2.265	Murchison	0.193	2.373
Murchison	0.211	2.245	Murchison	0.120	3.059
Murchison	0.099	3.336	Murchison	0.086	3.540
Murchison	0.152	2.718	Murchison	0.117	3.095
Murchison	0.105	3.252	Murchison	0.090	3.474
Murchison	0.293	1.771	Murchison	0.153	2.708
Murchison	0.146	2.776	Murchison	0.117	3.095
Murchison	0.213	2.231	Murchison	0.119	3.071
Murchison	0.188	2.411	Murchison	0.111	3.171
Murchison	0.322	1.635	Murchison	0.245	2.029
Murchison	0.107	3.224	Murchison	0.065	3.943
Murchison	0.079	3.662	Murchison	0.063	3.989
Murchison	0.325	1.621	Murchison	0.167	2.582
Murchison	0.149	2.747	Murchison	0.135	2.889
Murchison	0.280	1.837	Murchison	0.219	2.191
Murchison	0.272	1.878	Murchison	0.220	2.184
Murchison	0.145	2.786	Murchison	0.124	3.012
Murchison	0.217	2.204	Murchison	0.134	2.900
Murchison	0.130	2.943	Murchison	0.111	3.171
Murchison	0.148	2.756	Murchison	0.134	2.900
Murchison	0.159	2.653	Murchison	0.094	3.411
Murchison	0.253	1.983	Murchison	0.204	2.293
Murchison	0.592	0.756	Murchison	0.547	0.870
Murchison	0.323	1.630	Murchison	0.300	1.737
Murchison	0.353	1.502	Murchison	0.305	1.713
Murchison	0.145	2.786	Murchison	0.101	3.308
Murchison	0.163	2.617	Murchison	0.111	3.171
Murchison	0.217	2.204	Murchison	0.13	2.943
Murchison	0.129	2.955	Murchison	0.089	3.490
Murchison	0.321	1.639	Murchison	0.254	1.977
Murchison	0.323	1.630	Murchison	0.192	2.381
Murchison	0.149	2.747	Murchison	0.129	2.955
Murchison	0.110	3.184	Murchison	0.079	3.662
Murchison	0.134	2.900	Murchison	0.081	3.626
Murchison	0.086	3.540	Murchison	0.049	4.351
Murchison	0.074	3.756	Murchison	0.058	4.108
Murchison	0.181	2.466	Murchison	0.152	2.718
Murchison	0.067	3.900	Murchison	0.041	4.608
Murchison	0.053	4.238	Murchison	0.046	4.442
Murchison	0.104	3.265	Murchison	0.082	3.608
Murchison	0.243	2.041	Murchison	0.194	2.366
Murchison	0.142	2.816	Murchison	0.097	3.366
Murchison	0.167	2.582	Murchison	0.125	3.000
Murchison	0.145	2.786	Murchison	0.12	3.059
Murchison	0.151	2.727	Murchison	0.107	3.224
Murchison	0.106	3.238	Murchison	0.09	3.474
Murchison	0.312	1.680	Murchison	0.188	2.411
Murchison	0.181	2.466	Murchison	0.166	2.591
Murchison	0.110	3.184	Murchison	0.095	3.396
Murchison	0.035	4.837	Murchison	0.03	5.059
Murchison	0.074	3.756	Murchison	0.067	3.900
Murchison	0.045	4.474	Murchison	0.035	4.837
Murchison	0.131	2.932	Murchison	0.102	3.293
Murchison	0.242	2.047	Murchison	0.181	2.466
Murchison	0.057	4.133	Murchison	0.052	4.265
Murchison	0.090	3.474	Murchison	0.068	3.878
Murchison	0.130	2.943	Murchison	0.093	3.427
Murchison	0.067	3.900	Murchison	0.053	4.238
Murchison	0.057	4.133	Murchison	0.045	4.474
Murchison	0.083	3.591	Murchison	0.07	3.837
Murchison	0.147	2.766	Murchison	0.1290	2.955

Table continued

R1			R3		
Sample	**R_1 (mm)**	**R_1 (phi)**	**Sample**	**R_3 (mm)**	**R_3 (phi)**
Murchison	0.420	1.252	Murchison	0.2580	1.955
Murchison	0.475	1.074	Murchison	0.3370	1.569
Murchison	0.418	1.258	Murchison	0.2740	1.868
Murchison	0.294	1.766	Murchison	0.1860	2.427
Murchison	0.588	0.766	Murchison	0.3420	1.548
Murchison	0.177	2.498	Murchison	0.0670	3.900
Murchison	0.196	2.351	Murchison	0.1530	2.708
Murchison	0.088	3.506	Murchison	0.0850	3.556
Murchison	0.420	1.252	Murchison	0.1610	2.635
Murchison	0.212	2.238	Murchison	0.1880	2.411
Murchison	0.079	3.662	Murchison	0.0680	3.878
Murchison	0.067	3.900	Murchison	0.0590	4.083
Murchison	0.257	1.960	Murchison	0.2020	2.308
Aguas Zarcas	0.096	3.378	Aguas Zarcas	0.07566	3.724
Aguas Zarcas	0.174	2.521	Aguas Zarcas	0.11454	3.126
Aguas Zarcas	0.094	3.407	Aguas Zarcas	0.08041	3.636
Aguas Zarcas	0.078	3.683	Aguas Zarcas	0.0719	3.798
Aguas Zarcas	0.060	4.050	Aguas Zarcas	0.04579	4.449
Aguas Zarcas	0.218	2.197	Aguas Zarcas	0.18024	2.472
Aguas Zarcas	0.254	1.976	Aguas Zarcas	0.15862	2.656
Aguas Zarcas	0.036	4.789	Aguas Zarcas	0.02904	5.106
Aguas Zarcas	0.083	3.597	Aguas Zarcas	0.07537	3.730
Aguas Zarcas	0.144	2.796	Aguas Zarcas	0.125	3.000
Aguas Zarcas	0.228	2.133	Aguas Zarcas	0.178	2.490
Aguas Zarcas	0.311	1.685	Aguas Zarcas	0.272	1.878
Aguas Zarcas	0.087	3.523	Aguas Zarcas	0.064	3.966
Aguas Zarcas	0.143	2.806	Aguas Zarcas	0.116	3.108
Aguas Zarcas	0.269	1.894	Aguas Zarcas	0.201	2.315
Aguas Zarcas	0.668	0.582	Aguas Zarcas	0.403	1.311
Aguas Zarcas	0.558	0.842	Aguas Zarcas	0.484	1.047
Aguas Zarcas	0.066	3.921	Aguas Zarcas	0.059	4.083
Aguas Zarcas	0.243	2.041	Aguas Zarcas	0.212	2.238
Aguas Zarcas	0.117	3.095	Aguas Zarcas	0.087	3.523
Aguas Zarcas	0.286	1.806	Aguas Zarcas	0.127	2.977
Aguas Zarcas	0.066	3.921	Aguas Zarcas	0.054	4.211
Aguas Zarcas	0.179	2.482	Aguas Zarcas	0.122	3.035
Aguas Zarcas	0.221	2.178	Aguas Zarcas	0.121	3.047
Aguas Zarcas	0.145	2.786	Aguas Zarcas	0.133	2.911
Aguas Zarcas	0.072	3.796	Aguas Zarcas	0.055	4.184
Aguas Zarcas	0.170	2.556	Aguas Zarcas	0.104	3.265
Aguas Zarcas	0.093	3.427	Aguas Zarcas	0.064	3.966
Aguas Zarcas	0.057	4.133	Aguas Zarcas	0.044	4.506
Aguas Zarcas	0.126	2.989	Aguas Zarcas	0.102	3.293
Aguas Zarcas	0.589	0.764	Aguas Zarcas	0.455	1.136
Aguas Zarcas	0.067	3.900	Aguas Zarcas	0.059	4.083
Aguas Zarcas	0.104	3.265	Aguas Zarcas	0.084	3.573
Aguas Zarcas	0.168	2.573	Aguas Zarcas	0.157	2.671
Aguas Zarcas	0.203	2.300	Aguas Zarcas	0.192	2.381
Aguas Zarcas	0.105	3.252	Aguas Zarcas	0.095	3.396
Aguas Zarcas	0.232	2.108	Aguas Zarcas	0.171	2.548
Aguas Zarcas	0.163	2.617	Aguas Zarcas	0.138	2.857
Aguas Zarcas	0.302	1.727	Aguas Zarcas	0.216	2.211
Aguas Zarcas	0.183	2.450	Aguas Zarcas	0.158	2.662
Aguas Zarcas	0.726	0.462	Aguas Zarcas	0.506	0.983
Aguas Zarcas	0.650	0.621	Aguas Zarcas	0.367	1.446
Aguas Zarcas	0.062	4.012	Aguas Zarcas	0.057	4.133
Aguas Zarcas	0.258	1.955	Aguas Zarcas	0.179	2.482
Aguas Zarcas	0.203	2.300	Aguas Zarcas	0.109	3.198
Aguas Zarcas	0.056	4.158	Aguas Zarcas	0.052	4.265
Aguas Zarcas	0.180	2.474	Aguas Zarcas	0.121	3.047
LEW85311	0.148	2.756	LEW85311	0.113	3.146
LEW85311	0.084	3.573	LEW85311	0.059	4.083
LEW85311	0.179	2.482	LEW85311	0.127	2.977
LEW85311	0.166	2.591	LEW85311	0.145	2.786
LEW85311	0.391	1.355	LEW85311	0.341	1.552
LEW85311	0.243	2.041	LEW85311	0.136	2.878
LEW85311	0.181	2.466	LEW85311	0.108	3.211
LEW85311	0.074	3.756	LEW85311	0.051	4.293
LEW85311	0.111	3.171	LEW85311	0.073	3.776
LEW85311	0.422	1.245	LEW85311	0.291	1.781

Table continued

R$_1$			R$_3$		
Sample	**R$_1$ (mm)**	**R$_1$ (phi)**	**Sample**	**R$_3$ (mm)**	**R$_3$ (phi)**
LEW85311	0.128	2.966	LEW85311	0.111	3.171
LEW85311	0.240	2.059	LEW85311	0.125	3.000
LEW85311	0.103	3.279	LEW85311	0.085	3.556
LEW85311	0.181	2.466	LEW85311	0.160	2.644
LEW85311	0.182	2.458	LEW85311	0.174	2.523
LEW85311	0.155	2.690	LEW85311	0.121	3.047
LEW85311	0.100	3.322	LEW85311	0.081	3.626
LEW85311	0.090	3.474	LEW85311	0.072	3.796
LEW85311	0.091	3.458	LEW85311	0.072	3.796
LEW85311	0.079	3.662	LEW85311	0.070	3.837
LEW85311	0.138	2.857	LEW85311	0.131	2.932
LEW85311	0.092	3.442	LEW85311	0.063	3.989
LEW85311	0.170	2.556	LEW85311	0.120	3.059
LEW85311	0.367	1.446	LEW85311	0.203	2.300
LEW85311	0.061	4.035	LEW85311	0.056	4.158
LEW85311	0.290	1.786	LEW85311	0.157	2.671
LEW85311	0.093	3.427	LEW85311	0.085	3.556
LEW85311	0.155	2.690	LEW85311	0.133	2.911
LEW85311	0.285	1.811	LEW85311	0.148	2.756
LEW85311	0.266	1.911	LEW85311	0.155	2.690
LEW85311	0.192	2.381	LEW85311	0.165	2.599
LEW85311	0.207	2.272	LEW85311	0.157	2.671
LEW85311	0.469	1.092	LEW85311	0.242	2.047
LEW85311	0.186	2.427	LEW85311	0.185	2.434
LEW85311	0.170	2.556	LEW85311	0.100	3.322
LEW85311	0.126	2.989	LEW85311	0.112	3.158
LEW85311	0.082	3.608	LEW85311	0.056	4.158
LEW85311	1.140	-0.189	LEW85311	0.606	0.723
LEW85311	0.205	2.286	LEW85311	0.152	2.718
LEW85311	0.140	2.837	LEW85311	0.103	3.279
LEW85311	0.912	0.133	LEW85311	0.815	0.295
LEW85311	0.152	2.718	LEW85311	0.110	3.184
LEW85311	0.293	1.771	LEW85311	0.156	2.680
LEW85311	0.458	1.127	LEW85311	0.297	1.751
LEW85311	0.120	3.059	LEW85311	0.077	3.699
LEW85311	0.159	2.653	LEW85311	0.115	3.120
LEW85311	0.205	2.286	LEW85311	0.153	2.708
LEW85311	0.333	1.586	LEW85311	0.302	1.727
LEW85311	0.147	2.766	LEW85311	0.125	3.000
LEW85311	0.197	2.344	LEW85311	0.155	2.690
LEW85311	0.082	3.608	LEW85311	0.067	3.900
LEW85311	0.265	1.916	LEW85311	0.150	2.737
LEW85311	0.160	2.644	LEW85311	0.139	2.847
LEW85311	0.082	3.608	LEW85311	0.074	3.756
LEW85311	0.132	2.921	LEW85311	0.067	3.900
LEW85311	0.945	0.082	LEW85311	0.781	0.357
LEW85311	0.145	2.786	LEW85311	0.113	3.146
LEW85311	0.207	2.272	LEW85311	0.158	2.662
LEW85311	0.354	1.498	LEW85311	0.246	2.023
LEW85311	0.095	3.396	LEW85311	0.092	3.442
LEW85311	0.164	2.608	LEW85311	0.123	3.023
LEW85311	0.130	2.943	LEW85311	0.106	3.238
LEW85311	0.154	2.699	LEW85311	0.132	2.921
LEW85311	0.363	1.462	LEW85311	0.224	2.158
LEW85311	0.151	2.727	LEW85311	0.130	2.943
LEW85311	0.206	2.279	LEW85311	0.107	3.224
LEW85311	0.137	2.868	LEW85311	0.105	3.252
LEW85311	0.580	0.786	LEW85311	0.396	1.336
LEW85311	0.802	0.318	LEW85311	0.694	0.527
LEW85311	0.205	2.286	LEW85311	0.123	3.023
LEW85311	0.167	2.582	LEW85311	0.119	3.071
LEW85311	0.068	3.878	LEW85311	0.060	4.059
LEW85311	0.146	2.776	LEW85311	0.114	3.133
LEW85311	0.232	2.108	LEW85311	0.130	2.943
LEW85311	0.291	1.781	LEW85311	0.226	2.146
LEW85311	0.318	1.653	LEW85311	0.287	1.801
LEW85311	0.213	2.231	LEW85311	0.200	2.322
LEW85311	0.131	2.932	LEW85311	0.101	3.308
LEW85311	0.128	2.966	LEW85311	0.096	3.381
LEW85311	0.152	2.718	LEW85311	0.109	3.198

Table continued

R₁			R₃		
Sample	**R_1 (mm)**	**R_1 (phi)**	**Sample**	**R_3 (mm)**	**R_3 (phi)**
LEW85311	0.190	2.396	LEW85311	0.140	2.837
LEW85311	0.173	2.531	LEW85311	0.152	2.718
LEW85311	0.324	1.626	LEW85311	0.208	2.265
LEW85311	0.132	2.921	LEW85311	0.104	3.265
LEW85311	0.221	2.178	LEW85311	0.174	2.523
LEW85311	0.076	3.718	LEW85311	0.061	4.035
LEW85311	0.081	3.626	LEW85311	0.066	3.921
LEW85311	0.097	3.366	LEW85311	0.072	3.796
LEW85311	0.265	1.916	LEW85311	0.097	3.366
LEW85311	0.096	3.381	LEW85311	0.077	3.699
LEW85311	0.150	2.737	LEW85311	0.101	3.308
LEW85311	0.166	2.591	LEW85311	0.129	2.955
LEW85311	0.231	2.114	LEW85311	0.219	2.191
LEW85311	0.256	1.966	LEW85311	0.220	2.184
LEW85311	0.170	2.556	LEW85311	0.169	2.565
LEW85311	0.247	2.017	LEW85311	0.219	2.191
LEW85311	0.094	3.411	LEW85311	0.076	3.718
LEW85311	0.086	3.540	LEW85311	0.079	3.662
LEW85311	0.299	1.742	LEW85311	0.160	2.644
LEW85311	0.104	3.265	LEW85311	0.087	3.523
LEW85311	0.523	0.935	LEW85311	0.393	1.347
LEW85311	0.184	2.442	LEW85311	0.135	2.889
LEW85311	0.359	1.478	LEW85311	0.225	2.152
LEW85311	0.157	2.671	LEW85311	0.073	3.776
LEW85311	0.131	2.932	LEW85311	0.093	3.427
LEW85311	0.341	1.552	LEW85311	0.307	1.704
LEW85311	0.078	3.680	LEW85311	0.060	4.059
LEW85311	0.096	3.381	LEW85311	0.081	3.626
LEW85311	0.065	3.943	LEW85311	0.055	4.184
LEW85311	0.248	2.012	LEW85311	0.225	2.152
LEW85311	0.149	2.747	LEW85311	0.112	3.158
LEW85311	0.122	3.035	LEW85311	0.095	3.396
LEW85311	0.156	2.680	LEW85311	0.146	2.776
LEW85311	0.308	1.699	LEW85311	0.266	1.911
LEW85311	0.079	3.662	LEW85311	0.060	4.059
LEW85311	0.141	2.826	LEW85311	0.099	3.336
LEW85311	0.257	1.960	LEW85311	0.241	2.053
LEW85311	0.152	2.718	LEW85311	0.127	2.977
LEW85311	0.063	3.989	LEW85311	0.058	4.108
LEW85311	0.132	2.921	LEW85311	0.085	3.556
LEW85311	0.211	2.245	LEW85311	0.171	2.548
LEW85311	0.141	2.826	LEW85311	0.104	3.265
LEW85311	0.131	2.932	LEW85311	0.099	3.336
LEW85311	0.237	2.077	LEW85311	0.178	2.490
LEW85311	0.269	1.894	LEW85311	0.263	1.927
LEW85311	0.167	2.582	LEW85311	0.121	3.047
LEW85311	0.084	3.573	LEW85311	0.075	3.737
LEW85311	0.351	1.510	LEW85311	0.308	1.699
LEW85311	0.085	3.556	LEW85311	0.065	3.943
LEW85311	0.125	3.000	LEW85311	0.116	3.108
LEW85311	0.079	3.662	LEW85311	0.076	3.718
LEW85311	0.188	2.411	LEW85311	0.158	2.662
LEW85311	0.082	3.608	LEW85311	0.072	3.796
Kolang	0.710	0.494	Kolang	0.332	1.591
Kolang	0.344	1.540	Kolang	0.253	1.983
Kolang	0.604	0.727	Kolang	0.396	1.336
Kolang	0.229	2.127	Kolang	0.18	2.474
Kolang	0.176	2.506	Kolang	0.151	2.727
Kolang	0.332	1.591	Kolang	0.257	1.960
Kolang	0.528	0.921	Kolang	0.321	1.639
Kolang	0.285	1.811	Kolang	0.236	2.083
Kolang	0.560	0.837	Kolang	0.404	1.308
Kolang	0.255	1.971	Kolang	0.228	2.133
Kolang	0.679	0.559	Kolang	0.27	1.889
Kolang	0.205	2.286	Kolang	0.192	2.381
Kolang	0.275	1.862	Kolang	0.226	2.146
Kolang	0.319	1.648	Kolang	0.178	2.490
Kolang	0.283	1.821	Kolang	0.136	2.878
Kolang	0.258	1.955	Kolang	0.21	2.252
Kolang	1.379	-0.464	Kolang	0.48	1.059

Table continued

R1			R3		
Sample	R_1 (mm)	R_1 (phi)	Sample	R_3 (mm)	R_3 (phi)
Kolang	0.178	2.490	Kolang	0.146	2.776
Kolang	0.163	2.617	Kolang	0.116	3.108
Kolang	0.229	2.127	Kolang	0.211	2.245
Kolang	0.323	1.630	Kolang	0.22	2.184
Kolang	0.158	2.662	Kolang	0.127	2.977
Kolang	0.241	2.053	Kolang	0.142	2.816
Kolang	0.304	1.718	Kolang	0.165	2.599
Kolang	0.223	2.165	Kolang	0.194	2.366
Kolang	0.233	2.102	Kolang	0.175	2.515
Kolang	0.212	2.238	Kolang	0.134	2.900
Kolang	0.250	2.000	Kolang	0.206	2.279
Kolang	0.284	1.816	Kolang	0.208	2.265
Kolang	0.359	1.478	Kolang	0.24	2.059
Kolang	0.108	3.211	Kolang	0.083	3.591
Kolang	0.759	0.398	Kolang	0.423	1.241
Kolang	0.254	1.977	Kolang	0.213	2.231
Kolang	0.122	3.035	Kolang	0.101	3.308
Kolang	0.302	1.727	Kolang	0.251	1.994
Kolang	0.351	1.510	Kolang	0.299	1.742
Kolang	0.490	1.029	Kolang	0.28	1.837
Kolang	0.396	1.336	Kolang	0.255	1.971
Kolang	0.449	1.155	Kolang	0.296	1.756
Kolang	0.132	2.921	Kolang	0.109	3.198
Kolang	0.253	1.983	Kolang	0.184	2.442
Kolang	0.451	1.149	Kolang	0.22	2.184
Kolang	0.400	1.322	Kolang	0.138	2.857
Kolang	0.266	1.911	Kolang	0.156	2.680
Kolang	0.560	0.837	Kolang	0.414	1.272
Kolang	0.147	2.766	Kolang	0.131	2.932
Kolang	0.391	1.355	Kolang	0.265	1.916
Kolang	0.329	1.604	Kolang	0.218	2.198
Kolang	0.590	0.761	Kolang	0.38	1.396
Kolang	0.344	1.540	Kolang	0.243	2.041
Kolang	0.134	2.900	Kolang	0.116	3.108
Kolang	0.240	2.059	Kolang	0.204	2.293
Kolang	0.263	1.927	Kolang	0.218	2.198
Kolang	0.390	1.358	Kolang	0.271	1.884
Kolang	0.385	1.377	Kolang	0.248	2.012
Kolang	0.551	0.860	Kolang	0.506	0.983
Kolang	0.407	1.297	Kolang	0.395	1.340
Kolang	0.238	2.071	Kolang	0.204	2.293
Kolang	0.198	2.336	Kolang	0.161	2.635
Kolang	0.563	0.829	Kolang	0.434	1.204
Kolang	0.193	2.373	Kolang	0.142	2.816
Kolang	0.250	2.000	Kolang	0.2	2.322
Kolang	0.318	1.653	Kolang	0.22	2.184
Kolang	0.283	1.821	Kolang	0.17	2.556
Kolang	0.218	2.198	Kolang	0.164	2.608
Kolang	0.392	1.351	Kolang	0.304	1.718
Kolang	0.294	1.766	Kolang	0.263	1.927
Kolang	0.335	1.578	Kolang	0.296	1.756
Kolang	0.163	2.617	Kolang	0.123	3.023
Kolang	0.385	1.377	Kolang	0.258	1.955
Kolang	0.233	2.102	Kolang	0.162	2.626
Kolang	0.368	1.442	Kolang	0.331	1.595
Kolang	0.281	1.831	Kolang	0.218	2.198
Kolang	0.620	0.690	Kolang	0.574	0.801
Kolang	0.380	1.396	Kolang	0.308	1.699
Kolang	0.312	1.680	Kolang	0.118	3.083
Kolang	0.119	3.071	Kolang	0.102	3.293
Kolang	0.417	1.262	Kolang	0.241	2.053
Kolang	0.336	1.573	Kolang	0.223	2.165
Kolang	0.213	2.231	Kolang	0.185	2.434
LAP02239	0.141	2.826	LAP02239	0.093	3.427
LAP02239	0.185	2.434	LAP02239	0.084	3.573
LAP02239	0.132	2.921	LAP02239	0.100	3.322
LAP02239	0.533	0.908	LAP02239	0.365	1.454
LAP02239	0.467	1.099	LAP02239	0.211	2.245
LAP02239	0.103	3.279	LAP02239	0.089	3.490
LAP02239	0.117	3.095	LAP02239	0.112	3.158

Table continued

	R1			R3	
Sample	R_1 (mm)	R_1 (phi)	Sample	R_3 (mm)	R_3 (phi)
LAP02239	0.212	2.238	LAP02239	0.113	3.146
LAP02239	0.322	1.635	LAP02239	0.267	1.905
LAP02239	0.328	1.608	LAP02239	0.194	2.366
LAP02239	0.119	3.071	LAP02239	0.078	3.680
LAP02239	0.258	1.955	LAP02239	0.142	2.816
LAP02239	0.105	3.252	LAP02239	0.095	3.396
LAP02239	0.230	2.120	LAP02239	0.170	2.556
LAP02239	0.078	3.680	LAP02239	0.064	3.966
LAP02239	0.383	1.385	LAP02239	0.303	1.723
LAP02239	0.137	2.868	LAP02239	0.115	3.120
LAP02239	0.155	2.690	LAP02239	0.069	3.857
LAP02239	0.117	3.095	LAP02239	0.110	3.184
LAP02239	0.347	1.527	LAP02239	0.287	1.801
LAP02239	0.177	2.498	LAP02239	0.128	2.966
LAP02239	0.206	2.279	LAP02239	0.159	2.653
LAP02239	0.263	1.927	LAP02239	0.125	3.000
LAP02239	0.201	2.315	LAP02239	0.114	3.133
LAP02239	1.145	-0.195	LAP02239	0.900	0.152
LAP02239	0.150	2.737	LAP02239	0.125	3.000
LAP02239	1.038	-0.054	LAP02239	0.555	0.849
LAP02239	0.222	2.171	LAP02239	0.198	2.336
LAP02239	0.130	2.943	LAP02239	0.079	3.662
LAP02239	0.157	2.671	LAP02239	0.104	3.265
LAP02239	0.296	1.756	LAP02239	0.171	2.548
LAP02239	0.198	2.336	LAP02239	0.131	2.932
LAP02239	0.099	3.336	LAP02239	0.091	3.458
LAP02239	0.290	1.786	LAP02239	0.170	2.556
LAP02239	0.805	0.313	LAP02239	0.557	0.844
LAP02239	0.145	2.786	LAP02239	0.118	3.083
LAP02239	0.308	1.699	LAP02239	0.259	1.949
LAP02239	0.163	2.617	LAP02239	0.136	2.878
LAP02239	0.152	2.718	LAP02239	0.133	2.911
LAP02239	0.366	1.450	LAP02239	0.314	1.671
LAP02239	0.136	2.878	LAP02239	0.075	3.737
LAP02239	0.161	2.635	LAP02239	0.097	3.366
LAP02239	0.170	2.556	LAP02239	0.151	2.727
LAP02239	0.072	3.796	LAP02239	0.051	4.293
LAP02239	0.278	1.847	LAP02239	0.227	2.139
LAP02239	0.198	2.336	LAP02239	0.185	2.434
LAP02239	0.130	2.943	LAP02239	0.074	3.756
LAP02239	0.259	1.949	LAP02239	0.222	2.171
LAP02239	0.123	3.023	LAP02239	0.090	3.474
LAP02239	0.196	2.351	LAP02239	0.086	3.540
LAP02239	0.314	1.671	LAP02239	0.263	1.927
LAP02239	0.168	2.573	LAP02239	0.145	2.786
LAP02239	0.136	2.878	LAP02239	0.098	3.351
LAP02239	0.353	1.502	LAP02239	0.263	1.927
LAP02239	0.121	3.047	LAP02239	0.110	3.184
LAP02239	0.113	3.146	LAP02239	0.074	3.756
LAP02239	0.222	2.171	LAP02239	0.173	2.531
LAP02239	0.250	2.000	LAP02239	0.217	2.204
LAP02239	0.102	3.293	LAP02239	0.070	3.837
LAP02239	0.145	2.786	LAP02239	0.137	2.868
LAP02239	0.223	2.165	LAP02239	0.128	2.966
LAP02239	0.288	1.796	LAP02239	0.252	1.989
LAP02239	0.490	1.029	LAP02239	0.348	1.523
LAP02239	0.225	2.152	LAP02239	0.212	2.238
LAP02239	0.106	3.238	LAP02239	0.084	3.573
LAP02239	0.141	2.826	LAP02239	0.136	2.878
LAP02239	0.244	2.035	LAP02239	0.205	2.286
LAP02239	0.150	2.737	LAP02239	0.110	3.184
LAP02239	0.210	2.252	LAP02239	0.198	2.336
LAP02239	0.794	0.333	LAP02239	0.596	0.747
LAP02239	0.221	2.178	LAP02239	0.129	2.955
LAP02239	0.522	0.938	LAP02239	0.385	1.377
LAP02239	0.297	1.751	LAP02239	0.163	2.617
LAP02239	0.788	0.344	LAP02239	0.485	1.044
LAP02239	0.254	1.977	LAP02239	0.102	3.293
LAP02239	0.370	1.434	LAP02239	0.166	2.591
LAP02239	0.206	2.279	LAP02239	0.147	2.766

Table continued

R1			R3		
Sample	R_1 (mm)	R_1 (phi)	Sample	R_3 (mm)	R_3 (phi)
LAP02239	0.297	1.751	LAP02239	0.240	2.059
LAP02239	0.087	3.523	LAP02239	0.063	3.989
LAP02239	0.125	3.000	LAP02239	0.098	3.351
LAP02239	0.382	1.388	LAP02239	0.351	1.510
LAP02239	0.273	1.873	LAP02239	0.248	2.012
LAP02239	0.254	1.977	LAP02239	0.121	3.047
LAP02239	0.199	2.329	LAP02239	0.155	2.690
LAP02239	0.245	2.029	LAP02239	0.126	2.989
LAP02239	0.293	1.771	LAP02239	0.211	2.245
LAP02239	0.385	1.377	LAP02239	0.338	1.565
LAP02239	0.360	1.474	LAP02239	0.312	1.680
LAP02239	0.203	2.300	LAP02239	0.155	2.690
LAP02239	0.668	0.582	LAP02239	0.337	1.569
LAP02239	0.230	2.120	LAP02239	0.225	2.152
LAP02239	0.264	1.921	LAP02239	0.211	2.245
LAP02239	0.201	2.315	LAP02239	0.141	2.826
LAP02239	0.336	1.573	LAP02239	0.294	1.766
LAP02239	0.357	1.486	LAP02239	0.286	1.806
LAP02239	0.199	2.329	LAP02239	0.119	3.071
LAP02239	0.196	2.351	LAP02239	0.163	2.617
LAP02239	0.299	1.742	LAP02239	0.154	2.699
LAP02239	0.238	2.071	LAP02239	0.159	2.653
LAP02239	0.167	2.582	LAP02239	0.113	3.146
LAP02239	0.174	2.523	LAP02239	0.152	2.718
LAP02239	0.123	3.023	LAP02239	0.081	3.626
LAP02239	0.721	0.472	LAP02239	0.245	2.029
LAP02239	0.183	2.450	LAP02239	0.139	2.847
LAP02239	0.360	1.474	LAP02239	0.248	2.012
LAP02239	0.550	0.862	LAP02239	0.367	1.446
LAP02239	0.073	3.776	LAP02239	0.065	3.943
LAP02239	0.335	1.578	LAP02239	0.244	2.035
LAP02239	0.347	1.527	LAP02239	0.243	2.041
LAP02239	0.691	0.533	LAP02239	0.308	1.699
LAP02239	0.151	2.727	LAP02239	0.087	3.523
LAP02239	0.254	1.977	LAP02239	0.250	2.000
LAP02239	0.204	2.293	LAP02239	0.179	2.482
LAP02239	0.151	2.727	LAP02239	0.105	3.252
LAP02239	0.323	1.630	LAP02239	0.221	2.178
LAP02239	0.485	1.044	LAP02239	0.306	1.708
LAP02239	0.626	0.676	LAP02239	0.398	1.329
LAP02239	0.304	1.718	LAP02239	0.215	2.218
LAP02239	0.217	2.204	LAP02239	0.198	2.336
LAP02239	0.265	1.916	LAP02239	0.145	2.786
LAP02239	0.250	2.000	LAP02239	0.159	2.653
LAP02239	0.207	2.272	LAP02239	0.197	2.344
LAP02239	0.094	3.411	LAP02239	0.083	3.591
LAP02239	0.415	1.269	LAP02239	0.309	1.694
LAP02239	0.207	2.272	LAP02239	0.197	2.344
LAP02239	0.293	1.771	LAP02239	0.158	2.662
LAP02239	0.915	0.128	LAP02239	0.581	0.783
LAP02239	0.283	1.821	LAP02239	0.262	1.932
LAP02239	0.185	2.434	LAP02239	0.122	3.035
LAP02239	0.279	1.842	LAP02239	0.193	2.373
LAP02239	0.143	2.806	LAP02239	0.107	3.224
LAP02239	0.265	1.916	LAP02239	0.164	2.608
LAP02239	0.227	2.139	LAP02239	0.173	2.531
LAP02239	0.218	2.198	LAP02239	0.095	3.396
LAP02239	0.103	3.279	LAP02239	0.097	3.366
LAP02239	0.180	2.474	LAP02239	0.164	2.608
LAP02239	0.284	1.816	LAP02239	0.257	1.960
LAP02239	0.171	2.548	LAP02239	0.123	3.023
LAP02239	0.282	1.826	LAP02239	0.206	2.279
LAP02239	0.324	1.626	LAP02239	0.181	2.466
LAP02239	0.226	2.146	LAP02239	0.152	2.718
LAP02239	0.513	0.963	LAP02239	0.421	1.248
LAP02239	0.259	1.949	LAP02239	0.168	2.573
LAP02239	0.293	1.771	LAP02239	0.213	2.231
LAP02239	0.203	2.300	LAP02239	0.164	2.608
LAP02239	0.147	2.766	LAP02239	0.129	2.955
LAP02239	0.587	0.769	LAP02239	0.257	1.960

Table continued

R1			R3		
Sample	**R_1 (mm)**	**R_1 (phi)**	**Sample**	**R_3 (mm)**	**R_3 (phi)**
LAP02239	0.107	3.224	LAP02239	0.074	3.756
LAP02239	0.339	1.561	LAP02239	0.286	1.806
LAP02239	0.247	2.017	LAP02239	0.192	2.381
Shidian	0.309	1.694	Shidian	0.16	2.644
Shidian	0.310	1.690	Shidian	0.258	1.955
Shidian	0.609	0.715	Shidian	0.411	1.283
Shidian	0.406	1.300	Shidian	0.212	2.238
Shidian	0.207	2.272	Shidian	0.144	2.796
Shidian	0.345	1.535	Shidian	0.167	2.582
Shidian	0.412	1.279	Shidian	0.285	1.811
Shidian	0.119	3.071	Shidian	0.102	3.293
Shidian	0.326	1.617	Shidian	0.231	2.114
Shidian	0.378	1.404	Shidian	0.199	2.329
Shidian	0.211	2.245	Shidian	0.125	3.000
Shidian	0.210	2.252	Shidian	0.129	2.955
Shidian	0.391	1.355	Shidian	0.299	1.742
Shidian	0.418	1.258	Shidian	0.371	1.431
Shidian	0.263	1.927	Shidian	0.233	2.102
Shidian	0.378	1.404	Shidian	0.266	1.911
Shidian	0.338	1.565	Shidian	0.23	2.120
Shidian	0.318	1.653	Shidian	0.166	2.591
Shidian	0.168	2.573	Shidian	0.147	2.766
Shidian	0.223	2.165	Shidian	0.162	2.626
Shidian	0.342	1.548	Shidian	0.231	2.114
Shidian	0.558	0.842	Shidian	0.386	1.373
Shidian	0.259	1.949	Shidian	0.194	2.366
Shidian	0.294	1.766	Shidian	0.189	2.404
Shidian	0.386	1.373	Shidian	0.311	1.685
Shidian	0.224	2.158	Shidian	0.176	2.506
Shidian	0.513	0.963	Shidian	0.407	1.297
Shidian	0.469	1.092	Shidian	0.407	1.297
Shidian	0.180	2.474	Shidian	0.108	3.211
Shidian	0.110	3.184	Shidian	0.092	3.442
Shidian	0.087	3.523	Shidian	0.078	3.680
Shidian	0.250	2.000	Shidian	0.188	2.411
Shidian	0.383	1.385	Shidian	0.237	2.077
Shidian	0.319	1.648	Shidian	0.172	2.540
Shidian	0.207	2.272	Shidian	0.158	2.662
Shidian	0.336	1.573	Shidian	0.318	1.653
Shidian	0.622	0.685	Shidian	0.388	1.366
Shidian	0.225	2.152	Shidian	0.197	2.344
Shidian	0.195	2.358	Shidian	0.139	2.847
Shidian	0.404	1.308	Shidian	0.27	1.889
Shidian	0.245	2.029	Shidian	0.212	2.238
Shidian	0.243	2.041	Shidian	0.204	2.293
Shidian	0.731	0.452	Shidian	0.251	1.994
Shidian	0.387	1.370	Shidian	0.253	1.983
Shidian	0.225	2.152	Shidian	0.183	2.450
Shidian	0.248	2.012	Shidian	0.129	2.955
Shidian	0.104	3.265	Shidian	0.09	3.474
Shidian	0.323	1.630	Shidian	0.267	1.905
Shidian	0.377	1.407	Shidian	0.185	2.434
Shidian	0.179	2.482	Shidian	0.152	2.718
Shidian	0.262	1.932	Shidian	0.176	2.506
Shidian	0.447	1.162	Shidian	0.391	1.355
Shidian	0.307	1.704	Shidian	0.143	2.806
Shidian	0.225	2.152	Shidian	0.209	2.258
Shidian	0.461	1.117	Shidian	0.381	1.392
Shidian	0.639	0.646	Shidian	0.486	1.041
Shidian	0.285	1.811	Shidian	0.223	2.165
Shidian	0.788	0.344	Shidian	0.591	0.759
Shidian	0.440	1.184	Shidian	0.279	1.842
Shidian	0.352	1.506	Shidian	0.215	2.218
Shidian	0.387	1.370	Shidian	0.225	2.152
Shidian	0.615	0.701	Shidian	0.491	1.026
Shidian	0.266	1.911	Shidian	0.127	2.977
Shidian	0.186	2.427	Shidian	0.145	2.786
Shidian	0.619	0.692	Shidian	0.407	1.297
Shidian	0.120	3.059	Shidian	0.101	3.308
Shidian	0.179	2.482	Shidian	0.146	2.776

Table continued

R₁			R₃		
Sample	**R_1 (mm)**	**R_1 (phi)**	**Sample**	**R_3 (mm)**	**R_3 (phi)**
Shidian	0.405	1.304	Shidian	0.365	1.454
Shidian	0.215	2.218	Shidian	0.175	2.515
Shidian	0.534	0.905	Shidian	0.486	1.041
Shidian	0.176	2.506	Shidian	0.123	3.023
Shidian	0.206	2.279	Shidian	0.127	2.977
Shidian	0.298	1.747	Shidian	0.247	2.017
Shidian	0.417	1.262	Shidian	0.216	2.211
Shidian	0.464	1.108	Shidian	0.338	1.565
Shidian	0.308	1.699	Shidian	0.216	2.211
Shidian	0.380	1.396	Shidian	0.169	2.565
Shidian	0.156	2.680	Shidian	0.121	3.047
Shidian	0.215	2.218	Shidian	0.128	2.966
Shidian	0.135	2.889	Shidian	0.095	3.396
Shidian	0.800	0.322	Shidian	0.455	1.136
Shidian	0.697	0.521	Shidian	0.45	1.152
Shidian	0.385	1.377	Shidian	0.211	2.245
Shidian	0.306	1.708	Shidian	0.205	2.286
Shidian	0.145	2.786	Shidian	0.122	3.035
Shidian	0.190	2.396	Shidian	0.153	2.708
Shidian	0.449	1.155	Shidian	0.289	1.791
Shidian	0.276	1.857	Shidian	0.174	2.523
Shidian	0.150	2.737	Shidian	0.094	3.411
Shidian	0.163	2.617	Shidian	0.147	2.766
Mighei	0.312	1.680	Mighei	0.233	2.102
Mighei	0.328	1.608	Mighei	0.133	2.911
Mighei	0.163	2.617	Mighei	0.139	2.847
Mighei	0.186	2.427	Mighei	0.129	2.955
Mighei	0.246	2.023	Mighei	0.220	2.184
Mighei	0.230	2.120	Mighei	0.183	2.450
Mighei	0.701	0.513	Mighei	0.505	0.986
Mighei	0.567	0.819	Mighei	0.525	0.930
Mighei	0.264	1.921	Mighei	0.198	2.336
Mighei	0.472	1.083	Mighei	0.432	1.211
Mighei	0.222	2.171	Mighei	0.132	2.921
Mighei	0.336	1.573	Mighei	0.268	1.900
Mighei	0.311	1.685	Mighei	0.201	2.315
Mighei	0.245	2.029	Mighei	0.206	2.279
Mighei	0.646	0.630	Mighei	0.542	0.884
Mighei	0.386	1.373	Mighei	0.339	1.561
Mighei	0.285	1.811	Mighei	0.236	2.083
Mighei	0.173	2.531	Mighei	0.135	2.889
Mighei	0.185	2.434	Mighei	0.168	2.573
Mighei	0.747	0.421	Mighei	0.486	1.041
Mighei	0.078	3.680	Mighei	0.074	3.756
Mighei	0.363	1.462	Mighei	0.315	1.667
Mighei	0.560	0.837	Mighei	0.370	1.434
Mighei	0.259	1.949	Mighei	0.235	2.089
Mighei	0.449	1.155	Mighei	0.304	1.718
Mighei	0.482	1.053	Mighei	0.373	1.423
Mighei	0.547	0.870	Mighei	0.289	1.791
Mighei	0.456	1.133	Mighei	0.312	1.680
Mighei	0.279	1.842	Mighei	0.246	2.023
Mighei	0.318	1.653	Mighei	0.255	1.971
Winchcombe	0.256	1.966	Winchcombe	0.202	2.308
Winchcombe	0.102	3.293	Winchcombe	0.08	3.644
Winchcombe	0.144	2.796	Winchcombe	0.114	3.133
Winchcombe	0.287	1.801	Winchcombe	0.24	2.059
Winchcombe	0.218	2.198	Winchcombe	0.136	2.878
Winchcombe	0.181	2.466	Winchcombe	0.128	2.966
Winchcombe	0.088	3.506	Winchcombe	0.054	4.211
Winchcombe	0.056	4.158	Winchcombe	0.052	4.265
Winchcombe	0.137	2.868	Winchcombe	0.101	3.308
Winchcombe	0.072	3.796	Winchcombe	0.066	3.921
Winchcombe	0.154	2.699	Winchcombe	0.078	3.680
Winchcombe	0.136	2.878	Winchcombe	0.093	3.427
Winchcombe	0.076	3.718	Winchcombe	0.064	3.966
Winchcombe	0.262	1.932	Winchcombe	0.226	2.146
Winchcombe	0.074	3.756	Winchcombe	0.054	4.211
Winchcombe	0.166	2.591	Winchcombe	0.087	3.523
Winchcombe	0.155	2.690	Winchcombe	0.105	3.252

Table continued

	R1			R3	
Sample	**R_1 (mm)**	**R_1 (phi)**	**Sample**	**R_3 (mm)**	**R_3 (phi)**
Winchcombe	0.081	3.626	Winchcombe	0.068	3.878
Winchcombe	0.17	2.556	Winchcombe	0.142	2.816
Winchcombe	0.274	1.868	Winchcombe	0.264	1.921
Winchcombe	0.265	1.916	Winchcombe	0.184	2.442
Winchcombe	0.369	1.438	Winchcombe	0.234	2.095
Winchcombe	0.152	2.718	Winchcombe	0.096	3.381
Winchcombe	0.15	2.737	Winchcombe	0.079	3.662
Winchcombe	0.212	2.238	Winchcombe	0.105	3.252
Winchcombe	0.101	3.308	Winchcombe	0.065	3.943
Winchcombe	0.07	3.837	Winchcombe	0.059	4.083
Winchcombe	0.094	3.411	Winchcombe	0.069	3.857
Winchcombe	0.146	2.776	Winchcombe	0.088	3.506
Winchcombe	0.053	4.238	Winchcombe	0.041	4.608
Winchcombe	0.157	2.671	Winchcombe	0.106	3.238
Winchcombe	0.362	1.466	Winchcombe	0.172	2.540
Winchcombe	0.194	2.366	Winchcombe	0.162	2.626
Winchcombe	0.233	2.102	Winchcombe	0.121	3.047
Winchcombe	0.196	2.351	Winchcombe	0.109	3.198
Winchcombe	0.167	2.582	Winchcombe	0.136	2.878
Winchcombe	0.184	2.442	Winchcombe	0.173	2.531
Winchcombe	0.126	2.989	Winchcombe	0.076	3.718

8.1.2 RAW 3D Chondrule Size Data

Table 8.2. *Table showing RAW 3D chondrule size data for long (R1) and short (R3) axes.*

	R1			R3	
Sample	**R_1 (mm)**	**R_1 (phi)**	**Sample**	**R_3 (mm)**	**R_3 (phi)**
Aguas Zarcas	0.928	0.107	Aguas Zarcas	0.536	0.900
Aguas Zarcas	1.098	-0.135	Aguas Zarcas	0.810	0.304
Aguas Zarcas	0.738	0.437	Aguas Zarcas	0.544	0.878
Aguas Zarcas	0.309	1.692	Aguas Zarcas	0.172	2.536
Aguas Zarcas	0.256	1.967	Aguas Zarcas	0.179	2.480
Aguas Zarcas	0.313	1.675	Aguas Zarcas	0.192	2.377
Aguas Zarcas	0.461	1.117	Aguas Zarcas	0.279	1.843
Aguas Zarcas	0.433	1.208	Aguas Zarcas	0.222	2.174
Aguas Zarcas	0.321	1.639	Aguas Zarcas	0.180	2.477
Aguas Zarcas	0.341	1.551	Aguas Zarcas	0.260	1.944
Aguas Zarcas	0.660	0.600	Aguas Zarcas	0.377	1.407
Aguas Zarcas	0.328	1.606	Aguas Zarcas	0.224	2.157
Aguas Zarcas	0.504	0.988	Aguas Zarcas	0.390	1.359
Aguas Zarcas	0.240	2.057	Aguas Zarcas	0.159	2.653
Aguas Zarcas	0.218	2.198	Aguas Zarcas	0.156	2.680
Aguas Zarcas	0.419	1.255	Aguas Zarcas	0.168	2.576
Aguas Zarcas	0.171	2.552	Aguas Zarcas	0.117	3.097
Aguas Zarcas	0.237	2.076	Aguas Zarcas	0.156	2.681
Aguas Zarcas	0.209	2.257	Aguas Zarcas	0.138	2.860
Aguas Zarcas	0.374	1.418	Aguas Zarcas	0.256	1.967
Aguas Zarcas	0.817	0.292	Aguas Zarcas	0.401	1.317
Aguas Zarcas	0.528	0.920	Aguas Zarcas	0.364	1.460
Aguas Zarcas	0.412	1.280	Aguas Zarcas	0.230	2.121
Aguas Zarcas	0.408	1.295	Aguas Zarcas	0.298	1.748
Aguas Zarcas	0.580	0.786	Aguas Zarcas	0.284	1.815
Aguas Zarcas	0.331	1.595	Aguas Zarcas	0.147	2.771
Aguas Zarcas	0.188	2.408	Aguas Zarcas	0.106	3.244
Aguas Zarcas	0.560	0.837	Aguas Zarcas	0.416	1.267
Aguas Zarcas	0.351	1.510	Aguas Zarcas	0.223	2.164
Aguas Zarcas	0.589	0.763	Aguas Zarcas	0.374	1.420
Aguas Zarcas	0.313	1.676	Aguas Zarcas	0.204	2.296
Aguas Zarcas	0.474	1.077	Aguas Zarcas	0.197	2.346
Aguas Zarcas	0.371	1.432	Aguas Zarcas	0.223	2.162
Aguas Zarcas	0.235	2.092	Aguas Zarcas	0.182	2.462
Aguas Zarcas	0.264	1.924	Aguas Zarcas	0.150	2.738

Table continued

R$_1$			R$_3$		
Sample	**R$_1$ (mm)**	**R$_1$ (phi)**	**Sample**	**R$_3$ (mm)**	**R$_3$ (phi)**
Aguas Zarcas	0.455	1.138	Aguas Zarcas	0.222	2.174
Aguas Zarcas	0.930	0.105	Aguas Zarcas	0.485	1.043
Aguas Zarcas	0.204	2.291	Aguas Zarcas	0.154	2.702
Aguas Zarcas	0.397	1.334	Aguas Zarcas	0.201	2.313
Aguas Zarcas	0.270	1.889	Aguas Zarcas	0.228	2.132
Aguas Zarcas	0.815	0.296	Aguas Zarcas	0.425	1.236
Aguas Zarcas	0.400	1.323	Aguas Zarcas	0.269	1.895
Aguas Zarcas	0.386	1.372	Aguas Zarcas	0.213	2.230
Aguas Zarcas	0.789	0.343	Aguas Zarcas	0.345	1.534
Aguas Zarcas	0.288	1.797	Aguas Zarcas	0.184	2.445
Aguas Zarcas	0.342	1.548	Aguas Zarcas	0.235	2.086
Aguas Zarcas	0.566	0.822	Aguas Zarcas	0.282	1.827
Aguas Zarcas	0.157	2.675	Aguas Zarcas	0.106	3.233
Aguas Zarcas	0.474	1.078	Aguas Zarcas	0.319	1.646
Aguas Zarcas	0.504	0.988	Aguas Zarcas	0.215	2.216
Aguas Zarcas	0.347	1.525	Aguas Zarcas	0.192	2.381
Aguas Zarcas	0.831	0.267	Aguas Zarcas	0.555	0.848
Aguas Zarcas	0.399	1.327	Aguas Zarcas	0.178	2.491
Aguas Zarcas	0.223	2.167	Aguas Zarcas	0.137	2.870
Aguas Zarcas	1.027	-0.038	Aguas Zarcas	0.470	1.089
Aguas Zarcas	0.336	1.572	Aguas Zarcas	0.205	2.288
Aguas Zarcas	0.355	1.496	Aguas Zarcas	0.175	2.517
Aguas Zarcas	0.658	0.605	Aguas Zarcas	0.173	2.534
Aguas Zarcas	0.233	2.100	Aguas Zarcas	0.164	2.604
Aguas Zarcas	0.394	1.342	Aguas Zarcas	0.201	2.318
Aguas Zarcas	0.471	1.085	Aguas Zarcas	0.251	1.996
Aguas Zarcas	0.318	1.651	Aguas Zarcas	0.172	2.540
Aguas Zarcas	0.281	1.832	Aguas Zarcas	0.140	2.839
Aguas Zarcas	0.352	1.507	Aguas Zarcas	0.152	2.716
Aguas Zarcas	0.239	2.063	Aguas Zarcas	0.173	2.535
Aguas Zarcas	0.459	1.125	Aguas Zarcas	0.252	1.990
Aguas Zarcas	0.180	2.471	Aguas Zarcas	0.129	2.952
Aguas Zarcas	0.435	1.200	Aguas Zarcas	0.226	2.146
Aguas Zarcas	0.298	1.746	Aguas Zarcas	0.199	2.331
Aguas Zarcas	0.258	1.955	Aguas Zarcas	0.151	2.727
Aguas Zarcas	0.281	1.831	Aguas Zarcas	0.168	2.571
Aguas Zarcas	0.285	1.813	Aguas Zarcas	0.141	2.822
Aguas Zarcas	0.221	2.177	Aguas Zarcas	0.133	2.915
Aguas Zarcas	0.711	0.492	Aguas Zarcas	0.438	1.191
Aguas Zarcas	0.558	0.843	Aguas Zarcas	0.374	1.419
Aguas Zarcas	0.387	1.371	Aguas Zarcas	0.282	1.825
Aguas Zarcas	0.709	0.496	Aguas Zarcas	0.342	1.548
Aguas Zarcas	0.524	0.932	Aguas Zarcas	0.201	2.315
Aguas Zarcas	0.492	1.024	Aguas Zarcas	0.281	1.831
Aguas Zarcas	0.438	1.191	Aguas Zarcas	0.271	1.884
Aguas Zarcas	0.324	1.627	Aguas Zarcas	0.219	2.194
Aguas Zarcas	0.213	2.234	Aguas Zarcas	0.148	2.753
Aguas Zarcas	0.421	1.247	Aguas Zarcas	0.221	2.176
Aguas Zarcas	0.599	0.738	Aguas Zarcas	0.257	1.961
Aguas Zarcas	0.249	2.006	Aguas Zarcas	0.155	2.686
Aguas Zarcas	0.260	1.944	Aguas Zarcas	0.169	2.564
Aguas Zarcas	0.421	1.247	Aguas Zarcas	0.239	2.068
Aguas Zarcas	0.364	1.458	Aguas Zarcas	0.175	2.517
Aguas Zarcas	0.190	2.397	Aguas Zarcas	0.161	2.639
Aguas Zarcas	0.294	1.765	Aguas Zarcas	0.217	2.206
Aguas Zarcas	0.286	1.805	Aguas Zarcas	0.200	2.323
Aguas Zarcas	0.356	1.489	Aguas Zarcas	0.204	2.295
Aguas Zarcas	0.294	1.764	Aguas Zarcas	0.196	2.353
Aguas Zarcas	0.312	1.682	Aguas Zarcas	0.201	2.313
Aguas Zarcas	0.334	1.583	Aguas Zarcas	0.279	1.840
Aguas Zarcas	0.469	1.093	Aguas Zarcas	0.252	1.986
Aguas Zarcas	0.329	1.604	Aguas Zarcas	0.270	1.891
Aguas Zarcas	0.503	0.992	Aguas Zarcas	0.291	1.781
Aguas Zarcas	0.418	1.258	Aguas Zarcas	0.194	2.367
Aguas Zarcas	0.302	1.727	Aguas Zarcas	0.193	2.376
Aguas Zarcas	0.245	2.030	Aguas Zarcas	0.162	2.625
Aguas Zarcas	0.346	1.533	Aguas Zarcas	0.222	2.174
Aguas Zarcas	0.376	1.410	Aguas Zarcas	0.248	2.014
Aguas Zarcas	0.484	1.046	Aguas Zarcas	0.328	1.606
Aguas Zarcas	0.526	0.927	Aguas Zarcas	0.308	1.700

Table continued

R1			R3		
Sample	R_1 (mm)	R_1 (phi)	Sample	R_3 (mm)	R_3 (phi)
Aguas Zarcas	0.374	1.420	Aguas Zarcas	0.266	1.910
Aguas Zarcas	0.370	1.433	Aguas Zarcas	0.238	2.068
Aguas Zarcas	0.312	1.680	Aguas Zarcas	0.239	2.067
Aguas Zarcas	0.545	0.875	Aguas Zarcas	0.334	1.581
Aguas Zarcas	0.335	1.577	Aguas Zarcas	0.193	2.373
Aguas Zarcas	0.310	1.688	Aguas Zarcas	0.239	2.062
Aguas Zarcas	0.315	1.666	Aguas Zarcas	0.197	2.344
Aguas Zarcas	0.400	1.321	Aguas Zarcas	0.283	1.822
Aguas Zarcas	0.380	1.394	Aguas Zarcas	0.228	2.135
Aguas Zarcas	0.600	0.736	Aguas Zarcas	0.344	1.541
Aguas Zarcas	0.371	1.430	Aguas Zarcas	0.195	2.359
Aguas Zarcas	0.421	1.247	Aguas Zarcas	0.277	1.854
Aguas Zarcas	0.411	1.284	Aguas Zarcas	0.306	1.709
Aguas Zarcas	0.305	1.714	Aguas Zarcas	0.206	2.278
Aguas Zarcas	0.251	1.993	Aguas Zarcas	0.187	2.421
Aguas Zarcas	0.447	1.160	Aguas Zarcas	0.298	1.746
Aguas Zarcas	0.349	1.521	Aguas Zarcas	0.201	2.313
Aguas Zarcas	0.287	1.802	Aguas Zarcas	0.146	2.773
Aguas Zarcas	0.269	1.892	Aguas Zarcas	0.182	2.455
Aguas Zarcas	0.463	1.112	Aguas Zarcas	0.334	1.584
Aguas Zarcas	0.291	1.779	Aguas Zarcas	0.176	2.509
Aguas Zarcas	0.285	1.810	Aguas Zarcas	0.217	2.201
Aguas Zarcas	0.473	1.079	Aguas Zarcas	0.239	2.064
Aguas Zarcas	0.454	1.141	Aguas Zarcas	0.249	2.004
Aguas Zarcas	0.470	1.089	Aguas Zarcas	0.232	2.110
Aguas Zarcas	0.306	1.710	Aguas Zarcas	0.264	1.920
Aguas Zarcas	0.327	1.612	Aguas Zarcas	0.224	2.159
Aguas Zarcas	0.370	1.435	Aguas Zarcas	0.207	2.270
Aguas Zarcas	0.271	1.885	Aguas Zarcas	0.172	2.536
Aguas Zarcas	0.570	0.810	Aguas Zarcas	0.406	1.301
Aguas Zarcas	0.411	1.283	Aguas Zarcas	0.265	1.917
Aguas Zarcas	0.262	1.932	Aguas Zarcas	0.173	2.533
Aguas Zarcas	0.357	1.486	Aguas Zarcas	0.213	2.229
Aguas Zarcas	0.396	1.338	Aguas Zarcas	0.263	1.928
Aguas Zarcas	0.522	0.939	Aguas Zarcas	0.347	1.526
Aguas Zarcas	0.396	1.338	Aguas Zarcas	0.254	1.975
Aguas Zarcas	0.354	1.497	Aguas Zarcas	0.262	1.931
Aguas Zarcas	0.418	1.258	Aguas Zarcas	0.358	1.483
Aguas Zarcas	0.263	1.924	Aguas Zarcas	0.165	2.603
Aguas Zarcas	0.249	2.009	Aguas Zarcas	0.178	2.488
Aguas Zarcas	0.274	1.866	Aguas Zarcas	0.204	2.294
Aguas Zarcas	0.307	1.703	Aguas Zarcas	0.221	2.175
Aguas Zarcas	0.370	1.435	Aguas Zarcas	0.219	2.191
Aguas Zarcas	0.324	1.627	Aguas Zarcas	0.231	2.115
Aguas Zarcas	0.264	1.922	Aguas Zarcas	0.176	2.504
Aguas Zarcas	0.248	2.010	Aguas Zarcas	0.154	2.695
Aguas Zarcas	0.245	2.028	Aguas Zarcas	0.143	2.809
Aguas Zarcas	0.492	1.022	Aguas Zarcas	0.394	1.342
Aguas Zarcas	0.240	2.056	Aguas Zarcas	0.129	2.960
Aguas Zarcas	0.364	1.457	Aguas Zarcas	0.289	1.792
Aguas Zarcas	0.252	1.988	Aguas Zarcas	0.194	2.363
Aguas Zarcas	0.432	1.211	Aguas Zarcas	0.256	1.964
Aguas Zarcas	0.364	1.457	Aguas Zarcas	0.147	2.762
Aguas Zarcas	0.176	2.510	Aguas Zarcas	0.149	2.742
Aguas Zarcas	0.252	1.987	Aguas Zarcas	0.158	2.661
Aguas Zarcas	0.460	1.120	Aguas Zarcas	0.239	2.067
Aguas Zarcas	0.245	2.032	Aguas Zarcas	0.166	2.589
Aguas Zarcas	0.253	1.981	Aguas Zarcas	0.187	2.420
Aguas Zarcas	0.310	1.688	Aguas Zarcas	0.196	2.354
Aguas Zarcas	0.461	1.118	Aguas Zarcas	0.270	1.889
Aguas Zarcas	0.261	1.936	Aguas Zarcas	0.169	2.567
Aguas Zarcas	0.681	0.555	Aguas Zarcas	0.532	0.912
Aguas Zarcas	0.333	1.585	Aguas Zarcas	0.235	2.089
Aguas Zarcas	0.281	1.830	Aguas Zarcas	0.152	2.717
Aguas Zarcas	0.250	2.001	Aguas Zarcas	0.153	2.708
Aguas Zarcas	0.434	1.203	Aguas Zarcas	0.266	1.913
Aguas Zarcas	0.252	1.988	Aguas Zarcas	0.171	2.548
Aguas Zarcas	0.252	1.990	Aguas Zarcas	0.168	2.572
Aguas Zarcas	0.187	2.421	Aguas Zarcas	0.145	2.786
Aguas Zarcas	0.440	1.185	Aguas Zarcas	0.236	2.081

Table continued

R1			R3		
Sample	R_1 (mm)	R_1 (phi)	Sample	R_3 (mm)	R_3 (phi)
Aguas Zarcas	0.421	1.248	Aguas Zarcas	0.256	1.963
Aguas Zarcas	0.262	1.930	Aguas Zarcas	0.134	2.902
Aguas Zarcas	0.262	1.934	Aguas Zarcas	0.157	2.675
Aguas Zarcas	0.595	0.749	Aguas Zarcas	0.259	1.948
Aguas Zarcas	0.484	1.047	Aguas Zarcas	0.253	1.980
Aguas Zarcas	0.338	1.564	Aguas Zarcas	0.229	2.127
Aguas Zarcas	0.396	1.335	Aguas Zarcas	0.285	1.810
Aguas Zarcas	0.441	1.180	Aguas Zarcas	0.237	2.078
Aguas Zarcas	0.481	1.057	Aguas Zarcas	0.313	1.678
Aguas Zarcas	0.267	1.902	Aguas Zarcas	0.150	2.733
Aguas Zarcas	0.196	2.349	Aguas Zarcas	0.122	3.030
Aguas Zarcas	0.400	1.322	Aguas Zarcas	0.260	1.944
Aguas Zarcas	0.353	1.502	Aguas Zarcas	0.190	2.397
Aguas Zarcas	0.175	2.513	Aguas Zarcas	0.135	2.890
Aguas Zarcas	0.344	1.541	Aguas Zarcas	0.259	1.951
Aguas Zarcas	0.272	1.876	Aguas Zarcas	0.171	2.552
Aguas Zarcas	0.272	1.876	Aguas Zarcas	0.192	2.378
Aguas Zarcas	0.224	2.161	Aguas Zarcas	0.158	2.666
Aguas Zarcas	0.361	1.469	Aguas Zarcas	0.259	1.950
Aguas Zarcas	0.392	1.351	Aguas Zarcas	0.242	2.045
Aguas Zarcas	0.464	1.107	Aguas Zarcas	0.216	2.212
Aguas Zarcas	0.301	1.734	Aguas Zarcas	0.198	2.334
Aguas Zarcas	0.249	2.005	Aguas Zarcas	0.185	2.431
Aguas Zarcas	0.408	1.295	Aguas Zarcas	0.229	2.128
Aguas Zarcas	0.438	1.191	Aguas Zarcas	0.317	1.659
Aguas Zarcas	0.335	1.578	Aguas Zarcas	0.219	2.190
Aguas Zarcas	0.342	1.549	Aguas Zarcas	0.247	2.016
Aguas Zarcas	0.343	1.544	Aguas Zarcas	0.207	2.274
Aguas Zarcas	0.313	1.674	Aguas Zarcas	0.210	2.249
Aguas Zarcas	0.266	1.910	Aguas Zarcas	0.189	2.402
Aguas Zarcas	0.274	1.870	Aguas Zarcas	0.164	2.609
Aguas Zarcas	0.485	1.045	Aguas Zarcas	0.379	1.400
Aguas Zarcas	0.346	1.533	Aguas Zarcas	0.192	2.378
Aguas Zarcas	1.178	-0.236	Aguas Zarcas	0.530	0.916
Aguas Zarcas	0.346	1.531	Aguas Zarcas	0.275	1.861
Aguas Zarcas	0.425	1.234	Aguas Zarcas	0.155	2.693
Aguas Zarcas	0.245	2.028	Aguas Zarcas	0.158	2.662
Aguas Zarcas	0.404	1.306	Aguas Zarcas	0.241	2.056
Aguas Zarcas	0.257	1.961	Aguas Zarcas	0.112	3.159
Aguas Zarcas	0.482	1.052	Aguas Zarcas	0.202	2.308
Aguas Zarcas	0.310	1.691	Aguas Zarcas	0.266	1.908
Aguas Zarcas	0.341	1.554	Aguas Zarcas	0.206	2.277
Aguas Zarcas	0.299	1.740	Aguas Zarcas	0.235	2.092
Aguas Zarcas	0.203	2.297	Aguas Zarcas	0.149	2.744
Aguas Zarcas	0.278	1.848	Aguas Zarcas	0.214	2.228
Aguas Zarcas	0.692	0.532	Aguas Zarcas	0.272	1.877
Aguas Zarcas	0.633	0.660	Aguas Zarcas	0.263	1.926
Aguas Zarcas	0.567	0.819	Aguas Zarcas	0.335	1.579
Aguas Zarcas	0.270	1.891	Aguas Zarcas	0.192	2.381
Aguas Zarcas	0.688	0.539	Aguas Zarcas	0.309	1.693
Aguas Zarcas	0.346	1.529	Aguas Zarcas	0.234	2.098
Aguas Zarcas	0.279	1.841	Aguas Zarcas	0.224	2.156
Aguas Zarcas	0.285	1.813	Aguas Zarcas	0.167	2.584
Aguas Zarcas	0.430	1.219	Aguas Zarcas	0.255	1.973
Aguas Zarcas	0.317	1.657	Aguas Zarcas	0.165	2.603
Aguas Zarcas	0.446	1.164	Aguas Zarcas	0.210	2.249
Aguas Zarcas	0.356	1.491	Aguas Zarcas	0.216	2.212
Aguas Zarcas	0.426	1.230	Aguas Zarcas	0.264	1.921
Aguas Zarcas	0.342	1.549	Aguas Zarcas	0.195	2.362
Aguas Zarcas	0.228	2.135	Aguas Zarcas	0.144	2.796
Aguas Zarcas	0.372	1.426	Aguas Zarcas	0.301	1.733
Aguas Zarcas	0.458	1.127	Aguas Zarcas	0.245	2.031
Aguas Zarcas	0.368	1.443	Aguas Zarcas	0.204	2.297
Aguas Zarcas	0.323	1.632	Aguas Zarcas	0.184	2.446
Aguas Zarcas	0.278	1.845	Aguas Zarcas	0.240	2.061
Aguas Zarcas	0.374	1.418	Aguas Zarcas	0.208	2.268
Aguas Zarcas	0.623	0.683	Aguas Zarcas	0.313	1.678
Aguas Zarcas	0.515	0.958	Aguas Zarcas	0.219	2.192
Aguas Zarcas	0.294	1.766	Aguas Zarcas	0.202	2.308
Aguas Zarcas	0.458	1.126	Aguas Zarcas	0.209	2.259

Table continued

R_1			R_3		
Sample	**R_1 (mm)**	**R_1 (phi)**	**Sample**	**R_3 (mm)**	**R_3 (phi)**
Aguas Zarcas	0.267	1.904	Aguas Zarcas	0.100	3.323
Aguas Zarcas	0.322	1.633	Aguas Zarcas	0.206	2.277
Aguas Zarcas	0.405	1.302	Aguas Zarcas	0.339	1.559
Aguas Zarcas	0.384	1.382	Aguas Zarcas	0.184	2.439
Aguas Zarcas	0.213	2.229	Aguas Zarcas	0.144	2.799
Aguas Zarcas	0.554	0.853	Aguas Zarcas	0.255	1.973
Aguas Zarcas	0.202	2.311	Aguas Zarcas	0.139	2.849
Aguas Zarcas	0.296	1.758	Aguas Zarcas	0.156	2.684
Aguas Zarcas	0.275	1.863	Aguas Zarcas	0.159	2.657
Aguas Zarcas	0.327	1.612	Aguas Zarcas	0.179	2.484
Aguas Zarcas	0.319	1.650	Aguas Zarcas	0.192	2.382
Aguas Zarcas	0.411	1.284	Aguas Zarcas	0.174	2.525
Aguas Zarcas	0.287	1.800	Aguas Zarcas	0.163	2.620
Aguas Zarcas	0.361	1.468	Aguas Zarcas	0.195	2.362
Aguas Zarcas	0.313	1.678	Aguas Zarcas	0.186	2.428
Aguas Zarcas	0.297	1.750	Aguas Zarcas	0.190	2.397
Aguas Zarcas	0.398	1.328	Aguas Zarcas	0.254	1.975
Aguas Zarcas	0.589	0.765	Aguas Zarcas	0.244	2.034
Aguas Zarcas	0.514	0.960	Aguas Zarcas	0.367	1.445
Aguas Zarcas	0.496	1.010	Aguas Zarcas	0.329	1.602
Aguas Zarcas	0.278	1.847	Aguas Zarcas	0.195	2.362
Aguas Zarcas	0.378	1.403	Aguas Zarcas	0.197	2.341
Aguas Zarcas	0.387	1.368	Aguas Zarcas	0.208	2.268
Aguas Zarcas	0.328	1.610	Aguas Zarcas	0.229	2.128
Aguas Zarcas	0.424	1.238	Aguas Zarcas	0.323	1.629
Aguas Zarcas	0.260	1.943	Aguas Zarcas	0.192	2.378
Aguas Zarcas	0.291	1.780	Aguas Zarcas	0.209	2.257
Aguas Zarcas	0.411	1.282	Aguas Zarcas	0.171	2.551
Aguas Zarcas	0.333	1.588	Aguas Zarcas	0.255	1.970
Aguas Zarcas	0.359	1.480	Aguas Zarcas	0.154	2.700
Aguas Zarcas	0.553	0.856	Aguas Zarcas	0.289	1.792
Aguas Zarcas	0.479	1.063	Aguas Zarcas	0.230	2.118
Aguas Zarcas	0.357	1.488	Aguas Zarcas	0.214	2.224
Aguas Zarcas	0.356	1.490	Aguas Zarcas	0.209	2.256
Aguas Zarcas	0.508	0.976	Aguas Zarcas	0.197	2.345
Aguas Zarcas	0.387	1.368	Aguas Zarcas	0.211	2.244
Aguas Zarcas	0.390	1.359	Aguas Zarcas	0.247	2.020
Aguas Zarcas	0.540	0.889	Aguas Zarcas	0.426	1.233
Aguas Zarcas	0.357	1.488	Aguas Zarcas	0.218	2.197
Aguas Zarcas	0.475	1.073	Aguas Zarcas	0.267	1.907
Aguas Zarcas	0.533	0.907	Aguas Zarcas	0.322	1.635
Aguas Zarcas	0.249	2.008	Aguas Zarcas	0.213	2.229
Aguas Zarcas	0.454	1.140	Aguas Zarcas	0.248	2.010
Aguas Zarcas	0.371	1.432	Aguas Zarcas	0.267	1.907
Aguas Zarcas	0.646	0.630	Aguas Zarcas	0.356	1.490
Aguas Zarcas	0.297	1.751	Aguas Zarcas	0.209	2.258
Aguas Zarcas	0.282	1.826	Aguas Zarcas	0.143	2.811
Aguas Zarcas	0.667	0.584	Aguas Zarcas	0.218	2.197
Aguas Zarcas	0.448	1.160	Aguas Zarcas	0.185	2.434
Aguas Zarcas	0.365	1.456	Aguas Zarcas	0.200	2.321
Aguas Zarcas	0.433	1.209	Aguas Zarcas	0.300	1.737
Aguas Zarcas	0.328	1.606	Aguas Zarcas	0.199	2.326
Aguas Zarcas	0.246	2.023	Aguas Zarcas	0.176	2.504
Aguas Zarcas	0.405	1.305	Aguas Zarcas	0.245	2.031
Aguas Zarcas	0.441	1.180	Aguas Zarcas	0.252	1.988
Aguas Zarcas	0.173	2.530	Aguas Zarcas	0.143	2.805
Aguas Zarcas	0.284	1.815	Aguas Zarcas	0.210	2.251
Aguas Zarcas	0.440	1.183	Aguas Zarcas	0.171	2.548
Aguas Zarcas	0.299	1.740	Aguas Zarcas	0.181	2.469
Aguas Zarcas	0.452	1.147	Aguas Zarcas	0.178	2.493
Aguas Zarcas	0.307	1.702	Aguas Zarcas	0.172	2.536
Aguas Zarcas	0.446	1.163	Aguas Zarcas	0.315	1.664
Aguas Zarcas	0.414	1.273	Aguas Zarcas	0.209	2.261
Aguas Zarcas	0.379	1.401	Aguas Zarcas	0.322	1.634
Aguas Zarcas	0.669	0.581	Aguas Zarcas	0.282	1.827
Aguas Zarcas	0.371	1.431	Aguas Zarcas	0.194	2.368
Aguas Zarcas	0.559	0.839	Aguas Zarcas	0.229	2.128
Aguas Zarcas	0.768	0.381	Aguas Zarcas	0.490	1.029
LEW85311	0.244	2.034	LEW85311	0.179	2.481
LEW85311	0.107	3.224	LEW85311	0.092	3.450

Table continued

	R$_1$			R$_3$	
Sample	**R$_1$ (mm)**	**R$_1$ (phi)**	**Sample**	**R$_3$ (mm)**	**R$_3$ (phi)**
LEW85311	0.124	3.017	LEW85311	0.083	3.589
LEW85311	0.597	0.744	LEW85311	0.373	1.425
LEW85311	0.222	2.174	LEW85311	0.093	3.434
LEW85311	0.403	1.310	LEW85311	0.144	2.801
LEW85311	0.270	1.888	LEW85311	0.198	2.335
LEW85311	0.125	3.000	LEW85311	0.110	3.184
LEW85311	0.160	2.643	LEW85311	0.102	3.300
LEW85311	0.172	2.537	LEW85311	0.097	3.373
LEW85311	0.381	1.391	LEW85311	0.217	2.201
LEW85311	0.134	2.895	LEW85311	0.084	3.577
LEW85311	0.176	2.509	LEW85311	0.108	3.215
LEW85311	0.131	2.931	LEW85311	0.064	3.966
LEW85311	0.166	2.588	LEW85311	0.107	3.223
LEW85311	0.169	2.567	LEW85311	0.081	3.625
LEW85311	0.229	2.127	LEW85311	0.128	2.961
LEW85311	0.223	2.166	LEW85311	0.099	3.336
LEW85311	0.128	2.962	LEW85311	0.072	3.795
LEW85311	0.094	3.406	LEW85311	0.061	4.032
LEW85311	0.211	2.246	LEW85311	0.156	2.677
LEW85311	0.139	2.844	LEW85311	0.089	3.498
LEW85311	0.093	3.430	LEW85311	0.053	4.241
LEW85311	0.258	1.957	LEW85311	0.100	3.325
LEW85311	0.271	1.881	LEW85311	0.215	2.218
LEW85311	0.293	1.769	LEW85311	0.208	2.269
LEW85311	0.131	2.934	LEW85311	0.099	3.340
LEW85311	0.174	2.521	LEW85311	0.092	3.439
LEW85311	0.077	3.699	LEW85311	0.050	4.309
LEW85311	0.142	2.816	LEW85311	0.079	3.669
LEW85311	0.132	2.921	LEW85311	0.078	3.677
LEW85311	0.192	2.378	LEW85311	0.106	3.236
LEW85311	0.157	2.669	LEW85311	0.107	3.218
LEW85311	0.458	1.127	LEW85311	0.225	2.154
LEW85311	0.174	2.520	LEW85311	0.118	3.079
LEW85311	0.191	2.386	LEW85311	0.094	3.419
LEW85311	0.275	1.860	LEW85311	0.145	2.787
LEW85311	0.081	3.619	LEW85311	0.052	4.276
LEW85311	0.124	3.016	LEW85311	0.083	3.590
LEW85311	0.300	1.737	LEW85311	0.201	2.313
LEW85311	0.185	2.432	LEW85311	0.104	3.270
LEW85311	0.248	2.012	LEW85311	0.172	2.542
LEW85311	0.173	2.533	LEW85311	0.115	3.125
LEW85311	0.190	2.395	LEW85311	0.164	2.610
LEW85311	0.355	1.496	LEW85311	0.179	2.485
LEW85311	0.240	2.056	LEW85311	0.145	2.789
LEW85311	0.126	2.989	LEW85311	0.110	3.189
LEW85311	0.149	2.749	LEW85311	0.131	2.928
LEW85311	0.141	2.829	LEW85311	0.111	3.175
LEW85311	0.231	2.115	LEW85311	0.151	2.725
LEW85311	0.197	2.340	LEW85311	0.134	2.902
LEW85311	0.234	2.096	LEW85311	0.160	2.646
LEW85311	0.276	1.857	LEW85311	0.161	2.639
LEW85311	0.081	3.619	LEW85311	0.065	3.941
LEW85311	0.174	2.525	LEW85311	0.115	3.116
LEW85311	0.127	2.973	LEW85311	0.109	3.196
LEW85311	0.239	2.062	LEW85311	0.196	2.351
LEW85311	0.105	3.258	LEW85311	0.093	3.422
LEW85311	0.118	3.079	LEW85311	0.082	3.601
LEW85311	0.114	3.130	LEW85311	0.086	3.534
LEW85311	0.135	2.888	LEW85311	0.068	3.888
LEW85311	0.143	2.805	LEW85311	0.076	3.727
LEW85311	0.143	2.804	LEW85311	0.090	3.476
LEW85311	0.275	1.862	LEW85311	0.130	2.941
LEW85311	0.179	2.483	LEW85311	0.134	2.895
LEW85311	0.173	2.529	LEW85311	0.099	3.332
LEW85311	0.082	3.611	LEW85311	0.075	3.737
LEW85311	0.382	1.389	LEW85311	0.127	2.975
LEW85311	0.149	2.750	LEW85311	0.088	3.504
LEW85311	0.219	2.189	LEW85311	0.133	2.914
LEW85311	0.287	1.802	LEW85311	0.160	2.642
LEW85311	0.140	2.836	LEW85311	0.083	3.589

Table continued

R$_1$			R$_3$		
Sample	**R$_1$ (mm)**	**R$_1$ (phi)**	**Sample**	**R$_3$ (mm)**	**R$_3$ (phi)**
LEW85311	0.102	3.298	LEW85311	0.066	3.920
LEW85311	0.146	2.774	LEW85311	0.070	3.838
LEW85311	0.232	2.105	LEW85311	0.133	2.916
LEW85311	0.175	2.513	LEW85311	0.123	3.023
LEW85311	0.170	2.560	LEW85311	0.107	3.228
LEW85311	0.191	2.386	LEW85311	0.128	2.961
LEW85311	0.224	2.158	LEW85311	0.112	3.156
LEW85311	0.127	2.980	LEW85311	0.110	3.191
LEW85311	0.283	1.821	LEW85311	0.147	2.762
LEW85311	0.200	2.322	LEW85311	0.121	3.052
LEW85311	0.138	2.854	LEW85311	0.085	3.564
LEW85311	0.152	2.722	LEW85311	0.102	3.299
LEW85311	0.200	2.324	LEW85311	0.120	3.063
LEW85311	0.099	3.333	LEW85311	0.071	3.813
LEW85311	0.187	2.418	LEW85311	0.067	3.902
LEW85311	0.136	2.873	LEW85311	0.074	3.752
LEW85311	0.145	2.786	LEW85311	0.075	3.737
LEW85311	0.358	1.484	LEW85311	0.241	2.053
LEW85311	0.094	3.417	LEW85311	0.065	3.936
LEW85311	0.340	1.558	LEW85311	0.200	2.323
LEW85311	0.190	2.393	LEW85311	0.131	2.932
LEW85311	0.280	1.837	LEW85311	0.169	2.569
LEW85311	0.161	2.636	LEW85311	0.153	2.707
LEW85311	0.136	2.884	LEW85311	0.109	3.204
LEW85311	0.208	2.264	LEW85311	0.122	3.031
LEW85311	0.087	3.515	LEW85311	0.067	3.896
LEW85311	0.180	2.470	LEW85311	0.079	3.666
LEW85311	0.075	3.743	LEW85311	0.069	3.867
LEW85311	0.144	2.796	LEW85311	0.114	3.127
LEW85311	0.321	1.641	LEW85311	0.204	2.295
LEW85311	0.087	3.517	LEW85311	0.078	3.676
LEW85311	0.173	2.529	LEW85311	0.111	3.167
LEW85311	0.143	2.802	LEW85311	0.094	3.412
LEW85311	0.135	2.892	LEW85311	0.118	3.078
LEW85311	0.153	2.713	LEW85311	0.127	2.981
LEW85311	0.216	2.213	LEW85311	0.159	2.650
LEW85311	0.234	2.094	LEW85311	0.186	2.428
LEW85311	0.147	2.768	LEW85311	0.105	3.245
LEW85311	0.199	2.328	LEW85311	0.145	2.781
LEW85311	0.160	2.647	LEW85311	0.087	3.519
LEW85311	0.147	2.768	LEW85311	0.104	3.265
LEW85311	0.095	3.392	LEW85311	0.077	3.699
LEW85311	0.117	3.098	LEW85311	0.087	3.521
LEW85311	0.188	2.409	LEW85311	0.137	2.865
LEW85311	0.177	2.498	LEW85311	0.123	3.023
LEW85311	0.097	3.360	LEW85311	0.063	3.994
LEW85311	0.179	2.480	LEW85311	0.104	3.266
LEW85311	0.183	2.452	LEW85311	0.092	3.447
LEW85311	0.186	2.425	LEW85311	0.106	3.237
LEW85311	0.269	1.897	LEW85311	0.144	2.794
LEW85311	0.205	2.285	LEW85311	0.125	2.997
LEW85311	0.152	2.715	LEW85311	0.096	3.385
LEW85311	0.223	2.164	LEW85311	0.144	2.800
LEW85311	0.117	3.097	LEW85311	0.090	3.473
LEW85311	0.102	3.293	LEW85311	0.079	3.669
LEW85311	0.170	2.555	LEW85311	0.108	3.209
LEW85311	0.079	3.656	LEW85311	0.067	3.893
LEW85311	0.126	2.994	LEW85311	0.089	3.484
LEW85311	0.228	2.136	LEW85311	0.119	3.076
LEW85311	0.104	3.271	LEW85311	0.084	3.565
LEW85311	0.170	2.556	LEW85311	0.082	3.608
LEW85311	0.185	2.438	LEW85311	0.130	2.940
LEW85311	0.124	3.012	LEW85311	0.090	3.480
LEW85311	0.112	3.161	LEW85311	0.063	3.988
LEW85311	0.198	2.337	LEW85311	0.130	2.947
LEW85311	0.246	2.023	LEW85311	0.106	3.244
LEW85311	0.097	3.363	LEW85311	0.084	3.574
LEW85311	0.354	1.500	LEW85311	0.280	1.834
LEW85311	0.234	2.097	LEW85311	0.144	2.795
LEW85311	0.120	3.055	LEW85311	0.112	3.159

Table continued

R_1			R_3		
Sample	**R_1 (mm)**	**R_1 (phi)**	**Sample**	**R_3 (mm)**	**R_3 (phi)**
LEW85311	0.215	2.217	LEW85311	0.151	2.726
LEW85311	0.189	2.404	LEW85311	0.135	2.887
LEW85311	0.464	1.107	LEW85311	0.182	2.462
LEW85311	0.142	2.821	LEW85311	0.124	3.013
LEW85311	0.316	1.660	LEW85311	0.164	2.611
LEW85311	0.081	3.623	LEW85311	0.074	3.764
LEW85311	0.180	2.477	LEW85311	0.122	3.032
LEW85311	0.201	2.316	LEW85311	0.113	3.145
LEW85311	0.181	2.467	LEW85311	0.114	3.130
LEW85311	0.152	2.718	LEW85311	0.096	3.380
LEW85311	0.250	1.998	LEW85311	0.116	3.106
LEW85311	0.140	2.832	LEW85311	0.098	3.350
Murchison	0.617	0.696	Murchison	0.434	1.204
Murchison	0.585	0.774	Murchison	0.277	1.852
Murchison	0.394	1.345	Murchison	0.203	2.298
Murchison	0.670	0.577	Murchison	0.336	1.572
Murchison	0.577	0.792	Murchison	0.315	1.667
Murchison	0.584	0.775	Murchison	0.379	1.401
Murchison	0.227	2.136	Murchison	0.176	2.505
Murchison	0.282	1.826	Murchison	0.231	2.115
Murchison	0.397	1.333	Murchison	0.254	1.978
Murchison	0.474	1.078	Murchison	0.166	2.593
Murchison	0.238	2.068	Murchison	0.160	2.646
Murchison	0.314	1.672	Murchison	0.189	2.407
Murchison	0.357	1.485	Murchison	0.179	2.480
Murchison	0.305	1.712	Murchison	0.174	2.519
Murchison	0.384	1.382	Murchison	0.239	2.066
Murchison	0.713	0.488	Murchison	0.461	1.116
Murchison	0.870	0.200	Murchison	0.386	1.372
Murchison	0.454	1.140	Murchison	0.355	1.493
Murchison	0.482	1.052	Murchison	0.265	1.914
Murchison	0.321	1.641	Murchison	0.268	1.899
Murchison	0.309	1.693	Murchison	0.239	2.065
Murchison	0.691	0.533	Murchison	0.529	0.920
Murchison	0.334	1.584	Murchison	0.192	2.380
Murchison	0.411	1.282	Murchison	0.309	1.696
Murchison	0.191	2.389	Murchison	0.108	3.211
Murchison	0.676	0.565	Murchison	0.299	1.743
Murchison	1.019	-0.028	Murchison	0.527	0.925
Murchison	0.253	1.980	Murchison	0.178	2.492
Murchison	0.232	2.111	Murchison	0.164	2.604
Murchison	0.661	0.597	Murchison	0.492	1.022
Murchison	0.269	1.895	Murchison	0.191	2.389
Murchison	0.475	1.073	Murchison	0.254	1.976
Murchison	0.734	0.445	Murchison	0.277	1.852
Murchison	0.639	0.647	Murchison	0.212	2.240
Murchison	0.371	1.429	Murchison	0.265	1.914
Murchison	0.729	0.455	Murchison	0.452	1.146
Murchison	0.431	1.215	Murchison	0.253	1.983
Murchison	0.946	0.080	Murchison	0.468	1.094
Murchison	0.478	1.065	Murchison	0.406	1.300
Murchison	0.880	0.185	Murchison	0.532	0.912
Murchison	0.269	1.894	Murchison	0.184	2.442
Murchison	0.449	1.156	Murchison	0.267	1.907
Murchison	0.746	0.423	Murchison	0.549	0.864
Murchison	0.408	1.294	Murchison	0.204	2.295
Murchison	0.375	1.414	Murchison	0.254	1.975
Murchison	0.419	1.253	Murchison	0.221	2.181
Murchison	0.485	1.045	Murchison	0.373	1.422
Murchison	0.384	1.380	Murchison	0.302	1.730
Murchison	0.216	2.209	Murchison	0.142	2.817
Murchison	0.548	0.867	Murchison	0.376	1.410
Murchison	1.492	-0.578	Murchison	0.486	1.041
Murchison	0.254	1.975	Murchison	0.179	2.479
Murchison	0.619	0.691	Murchison	0.400	1.324
Murchison	0.403	1.310	Murchison	0.175	2.516
Murchison	0.324	1.625	Murchison	0.227	2.142
Murchison	0.826	0.276	Murchison	0.464	1.109
Murchison	0.323	1.631	Murchison	0.200	2.319
Murchison	0.403	1.311	Murchison	0.261	1.936

Table continued

R1			R3		
Sample	R_1 (mm)	R_1 (phi)	Sample	R_3 (mm)	R_3 (phi)
Murchison	0.442	1.178	Murchison	0.254	1.976
Murchison	0.470	1.088	Murchison	0.292	1.777
Murchison	0.756	0.403	Murchison	0.310	1.688
Murchison	0.424	1.238	Murchison	0.214	2.224
Murchison	0.660	0.600	Murchison	0.323	1.632
Murchison	0.272	1.877	Murchison	0.142	2.812
Murchison	0.564	0.827	Murchison	0.341	1.551
Murchison	0.353	1.503	Murchison	0.222	2.169
Murchison	0.420	1.251	Murchison	0.212	2.241
Murchison	1.074	-0.103	Murchison	0.638	0.648
Murchison	0.466	1.102	Murchison	0.339	1.562
Murchison	0.536	0.899	Murchison	0.459	1.123
Murchison	0.864	0.211	Murchison	0.489	1.031
Murchison	0.616	0.700	Murchison	0.262	1.931
Murchison	0.468	1.095	Murchison	0.303	1.724
Murchison	0.282	1.827	Murchison	0.216	2.210
Murchison	0.526	0.926	Murchison	0.252	1.986
Murchison	0.475	1.073	Murchison	0.290	1.784
Murchison	0.510	0.972	Murchison	0.322	1.637
Murchison	0.718	0.477	Murchison	0.384	1.382
Murchison	0.339	1.561	Murchison	0.290	1.785
Murchison	0.509	0.974	Murchison	0.422	1.245
Murchison	0.673	0.571	Murchison	0.466	1.100
Murchison	0.423	1.241	Murchison	0.311	1.685
Murchison	0.537	0.896	Murchison	0.306	1.707
Murchison	2.134	-1.093	Murchison	0.806	0.312
Murchison	0.344	1.541	Murchison	0.267	1.905
Murchison	0.341	1.550	Murchison	0.224	2.158
Murchison	0.270	1.890	Murchison	0.172	2.538
Murchison	0.499	1.004	Murchison	0.250	2.003
Murchison	0.575	0.799	Murchison	0.316	1.660
Murchison	0.385	1.377	Murchison	0.265	1.916
Murchison	0.676	0.565	Murchison	0.353	1.504
Murchison	0.463	1.112	Murchison	0.239	2.065
Murchison	0.324	1.624	Murchison	0.247	2.019
Murchison	0.332	1.590	Murchison	0.186	2.427
Murchison	0.351	1.509	Murchison	0.235	2.090
Murchison	0.326	1.618	Murchison	0.206	2.281
Murchison	0.448	1.157	Murchison	0.338	1.566
Murchison	0.328	1.607	Murchison	0.242	2.046
Murchison	0.603	0.729	Murchison	0.334	1.584
Murchison	0.150	2.740	Murchison	0.099	3.335
Murchison	0.373	1.422	Murchison	0.231	2.116
Murchison	0.493	1.020	Murchison	0.327	1.615
Murchison	0.677	0.562	Murchison	0.450	1.151
Murchison	0.316	1.662	Murchison	0.166	2.587
Murchison	0.473	1.080	Murchison	0.288	1.796
Murchison	0.363	1.460	Murchison	0.210	2.249
Murchison	0.445	1.167	Murchison	0.225	2.150
Murchison	0.350	1.516	Murchison	0.204	2.295
Murchison	0.410	1.286	Murchison	0.385	1.379
Murchison	0.885	0.177	Murchison	0.489	1.032
Murchison	0.387	1.368	Murchison	0.237	2.076
Murchison	0.409	1.290	Murchison	0.296	1.755
Murchison	0.466	1.103	Murchison	0.277	1.853
Murchison	0.782	0.354	Murchison	0.419	1.255
Murchison	0.467	1.097	Murchison	0.323	1.632
Murchison	0.630	0.666	Murchison	0.438	1.192
Murchison	0.465	1.104	Murchison	0.445	1.168
Murchison	0.503	0.991	Murchison	0.204	2.293
Murchison	0.403	1.311	Murchison	0.284	1.819
Murchison	0.427	1.227	Murchison	0.194	2.366
Murchison	0.376	1.413	Murchison	0.268	1.902
Murchison	0.413	1.277	Murchison	0.249	2.006
Murchison	0.684	0.548	Murchison	0.291	1.779
Murchison	0.441	1.180	Murchison	0.257	1.961
Murchison	0.394	1.345	Murchison	0.292	1.774
Murchison	0.283	1.824	Murchison	0.199	2.331
Murchison	0.836	0.259	Murchison	0.360	1.473
Murchison	0.776	0.366	Murchison	0.367	1.448

Table continued

R1			R3		
Sample	R_1 (mm)	R_1 (phi)	Sample	R_3 (mm)	R_3 (phi)
Murchison	0.385	1.378	Murchison	0.284	1.814
Murchison	0.727	0.460	Murchison	0.367	1.448
Murchison	0.872	0.197	Murchison	0.371	1.432
Murchison	0.662	0.594	Murchison	0.329	1.605
Murchison	0.403	1.311	Murchison	0.318	1.651
Murchison	0.679	0.558	Murchison	0.481	1.057
Murchison	0.413	1.277	Murchison	0.318	1.654
Murchison	0.279	1.842	Murchison	0.247	2.018
Murchison	0.248	2.014	Murchison	0.165	2.604
Murchison	0.705	0.505	Murchison	0.444	1.170
Murchison	0.467	1.099	Murchison	0.291	1.780
Murchison	0.407	1.295	Murchison	0.218	2.199
Murchison	0.347	1.529	Murchison	0.266	1.908
Murchison	0.503	0.990	Murchison	0.378	1.404
Murchison	0.720	0.474	Murchison	0.485	1.044
Murchison	0.760	0.396	Murchison	0.333	1.588
Murchison	0.997	0.005	Murchison	0.467	1.099
Murchison	0.267	1.905	Murchison	0.190	2.398
Murchison	0.473	1.082	Murchison	0.245	2.028
Murchison	1.075	-0.104	Murchison	0.470	1.089
Murchison	0.289	1.790	Murchison	0.204	2.292
Murchison	0.303	1.721	Murchison	0.212	2.236
Murchison	0.358	1.484	Murchison	0.281	1.830
Murchison	0.470	1.088	Murchison	0.307	1.706
Murchison	0.298	1.745	Murchison	0.162	2.625
Murchison	0.600	0.738	Murchison	0.471	1.087
Murchison	0.455	1.137	Murchison	0.269	1.895
Murchison	0.574	0.802	Murchison	0.301	1.732
Murchison	0.496	1.011	Murchison	0.290	1.787
Murchison	0.727	0.459	Murchison	0.311	1.685
Murchison	0.477	1.069	Murchison	0.283	1.821
Murchison	0.376	1.413	Murchison	0.208	2.264
Murchison	0.885	0.177	Murchison	0.277	1.850
Murchison	0.329	1.606	Murchison	0.257	1.958
Murchison	0.238	2.071	Murchison	0.171	2.547
Murchison	0.517	0.951	Murchison	0.327	1.615
Murchison	0.438	1.191	Murchison	0.285	1.810
Murchison	0.482	1.052	Murchison	0.220	2.182
Murchison	0.516	0.954	Murchison	0.443	1.175
Murchison	0.378	1.402	Murchison	0.300	1.738
Murchison	0.747	0.421	Murchison	0.395	1.341
Murchison	0.419	1.256	Murchison	0.319	1.647
Murchison	0.447	1.163	Murchison	0.248	2.009
Murchison	0.351	1.511	Murchison	0.241	2.053
Murchison	0.284	1.815	Murchison	0.242	2.050
Murchison	0.428	1.223	Murchison	0.296	1.758
Murchison	0.491	1.027	Murchison	0.231	2.115
Murchison	0.323	1.631	Murchison	0.190	2.393
Murchison	0.388	1.366	Murchison	0.279	1.843
Murchison	0.471	1.088	Murchison	0.349	1.518
Murchison	0.560	0.837	Murchison	0.378	1.404
Murchison	1.090	-0.124	Murchison	0.431	1.216
Cold Bokkeveld	0.965	0.052	Cold Bokkeveld	0.629	0.668
Cold Bokkeveld	0.477	1.067	Cold Bokkeveld	0.372	1.425
Cold Bokkeveld	0.397	1.334	Cold Bokkeveld	0.206	2.279
Cold Bokkeveld	0.440	1.186	Cold Bokkeveld	0.283	1.824
Cold Bokkeveld	0.962	0.056	Cold Bokkeveld	0.648	0.627
Cold Bokkeveld	0.320	1.642	Cold Bokkeveld	0.215	2.221
Cold Bokkeveld	0.378	1.404	Cold Bokkeveld	0.314	1.669
Cold Bokkeveld	0.718	0.477	Cold Bokkeveld	0.462	1.115
Cold Bokkeveld	0.366	1.452	Cold Bokkeveld	0.299	1.742
Cold Bokkeveld	0.482	1.052	Cold Bokkeveld	0.270	1.886
Cold Bokkeveld	0.651	0.620	Cold Bokkeveld	0.298	1.746
Cold Bokkeveld	0.544	0.878	Cold Bokkeveld	0.325	1.623
Cold Bokkeveld	0.312	1.681	Cold Bokkeveld	0.212	2.240
Cold Bokkeveld	0.599	0.740	Cold Bokkeveld	0.398	1.329
Cold Bokkeveld	0.580	0.786	Cold Bokkeveld	0.274	1.869
Cold Bokkeveld	0.449	1.156	Cold Bokkeveld	0.389	1.364
Cold Bokkeveld	0.593	0.753	Cold Bokkeveld	0.378	1.405
Cold Bokkeveld	0.429	1.221	Cold Bokkeveld	0.283	1.819

Table continued

R1			R3		
Sample	**R_1 (mm)**	**R_1 (phi)**	**Sample**	**R_3 (mm)**	**R_3 (phi)**
Cold Bokkeveld	0.357	1.487	Cold Bokkeveld	0.234	2.098
Cold Bokkeveld	0.574	0.801	Cold Bokkeveld	0.365	1.455
Cold Bokkeveld	0.224	2.160	Cold Bokkeveld	0.176	2.504
Cold Bokkeveld	0.775	0.367	Cold Bokkeveld	0.525	0.931
Cold Bokkeveld	0.961	0.057	Cold Bokkeveld	0.611	0.710
Cold Bokkeveld	0.706	0.503	Cold Bokkeveld	0.352	1.508
Cold Bokkeveld	0.391	1.356	Cold Bokkeveld	0.258	1.957
Cold Bokkeveld	0.300	1.735	Cold Bokkeveld	0.170	2.560
Cold Bokkeveld	0.317	1.658	Cold Bokkeveld	0.248	2.009
Cold Bokkeveld	0.376	1.412	Cold Bokkeveld	0.306	1.708
Cold Bokkeveld	0.249	2.008	Cold Bokkeveld	0.176	2.509
Cold Bokkeveld	0.509	0.975	Cold Bokkeveld	0.295	1.760
Cold Bokkeveld	0.503	0.992	Cold Bokkeveld	0.338	1.565
Cold Bokkeveld	0.252	1.987	Cold Bokkeveld	0.190	2.393
Cold Bokkeveld	0.512	0.967	Cold Bokkeveld	0.286	1.808
Cold Bokkeveld	0.736	0.443	Cold Bokkeveld	0.455	1.137
Cold Bokkeveld	0.446	1.166	Cold Bokkeveld	0.308	1.697
Cold Bokkeveld	0.988	0.017	Cold Bokkeveld	0.617	0.696
Cold Bokkeveld	0.565	0.825	Cold Bokkeveld	0.450	1.151
Cold Bokkeveld	0.435	1.200	Cold Bokkeveld	0.309	1.696
Cold Bokkeveld	0.411	1.284	Cold Bokkeveld	0.313	1.677
Cold Bokkeveld	1.003	-0.005	Cold Bokkeveld	0.413	1.276
Cold Bokkeveld	0.289	1.792	Cold Bokkeveld	0.154	2.702
Cold Bokkeveld	0.399	1.326	Cold Bokkeveld	0.273	1.873
Cold Bokkeveld	0.352	1.507	Cold Bokkeveld	0.219	2.189
Cold Bokkeveld	0.584	0.776	Cold Bokkeveld	0.334	1.582
Cold Bokkeveld	0.518	0.948	Cold Bokkeveld	0.301	1.734
Cold Bokkeveld	0.347	1.525	Cold Bokkeveld	0.231	2.117
Cold Bokkeveld	0.352	1.507	Cold Bokkeveld	0.296	1.758
Cold Bokkeveld	0.432	1.211	Cold Bokkeveld	0.273	1.874
Cold Bokkeveld	0.380	1.395	Cold Bokkeveld	0.261	1.936
Cold Bokkeveld	0.324	1.624	Cold Bokkeveld	0.261	1.938
Cold Bokkeveld	0.475	1.075	Cold Bokkeveld	0.233	2.102
Cold Bokkeveld	0.397	1.333	Cold Bokkeveld	0.279	1.843
Cold Bokkeveld	0.324	1.626	Cold Bokkeveld	0.214	2.223
Cold Bokkeveld	0.476	1.070	Cold Bokkeveld	0.224	2.158
Cold Bokkeveld	0.472	1.084	Cold Bokkeveld	0.311	1.685
Cold Bokkeveld	0.476	1.072	Cold Bokkeveld	0.378	1.403
Cold Bokkeveld	0.357	1.486	Cold Bokkeveld	0.234	2.096
Cold Bokkeveld	0.307	1.706	Cold Bokkeveld	0.194	2.369
Cold Bokkeveld	0.463	1.111	Cold Bokkeveld	0.372	1.427
Cold Bokkeveld	0.596	0.746	Cold Bokkeveld	0.356	1.488
Cold Bokkeveld	1.024	-0.035	Cold Bokkeveld	0.769	0.379
Cold Bokkeveld	0.410	1.286	Cold Bokkeveld	0.283	1.823
Cold Bokkeveld	0.393	1.346	Cold Bokkeveld	0.328	1.609
Cold Bokkeveld	0.443	1.174	Cold Bokkeveld	0.246	2.021
Cold Bokkeveld	0.440	1.185	Cold Bokkeveld	0.248	2.014
Cold Bokkeveld	0.516	0.955	Cold Bokkeveld	0.312	1.679
Cold Bokkeveld	0.297	1.751	Cold Bokkeveld	0.187	2.416
Cold Bokkeveld	0.493	1.020	Cold Bokkeveld	0.348	1.524
Cold Bokkeveld	0.365	1.456	Cold Bokkeveld	0.268	1.898
Cold Bokkeveld	0.423	1.241	Cold Bokkeveld	0.254	1.977
Cold Bokkeveld	0.229	2.129	Cold Bokkeveld	0.183	2.451
Cold Bokkeveld	0.421	1.250	Cold Bokkeveld	0.277	1.850
Cold Bokkeveld	0.523	0.934	Cold Bokkeveld	0.345	1.535
Cold Bokkeveld	0.513	0.962	Cold Bokkeveld	0.352	1.505
Cold Bokkeveld	0.336	1.574	Cold Bokkeveld	0.231	2.112
Cold Bokkeveld	1.536	-0.620	Cold Bokkeveld	0.871	0.199
Cold Bokkeveld	0.587	0.768	Cold Bokkeveld	0.250	1.998
Cold Bokkeveld	0.255	1.971	Cold Bokkeveld	0.224	2.157
Cold Bokkeveld	0.581	0.783	Cold Bokkeveld	0.446	1.166
Cold Bokkeveld	0.357	1.488	Cold Bokkeveld	0.257	1.959
Cold Bokkeveld	0.660	0.599	Cold Bokkeveld	0.306	1.711
Cold Bokkeveld	0.357	1.485	Cold Bokkeveld	0.260	1.942
Cold Bokkeveld	0.449	1.154	Cold Bokkeveld	0.249	2.004
Cold Bokkeveld	0.365	1.455	Cold Bokkeveld	0.217	2.207
Cold Bokkeveld	0.320	1.643	Cold Bokkeveld	0.215	2.218
Cold Bokkeveld	0.436	1.199	Cold Bokkeveld	0.333	1.588
Cold Bokkeveld	0.324	1.628	Cold Bokkeveld	0.205	2.285
Cold Bokkeveld	0.444	1.171	Cold Bokkeveld	0.277	1.851

Table continued

	R₁			R₃	
Sample	**R_1 (mm)**	**R_1 (phi)**	**Sample**	**R_3 (mm)**	**R_3 (phi)**
Cold Bokkeveld	0.400	1.322	Cold Bokkeveld	0.200	2.325
Cold Bokkeveld	0.397	1.333	Cold Bokkeveld	0.271	1.883
Cold Bokkeveld	0.302	1.728	Cold Bokkeveld	0.157	2.671
Cold Bokkeveld	0.627	0.673	Cold Bokkeveld	0.560	0.837
Cold Bokkeveld	0.464	1.106	Cold Bokkeveld	0.286	1.805
Cold Bokkeveld	0.440	1.185	Cold Bokkeveld	0.265	1.918
Cold Bokkeveld	0.501	0.996	Cold Bokkeveld	0.324	1.628
Cold Bokkeveld	0.566	0.822	Cold Bokkeveld	0.412	1.280
Cold Bokkeveld	0.432	1.211	Cold Bokkeveld	0.271	1.882
Cold Bokkeveld	0.408	1.293	Cold Bokkeveld	0.240	2.059
Cold Bokkeveld	0.586	0.772	Cold Bokkeveld	0.330	1.598
Cold Bokkeveld	0.520	0.942	Cold Bokkeveld	0.266	1.912
Cold Bokkeveld	0.393	1.349	Cold Bokkeveld	0.270	1.888
Cold Bokkeveld	0.714	0.485	Cold Bokkeveld	0.413	1.275
Cold Bokkeveld	0.399	1.327	Cold Bokkeveld	0.263	1.924
Winchcombe	0.143	2.807	Winchcombe	0.106	3.233
Winchcombe	0.130	2.940	Winchcombe	0.094	3.408
Winchcombe	0.127	2.980	Winchcombe	0.089	3.497
Winchcombe	0.105	3.254	Winchcombe	0.080	3.651
Winchcombe	0.461	1.119	Winchcombe	0.294	1.766
Winchcombe	0.374	1.420	Winchcombe	0.256	1.965
Winchcombe	0.152	2.715	Winchcombe	0.093	3.419
Winchcombe	0.160	2.642	Winchcombe	0.092	3.436
Winchcombe	0.205	2.287	Winchcombe	0.133	2.911
Winchcombe	0.187	2.421	Winchcombe	0.118	3.082
Winchcombe	0.209	2.256	Winchcombe	0.148	2.758
Winchcombe	0.147	2.770	Winchcombe	0.084	3.582
Winchcombe	0.266	1.913	Winchcombe	0.156	2.679
Winchcombe	0.147	2.762	Winchcombe	0.095	3.397
Winchcombe	0.278	1.848	Winchcombe	0.232	2.107
Winchcombe	0.344	1.538	Winchcombe	0.291	1.782
Winchcombe	0.163	2.614	Winchcombe	0.111	3.165
Winchcombe	0.303	1.724	Winchcombe	0.137	2.865
Winchcombe	0.273	1.873	Winchcombe	0.154	2.703
Winchcombe	0.181	2.463	Winchcombe	0.074	3.762
Winchcombe	0.247	2.017	Winchcombe	0.141	2.829
Winchcombe	0.264	1.919	Winchcombe	0.154	2.697
Winchcombe	0.132	2.919	Winchcombe	0.100	3.328
Winchcombe	0.135	2.894	Winchcombe	0.073	3.769
Winchcombe	0.149	2.742	Winchcombe	0.125	3.004
Winchcombe	0.436	1.197	Winchcombe	0.241	2.053
Winchcombe	0.211	2.247	Winchcombe	0.122	3.030
Winchcombe	0.214	2.223	Winchcombe	0.108	3.207
Winchcombe	0.152	2.718	Winchcombe	0.116	3.107
Winchcombe	0.154	2.694	Winchcombe	0.124	3.009
Winchcombe	0.158	2.664	Winchcombe	0.102	3.299
Winchcombe	0.111	3.176	Winchcombe	0.066	3.926
Winchcombe	0.143	2.807	Winchcombe	0.112	3.159
Winchcombe	0.342	1.548	Winchcombe	0.246	2.026
Winchcombe	0.178	2.487	Winchcombe	0.077	3.702
Winchcombe	0.142	2.820	Winchcombe	0.112	3.154
Winchcombe	0.436	1.198	Winchcombe	0.182	2.458
Winchcombe	0.353	1.503	Winchcombe	0.196	2.352
Winchcombe	0.204	2.297	Winchcombe	0.122	3.039
Winchcombe	0.293	1.770	Winchcombe	0.154	2.698
Winchcombe	0.267	1.904	Winchcombe	0.113	3.143
Winchcombe	0.140	2.833	Winchcombe	0.077	3.692
Winchcombe	0.136	2.883	Winchcombe	0.069	3.850
Winchcombe	0.116	3.102	Winchcombe	0.059	4.077
Winchcombe	0.070	3.827	Winchcombe	0.047	4.423
Winchcombe	0.147	2.762	Winchcombe	0.094	3.409
Winchcombe	0.111	3.173	Winchcombe	0.091	3.459
Winchcombe	0.179	2.483	Winchcombe	0.105	3.255
Winchcombe	0.115	3.123	Winchcombe	0.092	3.438
Winchcombe	0.124	3.008	Winchcombe	0.087	3.520
Winchcombe	0.073	3.782	Winchcombe	0.046	4.429
Winchcombe	0.190	2.392	Winchcombe	0.114	3.127
Winchcombe	0.170	2.554	Winchcombe	0.098	3.353
Winchcombe	0.090	3.482	Winchcombe	0.076	3.722
Winchcombe	0.112	3.155	Winchcombe	0.055	4.188

Table continued

R_1			R_3		
Sample	**R_1 (mm)**	**R_1 (phi)**	**Sample**	**R_3 (mm)**	**R_3 (phi)**
Winchcombe	0.306	1.708	Winchcombe	0.197	2.341
Winchcombe	0.125	3.001	Winchcombe	0.098	3.352
Winchcombe	0.103	3.279	Winchcombe	0.051	4.291
Winchcombe	0.100	3.317	Winchcombe	0.049	4.341
Winchcombe	0.145	2.785	Winchcombe	0.073	3.779
Winchcombe	0.053	4.239	Winchcombe	0.039	4.690
Winchcombe	0.073	3.775	Winchcombe	0.069	3.851
Winchcombe	0.143	2.801	Winchcombe	0.112	3.159
Winchcombe	0.112	3.153	Winchcombe	0.044	4.496
Winchcombe	0.139	2.848	Winchcombe	0.082	3.602
Winchcombe	0.069	3.860	Winchcombe	0.054	4.218
Winchcombe	0.078	3.688	Winchcombe	0.037	4.757
Winchcombe	0.192	2.383	Winchcombe	0.089	3.488
Winchcombe	0.063	3.984	Winchcombe	0.045	4.484
Winchcombe	0.080	3.644	Winchcombe	0.036	4.803
Winchcombe	0.237	2.079	Winchcombe	0.138	2.857
Winchcombe	0.149	2.747	Winchcombe	0.108	3.209
Winchcombe	0.220	2.181	Winchcombe	0.163	2.620
Winchcombe	0.120	3.058	Winchcombe	0.088	3.502
Winchcombe	0.419	1.256	Winchcombe	0.232	2.106
Winchcombe	0.215	2.220	Winchcombe	0.096	3.376
Winchcombe	0.425	1.234	Winchcombe	0.294	1.767
Winchcombe	0.304	1.719	Winchcombe	0.222	2.170
Winchcombe	0.140	2.839	Winchcombe	0.091	3.463
Winchcombe	0.121	3.043	Winchcombe	0.064	3.959
Winchcombe	0.108	3.204	Winchcombe	0.081	3.619
Winchcombe	0.174	2.525	Winchcombe	0.103	3.278
Winchcombe	0.287	1.802	Winchcombe	0.161	2.633
Winchcombe	0.206	2.277	Winchcombe	0.157	2.674
Winchcombe	0.340	1.556	Winchcombe	0.162	2.630
Winchcombe	0.218	2.200	Winchcombe	0.135	2.885
Winchcombe	0.142	2.816	Winchcombe	0.105	3.245
Winchcombe	0.171	2.549	Winchcombe	0.095	3.402
Winchcombe	0.099	3.333	Winchcombe	0.064	3.958
Winchcombe	0.289	1.793	Winchcombe	0.117	3.093
Winchcombe	0.131	2.931	Winchcombe	0.085	3.562
Winchcombe	0.205	2.288	Winchcombe	0.131	2.933
Winchcombe	0.209	2.259	Winchcombe	0.129	2.954
Winchcombe	0.248	2.009	Winchcombe	0.151	2.729
Winchcombe	0.144	2.798	Winchcombe	0.112	3.164
Winchcombe	0.192	2.381	Winchcombe	0.134	2.899
Winchcombe	0.124	3.010	Winchcombe	0.091	3.453
Winchcombe	0.171	2.549	Winchcombe	0.104	3.271
Winchcombe	0.180	2.472	Winchcombe	0.106	3.242
Winchcombe	0.153	2.713	Winchcombe	0.084	3.569
Winchcombe	0.195	2.361	Winchcombe	0.131	2.931
Winchcombe	0.249	2.007	Winchcombe	0.163	2.619
Winchcombe	0.158	2.659	Winchcombe	0.098	3.349
Winchcombe	0.193	2.377	Winchcombe	0.103	3.286
Winchcombe	0.206	2.280	Winchcombe	0.152	2.716
Winchcombe	0.244	2.034	Winchcombe	0.135	2.893
Winchcombe	0.119	3.074	Winchcombe	0.102	3.298
Winchcombe	0.173	2.533	Winchcombe	0.128	2.966
Winchcombe	0.277	1.853	Winchcombe	0.161	2.634
Winchcombe	0.238	2.070	Winchcombe	0.198	2.338
Winchcombe	0.216	2.211	Winchcombe	0.160	2.647
Winchcombe	0.217	2.206	Winchcombe	0.189	2.406
Winchcombe	0.240	2.059	Winchcombe	0.121	3.042
Winchcombe	0.109	3.199	Winchcombe	0.071	3.816
Winchcombe	0.237	2.076	Winchcombe	0.129	2.956
Winchcombe	0.203	2.298	Winchcombe	0.163	2.620
Winchcombe	0.358	1.483	Winchcombe	0.139	2.852
Winchcombe	0.275	1.861	Winchcombe	0.189	2.400
Winchcombe	0.267	1.905	Winchcombe	0.177	2.497
Winchcombe	0.223	2.163	Winchcombe	0.138	2.854
Winchcombe	0.262	1.932	Winchcombe	0.151	2.725
Winchcombe	0.191	2.389	Winchcombe	0.120	3.061
Winchcombe	0.260	1.944	Winchcombe	0.101	3.305
Winchcombe	0.443	1.175	Winchcombe	0.284	1.814
Winchcombe	0.193	2.371	Winchcombe	0.128	2.961

Table continued

R1			R3		
Sample	R_1 (mm)	R_1 (phi)	Sample	R_3 (mm)	R_3 (phi)
Winchcombe	0.247	2.015	Winchcombe	0.144	2.795
Winchcombe	0.135	2.893	Winchcombe	0.094	3.418
Winchcombe	0.172	2.542	Winchcombe	0.117	3.100
Winchcombe	0.119	3.069	Winchcombe	0.085	3.549
Winchcombe	0.253	1.984	Winchcombe	0.145	2.789
Winchcombe	0.097	3.369	Winchcombe	0.080	3.652
Winchcombe	0.178	2.486	Winchcombe	0.118	3.079
Winchcombe	0.189	2.406	Winchcombe	0.084	3.565
Winchcombe	0.237	2.077	Winchcombe	0.145	2.789
Winchcombe	0.189	2.406	Winchcombe	0.110	3.179
Winchcombe	0.168	2.571	Winchcombe	0.116	3.108
Winchcombe	0.231	2.114	Winchcombe	0.131	2.929
Winchcombe	0.236	2.082	Winchcombe	0.159	2.649
Winchcombe	0.459	1.124	Winchcombe	0.293	1.772
Winchcombe	0.219	2.188	Winchcombe	0.120	3.057
Winchcombe	0.252	1.991	Winchcombe	0.151	2.729
Winchcombe	0.541	0.885	Winchcombe	0.213	2.232
Winchcombe	0.288	1.796	Winchcombe	0.197	2.344
Winchcombe	0.233	2.104	Winchcombe	0.119	3.067
Winchcombe	0.262	1.930	Winchcombe	0.219	2.189
Winchcombe	0.292	1.778	Winchcombe	0.211	2.242
Winchcombe	0.220	2.183	Winchcombe	0.120	3.054
Winchcombe	0.191	2.385	Winchcombe	0.132	2.924
Winchcombe	0.501	0.998	Winchcombe	0.140	2.836
Winchcombe	0.443	1.176	Winchcombe	0.165	2.603
Winchcombe	0.376	1.413	Winchcombe	0.285	1.813
Winchcombe	0.426	1.231	Winchcombe	0.170	2.554
Winchcombe	0.271	1.883	Winchcombe	0.147	2.762
Winchcombe	0.112	3.162	Winchcombe	0.079	3.664
Winchcombe	0.175	2.518	Winchcombe	0.103	3.284
Winchcombe	0.140	2.832	Winchcombe	0.068	3.888
Winchcombe	0.141	2.824	Winchcombe	0.075	3.738
Winchcombe	0.272	1.879	Winchcombe	0.183	2.448
Winchcombe	0.118	3.089	Winchcombe	0.066	3.924
Winchcombe	0.105	3.257	Winchcombe	0.075	3.741
Winchcombe	0.188	2.415	Winchcombe	0.114	3.138
Winchcombe	0.176	2.506	Winchcombe	0.085	3.557
Winchcombe	0.128	2.967	Winchcombe	0.070	3.845
Winchcombe	0.228	2.131	Winchcombe	0.143	2.809
Winchcombe	0.149	2.744	Winchcombe	0.114	3.137
Winchcombe	0.057	4.122	Winchcombe	0.049	4.350
Winchcombe	0.187	2.418	Winchcombe	0.100	3.328
Winchcombe	0.107	3.218	Winchcombe	0.057	4.124
Winchcombe	0.099	3.331	Winchcombe	0.065	3.935
Winchcombe	0.488	1.035	Winchcombe	0.271	1.884
Winchcombe	0.113	3.143	Winchcombe	0.062	4.006
Winchcombe	0.084	3.568	Winchcombe	0.071	3.810
Winchcombe	0.189	2.401	Winchcombe	0.136	2.879
Winchcombe	0.171	2.547	Winchcombe	0.137	2.866
Winchcombe	0.153	2.710	Winchcombe	0.106	3.241
Winchcombe	0.106	3.231	Winchcombe	0.056	4.161
Winchcombe	0.147	2.761	Winchcombe	0.073	3.782
Winchcombe	0.076	3.711	Winchcombe	0.060	4.061
Winchcombe	0.193	2.377	Winchcombe	0.070	3.838
Winchcombe	0.101	3.312	Winchcombe	0.067	3.904
Winchcombe	0.128	2.967	Winchcombe	0.100	3.328
Winchcombe	0.215	2.217	Winchcombe	0.151	2.731
Winchcombe	0.095	3.400	Winchcombe	0.086	3.540
Winchcombe	0.307	1.705	Winchcombe	0.175	2.512
Winchcombe	0.136	2.883	Winchcombe	0.082	3.610
Winchcombe	0.181	2.463	Winchcombe	0.139	2.851
Winchcombe	0.308	1.697	Winchcombe	0.220	2.187
Winchcombe	0.222	2.174	Winchcombe	0.117	3.096
Winchcombe	0.111	3.166	Winchcombe	0.065	3.934
Winchcombe	0.113	3.151	Winchcombe	0.069	3.854
Winchcombe	0.133	2.913	Winchcombe	0.097	3.372
Winchcombe	0.222	2.172	Winchcombe	0.115	3.122
Winchcombe	0.158	2.664	Winchcombe	0.065	3.943
Winchcombe	0.138	2.856	Winchcombe	0.091	3.451
Winchcombe	0.100	3.320	Winchcombe	0.049	4.347

Table continued

R_1			R_3		
Sample	**R_1 (mm)**	**R_1 (phi)**	**Sample**	**R_3 (mm)**	**R_3 (phi)**
Winchcombe	0.137	2.871	Winchcombe	0.117	3.092
Winchcombe	0.150	2.740	Winchcombe	0.080	3.653
Winchcombe	0.241	2.055	Winchcombe	0.110	3.185
Winchcombe	0.055	4.194	Winchcombe	0.048	4.369
Winchcombe	0.104	3.262	Winchcombe	0.059	4.079
Winchcombe	0.138	2.862	Winchcombe	0.103	3.284
Winchcombe	0.175	2.517	Winchcombe	0.117	3.091
Winchcombe	0.138	2.853	Winchcombe	0.099	3.340
Winchcombe	0.216	2.210	Winchcombe	0.147	2.770

8.2 Chapter 4 Specific Appendices

This section contains data and supplementary materials related to Chapter 4.

8.2.1 3D Orientation Data

Table 8.3*. Table showing RAW 3D chondrule orientation data Aguas Zarcas L1*

Aguas Zarcas L1 Chondrules								
Major Axis Directional Cosines			**Intermediate Axis Directional Cosines**			**Minor Axis Directional Cosines**		
PEllipsoid X1 (dmls)	**PEllipsoid Y1 (dmls)**	**PEllipsoid Z1 (dmls)**	**PEllipsoid X2 (dmls)**	**PEllipsoid Y2 (dmls)**	**PEllipsoid Z2 (dmls)**	**PEllipsoid X3 (dmls)**	**PEllipsoid Y3 (dmls)**	**PEllipsoid Z3 (dmls)**
-0.74540	0.20247	0.63513	0.30739	-0.74104	0.59698	0.59152	0.64022	0.49013
0.99752	0.06987	0.00866	-0.04637	0.55949	0.82754	0.05298	-0.82589	0.56134
-0.77545	0.57137	0.26873	-0.32173	-0.72376	0.61046	0.54330	0.38692	0.74506
-0.48198	-0.41379	0.77232	-0.55866	0.82418	0.09292	0.67497	0.38667	0.62841
-0.18603	0.97117	0.14909	-0.52958	-0.22692	0.81734	0.82761	0.07309	0.55652
0.15606	-0.98333	0.09328	-0.02763	0.09005	0.99555	0.98736	0.15795	0.01312
-0.46611	0.86606	0.18078	0.87644	0.42411	0.22800	-0.12080	-0.26472	0.95673
-0.41682	0.78949	0.45052	0.55221	-0.17375	0.81540	-0.72203	-0.58866	0.36354
-0.79430	0.34057	0.50309	0.50947	-0.07769	0.85698	-0.33095	-0.93700	0.11180
-0.55316	0.12228	0.82405	0.49850	0.84112	0.20981	0.66747	-0.52685	0.52623
-0.32797	0.22493	0.91752	0.45098	-0.81614	0.36128	0.83009	0.53228	0.16623
-0.51283	-0.74334	0.42948	0.03121	0.48380	0.87462	0.85793	-0.46193	0.22491
0.70884	0.09752	0.69859	-0.70243	0.18791	0.68650	-0.06433	-0.97733	0.20170
-0.26933	-0.82203	0.50174	-0.34949	0.56890	0.74446	0.89740	-0.02515	0.44051
-0.68763	0.52559	0.50092	0.58444	-0.00868	0.81139	-0.43081	-0.85069	0.30121
0.02418	0.19329	0.98084	-0.91255	-0.39640	0.10061	0.40825	-0.89750	0.16680
-0.34972	-0.13469	0.92712	0.90072	-0.32053	0.29319	0.25767	0.93762	0.23342
-0.59857	0.48151	0.64021	0.27958	-0.62337	0.73024	0.75070	0.61609	0.23851
-0.72114	0.54319	0.43001	-0.27080	-0.79231	0.54673	0.63768	0.27782	0.71846
0.97785	0.20857	0.01775	-0.19528	0.87842	0.43617	0.07537	-0.42997	0.89969
-0.18941	-0.65647	0.73018	-0.43888	0.72183	0.53512	0.87836	0.21911	0.42483
0.20411	-0.63583	0.74436	-0.97890	-0.12470	0.16191	0.01012	0.76169	0.64786
0.57094	-0.65335	0.49715	0.50248	0.75697	0.41775	-0.64927	0.01129	0.76048
-0.39848	-0.44001	0.80474	0.90760	-0.06275	0.41511	-0.13216	0.89580	0.42436
-0.34492	-0.47837	0.80759	-0.56832	0.79119	0.22592	0.74703	0.38104	0.54476
-0.32112	-0.90477	0.27977	-0.85711	0.40330	0.32050	0.40281	0.13688	0.90499
0.30030	0.69175	0.65674	-0.58854	-0.40745	0.69828	0.75062	-0.59622	0.28477
-0.52062	-0.41418	0.74660	0.82100	-0.48286	0.30463	0.23433	0.77156	0.59143
-0.81222	0.11647	0.57160	0.41704	-0.56921	0.70857	0.40789	0.81390	0.41376
0.30798	-0.74422	0.59270	-0.44416	0.43845	0.78133	0.84135	0.50389	0.19552
-0.53429	-0.39875	0.74534	-0.38063	0.90079	0.20906	0.75475	0.17200	0.63306
0.40420	0.85366	0.32847	-0.83656	0.19981	0.51014	0.36986	-0.48098	0.79490
-0.21649	0.70155	0.67894	0.87085	-0.17559	0.45912	-0.44131	-0.69065	0.57293
0.37171	-0.63720	0.67514	0.57028	0.73058	0.37555	-0.73254	0.24542	0.63494
0.19928	-0.31404	0.92826	-0.95080	0.16735	0.26074	0.23722	0.93454	0.26524
-0.09292	0.81259	0.57538	0.81395	-0.27083	0.51394	-0.57346	-0.51608	0.63624
0.04576	0.64239	0.76501	0.78618	-0.49563	0.36916	-0.61631	-0.58454	0.52771
0.06767	-0.91460	0.39865	-0.99750	-0.07010	0.00851	-0.02016	0.39823	0.91706
0.60560	-0.78793	0.11147	-0.67135	-0.43067	0.60317	0.42725	0.44011	0.78979
-0.33409	0.82047	0.46392	0.79550	-0.01854	0.60567	-0.50553	-0.57140	0.64649
0.03118	-0.95064	0.30872	-0.06066	0.30650	0.94994	0.99767	0.04834	0.04811
-0.29489	-0.95381	0.05739	0.03385	0.04959	0.99820	-0.95493	0.29630	0.01767
-0.80694	0.24489	0.53747	0.49262	-0.22297	0.84120	0.32584	0.94357	0.05928
0.54562	0.53816	0.64240	-0.45293	-0.45559	0.76635	-0.70509	0.70910	0.00483
-0.36281	0.80225	0.47409	-0.59740	-0.59070	0.54239	0.71518	-0.08643	0.69358
-0.30777	-0.47402	0.82498	0.82098	0.30595	0.48207	-0.48091	0.82565	0.29500
-0.50019	0.79262	0.34866	-0.69174	-0.60796	0.38972	0.52087	-0.04625	0.85238
-0.63205	-0.75965	0.15310	0.67111	-0.43781	0.59827	-0.38745	0.48089	0.78653
0.17109	0.26609	0.94864	0.06010	-0.96387	0.25952	-0.98342	-0.01261	0.18090
-0.89704	0.05557	0.43844	0.11088	0.98863	0.10156	0.42781	-0.13972	0.89300
-0.79338	0.49396	0.35573	-0.22100	-0.77825	0.58778	0.56719	0.38772	0.72662
-0.27968	0.35039	0.89387	0.16037	-0.90090	0.40332	0.94661	0.25615	0.19577
-0.89301	0.28099	0.35153	0.43672	0.35250	0.82766	-0.10865	-0.89263	0.43750
-0.99009	0.12160	0.07022	-0.12113	-0.99258	0.01095	0.07103	0.00234	0.99747
-0.68773	-0.26167	0.67717	0.60177	-0.72724	0.33013	0.40608	0.63454	0.65762
0.59965	0.62810	0.49590	-0.80025	0.46669	0.37657	0.00509	-0.62265	0.78249

0.88989	-0.45616	0.00428	-0.27248	-0.52400	0.80696	0.36586	0.71927	0.59059
-0.52764	-0.54050	0.65533	-0.63150	0.76556	0.12296	0.56815	0.34897	0.74527
-0.81482	-0.16659	0.55526	0.57401	-0.09793	0.81297	-0.08105	0.98115	0.17542
0.18394	0.94498	0.27052	-0.98211	0.18800	0.01103	-0.04043	-0.26770	0.96265
-0.69852	-0.55436	0.45250	0.71285	-0.59435	0.37229	0.06257	0.58262	0.81034
-0.44736	0.80604	0.38753	-0.69168	-0.58650	0.42142	0.56697	-0.07952	0.81990
0.18413	-0.60116	0.77763	-0.19932	0.75188	0.62845	-0.96248	-0.27071	0.01862
-0.36415	-0.82565	0.43093	-0.89671	0.43582	0.07727	0.25160	0.35828	0.89907
0.28508	-0.93778	0.19824	-0.86690	-0.16402	0.47073	0.40892	0.30605	0.85972
-0.25128	-0.94464	0.21101	0.24834	0.14779	0.95733	-0.93551	0.29296	0.19746
0.38859	-0.66907	0.63352	-0.89990	-0.12788	0.41693	0.19795	0.73212	0.65178
-0.43738	0.88072	0.18176	0.85329	0.34265	0.39305	-0.28389	-0.32700	0.90138
0.17263	0.94955	0.26185	-0.77306	-0.03413	0.63341	0.61039	-0.31177	0.72817
-0.16397	-0.62408	0.76396	-0.45517	0.73494	0.50268	0.87517	0.26531	0.40457
-0.23505	0.47509	0.84797	-0.19205	-0.87791	0.43863	0.95282	-0.05976	0.29759
-0.86522	-0.35653	0.35252	-0.25420	0.91796	0.30451	0.43217	-0.17386	0.88487
-0.17157	-0.91090	0.37526	-0.84484	0.33198	0.41957	0.50676	0.24505	0.82653
0.38922	0.06129	0.91910	-0.87869	-0.27473	0.39043	-0.27644	0.95957	0.05307
-0.94941	0.30487	0.07532	-0.08955	-0.49272	0.86557	0.30100	0.81503	0.49510
-0.00301	0.21197	0.97727	0.13895	-0.96771	0.21033	-0.99030	-0.13642	0.02654
0.28052	-0.46414	0.84017	0.21791	0.88325	0.41519	-0.93479	0.06662	0.34891
0.62037	0.67001	0.40772	0.72787	-0.68546	0.01893	-0.29215	-0.28502	0.91291
-0.28936	-0.87165	0.39560	0.95498	-0.29111	0.05712	0.06538	0.39432	0.91665
-0.90427	0.41025	0.11830	0.37056	0.61644	0.69476	-0.21211	-0.67208	0.70945
-0.15369	-0.92579	0.34540	-0.84621	0.30380	0.43776	0.51020	0.22500	0.83010
-0.62387	-0.39778	0.67272	0.77462	-0.42890	0.46477	0.10366	0.81106	0.57571
0.39475	-0.91669	0.06208	-0.01219	0.06233	0.99798	-0.91871	-0.39471	0.01343
0.20335	0.97585	0.07977	-0.68941	0.08485	0.71939	0.69525	-0.20128	0.69001
-0.06853	0.05249	0.99627	0.35488	-0.93202	0.07352	0.93240	0.35860	0.04525
-0.03623	0.99021	0.13480	0.99699	0.02657	0.07281	-0.06852	-0.13703	0.98819
-0.83353	0.46041	0.30537	-0.23687	-0.79717	0.55535	0.49912	0.39056	0.77352
-0.42551	0.84346	0.32791	-0.78298	-0.52482	0.33393	0.45374	-0.11465	0.88373
0.97090	-0.23913	0.01294	-0.23913	-0.96511	0.10667	0.01302	0.10666	0.99421
-0.17039	-0.11878	0.97819	0.74544	-0.66476	0.04913	0.64443	0.73755	0.20181
-0.36528	-0.92391	0.11382	0.26076	0.01582	0.96527	-0.89363	0.38228	0.23514
-0.17249	0.97749	0.12148	-0.97472	-0.18717	0.12202	0.14201	-0.09736	0.98507
-0.43395	0.10391	0.89492	0.02207	-0.99180	0.12586	0.90067	0.07437	0.42810
0.31894	0.83638	0.44581	-0.20621	-0.39787	0.89397	0.92507	-0.37705	0.04558
0.48008	-0.75971	0.43860	-0.29558	0.33066	0.89627	0.82593	0.55992	0.06581
-0.17162	0.78842	0.59071	-0.46864	-0.59276	0.65499	0.86656	-0.16443	0.47121
-0.98679	-0.09370	0.13216	0.16200	-0.57320	0.80324	0.00049	0.81404	0.58081
-0.48096	0.87627	0.02874	-0.84876	-0.47358	0.23521	0.21972	0.08874	0.97152
-0.51302	-0.85793	0.02754	-0.85074	0.51247	0.11668	0.11422	-0.03643	0.99279
-0.41424	0.23020	0.88057	0.65821	-0.59244	0.46452	0.62862	0.77202	0.09389
0.18220	0.89019	0.41758	0.52818	-0.44682	0.72207	-0.82936	-0.08900	0.55159
0.34904	-0.80760	0.47535	-0.08665	0.47727	0.87448	-0.93309	-0.34642	0.09661

Table 8.4. *Table showing RAW 3D chondrule orientation data Aguas Zarcas L2*

Aguas Zarcas L2 Chondrules								
Major Axis Directional Cosines			**Intermediate Axis Directional Cosines**			**Minor Axis Directional Cosines**		
PEllipsoid X1 (dmls)	**PEllipsoid Y1 (dmls)**	**PEllipsoid Z1 (dmls)**	**PEllipsoid X2 (dmls)**	**PEllipsoid Y2 (dmls)**	**PEllipsoid Z2 (dmls)**	**PEllipsoid X3 (dmls)**	**PEllipsoid Y3 (dmls)**	**PEllipsoid Z3 (dmls)**
-0.06141	-0.84636	0.52906	-0.50861	0.48261	0.71302	0.85880	0.22530	0.46011
-0.51601	0.50431	0.69239	-0.24777	-0.86164	0.44293	0.81996	0.05700	0.56957
0.33954	0.82110	0.45882	0.74032	-0.53419	0.40813	-0.58021	-0.20110	0.78925
0.20645	-0.66806	0.71490	-0.97503	-0.07939	0.20739	0.08179	0.73986	0.66777
-0.22749	-0.88970	0.39583	-0.90519	0.34307	0.25089	0.35901	0.30122	0.88339
-0.08587	-0.94425	0.31782	-0.38729	0.32555	0.86257	0.91795	0.04902	0.39366
-0.52129	0.83069	0.19547	-0.64942	-0.53475	0.54064	0.55363	0.15489	0.81823
0.26811	-0.94249	0.19961	-0.90259	-0.17330	0.39407	0.33681	0.28582	0.89714
-0.01473	0.99938	0.03204	0.99980	0.01428	0.01407	-0.01360	-0.03224	0.99939
-0.50196	-0.01604	0.86474	0.36118	-0.91236	0.19273	0.78586	0.40907	0.46376
-0.25404	-0.79376	0.55265	0.73668	0.21145	0.64233	-0.62671	0.57030	0.53103
-0.31670	0.92558	0.20738	-0.88090	-0.36808	0.29755	0.35174	-0.08844	0.93191
-0.41427	-0.66950	0.61656	-0.47495	0.73690	0.48105	0.77640	0.09355	0.62326
-0.34185	-0.56693	0.74949	-0.62749	0.73140	0.26704	0.69957	0.37901	0.60577
0.34307	-0.44027	0.82974	-0.39184	0.73574	0.55241	-0.85368	-0.51464	0.07989
0.27079	0.47859	0.83524	0.73106	-0.66673	0.14502	-0.62628	-0.57134	0.53041
0.19928	0.95643	0.21339	0.97515	-0.21505	0.05322	-0.09679	-0.19748	0.97552

-0.29372	0.90733	0.30080	-0.95040	-0.31087	0.00967	0.10228	-0.28304	0.95364
0.68129	-0.52093	0.51428	-0.06224	0.65878	0.74975	-0.72937	-0.54281	0.41640
-0.04464	-0.98730	0.15247	-0.53675	0.15242	0.82986	0.84256	0.04480	0.53674
-0.86839	0.10492	0.48466	0.16405	0.98311	0.08111	0.46796	-0.14995	0.87094
0.27916	-0.68608	0.67184	-0.27201	0.61450	0.74055	0.92091	0.38947	0.01508
0.90786	0.38524	0.16544	0.34308	-0.90943	0.23501	-0.24099	0.15660	0.95781
-0.61509	-0.68979	0.38191	-0.37882	0.68335	0.62413	0.69149	-0.23922	0.68163
-0.14190	-0.66542	0.73286	0.97554	0.03155	0.21753	-0.16787	0.74580	0.64467
0.11002	-0.99147	0.06994	-0.48106	0.00846	0.87665	0.86976	0.13009	0.47603
0.29209	-0.78563	0.54541	-0.95500	-0.20879	0.21069	0.05165	0.58240	0.81126
-0.47570	-0.35182	0.80619	0.87002	-0.32313	0.37236	0.12950	0.87853	0.45980
0.67687	-0.72278	0.13942	-0.38667	-0.18795	0.90286	0.62637	0.66503	0.40670
-0.37077	0.69298	0.61831	0.54595	-0.37595	0.74873	-0.75131	-0.61518	0.23895
0.10930	0.52479	0.84419	-0.64751	-0.60678	0.46103	0.75418	-0.59701	0.27349
-0.82716	0.26810	0.49390	-0.21878	-0.96316	0.15642	0.51764	0.02133	0.85533
-0.20923	0.89479	0.39444	-0.49562	-0.44475	0.74603	0.84296	-0.03941	0.53653
0.04693	-0.55044	0.83356	0.96026	0.25470	0.11413	-0.27513	0.79508	0.54052
-0.02634	-0.82899	0.55864	-0.82813	0.33110	0.45230	0.55992	0.45072	0.69523
0.06713	0.93180	0.35670	-0.46807	-0.28632	0.83602	0.88114	-0.22309	0.41693
0.14492	0.15626	0.97703	-0.98348	0.13102	0.12492	-0.10849	-0.97899	0.17267
-0.12489	-0.92049	0.37026	0.35690	0.30653	0.88242	-0.92576	0.24235	0.29024
0.62085	-0.78382	0.01326	0.70315	0.56428	0.43263	-0.34659	-0.25928	0.90147
-0.83292	-0.07791	0.54788	0.23486	-0.94622	0.22249	0.50109	0.31399	0.80643
-0.22292	-0.68110	0.69743	-0.90441	0.41149	0.11277	0.36379	0.60562	0.70773
-0.27762	0.95072	0.13805	-0.65078	-0.29181	0.70095	0.70669	0.10476	0.69972
-0.16626	-0.57798	0.79894	-0.89101	0.43516	0.12940	0.42245	0.69035	0.58733
0.57865	-0.79357	0.18817	-0.32262	-0.01082	0.94647	0.74905	0.60838	0.26229
-0.51436	0.24837	0.82082	0.47528	0.87926	0.03178	0.71382	-0.40647	0.57030
-0.66295	-0.03791	0.74770	0.03376	0.99619	0.08044	0.74790	-0.07857	0.65915
-0.54283	-0.74522	0.38728	-0.78359	0.61534	0.08575	0.30222	0.25692	0.91796
-0.68406	0.67791	0.26928	-0.21353	-0.53909	0.81473	0.69748	0.49982	0.51352
0.12312	-0.97802	0.16827	-0.33139	0.11931	0.93592	0.93543	0.17100	0.30942
-0.75064	0.37736	0.54234	-0.05966	-0.85621	0.51317	0.65801	0.35286	0.66522
0.69114	-0.61804	0.37463	-0.69403	-0.71218	0.10549	-0.20161	0.33291	0.92115
-0.12398	-0.97838	0.16555	-0.90273	0.18048	0.39053	0.41196	0.10103	0.90559
-0.53432	-0.83763	0.11349	-0.65239	0.49403	0.57474	0.53749	-0.23305	0.81043
-0.27883	0.28198	0.91801	-0.04360	-0.95865	0.28123	0.95935	0.03839	0.27959
-0.08675	0.97925	0.18314	-0.93621	-0.14298	0.32105	0.34058	-0.14361	0.92919
0.26582	-0.96267	0.05114	0.38202	0.15390	0.91125	-0.88510	-0.22269	0.40867
-0.04644	-0.73745	0.67380	-0.86414	0.36804	0.34324	0.50111	0.56632	0.65435
-0.28303	-0.95839	0.03711	-0.69772	0.23229	0.67766	0.65809	-0.16591	0.73444
0.65257	-0.75176	0.09491	-0.75603	-0.63759	0.14799	0.05074	0.16833	0.98442
-0.53311	0.15676	0.83140	0.06704	-0.97177	0.22621	0.84339	0.17633	0.50755
-0.12379	-0.92075	0.36999	-0.73984	0.33412	0.58396	0.66130	0.20144	0.72257
0.34881	-0.93694	0.02191	0.79108	0.30688	0.52916	-0.50251	-0.16725	0.84824
-0.14517	0.89252	0.42701	-0.43091	-0.44553	0.78474	0.89064	-0.07009	0.44927
-0.76486	0.06550	0.64086	0.21980	-0.90859	0.35519	0.60554	0.41253	0.68055
-0.47529	0.87564	0.08573	-0.34833	-0.27675	0.89559	0.80794	0.39580	0.43655
-0.35734	-0.36194	0.86099	-0.36816	0.90180	0.22630	0.85835	0.23612	0.45550
-0.91947	0.38489	0.08026	-0.34717	-0.89062	0.29374	0.18454	0.24222	0.95251
-0.23898	0.29373	0.92553	0.45609	-0.80751	0.37404	0.85724	0.51152	0.05901
0.45303	0.84880	0.27260	-0.47883	-0.02626	0.87751	0.75199	-0.52806	0.39454
-0.32350	-0.92748	0.18740	-0.87175	0.36915	0.32213	0.36795	0.05916	0.92796
0.69003	-0.02727	0.72327	-0.72068	0.06655	0.69007	-0.06695	-0.99741	0.02627
-0.67154	0.62518	0.39773	0.16036	-0.40142	0.90175	0.72341	0.66934	0.16932
0.52581	-0.60502	0.59789	0.65148	0.73839	0.17425	-0.54690	0.29789	0.78241
0.04035	0.16371	0.98568	-0.95116	-0.29586	0.08807	0.30604	-0.94110	0.14377
0.05401	-0.99057	0.12594	-0.92717	-0.00292	0.37462	0.37072	0.13701	0.91858
-0.12290	-0.96415	0.23520	0.09549	0.22441	0.96980	-0.98781	0.14165	0.06449
-0.15099	-0.66468	0.73172	-0.73689	0.56909	0.36489	0.65894	0.48410	0.57572
0.04084	0.56715	0.82260	0.32390	-0.78635	0.52607	-0.94521	-0.24496	0.21581
0.18191	-0.81396	0.55171	0.15960	0.57807	0.80023	-0.97028	-0.05752	0.23506
-0.57013	-0.40837	0.71287	-0.56345	0.82584	0.02246	0.59789	0.38886	0.70093
-0.61857	0.57002	0.54079	0.61573	-0.07590	0.78429	-0.48811	-0.81812	0.30403
0.73310	-0.34316	0.58721	0.39490	0.91770	0.04329	-0.55374	0.20015	0.80828
0.19818	-0.96908	0.14698	0.96541	0.21891	0.14167	-0.16946	0.11382	0.97894
-0.93089	-0.28222	0.23195	0.32477	-0.93008	0.17172	0.16727	0.23518	0.95745
-0.43054	-0.71974	0.54462	0.06626	0.57658	0.81435	0.90014	-0.38669	0.20055
0.56106	-0.80643	0.18677	-0.56000	-0.20361	0.80309	0.60961	0.55517	0.56584
-0.86959	-0.29540	0.39567	0.44587	-0.81408	0.37213	0.21218	0.50001	0.83962
0.71063	-0.66865	0.21890	-0.34556	-0.06070	0.93643	0.61286	0.74110	0.27419
0.15710	0.91479	0.37213	0.64760	-0.37991	0.66051	-0.74561	-0.13723	0.65210
0.44385	0.76545	0.46592	-0.89430	0.41134	0.17616	-0.05681	-0.49486	0.86712
0.14614	0.93806	0.31416	-0.89516	-0.00979	0.44564	0.42111	-0.34635	0.83828
-0.11567	0.93950	0.32242	0.93191	-0.00968	0.36256	-0.34374	-0.34240	0.87442

-0.56445	0.77231	0.29144	0.80814	0.58897	0.00440	0.16825	-0.23801	0.95658
-0.15945	0.98635	0.04100	-0.84263	-0.15762	0.51491	0.51435	0.04755	0.85626
-0.62826	-0.69348	0.35267	-0.48432	0.70337	0.52029	0.60887	-0.15607	0.77777
-0.30733	-0.23199	0.92289	0.93165	-0.27092	0.24214	0.19386	0.93423	0.29940
-0.76134	0.47557	0.44068	0.10129	-0.58410	0.80534	0.64039	0.65777	0.39653
-0.58310	0.42307	0.69355	-0.41768	-0.88835	0.19074	0.69681	-0.17846	0.69470
-0.10343	0.95077	0.29212	-0.65683	-0.28584	0.69776	0.74691	-0.11971	0.65406
-0.70254	-0.37339	0.60582	0.70305	-0.23223	0.67216	-0.11029	0.89814	0.42566
0.54398	-0.23717	0.80489	-0.51409	-0.85231	0.09631	-0.66317	0.46617	0.58556
-0.13258	-0.83165	0.53924	-0.88628	0.34305	0.31117	0.44377	0.43666	0.78256
0.07789	0.34144	0.93667	0.80464	-0.57626	0.14314	-0.58864	-0.74253	0.31962
-0.48773	0.77069	0.41008	-0.71650	-0.62175	0.31632	0.49875	-0.13954	0.85544

Table 8.8.5. *Table showing RAW 3D chondrule orientation data Aguas Zarcas L3*

Aguas Zarcas L3 Chondrules								
Major Axis Directional Cosines			**Intermediate Axis Directional Cosines**			**Minor Axis Directional Cosines**		
PEllipsoid X1 (dmls)	**PEllipsoid Y1 (dmls)**	**PEllipsoid Z1 (dmls)**	**PEllipsoid X2 (dmls)**	**PEllipsoid Y2 (dmls)**	**PEllipsoid Z2 (dmls)**	**PEllipsoid X3 (dmls)**	**PEllipsoid Y3 (dmls)**	**PEllipsoid Z3 (dmls)**
-0.20156	0.90849	0.36610	0.40502	-0.26301	0.87566	-0.89182	-0.32477	0.31494
-0.29366	0.87892	0.37587	0.81417	0.02393	0.58013	-0.50089	-0.47638	0.72262
-0.62403	0.43424	0.64963	0.75964	0.53196	0.37413	0.18312	-0.72695	0.66182
-0.18994	0.18306	0.96458	0.47880	-0.84045	0.25378	0.85713	0.51004	0.07199
-0.52356	0.68333	0.50887	0.40767	-0.32354	0.85389	-0.74812	-0.65451	0.10918
-0.69108	0.71962	0.06750	-0.67857	-0.67813	0.28229	0.24891	0.14928	0.95695
0.46606	-0.85476	0.22842	-0.59259	-0.10986	0.79798	0.65698	0.50727	0.55772
-0.82639	0.48849	0.28010	-0.39703	-0.85821	0.32533	0.39931	0.15764	0.90316
-0.42235	0.90395	0.06711	0.90624	0.42262	0.01086	0.01855	-0.06540	0.99769
0.96900	-0.24480	0.03335	-0.15425	-0.49397	0.85569	0.19300	0.83431	0.51642
-0.38229	0.43581	0.81481	-0.32547	-0.88879	0.32268	0.86483	-0.14183	0.48162
0.51041	-0.77643	0.36964	-0.01573	0.42135	0.90676	-0.85979	-0.46864	0.20284
0.54838	-0.80942	0.21004	-0.83394	-0.51079	0.20888	0.06179	0.28971	0.95512
-0.58537	0.80069	0.12744	0.78600	0.52189	0.33141	-0.19884	-0.29417	0.93484
0.83325	0.15787	0.52987	-0.43831	0.77277	0.45903	-0.33700	-0.61474	0.71311
-0.55016	0.78315	0.28982	0.33717	-0.10920	0.93509	-0.76397	-0.61217	0.20398
0.65377	-0.69777	0.29276	0.69516	0.70665	0.13188	-0.29890	0.11730	0.94705
0.11855	0.75287	0.64741	0.81686	-0.44464	0.36749	-0.56453	-0.48527	0.66770
-0.80272	0.55184	0.22609	-0.53488	-0.83387	0.13627	0.26373	-0.01154	0.96453
-0.56896	0.81989	0.06374	-0.48710	-0.39844	0.77716	0.66258	0.41113	0.62606
0.20241	0.97897	0.02529	-0.86606	0.16689	0.47127	0.45714	-0.11729	0.88163
0.36047	0.77520	0.51877	-0.87794	0.09409	0.46944	0.31510	-0.62467	0.71449
-0.29829	0.93901	0.17112	0.20966	-0.11044	0.97152	-0.93116	-0.32567	0.16393
-0.69756	0.47998	0.53200	-0.49662	-0.85908	0.12390	0.51650	-0.17778	0.83763
0.71511	0.20107	0.66947	-0.62314	0.61732	0.48021	-0.31673	-0.76058	0.56675
-0.90461	0.31768	0.28418	0.27623	-0.07082	0.95848	-0.32462	-0.94555	0.02368
0.73149	-0.61531	0.29382	-0.17609	0.24582	0.95319	-0.65873	-0.74898	0.07146
0.93116	-0.08728	0.35402	-0.30137	0.36233	0.88199	-0.20525	-0.92796	0.31108
0.54299	-0.76691	0.34207	0.25208	0.53743	0.80475	-0.80101	-0.35075	0.48514
-0.42945	0.59843	0.67636	0.55045	-0.42029	0.72137	-0.71595	-0.68209	0.14892
-0.27813	0.63186	0.72347	0.61831	-0.45862	0.63825	-0.73508	-0.62484	0.26312
-0.12904	0.32750	0.93600	0.95086	-0.22704	0.21052	-0.28145	-0.91717	0.28211
-0.27664	-0.20769	0.93826	0.59116	0.73299	0.33655	0.75763	-0.64776	0.07999
0.09628	-0.07917	0.99220	-0.99510	0.01498	0.09775	0.02261	0.99675	0.07734
0.54036	-0.83973	0.05364	0.83985	0.54216	0.02696	-0.05172	0.03048	0.99820
0.26261	0.42123	0.86810	-0.87919	0.47516	0.03541	-0.39757	-0.77252	0.49513
-0.00969	-0.01588	0.99983	-0.32443	0.94584	0.01188	0.94586	0.32425	0.01432
0.13193	0.39998	0.90698	0.56526	-0.78199	0.26263	-0.81429	-0.47803	0.32926
0.23609	-0.18599	0.95377	-0.40834	0.87166	0.27105	-0.88177	-0.45346	0.12984
-0.13134	-0.94955	0.28479	0.99130	-0.12342	0.04567	-0.00822	0.28831	0.95750
0.07452	0.68145	0.72807	0.74979	-0.51964	0.40963	-0.65747	-0.51537	0.54966
-0.57925	0.76015	0.29437	0.14672	-0.25800	0.95494	0.80184	0.59633	0.03792
-0.16696	0.91556	0.36589	0.45175	-0.25883	0.85378	-0.87639	-0.30783	0.37039
-0.09124	-0.90070	0.42475	-0.47220	0.41466	0.77787	0.87676	0.12960	0.46314
-0.99849	0.00228	0.05490	0.05442	0.17875	0.98239	0.00757	-0.98389	0.17861
0.57650	0.72866	0.36974	-0.18098	-0.32739	0.92740	-0.79680	0.60156	0.05687
-0.55128	-0.63558	0.54049	0.81616	-0.54525	0.19128	0.17313	0.54658	0.81932
-0.38356	0.90817	0.16766	0.88569	0.31031	0.34535	-0.26161	-0.28096	0.92337
-0.01197	-0.96843	0.24901	-0.83652	0.14613	0.52809	0.54780	0.20198	0.81186
-0.56318	0.54111	0.62453	0.69215	-0.10395	0.71423	-0.45139	-0.83450	0.31599
-0.50754	0.65590	0.55875	0.85807	0.44365	0.25863	0.07825	-0.61071	0.78798

0.25222	-0.90801	0.33451	0.58275	0.41850	0.69660	-0.77252	0.01924	0.63470
0.24002	-0.69930	0.67333	0.46191	0.69232	0.55437	-0.85383	0.17796	0.48919
-0.35868	0.68630	0.63273	0.64931	-0.30355	0.69732	-0.67063	-0.66095	0.33675
0.00628	-0.06672	0.99775	-0.06874	0.99538	0.06699	-0.99762	-0.06901	0.00166
0.37453	0.76374	0.52577	0.07206	-0.58930	0.80469	-0.92441	0.26349	0.27574
0.43660	-0.37497	0.81779	-0.66292	0.48045	0.57420	0.60822	0.79282	0.03881
0.67995	-0.38993	0.62098	-0.68087	-0.65011	0.33731	-0.27217	0.65216	0.70754
0.93795	0.02185	0.34607	-0.33866	-0.15678	0.92776	-0.07453	0.98739	0.13966
0.60584	-0.21102	0.76709	-0.75414	0.15480	0.63820	0.25342	0.96515	0.06535
-0.37480	0.88548	0.27468	0.65877	0.04589	0.75094	-0.65234	-0.46240	0.60053
0.19706	0.91370	0.35541	0.87027	-0.32995	0.36573	-0.45144	-0.23724	0.86019
0.80377	0.31632	0.50388	-0.16872	-0.69098	0.70291	-0.57052	0.64999	0.50202
0.48915	-0.78767	0.37459	0.09348	0.47435	0.87536	-0.86718	-0.39317	0.30566
0.71284	-0.11950	0.69108	-0.69823	-0.21356	0.68328	-0.06593	0.96959	0.23567
0.61103	-0.45490	0.64785	-0.67344	0.13144	0.72746	0.41608	0.88079	0.22604
0.02509	0.65474	0.75543	0.20710	-0.74268	0.63681	-0.97800	-0.14047	0.15424
0.21062	0.15002	0.96599	-0.58539	0.81075	0.00172	-0.78292	-0.56584	0.25858
-0.38950	0.80186	0.45311	0.61857	-0.13674	0.77374	-0.68239	-0.58165	0.44275
0.15581	-0.98734	0.02976	-0.45625	-0.04522	0.88870	0.87611	0.15205	0.45752
0.44096	0.62839	0.64084	0.81508	-0.57930	0.00718	-0.37575	-0.51917	0.76764
0.20163	0.49875	0.84297	0.74428	-0.63748	0.19914	-0.63670	-0.58726	0.49975
-0.12173	0.72995	0.67258	0.36196	-0.59831	0.71485	-0.92421	-0.33046	0.19138
0.53594	0.71198	0.45371	-0.77660	0.20496	0.59572	0.33115	-0.67162	0.66277
0.62406	0.53921	0.56551	-0.66635	-0.01072	0.74557	0.40808	-0.84210	0.35261
-0.31694	0.94767	0.03829	0.87027	0.27453	0.40897	-0.37706	-0.16295	0.91174
0.80376	-0.25475	0.53766	0.18669	0.96604	0.17863	-0.56491	-0.04320	0.82402
-0.25647	0.32435	0.91051	0.37078	-0.83693	0.40258	0.89260	0.44085	0.09439
-0.15849	0.76875	0.61960	-0.15991	-0.63923	0.75221	0.97433	0.02014	0.22424
-0.57477	0.72390	0.38158	0.62888	0.09239	0.77199	-0.52359	-0.68369	0.50835
-0.24968	0.95884	0.13526	0.34477	-0.04250	0.93773	-0.90487	-0.28076	0.31996
-0.40358	0.67041	0.62263	0.86735	0.06370	0.49361	-0.29126	-0.73925	0.60719
-0.30326	0.72136	0.62264	0.94936	0.17235	0.26271	-0.08219	-0.67078	0.73709
-0.11946	0.72852	0.67453	0.67173	-0.44098	0.59524	-0.73110	-0.52420	0.43669
0.91653	-0.39869	0.03188	0.31056	0.75962	0.57143	-0.25205	-0.51383	0.82003
-0.00647	0.69217	0.72171	0.53215	-0.60866	0.58852	-0.84662	-0.38787	0.36440
-0.48035	0.69505	0.53495	0.77983	0.05930	0.62318	-0.40142	-0.71651	0.57050
0.17456	0.70031	0.69216	0.85799	-0.45308	0.24203	-0.48310	-0.55162	0.67995
-0.06605	0.88592	0.45911	0.63257	-0.31867	0.70591	-0.77168	-0.33705	0.53935
-0.37585	0.52616	0.76282	0.45012	-0.61589	0.64659	-0.81002	-0.58638	0.00535
-0.03341	0.01537	0.99932	0.51351	0.85807	0.00397	0.85743	-0.51330	0.03656
0.23062	0.95680	0.17708	-0.47440	-0.04833	0.87898	0.84956	-0.28672	0.44276
0.29806	0.87037	0.39194	-0.34862	-0.28299	0.89352	0.88861	-0.40296	0.21908
0.49127	-0.57818	0.65143	-0.84863	-0.14929	0.50748	0.19616	0.80214	0.56400
-0.58390	-0.68206	0.44030	0.53658	0.08276	0.83978	-0.60922	0.72660	0.31765
0.79487	-0.08604	0.60066	-0.55685	0.28983	0.77841	-0.24106	-0.95320	0.18247
0.55143	-0.44389	0.70633	0.28176	0.89603	0.34314	-0.78520	0.00980	0.61916
-0.21731	0.90464	0.36662	0.95832	0.12635	0.25625	-0.18549	-0.40703	0.89439
0.08698	-0.36249	0.92792	0.97240	0.23333	0.00000	-0.21651	0.90231	0.37278
-0.42701	0.57622	0.69687	-0.77551	-0.62970	0.04549	0.46503	-0.52100	0.71575
0.59095	-0.32621	0.73781	-0.22994	0.80854	0.54166	-0.77324	-0.48975	0.40279
-0.84895	0.52835	0.01153	0.13928	0.20264	0.96930	-0.50979	-0.82449	0.24562
-0.14889	0.98879	0.01154	-0.33488	-0.06140	0.94026	0.93042	0.13613	0.34027
0.28607	0.68169	0.67340	0.80255	-0.55442	0.22032	-0.52353	-0.47741	0.70569
-0.60716	0.70785	0.36099	-0.66878	-0.70057	0.24888	0.42906	-0.09031	0.89875
-0.38020	0.13023	0.91569	0.20214	-0.95440	0.21967	0.90254	0.26862	0.33654
-0.29160	0.54130	0.78865	-0.65818	-0.71181	0.24520	0.69409	-0.44757	0.56384

Table 8.6*. Table showing RAW 3D chondrule orientation data Cold Bokkeveld L1*

Cold Bokkeveld L1 Chondrules								
Major Axis Directional Cosines			**Intermediate Axis Directional Cosines**			**Minor Axis Directional Cosines**		
PEllipsoid X1 (dmls)	**PEllipsoid Y1 (dmls)**	**PEllipsoid Z1 (dmls)**	**PEllipsoid X2 (dmls)**	**PEllipsoid Y2 (dmls)**	**PEllipsoid Z2 (dmls)**	**PEllipsoid X3 (dmls)**	**PEllipsoid Y3 (dmls)**	**PEllipsoid Z3 (dmls)**
-0.07056	0.00316	0.99750	0.81725	0.57356	0.05599	0.57195	-0.81916	0.04305
-0.40339	-0.37149	0.83623	0.28499	0.81742	0.50061	0.86952	-0.44026	0.22387
-0.56073	-0.28989	0.77559	0.76255	0.18420	0.62015	-0.32264	0.93917	0.11777
-0.17926	0.06040	0.98195	0.48388	0.87446	0.03454	0.85658	-0.48133	0.18598
-0.29983	-0.26684	0.91591	0.90962	0.20943	0.35878	-0.28755	0.94071	0.17993
-0.46722	-0.43939	0.76723	0.86094	-0.02861	0.50790	-0.20122	0.89784	0.39166

-0.65864	-0.50921	0.55398	0.59561	0.09709	0.79739	-0.45983	0.85515	0.23934
0.86663	-0.13802	0.47948	-0.49156	-0.07134	0.86792	0.08558	0.98786	0.12967
-0.85428	-0.50816	0.10944	0.15166	-0.04228	0.98753	-0.49720	0.86022	0.11318
-0.91021	-0.01485	0.41389	0.41416	-0.03037	0.90970	-0.00094	0.99943	0.03379
0.11942	-0.18283	0.97587	-0.99007	-0.09534	0.10329	-0.07416	0.97851	0.19240
-0.91472	0.21817	0.34012	0.37065	0.11777	0.92128	-0.16093	-0.96878	0.18859
-0.25041	-0.54109	0.80282	0.95447	0.00090	0.29832	-0.16214	0.84096	0.51623
-0.74920	-0.64963	0.12915	0.65992	-0.74878	0.06183	0.05654	0.13155	0.98970
0.18854	-0.24372	0.95134	-0.95374	0.18553	0.23654	0.23415	0.95194	0.19747
-0.96094	0.27529	0.02833	0.27662	0.95853	0.06860	0.00827	-0.07376	0.99724
0.46851	-0.27748	0.83875	-0.83493	0.17126	0.52304	0.28877	0.94534	0.15144
-0.89774	-0.40171	0.18080	0.14304	0.12238	0.98212	0.41665	-0.90755	0.05241
0.91267	-0.40319	0.06681	-0.31962	-0.60227	0.73152	0.25470	0.68899	0.67854
-0.32517	-0.08089	0.94219	0.36188	0.90985	0.20301	0.87367	-0.40697	0.26659
0.91627	-0.32659	0.23193	-0.27703	-0.09845	0.95581	0.28932	0.94002	0.18068
0.28143	0.17496	0.94350	-0.85102	-0.40878	0.32965	0.44336	-0.89571	0.03385
-0.35281	-0.58934	0.72678	0.72866	0.31424	0.60853	-0.58702	0.74427	0.31856
-0.55196	-0.05145	0.83228	0.11654	-0.99306	0.01590	0.82568	0.10577	0.55413
0.70983	-0.23441	0.66422	-0.69751	-0.10260	0.70919	0.09809	0.96671	0.23633
-0.44791	-0.05225	0.89255	0.89215	0.03948	0.45002	-0.05875	0.99785	0.02893
0.49780	0.57900	0.64573	-0.45012	-0.46394	0.76299	0.74135	-0.67047	0.02967
-0.59567	0.07777	0.79946	0.78357	0.27512	0.55707	0.17663	-0.95826	0.22482
-0.38503	-0.17322	0.90650	0.82971	-0.49510	0.25780	0.40416	0.85139	0.33435
0.35819	-0.43317	0.82709	-0.83458	-0.54567	0.07565	-0.41855	0.71736	0.55696
-0.10506	0.24370	0.96415	0.85960	-0.46525	0.21126	-0.50005	-0.85097	0.16060
-0.11785	-0.63133	0.76651	0.91948	0.22217	0.32435	-0.37507	0.74301	0.55431
-0.45454	-0.25433	0.85365	0.86034	-0.37356	0.34680	0.23069	0.89206	0.38861
0.95771	-0.22642	0.17754	-0.21761	-0.16632	0.96176	0.18824	0.95973	0.20855
-0.94817	-0.12097	0.29384	0.31777	-0.35862	0.87773	-0.00080	0.92561	0.37847
-0.12413	-0.21594	0.96849	0.97325	0.16369	0.16124	-0.19335	0.96259	0.18984
-0.23991	0.34140	0.90879	-0.36263	-0.89988	0.24232	0.90052	-0.27142	0.33969
0.91113	0.15911	0.38016	-0.34961	-0.19001	0.91743	-0.21821	0.96880	0.11750
-0.22401	-0.40237	0.88765	0.88441	-0.46657	0.01170	0.40944	0.78766	0.46038
0.40117	0.61918	0.67504	-0.83089	-0.06424	0.55272	0.38560	-0.78262	0.48870
-0.96275	-0.26676	0.04410	0.10836	-0.23125	0.96684	-0.24772	0.93561	0.25154
-0.70588	0.06798	0.70506	0.57081	0.64398	0.50938	0.41942	-0.76202	0.49338
-0.62076	-0.61598	0.48501	-0.34489	0.77011	0.53665	0.70407	-0.16585	0.69049
-0.14450	0.09934	0.98451	0.56405	-0.80920	0.16444	0.81300	0.57907	0.06090
0.03732	0.03429	0.99872	-0.99760	-0.05712	0.03924	0.05839	-0.99778	0.03208
-0.60885	0.25852	0.74998	0.71851	-0.22097	0.65948	-0.33621	-0.94039	0.05122
0.10019	-0.25671	0.96128	-0.69227	0.67596	0.25267	0.71465	0.69079	0.10999
-0.07889	0.23376	0.96909	0.75783	-0.61751	0.21065	-0.64766	-0.75102	0.12843
-0.30727	-0.13298	0.94229	0.89186	-0.38563	0.23640	0.33193	0.91302	0.23709
-0.81717	0.49664	0.29255	-0.03374	-0.54790	0.83586	0.57541	0.67317	0.46448
-0.98968	0.10194	0.10073	0.00460	-0.67995	0.73324	0.14323	0.72614	0.67247
-0.99863	0.04617	0.02446	0.02475	0.00580	0.99968	-0.04602	-0.99892	0.00694
-0.67848	-0.18283	0.71151	0.73096	-0.07136	0.67868	-0.07330	0.98055	0.18206
0.97227	0.17197	0.15851	-0.11550	-0.23630	0.96479	-0.20337	0.95634	0.20989
-0.35708	-0.81622	0.45418	-0.81774	0.50816	0.27032	0.45143	0.27488	0.84891
-0.39722	-0.85965	0.32127	0.39978	0.15303	0.90375	-0.82607	0.48742	0.28289
-0.14509	0.77555	0.61439	0.92045	-0.12198	0.37133	-0.36293	-0.61940	0.69616
0.68000	-0.58284	0.44485	-0.27408	0.36068	0.89151	-0.68006	-0.72816	0.08552
-0.77086	0.15446	0.61799	0.63021	0.04359	0.77520	-0.09280	-0.98704	0.13094
-0.27892	-0.06023	0.95842	0.93342	-0.25157	0.25583	0.22570	0.96596	0.12639
-0.40329	-0.23653	0.88398	0.90993	-0.00137	0.41476	-0.09689	0.97162	0.21577
0.08873	0.16010	0.98310	-0.96983	-0.21111	0.12191	0.22706	-0.96426	0.13654
-0.76961	0.39120	0.50464	0.60955	0.21480	0.76309	-0.19012	-0.89489	0.40377
-0.11746	0.06180	0.99115	0.78578	0.61608	0.05471	0.60725	-0.78526	0.12093
-0.97017	-0.21393	0.11403	0.19660	-0.41909	0.88641	-0.14184	0.88238	0.44864
0.42510	-0.01666	0.90499	-0.56921	-0.78231	0.25297	-0.70377	0.62267	0.34205
0.02121	0.02989	0.99933	-0.98896	-0.14599	0.02536	0.14665	-0.98884	0.02646
-0.22731	-0.10204	0.96846	0.87450	0.41618	0.24910	0.42847	-0.90354	0.00537
0.79730	-0.50282	0.33389	-0.49134	-0.21940	0.84288	0.35056	0.83609	0.42198
0.40956	-0.04743	0.91105	-0.52657	-0.82779	0.19363	-0.74497	0.55904	0.36400
-0.91702	-0.26311	0.29974	0.36878	-0.27318	0.88847	-0.15188	0.92528	0.34754
-0.92385	-0.25063	0.28929	0.35577	-0.84104	0.40754	0.14116	0.47942	0.86616
-0.79124	0.14540	0.59396	0.56458	0.54686	0.61823	0.23492	-0.82450	0.51479
-0.53250	-0.81380	0.23276	-0.64042	0.56717	0.51786	0.55345	-0.12669	0.82319
-0.09099	-0.07629	0.99293	0.95416	0.27878	0.10886	-0.28512	0.95732	0.04743
0.20722	0.30766	0.92866	-0.55564	-0.74428	0.37056	0.80519	-0.59278	0.01672
-0.92466	0.14091	0.35378	0.37739	0.21492	0.90077	-0.05089	-0.96641	0.25191
0.93972	-0.00448	0.34192	-0.10089	-0.95903	0.26472	-0.32672	0.28326	0.90167
-0.03556	-0.36111	0.93185	0.99867	0.02197	0.04663	-0.03731	0.93227	0.35985
0.29964	-0.16762	0.93922	-0.94292	0.09796	0.31830	0.14536	0.98097	0.12870
-0.59494	-0.24672	0.76497	0.79387	-0.03146	0.60728	-0.12576	0.96858	0.21458

-0.55234	0.00332	0.83361	0.81338	-0.21686	0.53980	0.18257	0.97620	0.11708
0.74430	0.18983	0.64030	-0.66778	0.19738	0.71772	0.00986	-0.96177	0.27367
0.97992	0.08418	0.18076	-0.19395	0.61274	0.76612	-0.04627	-0.78579	0.61676
-0.89732	-0.33966	0.28187	-0.01414	0.66040	0.75078	0.44116	-0.66970	0.59740
-0.10582	-0.84536	0.52361	0.97390	0.01822	0.22623	-0.20078	0.53388	0.82137
-0.51573	-0.25850	0.81682	0.83769	-0.35211	0.41748	0.17970	0.89955	0.39814
-0.31561	0.33894	0.88629	0.92831	-0.08319	0.36239	-0.19655	-0.93712	0.28839
-0.31758	-0.54010	0.77938	0.89674	-0.43824	0.06171	0.30823	0.71850	0.62351
0.17437	-0.89090	0.41939	0.89052	0.32443	0.31893	-0.42020	0.31786	0.84994
-0.65491	-0.42460	0.62515	-0.25457	0.90284	0.34653	0.71154	-0.06780	0.69936
-0.72374	-0.39580	0.56528	0.56037	0.14097	0.81616	-0.40273	0.90745	0.11977
-0.40219	-0.64655	0.64824	0.26270	0.59677	0.75819	0.87706	-0.47523	0.07016
-0.38294	-0.37819	0.84281	-0.04045	0.91835	0.39371	0.92289	-0.11668	0.36697
-0.35666	-0.56010	0.74772	0.86708	0.09951	0.48813	-0.34780	0.82243	0.45016

Table 8.7. *Table showing RAW 3D orientation data Cold Bokkeveld L1 metal grains*

Cold Bokkeveld L1 Metal Grains								
Major Axis Directional Cosines			Intermediate Axis Directional Cosines			Minor Axis Directional Cosines		
PEllipsoid X1 (dmls)	PEllipsoid Y1 (dmls)	PEllipsoid Z1 (dmls)	PEllipsoid X2 (dmls)	PEllipsoid Y2 (dmls)	PEllipsoid Z2 (dmls)	PEllipsoid X3 (dmls)	PEllipsoid Y3 (dmls)	PEllipsoid Z3 (dmls)
-0.31316	0.14809	0.93809	0.71034	-0.61911	0.33486	0.63036	0.77122	0.08868
0.17275	0.06749	0.98265	-0.96546	0.20917	0.15536	-0.19505	-0.97555	0.10129
-0.60574	-0.18727	0.77331	0.43749	-0.89019	0.12711	0.66459	0.41531	0.62115
-0.36777	0.71690	0.59229	-0.10275	-0.66435	0.74033	0.92423	0.21141	0.31799
0.27567	-0.75473	0.59531	-0.40697	0.46943	0.78359	0.87085	0.45828	0.17775
-0.98320	-0.09646	0.15499	0.12619	-0.97261	0.19523	0.13191	0.21151	0.96843
-0.37469	0.40283	0.83506	0.92557	0.10990	0.36229	-0.05417	-0.90865	0.41403
-0.29007	-0.41290	0.86335	-0.26691	0.90124	0.34135	0.91903	0.13142	0.37163
0.31351	-0.17250	0.93379	-0.87236	0.33612	0.35498	0.37510	0.92589	0.04510
-0.36640	0.31596	0.87517	-0.64961	-0.76026	0.00251	0.66615	-0.56760	0.48381
-0.74843	-0.58637	0.30987	0.27738	0.14765	0.94935	-0.60242	0.79647	0.05214
-0.59343	0.05047	0.80331	0.77670	0.29774	0.55506	0.21117	-0.95331	0.21589
-0.24468	0.10834	0.96353	0.90166	-0.34003	0.26720	-0.35658	-0.93415	0.01449
0.98267	-0.03584	0.18188	-0.17320	-0.52723	0.83189	-0.06608	0.84897	0.52429
-0.17336	-0.95880	0.22506	0.00877	0.22701	0.97385	0.98482	-0.17080	0.03095
0.48587	-0.22920	0.84345	-0.87162	-0.05536	0.48705	0.06494	0.97180	0.22667
0.42975	0.18579	0.88363	0.20878	-0.97253	0.10294	-0.87848	-0.14024	0.45673
0.79756	0.41031	0.44221	-0.44496	-0.09484	0.89051	0.40732	-0.90700	0.10693
0.02180	-0.44348	0.89602	0.35296	0.84194	0.40812	-0.93539	0.30736	0.17488
-0.75674	0.53593	0.37434	0.17288	-0.38818	0.90522	0.63045	0.74973	0.20110
-0.95880	-0.13489	0.25001	0.21629	0.22395	0.95030	0.18418	-0.96522	0.18555
-0.68477	0.64993	0.32967	0.50608	0.09860	0.85683	-0.52438	-0.75357	0.39644
-0.02648	0.89632	0.44262	0.32941	-0.41022	0.85042	-0.94382	-0.16833	0.28440
-0.70813	0.53700	0.45846	0.45878	-0.14363	0.87687	-0.53673	-0.83126	0.14466
-0.95306	-0.19596	0.23081	0.28762	-0.82416	0.48789	0.09462	0.53138	0.84183
-0.54799	-0.76247	0.34402	0.64790	-0.12676	0.75110	-0.52909	0.63449	0.56347
0.71813	-0.55388	0.42131	-0.32465	0.26885	0.90682	-0.61554	-0.78800	0.01325
-0.01804	-0.29619	0.95496	-0.05328	0.95404	0.29490	0.99842	0.04556	0.03299
0.65300	0.58915	0.47592	-0.22659	-0.44764	0.86503	-0.72267	0.67270	0.15881
0.63973	-0.44040	0.62992	-0.68862	0.03562	0.72425	0.34140	0.89709	0.28048
-0.47185	0.05395	0.88003	0.80328	0.43777	0.40386	0.36346	-0.89747	0.24990
0.62348	0.10763	0.77440	-0.56425	-0.62369	0.54096	-0.54121	0.77423	0.32813
0.58633	-0.15947	0.79422	-0.78185	-0.36792	0.50333	-0.21195	0.91608	0.34041
-0.53874	-0.32894	0.77560	0.83495	-0.08569	0.54362	-0.11235	0.94046	0.32081
-0.38787	-0.22367	0.89417	-0.05061	0.97382	0.22164	0.92033	-0.04071	0.38903
-0.28882	-0.11486	0.95047	0.88784	-0.40361	0.22102	0.35823	0.90769	0.21855
0.72508	0.16847	0.66774	-0.68578	0.08807	0.72246	0.06290	-0.98177	0.17939
0.48634	0.06223	0.87155	-0.84970	0.26618	0.45515	-0.20366	-0.96191	0.18233
0.45286	-0.23401	0.86032	-0.79149	0.33870	0.50875	0.41045	0.91133	0.03183
-0.63144	0.75658	0.16992	0.66218	0.41209	0.62586	-0.40349	-0.50771	0.76120
0.67552	0.56521	0.47351	-0.54228	-0.05429	0.83844	0.49960	-0.82316	0.26983
0.27141	-0.11203	0.95592	-0.90459	0.30952	0.29311	0.32871	0.94427	0.01734
-0.14419	0.04765	0.98840	0.75055	-0.64568	0.14062	0.64489	0.76212	0.05733
-0.75749	-0.26482	0.59672	0.65211	-0.26346	0.71088	-0.03104	0.92761	0.37226
0.16243	0.36280	0.91760	-0.29194	-0.87064	0.39592	-0.94254	0.33220	0.03550
-0.59745	0.05282	0.80016	0.05646	-0.99258	0.10767	0.79992	0.10951	0.59004
-0.44627	-0.60300	0.66124	0.13470	0.68522	0.71577	0.88470	-0.40849	0.22457

-0.43543	-0.84389	0.31345	0.73457	-0.13179	0.66561	-0.52039	0.52008	0.67728
-0.06809	-0.54711	0.83429	-0.30740	0.80705	0.50416	0.94914	0.22213	0.22313
-0.61581	0.54997	0.56419	0.70956	0.07583	0.70056	-0.34251	-0.83173	0.43693
0.39309	0.22464	0.89164	-0.88194	-0.18221	0.43472	0.26012	-0.95726	0.12649
-0.60405	-0.10882	0.78948	0.54351	0.66826	0.50796	0.58286	-0.73592	0.34452
-0.33069	-0.15881	0.93028	0.88838	-0.38502	0.25007	0.31847	0.90914	0.26841
-0.97868	0.02028	0.20440	0.10035	-0.82106	0.56196	0.17922	0.57049	0.80152
-0.88266	0.20395	0.42346	0.46905	0.32461	0.82135	-0.03006	-0.92360	0.38218
0.74703	-0.53364	0.39645	-0.11876	0.47964	0.86939	-0.65409	-0.69655	0.29493
0.32365	0.91852	0.22709	0.92355	-0.35885	0.13523	-0.20570	-0.16597	0.96444
-0.30466	-0.80335	0.51168	-0.05533	0.55124	0.83251	0.95085	-0.22532	0.21239
0.89983	-0.42255	0.10842	0.16766	0.56444	0.80827	-0.40273	-0.70913	0.57875
-0.36734	-0.49118	0.78982	0.92121	-0.30920	0.23616	0.12821	0.81434	0.56606
0.45846	-0.76924	0.44507	-0.88757	-0.42171	0.18541	-0.04507	0.48004	0.87609
-0.27285	0.47172	0.83847	-0.20645	-0.87994	0.42788	0.93964	-0.05636	0.33749
-0.84029	-0.42768	0.33318	-0.36510	0.90072	0.23541	0.40078	-0.07617	0.91300
-0.16516	0.54802	0.82000	0.98333	0.02737	0.17977	-0.07608	-0.83602	0.54340
-0.64447	0.70888	0.28663	0.51036	0.11964	0.85160	-0.56939	-0.69511	0.43888
0.15633	0.29423	0.94286	-0.18703	-0.92851	0.32076	-0.96983	0.22649	0.09013
-0.34723	-0.02691	0.93740	0.80866	0.49758	0.31383	0.47487	-0.86700	0.15101
-0.81027	0.51824	0.27367	0.40838	0.16435	0.89790	-0.42035	-0.83930	0.34481
0.67398	0.20433	0.70993	-0.36455	-0.74385	0.56017	-0.64255	0.63635	0.42685
0.33773	-0.26858	0.90211	-0.92375	0.08934	0.37243	0.18062	0.95911	0.21793
0.71729	-0.63829	0.27945	-0.07579	0.32721	0.94191	-0.69265	-0.69680	0.18633
-0.78803	0.01523	0.61546	0.61461	-0.03858	0.78789	0.03574	0.99914	0.02104
-0.50182	-0.56491	0.65502	0.56284	0.36176	0.74320	-0.65680	0.74162	0.13641
-0.25974	0.26419	0.92884	-0.18708	-0.95739	0.22000	0.94738	-0.11663	0.29810
-0.56798	0.29178	0.76959	0.34496	-0.76457	0.54447	0.74726	0.57472	0.33361
0.20204	0.33141	0.92160	0.73154	-0.67673	0.08298	-0.65117	-0.65743	0.37916
-0.77722	-0.50983	0.36879	0.58796	-0.79719	0.13706	0.22412	0.32336	0.91935
-0.49761	0.61663	0.61004	0.60574	-0.25636	0.75323	-0.62086	-0.74434	0.24595
-0.42110	-0.40944	0.80934	0.87538	-0.41709	0.24446	0.23748	0.81142	0.53405
-0.51342	-0.31924	0.79655	0.77559	0.22461	0.58992	-0.36723	0.92067	0.13228
0.36029	0.19672	0.91186	0.23936	-0.96428	0.11346	-0.90161	-0.17739	0.39450
0.45259	-0.32083	0.83200	-0.68221	0.47627	0.55476	0.57424	0.81868	0.00331
-0.53885	0.09287	0.83727	0.73167	-0.44099	0.51980	0.41750	0.89270	0.16967
-0.60366	0.79399	0.07193	-0.04142	-0.12133	0.99175	0.79617	0.59570	0.10613
-0.43896	-0.60586	0.66352	-0.15550	0.77855	0.60802	0.88495	-0.16372	0.43596
0.76594	0.00624	0.64288	-0.26491	-0.90806	0.32442	-0.58580	0.41880	0.69387
-0.34903	0.76365	0.54315	0.85856	0.02829	0.51194	-0.37557	-0.64501	0.66552
-0.41602	-0.41850	0.80733	0.75292	-0.65638	0.04773	0.50994	0.62771	0.58817
0.56161	-0.63816	0.52664	0.71098	0.69777	0.08733	-0.42320	0.32538	0.84559
-0.76718	-0.42526	0.48020	-0.23454	0.88277	0.40706	0.59702	-0.19966	0.77698
-0.92670	0.30611	0.21799	-0.08205	-0.73088	0.67755	0.36673	0.61001	0.70243
-0.45211	-0.76653	0.45609	-0.77511	0.59065	0.22434	0.44136	0.25210	0.86119
0.47325	-0.10955	0.87409	-0.87700	0.03498	0.47921	0.08307	0.99337	0.07952
-0.23158	0.47939	0.84650	0.83686	-0.34550	0.42461	-0.49602	-0.80673	0.32117
-0.00185	0.50674	0.86210	-0.60088	-0.68968	0.40410	0.79934	-0.51727	0.30576

Table 8.8*. Table showing RAW 3D chondrule orientation data Cold Bokkeveld L2*

Cold Bokkeveld L2 Chondrules								
Major Axis Directional Cosines			Intermediate Axis Directional Cosines			Minor Axis Directional Cosines		
PEllipsoid X1 (dmls)	PEllipsoid Y1 (dmls)	PEllipsoid Z1 (dmls)	PEllipsoid X2 (dmls)	PEllipsoid Y2 (dmls)	PEllipsoid Z2 (dmls)	PEllipsoid X3 (dmls)	PEllipsoid Y3 (dmls)	PEllipsoid Z3 (dmls)
-0.69714	0.03610	0.71602	0.71591	-0.01827	0.69796	-0.03828	-0.99918	0.01310
-0.85724	0.11823	0.50117	0.50302	-0.01583	0.86413	-0.11010	-0.99286	0.04590
0.82138	-0.40407	0.40257	-0.26294	0.35808	0.89590	-0.50616	-0.84173	0.18787
-0.87726	-0.30613	0.36972	0.43121	-0.16425	0.88718	-0.21087	0.93772	0.27609
-0.69642	-0.08807	0.71221	0.69921	0.14022	0.70104	0.16160	-0.98620	0.03607
0.19924	0.04383	0.97897	-0.79554	0.59056	0.13547	-0.57220	-0.80580	0.15253
0.10166	0.16494	0.98105	-0.91605	0.40012	0.02765	-0.38798	-0.90150	0.19177
-0.71205	0.64588	0.27537	0.40723	0.06041	0.91133	-0.57197	-0.76105	0.30603
-0.66638	0.18840	0.72142	0.73584	0.01000	0.67709	-0.12035	-0.98204	0.14530
-0.45542	-0.02931	0.88980	0.67411	-0.66419	0.32315	0.58152	0.74699	0.32224
-0.28289	0.01963	0.95895	0.95915	0.00570	0.28283	-0.00008	-0.99979	0.02044
0.88968	-0.23055	0.39411	-0.43060	-0.13661	0.89215	0.15184	0.96343	0.22081
0.91444	-0.35294	0.19805	-0.06616	0.35241	0.93351	-0.39927	-0.86674	0.29890
-0.96798	-0.13773	0.20988	0.25084	-0.49792	0.83015	-0.00983	0.85621	0.51653
0.03236	-0.09342	0.99510	-0.99466	-0.10059	0.02290	-0.09796	0.99053	0.09618

-0.52933	-0.66039	0.53264	0.25143	0.47750	0.84189	0.81031	-0.57956	0.08671
0.33064	-0.28544	0.89956	-0.84012	0.34524	0.41834	0.42998	0.89405	0.12566
0.91175	0.16355	0.37679	-0.38443	0.01669	0.92300	0.14467	-0.98639	0.07809
-0.11368	0.00774	0.99349	0.98835	-0.10099	0.11388	0.10121	0.99486	0.00384
-0.42799	0.43538	0.79200	-0.64192	-0.76331	0.07272	0.63621	-0.47728	0.60617
-0.34822	-0.33468	0.87563	-0.21461	0.93775	0.27308	0.91251	0.09283	0.39837
0.93825	0.16621	0.30343	-0.33304	0.19633	0.92225	0.09371	-0.96635	0.23956
-0.70890	-0.53092	0.46430	0.67071	-0.71110	0.21092	0.21818	0.46093	0.86020
0.62887	0.12864	0.76680	-0.77748	0.09459	0.62176	0.00745	-0.98717	0.15950
0.88581	-0.46400	0.00727	-0.00374	0.00852	0.99996	-0.46404	-0.88579	0.00581
-0.47733	0.40681	0.77889	0.65586	-0.42499	0.62389	-0.58482	-0.80864	0.06395
-0.69101	0.05448	0.72079	0.68716	0.35893	0.63165	0.22430	-0.93177	0.28546
-0.12821	0.07565	0.98886	0.98928	-0.06055	0.13289	-0.06993	-0.99529	0.06708
-0.41971	0.89785	0.13307	-0.75846	-0.42746	0.49195	0.49858	0.10555	0.86039
0.47576	0.10439	0.87336	-0.81425	-0.32324	0.48219	-0.33264	0.94054	0.06879
0.02301	0.29470	0.95531	-0.99738	0.07233	0.00171	-0.06859	-0.95285	0.29559
0.83634	-0.26221	0.48145	-0.44485	0.18865	0.87551	-0.32039	-0.94639	0.04113
-0.45386	0.52361	0.72100	0.87225	0.09563	0.47962	-0.18219	-0.84657	0.50012
0.21245	0.21837	0.95246	-0.24324	-0.93221	0.26798	-0.94642	0.28861	0.14493
0.83685	-0.46707	0.28554	-0.22109	0.18880	0.95680	-0.50080	-0.86383	0.05474
0.67911	-0.70962	0.18774	-0.34628	-0.08421	0.93434	0.64722	0.69954	0.30292
-0.14995	0.15360	0.97669	0.62470	-0.75097	0.21401	0.76634	0.64222	0.01666
-0.76541	-0.13406	0.62943	0.58885	0.24871	0.76903	0.25964	-0.95926	0.11143
-0.12766	-0.20385	0.97064	0.75453	0.61522	0.22844	-0.64373	0.76155	0.07527
-0.99038	0.03060	0.13497	0.10453	-0.47374	0.87444	0.09069	0.88013	0.46598
-0.83658	-0.42992	0.33958	0.30150	0.15625	0.94058	0.45743	-0.88925	0.00109
-0.85695	-0.42444	0.29238	0.31049	0.02764	0.95018	-0.41137	0.90503	0.10810

Table 8.9. *Table showing RAW 3D chondrule orientation data Cold Bokkeveld L3*

Cold Bokkeveld L3 Chondrules								
Major Axis Directional Cosines			Intermediate Axis Directional Cosines			Minor Axis Directional Cosines		
PEllipsoid X1 (dmls)	PEllipsoid Y1 (dmls)	PEllipsoid Z1 (dmls)	PEllipsoid X2 (dmls)	PEllipsoid Y2 (dmls)	PEllipsoid Z2 (dmls)	PEllipsoid X3 (dmls)	PEllipsoid Y3 (dmls)	PEllipsoid Z3 (dmls)
0.23666	0.12018	0.96413	-0.88397	-0.38519	0.26500	0.40322	-0.91498	0.01508
0.61263	-0.63830	0.46611	-0.01214	0.58207	0.81305	-0.79027	-0.50376	0.34884
0.71018	0.69555	0.10888	0.27898	-0.42003	0.86357	-0.64639	0.58291	0.49234
0.02044	0.49695	0.86754	0.01899	-0.86776	0.49662	-0.99961	-0.00633	0.02718
0.86561	0.35321	0.35492	-0.48935	0.44643	0.74916	0.10616	-0.82216	0.55928
0.09976	0.04904	0.99380	-0.75257	0.65709	0.04312	-0.65091	-0.75221	0.10246
0.18204	0.84813	0.49754	-0.31183	-0.43008	0.84723	0.93254	-0.30937	0.18618
0.53463	-0.08115	0.84118	-0.80635	-0.34690	0.47902	-0.25293	0.93439	0.25089
-0.18244	-0.21670	0.95904	-0.29981	0.94122	0.15564	0.93639	0.25914	0.23668
-0.38988	-0.90196	0.18564	-0.77705	0.43041	0.45928	0.49415	-0.03481	0.86868
0.02336	-0.88272	0.46933	-0.89549	0.19024	0.40237	0.44446	0.42968	0.78602
-0.62322	-0.19132	0.75828	0.75682	0.09671	0.64643	-0.19701	0.97675	0.08452
-0.61765	-0.78420	0.05952	0.02405	0.05682	0.99810	0.78608	-0.61791	0.01623
-0.52251	-0.85152	0.04347	-0.74758	0.48205	0.45688	0.41000	-0.20623	0.88846
0.41326	0.34709	0.84187	-0.80169	-0.29978	0.51713	0.43187	-0.88863	0.15437
0.68777	-0.64209	0.33866	-0.72446	-0.57749	0.37638	0.04609	0.50421	0.86235
0.87599	0.45737	0.15314	-0.46331	0.70964	0.53082	0.13411	-0.53594	0.83354
0.79536	0.60499	0.03745	-0.21459	0.22326	0.95085	0.56689	-0.76430	0.30739
-0.77458	-0.56777	0.27868	-0.05040	0.49463	0.86764	0.63046	-0.65802	0.41174
0.66707	-0.36462	0.64967	-0.57878	0.29543	0.76009	0.46908	0.88305	0.01396
-0.90732	0.40849	0.09954	0.21403	0.24497	0.94561	-0.36188	-0.87928	0.30970
-0.83243	-0.30252	0.46427	0.48034	0.02381	0.87676	-0.27629	0.95285	0.12550
0.64810	-0.75552	0.09569	0.72920	0.65189	0.20812	-0.21961	-0.06511	0.97341
-0.72867	-0.68138	0.06895	-0.59848	0.68248	0.41958	0.33295	-0.26447	0.90510
-0.36085	0.06852	0.93010	0.76737	0.58860	0.25436	0.53003	-0.80552	0.26498
0.93235	0.35835	0.04813	-0.35901	0.90172	0.24086	0.04291	-0.24184	0.96937
0.80857	-0.57905	0.10452	0.22735	0.47129	0.85217	-0.54271	-0.66527	0.51272
-0.44374	0.08491	0.89212	0.87977	-0.14822	0.45171	-0.17059	-0.98530	0.00893
-0.44103	-0.43231	0.78651	0.89577	-0.26637	0.35588	0.05565	0.86148	0.50473
0.61227	0.10042	0.78425	-0.77701	-0.10703	0.62032	0.14624	-0.98917	0.01250
-0.13271	0.28520	0.94924	0.15414	-0.94012	0.30401	0.97910	0.18666	0.08080
-0.66486	0.01980	0.74671	0.74667	0.04579	0.66361	0.02105	-0.99876	0.04523

-0.84698	-0.28950	0.44589	-0.29539	0.95361	0.05806	0.44202	0.08254	0.89320
0.98613	-0.10793	0.12610	0.02635	0.85189	0.52307	-0.16387	-0.51249	0.84291
0.89541	0.04022	0.44343	-0.23048	0.89397	0.38431	-0.38096	-0.44632	0.80974
-0.30897	-0.34123	0.88775	0.94941	-0.05550	0.30910	-0.05620	0.93834	0.34112
-0.03153	-0.47407	0.87993	-0.64384	0.68301	0.34491	0.76451	0.55566	0.32676
-0.34189	-0.56252	0.75279	0.77824	0.27952	0.56232	-0.52674	0.77810	0.34221
0.82498	-0.17068	0.53877	-0.51569	0.16271	0.84118	-0.23123	-0.97180	0.04621
-0.59427	-0.10110	0.79789	0.76885	0.21977	0.60048	0.23606	-0.97030	0.05287
0.97565	0.03755	0.21612	-0.20917	-0.13747	0.96817	-0.06606	0.98979	0.12627
-0.27374	-0.29737	0.91468	0.96116	-0.04978	0.27147	-0.03520	0.95346	0.29945
0.45716	-0.11592	0.88180	-0.86320	-0.29662	0.40853	-0.21420	0.94794	0.23566
0.49339	0.64153	0.58737	-0.76338	-0.00431	0.64594	0.41692	-0.76708	0.48760
0.82487	0.48559	0.28947	0.36043	-0.84621	0.39244	-0.43552	0.21938	0.87304
-0.69011	-0.58537	0.42554	0.64531	-0.23158	0.72797	-0.32759	0.77699	0.53757
0.98256	-0.13813	0.12452	0.11374	0.97609	0.18525	-0.14713	-0.16786	0.97477
0.22141	0.95933	0.17509	0.69134	-0.28105	0.66563	-0.68777	0.02633	0.72545
-0.64788	0.07365	0.75817	0.67073	0.52694	0.52197	0.36107	-0.84671	0.39079
0.80946	-0.36444	0.46039	0.17007	0.89598	0.41025	-0.56201	-0.25379	0.78724
0.12999	-0.10003	0.98646	-0.87340	-0.48249	0.06616	-0.46934	0.87017	0.15008
-0.96878	0.14218	0.20308	0.24431	0.40853	0.87944	-0.04208	-0.90160	0.43052
-0.28531	-0.08754	0.95443	0.75354	-0.63586	0.16694	0.59227	0.76683	0.24738
-0.66891	-0.55664	0.49266	-0.17178	0.76058	0.62611	0.72322	-0.33418	0.60438
0.41978	-0.26092	0.86931	-0.90532	-0.18865	0.38055	-0.06470	0.94675	0.31541
0.81084	0.53203	0.24389	-0.38140	0.16426	0.90970	0.44393	-0.83064	0.33610
0.97785	0.20912	0.00885	-0.00899	-0.00027	0.99996	0.20912	-0.97789	0.00162
-0.44326	-0.38950	0.80735	-0.62929	0.77662	0.02917	0.63836	0.49513	0.58936
0.48015	0.32592	0.81439	0.23754	-0.94204	0.23695	-0.84441	-0.07968	0.52974
-0.49613	-0.81153	0.30868	-0.84741	0.53001	0.03141	0.18909	0.24600	0.95065
0.92408	0.14351	0.35423	-0.38198	0.31624	0.86838	0.01260	-0.93776	0.34705
0.99018	0.06202	0.12531	-0.13951	0.49722	0.85633	-0.00920	-0.86540	0.50099

***Table 8.10**. Table showing RAW 3D chondrule orientation data LEW 85311*

Lewis Cliff 85311 Chondrules								
Major Axis Directional Cosines			Intermediate Axis Directional Cosines			Minor Axis Directional Cosines		
PEllipsoid X1 (dmls)	PEllipsoid Y1 (dmls)	PEllipsoid Z1 (dmls)	PEllipsoid X2 (dmls)	PEllipsoid Y2 (dmls)	PEllipsoid Z2 (dmls)	PEllipsoid X3 (dmls)	PEllipsoid Y3 (dmls)	PEllipsoid Z3 (dmls)
-0.45626	0.83702	0.30204	0.13052	-0.27281	0.95317	0.88023	0.47431	0.01523
-0.99238	0.10949	0.05649	-0.02679	-0.63932	0.76847	0.12025	0.76110	0.63739
0.11665	-0.72850	0.67504	0.51684	0.62492	0.58511	-0.84810	0.28064	0.44941
-0.68929	0.71217	0.13302	-0.52805	-0.61956	0.58079	0.49603	0.33009	0.80311
-0.45902	0.87000	0.18000	0.84348	0.36313	0.39582	-0.27900	-0.33351	0.90052
-0.75483	-0.46893	0.45863	-0.46658	0.87531	0.12705	0.46102	0.11808	0.87950
-0.78792	-0.32483	0.52314	-0.00049	0.84988	0.52697	0.61578	-0.41496	0.66979
0.80587	-0.59207	0.00613	0.22293	0.31298	0.92323	-0.54853	-0.74263	0.38421
-0.51837	0.85261	0.06601	-0.82018	-0.51754	0.24384	0.24206	0.07226	0.96757
-0.76734	-0.59362	0.24250	0.33145	-0.04343	0.94247	-0.54894	0.80357	0.23009
0.85185	0.43074	0.29803	-0.48528	0.43487	0.75855	0.19713	-0.79079	0.57947
0.37328	0.44088	0.81626	-0.82380	-0.24711	0.51019	0.42664	-0.86288	0.27096
-0.48460	-0.68829	0.53984	-0.38226	0.72173	0.57705	0.78679	-0.07327	0.61285
0.61337	-0.45705	0.64411	0.07020	0.84386	0.53195	-0.78667	-0.28106	0.54969
-0.96476	0.22181	0.14159	0.19525	0.24261	0.95027	-0.17643	-0.94443	0.27737
-0.86491	-0.46967	0.17703	-0.29805	0.76438	0.57174	0.40385	-0.44174	0.80111
0.89734	-0.34511	0.27511	0.24681	0.90915	0.33546	-0.36589	-0.23312	0.90099
0.03234	0.59074	0.80621	-0.15265	-0.79425	0.58810	0.98775	-0.14209	0.06449
0.62574	0.44804	0.63852	-0.37412	-0.54591	0.74968	-0.68446	0.70799	0.17398
-0.90132	-0.38216	0.20388	0.11262	0.24774	0.96226	0.41825	-0.89027	0.18025
0.07757	0.11051	0.99084	-0.22133	-0.96713	0.12519	-0.97211	0.22902	0.05056
-0.90160	0.06352	0.42788	-0.02844	-0.99572	0.08789	0.43163	0.06707	0.89955
0.95240	0.13709	0.27230	-0.29282	0.65990	0.69195	-0.08483	-0.73874	0.66863
0.55615	0.70000	0.44799	-0.73237	0.15798	0.66232	0.39285	-0.69645	0.60052
-0.93293	0.28117	0.22493	0.29330	0.95577	0.02175	0.20887	-0.08626	0.97413
-0.12671	-0.19669	0.97224	0.46101	0.85618	0.23329	0.87830	-0.47778	0.01781
-0.79538	-0.49030	0.35633	0.04944	0.53346	0.84438	0.60409	-0.68922	0.40006
-0.69869	-0.54464	0.46389	-0.25572	0.79570	0.54906	0.66816	-0.26500	0.69523
0.11868	-0.99121	0.05848	0.98164	0.12598	0.14325	-0.14936	0.04040	0.98796
-0.43941	0.84312	0.30994	-0.34108	-0.47579	0.81073	0.83102	0.25053	0.49664
-0.38790	0.79208	0.47133	-0.72425	-0.57823	0.37566	0.57009	-0.19564	0.79795
-0.72258	-0.30264	0.62152	0.59070	0.19675	0.78254	-0.35912	0.93258	0.03661
0.81642	-0.37853	0.43609	-0.51138	-0.82472	0.24152	-0.26823	0.42019	0.86689
-0.14563	0.73022	0.66751	-0.15313	-0.68321	0.71399	0.97742	0.00176	0.21132

-0.14644	-0.66179	0.73525	0.75643	0.40406	0.51434	-0.63747	0.63149	0.44143
-0.37873	-0.43858	0.81499	0.75764	0.35883	0.54518	-0.53155	0.82395	0.19638
-0.83346	-0.54620	0.08367	0.49854	-0.67798	0.54019	-0.23832	0.49194	0.83738
0.48459	-0.87442	0.02388	0.61860	0.36187	0.69742	-0.61847	-0.32319	0.71627
0.22261	0.09373	0.97039	-0.91859	0.35356	0.17658	-0.32654	-0.93070	0.16481
0.72082	0.69113	0.05264	0.15791	-0.23769	0.95842	-0.67490	0.68253	0.28046
0.42363	0.90047	0.09845	-0.35736	0.06627	0.93161	0.83237	-0.42984	0.34987
0.54566	-0.09796	0.83226	-0.75117	0.38306	0.53759	-0.37147	-0.91851	0.13543
-0.81094	-0.52133	0.26570	-0.06214	0.52824	0.84682	0.58182	-0.67021	0.46076
0.48023	0.28501	0.82955	-0.87670	0.12584	0.46429	0.02794	-0.95023	0.31030
-0.18713	0.53233	0.82560	-0.14801	-0.84613	0.51202	0.97112	-0.02639	0.23713
-0.69778	-0.59914	0.39261	0.66004	-0.32482	0.67737	-0.27831	0.73180	0.62211
-0.20985	0.19523	0.95804	-0.62870	-0.77737	0.02071	0.74880	-0.59798	0.28587
-0.99046	0.00350	0.13776	0.00982	-0.99534	0.09593	0.13745	0.09636	0.98581
-0.05886	-0.78799	0.61287	-0.95640	0.22044	0.19157	0.28606	0.57488	0.76661
-0.10569	0.39256	0.91364	-0.78819	-0.59326	0.16372	0.60629	-0.70281	0.37211
-0.04305	0.07220	0.99646	0.98714	-0.15063	0.05356	-0.15396	-0.98595	0.06479
0.44141	-0.06953	0.89461	-0.80614	-0.46858	0.36134	-0.39407	0.88068	0.26289
0.14264	0.02543	0.98945	-0.85773	0.50203	0.11075	-0.49392	-0.86448	0.09343
-0.39250	0.89360	0.21779	0.09182	-0.19754	0.97599	-0.91516	-0.40307	0.00451
-0.68413	-0.62695	0.37269	0.70249	-0.42900	0.56787	-0.19614	0.65031	0.73392
-0.01007	-0.98128	0.19234	0.99833	0.00108	0.05779	-0.05692	0.19260	0.97963
0.57678	0.76840	0.27729	-0.79983	0.46218	0.38296	0.16611	-0.44267	0.88117
-0.98529	-0.11357	0.12772	0.06231	0.45713	0.88721	0.15914	-0.88212	0.44333
-0.11993	-0.35796	0.92600	0.99012	0.02520	0.13797	-0.07272	0.93340	0.35140
-0.72300	0.65241	0.22724	0.14298	-0.18050	0.97313	0.67590	0.73606	0.03722
-0.43174	0.44094	0.78687	0.08458	-0.84873	0.52202	0.89802	0.29193	0.32914
-0.26600	-0.89639	0.35459	-0.36269	0.43388	0.82475	0.89314	-0.09077	0.44052
-0.45747	-0.67273	0.58151	0.22227	0.54668	0.80730	0.86100	-0.49857	0.10057
0.87510	-0.04285	0.48205	-0.28477	-0.85096	0.44133	-0.39129	0.52348	0.75688
-0.18099	-0.78416	0.59358	0.02327	0.59997	0.79969	0.98321	-0.15855	0.09034
-0.59414	-0.64933	0.47472	0.80345	-0.50717	0.31186	0.03827	0.56670	0.82303
-0.57116	0.24233	0.78425	0.10413	-0.92632	0.36207	0.81421	0.28847	0.50384
0.98803	-0.00293	0.15423	-0.14732	0.27839	0.94910	-0.04572	-0.96047	0.27462
-0.76643	-0.49825	0.40537	-0.22181	0.79758	0.56095	0.60281	-0.34001	0.72181
-0.54549	0.14776	0.82499	0.21586	-0.92636	0.30864	0.80985	0.34644	0.47342
-0.83150	0.20927	0.51460	0.35814	0.91007	0.20860	0.42467	-0.35776	0.83167
0.62853	-0.72829	0.27302	0.45399	0.62855	0.63152	-0.63154	-0.27298	0.72570
0.33373	-0.91355	0.23248	0.64837	0.40147	0.64687	-0.68428	-0.06515	0.72630
0.98693	-0.03877	0.15640	-0.15014	0.13114	0.97993	-0.05850	-0.99061	0.12360
-0.04075	-0.83051	0.55552	-0.42112	0.51846	0.74422	0.90609	0.20361	0.37086
-0.40012	0.89393	0.20196	-0.76010	-0.44681	0.47182	0.51201	0.03528	0.85825
-0.91474	0.22276	0.33709	0.06507	-0.74219	0.66702	0.39877	0.63209	0.66441
0.63333	-0.26013	0.72885	-0.71518	-0.55653	0.42283	-0.29564	0.78905	0.53851
-0.54866	-0.67736	0.49006	-0.74739	0.66008	0.07561	0.37469	0.32478	0.86841
-0.52324	0.80829	0.26998	0.81257	0.37773	0.44391	-0.25683	-0.45165	0.85443
0.55375	-0.00002	0.83268	-0.83102	-0.06318	0.55265	-0.05260	0.99800	0.03501
-0.91392	-0.30254	0.27061	-0.21940	0.92909	0.29775	0.34150	-0.21274	0.91549
0.02528	0.99834	0.05167	-0.51437	-0.03132	0.85699	0.85719	-0.04824	0.51273
-0.27765	0.86141	0.42531	0.95519	0.29481	0.02646	0.10259	-0.41360	0.90466
-0.48858	0.87245	0.01137	-0.85869	-0.48310	0.17108	0.15475	0.07382	0.98519
0.55267	0.76831	0.32289	-0.67189	0.18154	0.71806	0.49307	-0.61380	0.61655
-0.58030	-0.36802	0.72651	0.77576	0.02176	0.63066	-0.24791	0.92956	0.27287
0.83876	-0.45661	0.29663	-0.49840	-0.86320	0.08052	-0.21929	0.21537	0.95159
0.70669	0.70604	0.04574	-0.67404	0.65218	0.34689	0.21509	-0.27598	0.93679
-0.96072	-0.19150	0.20086	0.21687	-0.06642	0.97394	-0.17316	0.97924	0.10534
-0.26801	0.36772	0.89048	-0.79679	-0.60419	0.00968	0.54157	-0.70693	0.45492
-0.12469	-0.96952	0.21091	0.67336	0.07343	0.73566	-0.72873	0.23375	0.64368
-0.01640	0.29247	0.95614	-0.82398	-0.54564	0.15276	0.56638	-0.78533	0.24994
0.08530	0.17303	0.98122	-0.88542	-0.43843	0.15428	0.45689	-0.88195	0.11581
0.53588	0.63016	0.56190	-0.63078	-0.14357	0.76257	0.56121	-0.76308	0.32056
-0.54943	0.16067	0.81994	0.35118	0.93486	0.05213	0.75815	-0.31659	0.57006
-0.47907	-0.82655	0.29550	-0.34047	0.48526	0.80536	0.80906	-0.28521	0.51389
-0.82521	-0.36170	0.43383	0.07641	0.68952	0.72022	0.55964	-0.62748	0.54136
0.03336	0.07919	0.99630	-0.45006	-0.88888	0.08572	0.89238	-0.45125	0.00598
0.83319	0.44433	0.32919	-0.35000	-0.03716	0.93601	0.42813	-0.89509	0.12455
-0.98271	-0.00866	0.18495	0.14794	0.56393	0.81246	0.11133	-0.82578	0.55290
0.22335	-0.73888	0.63574	0.67976	0.58552	0.44170	-0.69860	0.33350	0.63304
0.38798	0.84055	0.37809	-0.51755	-0.14075	0.84400	0.76264	-0.52314	0.38041
0.60714	0.78966	0.08847	0.43462	-0.42323	0.79497	-0.66520	0.44420	0.60016
-0.64192	-0.75950	0.10536	-0.75793	0.64930	0.06280	0.11611	0.03954	0.99245
-0.95934	0.02348	0.28128	0.23737	0.60633	0.75896	0.15273	-0.79486	0.58725
-0.08277	0.88557	0.45707	0.28691	-0.41805	0.86193	-0.95438	-0.20248	0.21947
-0.43364	-0.89435	0.11002	-0.88106	0.44643	0.15632	0.18892	0.02915	0.98156
0.51437	0.65863	0.54921	0.64069	-0.72084	0.26441	-0.57004	-0.21587	0.79275

0.20163	-0.83671	0.50918	0.96973	0.24362	0.01632	-0.13770	0.49048	0.86050
-0.78099	-0.34843	0.51832	0.54119	-0.79179	0.28318	0.31173	0.50167	0.80694
0.26584	0.91997	0.28807	-0.74914	0.00907	0.66235	0.60673	-0.39189	0.69160
-0.08805	-0.76087	0.64291	-0.16324	0.64771	0.74419	0.98265	0.03943	0.18124
0.68558	-0.70811	0.16899	0.54114	0.65097	0.53237	-0.48698	-0.27354	0.82948
-0.05924	-0.82330	0.56451	0.20171	0.54396	0.81450	-0.97765	0.16212	0.13385
0.89774	0.43877	0.03934	-0.19381	0.31318	0.92971	0.39561	-0.84226	0.36619
-0.92010	0.33258	0.20691	0.38595	0.67969	0.62375	-0.06681	-0.65377	0.75374
-0.29738	-0.00143	0.95476	0.45495	0.87896	0.14302	0.83940	-0.47690	0.26073
0.41878	0.82988	0.36869	0.81645	-0.52182	0.24719	-0.39753	-0.19750	0.89608
-0.52793	-0.79162	0.30761	-0.06025	0.39619	0.91619	0.84715	-0.46515	0.25685
-0.16752	0.81999	0.54731	-0.03582	-0.55985	0.82782	0.98522	0.11908	0.12316
0.13617	-0.08783	0.98679	0.39651	0.91763	0.02696	-0.90788	0.38760	0.15978
-0.35011	-0.92364	0.15594	0.93670	-0.34452	0.06241	-0.00392	0.16792	0.98579
-0.21171	0.06505	0.97517	0.95998	0.20101	0.19501	0.18333	-0.97743	0.10500
0.33498	0.94052	0.05663	-0.36175	0.07288	0.92942	0.87002	-0.33182	0.36465
-0.89639	-0.43494	0.08553	0.38031	-0.65549	0.65245	-0.22771	0.61738	0.75299
0.30369	0.54628	0.78061	0.27653	-0.83457	0.47646	-0.91176	-0.07117	0.40452
-0.72009	0.47271	0.50795	0.39841	-0.31767	0.86044	0.56810	0.82197	0.04042
-0.44157	0.37821	0.81362	0.49656	-0.65226	0.57270	0.74729	0.65690	0.10022
0.96812	0.24290	0.06122	0.21360	-0.92817	0.30475	-0.13085	0.28196	0.95046
0.21649	-0.91261	0.34681	0.97232	0.23354	0.00760	-0.08793	0.33557	0.93790
0.77899	0.51264	0.36107	-0.20254	-0.33926	0.91863	-0.59343	0.78874	0.16045
0.33672	0.37200	0.86501	-0.91292	0.35402	0.20313	-0.23066	-0.85807	0.45881
-0.58466	-0.63301	0.50742	0.16402	0.52030	0.83808	0.79453	-0.57322	0.20037
0.70357	-0.24881	0.66565	-0.67905	0.04074	0.73296	0.20949	0.96769	0.14029
-0.06436	0.35473	0.93275	0.92090	-0.33897	0.19245	-0.38445	-0.87136	0.30486
0.23537	0.96705	0.09700	0.64857	-0.23061	0.72538	-0.72385	0.10782	0.68148
-0.49683	-0.85070	0.17168	0.85386	-0.44377	0.27203	-0.15523	0.28174	0.94685
-0.29858	0.45970	0.83638	0.93982	0.29413	0.17385	0.16608	-0.83796	0.51985
0.22909	-0.95403	0.19327	-0.54532	0.03868	0.83734	0.80632	0.29722	0.51138
-0.91028	0.36450	0.19631	0.39892	0.64544	0.65136	-0.11072	-0.67123	0.73293
-0.76812	-0.25984	0.58521	0.31619	0.64082	0.69955	0.55679	-0.72238	0.41007
0.37555	0.82061	0.43077	0.89980	-0.43421	0.04272	-0.22210	-0.37156	0.90145
0.24258	-0.53005	0.81253	-0.96990	-0.11399	0.21519	0.02144	0.84027	0.54174
-0.27620	-0.64134	0.71582	-0.46108	0.74191	0.48681	0.84328	0.19559	0.50062
0.44435	0.62311	0.64365	0.03945	-0.73140	0.68081	-0.89498	0.27713	0.34958
-0.60916	-0.78810	0.08843	-0.25405	0.29955	0.91963	0.75126	-0.53773	0.38270
-0.21988	-0.56700	0.79383	0.76323	0.40681	0.50198	-0.60756	0.71625	0.34331
-0.18894	-0.02416	0.98169	0.70613	-0.69806	0.11873	0.68241	0.71563	0.14895
0.80759	0.30690	0.50361	0.27862	-0.95117	0.13286	-0.51979	-0.03302	0.85366
0.11594	-0.81257	0.57122	0.97772	0.19467	0.07848	-0.17497	0.54940	0.81704
-0.87836	0.35172	0.32369	0.40347	0.18244	0.89662	-0.25631	-0.91815	0.30216
0.93592	0.06153	0.34679	-0.13501	0.97209	0.19187	-0.32531	-0.22639	0.91811
-0.18855	0.98181	0.02237	-0.69002	-0.14865	0.70836	0.69880	0.11812	0.70550
0.82325	-0.09923	0.55893	-0.22357	-0.96170	0.15856	-0.52180	0.25550	0.81391

Table 8.11. *Table showing RAW 3D chondrule orientation data Murchison*

Murchison Chondrules								
Major Axis Directional Cosines			Intermediate Axis Directional Cosines			Minor Axis Directional Cosines		
PEllipsoid X1 (dmls)	PEllipsoid Y1 (dmls)	PEllipsoid Z1 (dmls)	PEllipsoid X2 (dmls)	PEllipsoid Y2 (dmls)	PEllipsoid Z2 (dmls)	PEllipsoid X3 (dmls)	PEllipsoid Y3 (dmls)	PEllipsoid Z3 (dmls)
0.47674	0.64918	0.59270	0.78043	-0.62287	0.05448	-0.40454	-0.43659	0.80358
-0.25226	0.68746	0.68100	-0.15574	-0.72343	0.67260	0.95504	0.06361	0.28956
0.15139	-0.39809	0.90477	0.56459	0.78615	0.25142	-0.81137	0.47276	0.34377
-0.10828	0.94540	0.30739	0.56858	-0.19474	0.79925	-0.81547	-0.26132	0.51645
-0.07719	0.46769	0.88051	0.18027	-0.86205	0.47369	-0.98058	-0.19529	0.01777
-0.41114	-0.01880	0.91138	0.41542	-0.89380	0.16896	0.81142	0.44807	0.37529
-0.55017	0.41635	0.72386	0.71829	-0.20614	0.66450	-0.42588	-0.88553	0.18565
0.36845	-0.20308	0.90720	-0.38563	0.85455	0.34791	-0.84590	-0.47803	0.23654
0.26167	-0.96247	0.07196	-0.04655	0.06189	0.99700	0.96404	0.26423	0.02860
-0.24344	0.77962	0.57701	-0.83890	-0.46783	0.27817	0.48681	-0.41633	0.76791
0.32751	-0.03210	0.94430	-0.29711	0.94523	0.13518	-0.89692	-0.32483	0.30004
0.12012	0.93414	0.33609	0.72577	-0.31362	0.61230	-0.67738	-0.17037	0.71564
0.68332	-0.13989	0.71659	0.03485	0.98660	0.15938	-0.72929	-0.08394	0.67904
-0.90055	0.23530	0.36558	-0.07849	-0.91506	0.39562	0.42762	0.32758	0.84252
-0.24565	0.96317	0.10941	0.77983	0.12931	0.61250	-0.57579	-0.23578	0.78287
0.40912	-0.03899	0.91165	-0.07254	0.99454	0.07509	-0.90959	-0.09685	0.40406

-0.14384	0.93612	0.32093	0.98950	0.13131	0.06048	-0.01448	-0.32626	0.94517
0.95112	0.17453	0.25479	-0.24411	0.93022	0.27404	-0.18919	-0.32284	0.92735
0.27650	-0.73436	0.61989	0.10857	0.66478	0.73911	-0.95486	-0.13706	0.26354
0.28157	0.67801	0.67899	0.38251	-0.72828	0.56860	-0.88000	-0.09962	0.46440
-0.36370	0.90307	0.22843	0.86399	0.23537	0.44510	-0.34819	-0.35925	0.86586
-0.01428	0.68799	0.72558	0.51485	-0.61701	0.59518	-0.85716	-0.38206	0.34540
0.13987	0.61402	0.77680	-0.77181	-0.42383	0.47400	0.62028	-0.66584	0.41463
0.22943	0.46590	0.85458	0.38616	-0.84951	0.35947	-0.89344	-0.24753	0.37482
0.06380	0.78154	0.62059	0.20349	-0.61898	0.75859	-0.97700	-0.07789	0.19852
-0.14093	0.99002	0.00305	0.37367	0.05034	0.92619	-0.91679	-0.13167	0.37704
0.33649	0.32934	0.88222	0.60895	-0.79071	0.06291	-0.71830	-0.51606	0.46662
0.48570	-0.72895	0.48242	0.67542	0.66330	0.32226	-0.55490	0.16931	0.81451
0.23124	0.74745	0.62278	-0.11765	-0.61395	0.78053	-0.96576	0.25376	0.05403
-0.39900	0.52369	0.75270	0.04276	-0.80935	0.58577	0.91596	0.26590	0.30054
-0.66152	-0.26566	0.70130	-0.00004	0.93516	0.35421	0.74993	-0.23429	0.61864
-0.01636	-0.12466	0.99206	-0.74658	0.66152	0.07082	0.66510	0.73949	0.10389
0.02991	0.70991	0.70366	0.43399	-0.64338	0.63065	-0.90042	-0.28652	0.32734
-0.39201	-0.55950	0.73026	0.87310	0.02383	0.48695	-0.28985	0.82849	0.47916
-0.80644	0.58522	0.08469	0.56333	0.71681	0.41090	-0.17976	-0.37908	0.90774
0.66490	-0.30570	0.68151	-0.22721	0.78639	0.57443	-0.71153	-0.53679	0.45341
-0.03945	0.80551	0.59126	0.36833	-0.53833	0.75798	-0.92886	-0.24768	0.27545
0.07400	0.14170	0.98714	0.34089	-0.93382	0.10849	-0.93719	-0.32848	0.11741
0.17173	-0.32681	0.92936	-0.11933	0.92953	0.34891	-0.97789	-0.17082	0.12062
-0.21629	0.63196	0.74421	0.97312	0.07779	0.21676	-0.07909	-0.77109	0.63179
0.52303	-0.73949	0.42379	-0.10933	0.43490	0.89382	-0.84528	-0.51382	0.14661
0.06050	0.82339	0.56424	-0.43113	-0.48827	0.75876	0.90026	-0.28917	0.32545
0.55853	0.08440	0.82518	-0.81040	0.26773	0.52113	-0.17694	-0.95979	0.21793
-0.06092	0.69821	0.71329	0.40650	-0.63532	0.65660	-0.91162	-0.32995	0.24512
0.05306	-0.39397	0.91759	-0.11226	0.91071	0.39750	-0.99226	-0.12410	0.00410
-0.49520	-0.53535	0.68423	0.39767	0.56056	0.72639	0.77242	-0.63180	0.06470
0.42627	-0.77979	0.45850	-0.42166	0.27714	0.86337	0.80031	0.56136	0.21067
0.44128	-0.88907	0.12176	-0.76190	-0.29951	0.57428	0.47411	0.34619	0.80955
-0.27453	0.84708	0.45507	0.84580	-0.01241	0.53336	-0.45745	-0.53132	0.71305
0.13063	0.79007	0.59894	0.06632	-0.60972	0.78983	-0.98921	0.06345	0.13204
0.24381	0.16392	0.95587	0.22168	-0.96894	0.10962	-0.94415	-0.18517	0.27257
0.15379	0.48439	0.86123	0.21382	-0.86726	0.44961	-0.96469	-0.11500	0.23695
-0.00659	0.92791	0.37275	-0.94667	-0.12587	0.29661	0.32215	-0.35092	0.87925
0.06580	0.91959	0.38734	0.48273	-0.36907	0.79421	-0.87330	-0.13472	0.46819
0.58922	-0.80766	0.02260	-0.72788	-0.51847	0.44875	0.35072	0.28086	0.89337
-0.07318	0.60370	0.79384	0.54993	-0.63961	0.53711	-0.83200	-0.47586	0.28519
0.32937	0.93430	0.13639	0.81816	-0.35451	0.45270	-0.47131	0.03752	0.88117
0.15899	0.01702	0.98713	-0.36248	0.93103	0.04233	-0.91833	-0.36454	0.15419
0.68991	0.26122	0.67512	-0.67632	0.56511	0.47249	-0.25809	-0.78257	0.56654
-0.04042	0.70069	0.71232	0.06344	-0.70966	0.70168	-0.99717	-0.07355	0.01577
0.51093	-0.82822	0.23021	-0.08567	0.21741	0.97231	-0.85534	-0.51650	0.04013
0.33802	-0.90194	0.26878	0.73592	0.43133	0.52190	-0.58666	0.02139	0.80955
-0.22807	0.95318	0.19858	0.40132	-0.09379	0.91112	-0.88709	-0.28749	0.36114
-0.95400	0.29206	0.06776	0.20207	0.45937	0.86495	-0.22149	-0.83886	0.49726
-0.06998	0.78168	0.61975	-0.63291	-0.51500	0.57810	0.77106	-0.35179	0.53077
0.51075	0.03316	0.85909	0.02384	-0.99942	0.02440	-0.85940	-0.00802	0.51124
0.19386	-0.94896	0.24880	0.47974	0.31292	0.81972	-0.85573	-0.03955	0.51591
-0.03855	0.68660	0.72601	0.40853	-0.65223	0.63852	-0.91193	-0.32121	0.25535
0.33682	-0.92525	0.17452	0.23877	0.26323	0.93472	-0.91079	-0.27317	0.30958
-0.04369	0.83284	0.55179	0.22178	-0.53045	0.81819	-0.97412	-0.15812	0.16153
0.53107	0.13891	0.83587	-0.05711	-0.97836	0.19887	-0.84540	0.15335	0.51164
-0.04544	0.95993	0.27653	0.45808	-0.22597	0.85971	-0.88775	-0.16574	0.42946
0.00008	0.50118	0.86534	0.16637	-0.85329	0.49419	-0.98606	-0.14393	0.08345
0.02789	-0.65141	0.75821	0.10823	0.75602	0.64554	-0.99373	0.06406	0.09159
-0.14665	0.91244	0.38204	-0.53273	-0.39827	0.74671	0.83349	-0.09402	0.54448
-0.03681	0.95992	0.27784	0.86781	-0.10716	0.48521	-0.49554	-0.25897	0.82908
-0.10592	0.98394	0.14369	0.43462	-0.08416	0.89667	-0.89436	-0.15743	0.41873
0.43660	0.36342	0.82299	-0.75022	-0.35782	0.55600	0.49654	-0.86017	0.11642
0.16192	-0.51899	0.83930	-0.35415	0.76331	0.54032	0.92107	0.38473	0.06021
0.33196	-0.03535	0.94263	-0.45116	0.87164	0.19157	-0.82841	-0.48887	0.27340
-0.14581	-0.81030	0.56759	0.19933	0.53789	0.81911	-0.96902	0.23257	0.08308
-0.15125	-0.09880	0.98355	-0.06396	0.99389	0.09001	0.98642	0.04930	0.15665
0.56662	-0.81541	0.11855	-0.14423	0.04351	0.98859	0.81126	0.57725	0.09295
-0.13642	0.86298	0.48648	0.19373	-0.45835	0.86740	-0.97152	-0.21257	0.10466
0.53282	0.27618	0.79989	-0.26293	-0.84443	0.46670	-0.80434	0.45899	0.37731
0.37891	-0.90481	0.19426	0.06013	0.23354	0.97049	-0.92348	-0.35605	0.14290
0.33069	-0.85099	0.40800	-0.01343	0.42803	0.90366	-0.94364	-0.30431	0.13012
-0.29155	0.94876	0.12189	0.79681	0.17039	0.57971	-0.52924	-0.26614	0.80566
0.55318	-0.08333	0.82889	-0.16620	0.96395	0.20782	-0.81632	-0.25272	0.51938
0.25187	0.19615	0.94767	-0.90165	0.40330	0.15616	-0.35156	-0.89380	0.27844
-0.33702	0.82865	0.44695	0.91162	0.16857	0.37487	-0.23529	-0.53379	0.81223

0.12068	0.57930	0.80613	0.70973	-0.61812	0.33795	-0.69406	-0.53135	0.48575
0.64388	-0.37582	0.66647	0.11141	0.90782	0.40429	-0.75697	-0.18607	0.62640
0.32423	-0.81288	0.48383	0.46828	0.58232	0.66454	-0.82194	0.01111	0.56947
0.18840	0.51833	0.83417	-0.24763	-0.79686	0.55108	-0.95036	0.31039	0.02177
0.17923	-0.88647	0.42667	0.97332	0.22293	0.05429	-0.14324	0.40556	0.90278
0.08874	0.79804	0.59604	0.37940	-0.58037	0.72058	-0.92097	-0.16219	0.35427
0.39880	-0.01922	0.91684	-0.82025	-0.45454	0.34726	-0.41006	0.89052	0.19704
0.30042	0.35849	0.88388	0.37962	-0.89506	0.23399	-0.87501	-0.26525	0.40498
0.16390	-0.39724	0.90296	0.14730	0.91493	0.37577	-0.97542	0.07142	0.20847
0.11593	-0.32315	0.93922	0.50596	0.83293	0.22413	-0.85473	0.44923	0.26007
-0.60310	0.73888	0.30054	-0.23059	-0.52219	0.82107	0.76361	0.42588	0.48531
0.30350	-0.80424	0.51097	-0.89811	-0.06234	0.43533	0.31826	0.59103	0.74121
0.20690	0.10394	0.97283	-0.49750	0.86737	0.01314	-0.84243	-0.48670	0.23117
-0.60967	0.66219	0.43566	0.77021	0.62476	0.12824	0.18727	-0.41374	0.89093
0.21186	0.76503	0.60815	0.57030	-0.60212	0.55876	-0.79365	-0.22845	0.56386
0.25505	-0.15933	0.95371	0.04598	0.98721	0.15263	-0.96583	0.00493	0.25911
-0.55071	-0.78248	0.29060	0.78953	-0.37534	0.48556	-0.27087	0.49684	0.82449
-0.44487	-0.88008	0.16598	-0.80240	0.47399	0.36262	0.39781	-0.02814	0.91704
0.65846	-0.14749	0.73802	-0.08998	0.95815	0.27176	-0.74722	-0.24535	0.61763
0.08926	0.62377	0.77650	-0.06542	-0.77426	0.62948	-0.99386	0.10699	0.02830
-0.58096	-0.32989	0.74409	0.68720	0.29109	0.66560	-0.43617	0.89802	0.05759
-0.35498	0.89674	0.26430	-0.03475	-0.29517	0.95481	0.93423	0.32976	0.13595
0.30372	0.69682	0.64977	0.11228	-0.70341	0.70186	-0.94612	0.14021	0.29187
-0.30792	0.85074	0.42594	-0.15362	-0.48627	0.86020	0.93893	0.19944	0.28042
0.09078	-0.90084	0.42455	-0.44426	0.34491	0.82684	0.89129	0.26367	0.36890
-0.67993	-0.24313	0.69180	-0.15563	0.96979	0.18787	0.71657	-0.02007	0.69722
-0.15455	0.98655	0.05327	0.33682	0.00192	0.94157	-0.92880	-0.16346	0.33258
-0.12204	-0.66377	0.73791	0.04388	0.73913	0.67213	0.99155	-0.11441	0.06108
0.67315	-0.57611	0.46365	0.37483	0.80627	0.45764	-0.63747	-0.13427	0.75869
0.38692	-0.36847	0.84530	-0.70561	-0.70846	0.01416	-0.59364	0.60192	0.53411
-0.22802	0.90685	0.35445	0.64782	-0.13047	0.75054	-0.72687	-0.40076	0.55772
0.52691	0.62161	0.57963	-0.18855	-0.57949	0.79287	-0.82874	0.52706	0.18813
0.25852	-0.96159	0.09232	0.15107	0.13464	0.97931	-0.95412	-0.23922	0.18008
0.48242	0.16432	0.86039	-0.83199	0.39319	0.39140	-0.27398	-0.90466	0.32639
0.13569	-0.87141	0.47141	0.19759	0.49005	0.84901	-0.97085	-0.02206	0.23867
0.17462	0.98257	0.06376	0.31683	-0.11738	0.94119	-0.93227	0.14415	0.33180
-0.17956	0.82835	0.53065	-0.01093	-0.54106	0.84091	0.98369	0.14520	0.10621
0.53104	-0.66984	0.51895	0.50645	0.74192	0.43939	-0.67934	0.02949	0.73323
0.02480	0.82235	0.56844	0.09438	-0.56800	0.81760	-0.99523	-0.03338	0.09170
0.19897	0.49821	0.84392	-0.25301	-0.80583	0.53538	-0.94678	0.32004	0.03428
0.02556	0.89811	0.43902	0.49926	-0.39194	0.77274	-0.86607	-0.19943	0.45841
-0.31595	-0.42071	0.85040	-0.51806	0.82740	0.21686	0.79485	0.37204	0.47937
-0.04067	0.64443	0.76358	-0.34283	-0.72682	0.59515	0.93852	-0.23757	0.25049
0.22432	0.88465	0.40874	-0.97400	0.21720	0.06446	-0.03175	-0.41257	0.91037
-0.63791	0.61744	0.46026	0.45544	-0.17948	0.87199	-0.62101	-0.76587	0.16671
-0.35386	0.09433	0.93053	0.46028	-0.84853	0.26105	0.81420	0.52068	0.25685
0.05979	0.54097	0.83892	0.26897	-0.81807	0.50835	-0.96129	-0.19525	0.19442
-0.26174	0.86331	0.43150	0.13190	-0.41089	0.90209	-0.95608	-0.29302	0.00632
0.01580	-0.85234	0.52276	-0.34114	0.48685	0.80411	0.93988	0.19104	0.28307
0.22511	-0.90094	0.37098	-0.20182	0.32938	0.92238	0.95320	0.28251	0.10768
-0.21418	0.80928	0.54699	-0.73632	-0.50172	0.45400	0.64185	-0.30552	0.70334
0.43866	0.88804	0.13769	0.31791	-0.29666	0.90052	-0.84054	0.35125	0.41245
-0.42777	0.81540	0.39006	0.43961	-0.18938	0.87800	-0.78979	-0.54705	0.27745
0.15459	0.21568	0.96415	0.14935	-0.96977	0.19299	-0.97663	-0.11417	0.18213
0.10412	0.63808	0.76290	0.24578	-0.75978	0.60194	-0.96372	-0.12483	0.23593
-0.32946	0.94370	0.02993	0.10761	0.00603	0.99418	-0.93802	-0.33076	0.10354
-0.07986	0.59927	0.79655	0.00470	-0.79887	0.60149	0.99680	0.05178	0.06098
-0.33681	-0.04560	0.94047	-0.05117	0.99824	0.03007	0.94018	0.03800	0.33855
-0.27405	0.96134	0.02681	0.22393	0.03667	0.97392	-0.93528	-0.27290	0.22532
-0.04583	0.59281	0.80404	0.38184	-0.73336	0.56247	-0.92309	-0.33279	0.19275
0.06394	0.19593	0.97853	0.10567	-0.97636	0.18859	-0.99234	-0.09134	0.08314
-0.03847	0.93242	0.35931	-0.06633	-0.36117	0.93014	0.99706	0.01195	0.07574
0.20415	0.62851	0.75053	0.29186	-0.77089	0.56617	-0.93442	-0.10346	0.34081
0.14942	0.98626	0.07054	0.10581	-0.08688	0.99058	-0.98310	0.14055	0.11734
0.27963	-0.96009	0.00558	0.71495	0.21211	0.66623	-0.64082	-0.18231	0.74573
-0.18033	0.89529	0.40734	-0.38701	-0.44531	0.80742	0.90427	-0.01204	0.42679
-0.04779	0.94117	0.33454	0.24370	-0.31381	0.91768	-0.96867	-0.12538	0.21437
-0.12041	0.23707	0.96400	0.95438	-0.23963	0.17814	-0.27323	-0.94148	0.19740
-0.18608	0.96670	0.17570	-0.05077	-0.18804	0.98085	0.98122	0.17359	0.08407
0.10950	0.90570	0.40954	0.28503	-0.42332	0.85997	-0.95224	-0.02257	0.30450
-0.34319	0.91573	0.20897	0.44548	-0.03717	0.89452	-0.82691	-0.40008	0.39518
-0.12257	0.08578	0.98875	0.07420	-0.99268	0.09532	0.98968	0.08505	0.11531
-0.03261	-0.99527	0.09157	0.52953	0.06050	0.84613	-0.84767	0.07608	0.52505
0.33013	-0.89094	0.31183	-0.00208	0.32966	0.94410	-0.94393	-0.31233	0.10698
0.58854	-0.69157	0.41875	0.58489	0.72180	0.37002	-0.55814	0.02715	0.82930

0.07729	0.04919	0.99579	-0.12390	-0.99057	0.05855	-0.98928	0.12790	0.07047
0.39124	-0.64367	0.65774	-0.45815	0.48362	0.74580	0.79814	0.59313	0.10569
-0.10581	0.43569	0.89386	-0.48577	-0.80700	0.33585	0.86766	-0.39867	0.29703
-0.12068	0.98323	0.13673	0.44926	-0.06873	0.89075	-0.88521	-0.16893	0.43343
-0.12429	0.17545	0.97661	0.47550	-0.85333	0.21382	0.87089	0.49096	0.02263
-0.19580	0.41010	0.89077	0.12016	-0.89148	0.43684	0.97325	0.19257	0.12527
-0.13988	0.99013	0.00854	0.97922	0.13705	0.14951	-0.14686	-0.02928	0.98872
0.41152	0.54815	0.72814	0.44936	-0.81710	0.36115	-0.79293	-0.17858	0.58256
0.36386	-0.91470	0.17588	0.25610	0.27979	0.92527	-0.89555	-0.29163	0.33606
0.27808	0.11950	0.95309	0.36869	-0.92951	0.00897	-0.88698	-0.34890	0.30254
-0.32454	0.81708	0.47650	0.79825	-0.03366	0.60138	-0.50742	-0.57554	0.64132
-0.22141	-0.96972	0.10305	0.58638	-0.04795	0.80862	-0.77919	0.23946	0.57924
0.69015	-0.56041	0.45786	0.62117	0.78336	0.02249	-0.37127	0.26889	0.88874
-0.62459	0.67937	0.38516	0.23525	-0.30661	0.92231	0.74468	0.66667	0.03168

Table 8.12. *Table showing RAW 3D chondrule orientation data Winchcombe L1*

Winchcombe L1 Chondrules								
Major Axis Directional Cosines			**Intermediate Axis Directional Cosines**			**Minor Axis Directional Cosines**		
PEllipsoid X1 (dmls)	**PEllipsoid Y1 (dmls)**	**PEllipsoid Z1 (dmls)**	**PEllipsoid X2 (dmls)**	**PEllipsoid Y2 (dmls)**	**PEllipsoid Z2 (dmls)**	**PEllipsoid X3 (dmls)**	**PEllipsoid Y3 (dmls)**	**PEllipsoid Z3 (dmls)**
-0.77292	-0.23825	0.58807	0.06388	0.89290	0.44571	0.63128	-0.38206	0.67492
-0.91763	-0.12506	0.37724	0.14098	-0.98990	0.01475	0.37159	0.06671	0.92600
0.14679	0.82589	0.54440	-0.61424	-0.35529	0.70462	0.77535	-0.43782	0.45513
0.26725	-0.93156	0.24654	-0.88322	-0.13449	0.44926	0.38536	0.33781	0.85871
-0.66273	0.53975	0.51909	0.66358	0.74453	0.07305	0.34705	-0.39287	0.85159
0.29912	0.95277	0.05247	-0.41930	0.08185	0.90415	0.85716	-0.29245	0.42398
0.07830	0.33604	0.93859	0.71991	-0.67033	0.17994	-0.68964	-0.66161	0.29441
0.22091	-0.33345	0.91652	-0.91144	0.26387	0.31569	0.34710	0.90509	0.24563
0.07238	0.91241	0.40283	-0.52643	-0.30810	0.79243	0.84713	-0.26942	0.45802
-0.65798	-0.60548	0.44772	-0.27641	0.74725	0.60433	0.70047	-0.27388	0.65904
0.38749	0.90644	0.16801	0.85840	-0.42122	0.29279	-0.33617	-0.03077	0.94130
-0.79439	0.05431	0.60497	0.11724	-0.96356	0.24045	0.59598	0.26194	0.75907
0.18196	0.77539	0.60470	-0.35146	-0.52306	0.77646	0.91835	-0.35381	0.17735
-0.00528	0.99847	0.05513	-0.85188	-0.03337	0.52268	0.52372	-0.04421	0.85075
-0.61260	-0.65731	0.43894	-0.39741	0.73619	0.54781	0.68322	-0.16115	0.71221
0.31277	-0.94014	0.13533	0.91323	0.33682	0.22928	-0.26113	0.05187	0.96391
0.20592	0.95624	0.20785	0.58789	-0.29069	0.75491	-0.78229	0.03326	0.62202
0.95112	-0.02331	0.30793	-0.08518	0.93867	0.33415	-0.29683	-0.34404	0.89080
-0.29865	-0.80498	0.51266	-0.62930	0.56995	0.52834	0.71749	0.16482	0.67678
-0.23159	0.93742	0.26004	0.96684	0.19221	0.16816	-0.10765	-0.29036	0.95084
-0.62207	0.47641	0.62134	-0.12613	-0.84419	0.52100	0.77273	0.24573	0.58524
-0.57188	-0.61681	0.54084	0.74365	-0.66813	0.02435	0.34633	0.41612	0.84078
-0.00986	-0.94594	0.32418	-0.66545	0.24820	0.70397	0.74638	0.20878	0.63192
-0.09404	0.82131	0.56268	0.11185	-0.55289	0.82571	-0.98927	-0.14058	0.03987
0.96490	-0.11250	0.23732	-0.15462	-0.97375	0.16703	-0.21230	0.19786	0.95697
0.21495	-0.96517	0.14918	0.96568	0.23285	0.11505	-0.14578	0.11933	0.98209
-0.33482	-0.35212	0.87402	-0.20828	0.93227	0.29579	0.91898	0.08301	0.38548
-0.68856	0.51720	0.50832	0.09878	-0.62754	0.77230	0.71842	0.58198	0.38101
0.47876	0.87786	0.01222	-0.86293	0.46796	0.19072	0.16171	-0.10185	0.98157
-0.72140	0.18376	0.66770	0.46343	-0.58836	0.66262	0.51461	0.78744	0.33928
-0.06625	-0.31468	0.94688	-0.57830	0.78544	0.22057	0.81313	0.53297	0.23402
-0.12336	-0.36634	0.92227	0.94975	0.22582	0.21673	-0.28767	0.90266	0.32007
-0.63214	-0.37807	0.67636	0.19157	0.76954	0.60919	0.75080	-0.51467	0.41403
-0.17081	0.98369	0.05639	-0.16549	-0.08506	0.98254	0.97131	0.15849	0.17731
0.00916	0.28497	0.95849	-0.99996	0.00161	0.00907	0.00104	-0.95854	0.28497
-0.56223	-0.22013	0.79715	0.11573	0.93349	0.33941	0.81885	-0.28308	0.49936
0.83600	-0.54219	0.08448	0.43715	0.75112	0.49468	-0.33167	-0.37662	0.86496
-0.90649	0.36660	0.20948	-0.37119	-0.92838	0.01843	0.20123	-0.06105	0.97764
-0.16335	0.04333	0.98562	0.78094	-0.60481	0.15602	0.60287	0.79519	0.06496
-0.29733	0.04623	0.95366	0.05830	-0.99608	0.06647	0.95299	0.07536	0.29347
-0.17435	0.20130	0.96389	0.95418	0.27631	0.11489	0.24320	-0.93975	0.24025
-0.75207	-0.61474	0.23766	-0.49796	0.76622	0.40614	0.43177	-0.18710	0.88237
0.05258	0.84025	0.53964	-0.80465	-0.28439	0.52121	0.59142	-0.46163	0.66116
-0.28259	0.00561	0.95923	0.04843	0.99879	0.00843	0.95802	-0.04884	0.28252
0.42183	-0.13644	0.89635	-0.76088	0.48436	0.43181	-0.49307	-0.86416	0.10050
-0.01145	-0.90881	0.41705	-0.47397	0.37217	0.79802	0.88047	0.18853	0.43501
-0.27740	0.44961	0.84906	0.94922	0.26477	0.16992	0.14841	-0.85308	0.50023

0.45406	0.86620	0.20863	-0.41906	0.00098	0.90796	0.78627	-0.49970	0.36343
-0.01615	-0.80810	0.58882	0.24263	0.56813	0.78636	-0.96999	0.15557	0.18689
0.08157	-0.92066	0.38174	0.97434	0.15427	0.16387	-0.20976	0.35858	0.90963
-0.07289	0.16472	0.98364	-0.74351	-0.66634	0.05649	0.66474	-0.72723	0.17104
0.30018	0.42857	0.85219	-0.87619	-0.22927	0.42394	0.37707	-0.87394	0.30668
-0.08263	-0.59918	0.79634	0.17771	0.77740	0.60338	-0.98061	0.19137	0.04224
-0.55827	-0.31131	0.76904	0.74077	-0.60447	0.29306	0.37363	0.73328	0.56806
-0.83595	-0.15416	0.52670	0.03931	0.94045	0.33765	0.54739	-0.30297	0.78011
-0.22196	-0.28762	0.93167	0.93819	-0.32327	0.12371	0.26560	0.90154	0.34160
-0.66900	-0.37158	0.64371	0.18774	0.75350	0.63007	0.71916	-0.54237	0.43433
-0.63623	-0.42081	0.64663	0.61686	-0.78085	0.09878	0.46336	0.46173	0.75638
-0.22907	0.53497	0.81322	-0.58011	-0.74590	0.32728	0.78167	-0.39679	0.48120
-0.40041	-0.91391	0.06670	-0.86481	0.40096	0.30223	0.30296	-0.06334	0.95090
0.18123	0.95929	0.21660	-0.92821	0.09408	0.35997	0.32494	-0.26629	0.90747
0.63309	0.77082	0.07098	-0.09981	-0.00965	0.99496	0.76762	-0.63698	0.07083
0.40862	0.60207	0.68596	-0.77571	-0.16694	0.60861	0.48093	-0.78080	0.39882
-0.70056	-0.66137	0.26797	-0.36571	0.65522	0.66102	0.61276	-0.36509	0.70089

***Table 8.13**. Table showing RAW 3D chondrule orientation data Winchcombe L2*

Winchcombe L2 Chondrules								
Major Axis Directional Cosines			Intermediate Axis Directional Cosines			Minor Axis Directional Cosines		
PEllipsoid X1 (dmls)	PEllipsoid Y1 (dmls)	PEllipsoid Z1 (dmls)	PEllipsoid X2 (dmls)	PEllipsoid Y2 (dmls)	PEllipsoid Z2 (dmls)	PEllipsoid X3 (dmls)	PEllipsoid Y3 (dmls)	PEllipsoid Z3 (dmls)
0.25056	-0.67238	0.69651	0.64253	0.65365	0.39987	-0.72414	0.34734	0.59580
0.58785	-0.01101	0.80889	-0.78706	-0.23889	0.56874	-0.18698	0.97098	0.14910
-0.87442	0.41192	0.25633	0.07580	-0.40587	0.91078	0.47921	0.81584	0.32368
0.78860	-0.34519	0.50887	-0.09259	0.75146	0.65325	-0.60789	-0.56227	0.56064
-0.60004	-0.55127	0.57970	0.78382	-0.55002	0.28828	0.15993	0.62736	0.76213
-0.73616	-0.31142	0.60091	0.62202	-0.66126	0.41932	0.26678	0.68246	0.68050
0.80068	0.53969	0.26009	-0.39854	0.15568	0.90384	0.44731	-0.82734	0.33974
0.26988	-0.85752	0.43797	0.93876	0.33552	0.07845	-0.21422	0.38998	0.89556
0.60654	0.74696	0.27232	-0.76582	0.45689	0.45252	0.21360	-0.48302	0.84916
0.75879	-0.58057	0.29525	-0.65131	-0.67238	0.35171	0.00568	0.45917	0.88833
0.67488	-0.71529	0.18138	-0.70397	-0.55037	0.44891	0.22128	0.43065	0.87498
0.94304	-0.31539	0.10588	-0.00215	0.31245	0.94993	-0.33268	-0.89605	0.29397
-0.30230	0.33667	0.89178	0.84339	-0.34149	0.41482	-0.44419	-0.87752	0.18071
-0.11532	0.67959	0.72447	-0.73175	-0.55134	0.40071	0.67174	-0.48392	0.56088
0.20251	0.93490	0.29148	0.33986	-0.34625	0.87442	-0.91841	0.07802	0.38785
-0.88179	-0.42772	0.19875	0.46237	-0.70082	0.54320	-0.09305	0.57088	0.81574
-0.96543	-0.26045	0.01010	0.20148	-0.72114	0.66285	-0.16535	0.64197	0.74869
0.62068	-0.73534	0.27208	-0.43603	-0.03532	0.89924	0.65164	0.67678	0.34255
-0.04862	0.18160	0.98217	0.13369	-0.97330	0.18658	0.98983	0.14038	0.02305
-0.30450	-0.93839	0.16344	-0.57550	0.31798	0.75346	0.75900	-0.13537	0.63686
-0.46649	-0.62792	0.62299	0.77759	0.04458	0.62719	-0.42159	0.77700	0.46747
0.30294	0.56767	0.76549	-0.40284	-0.65167	0.64269	0.86368	-0.50307	0.03126
0.86426	0.42947	0.26194	0.39663	-0.90204	0.17030	-0.30943	0.04329	0.94994
-0.43216	-0.72964	0.52996	0.88869	-0.44441	0.11283	0.15319	0.51973	0.84048
0.51104	0.85935	0.01907	0.05915	-0.05729	0.99660	-0.85752	0.50817	0.08011
0.85317	0.16607	0.49449	-0.51742	0.38963	0.76188	-0.06614	-0.90588	0.41835
-0.20984	-0.85826	0.46836	-0.95316	0.28630	0.09760	0.21785	0.42594	0.87813
-0.76074	0.06132	0.64615	0.05469	-0.98593	0.15795	0.64675	0.15549	0.74669
-0.77042	-0.22994	0.59462	0.32750	-0.94297	0.05968	0.54699	0.24071	0.80179
-0.92456	0.18836	0.33123	0.03462	-0.82415	0.56532	0.37947	0.53413	0.75545
0.12196	-0.47572	0.87110	0.96162	0.27397	0.01499	-0.24578	0.83584	0.49088
0.75194	0.25147	0.60939	-0.23141	-0.76488	0.60117	-0.61728	0.59306	0.51695
0.29677	-0.94207	0.15630	-0.82228	-0.16887	0.54345	0.48557	0.28980	0.82477
-0.42171	0.55636	0.71598	-0.35347	-0.82803	0.43523	0.83500	-0.06954	0.54584
-0.90547	0.21589	0.36541	0.40563	0.69352	0.59539	0.12488	-0.68733	0.71553
0.65848	0.52348	0.54071	-0.55128	-0.15360	0.82006	0.51234	-0.83808	0.18744
0.15318	0.88303	0.44362	-0.98815	0.14149	0.05957	-0.01017	-0.44749	0.89423
0.35885	-0.70879	0.60732	0.10741	0.67770	0.72746	-0.92720	-0.19581	0.31932
0.31133	0.37968	0.87116	-0.49845	-0.71525	0.48987	-0.80909	0.58674	0.03342
0.80271	-0.59588	0.02410	-0.53119	-0.69604	0.48308	0.27108	0.40057	0.87525
0.02647	-0.63543	0.77171	-0.66859	0.56266	0.48622	0.74317	0.52882	0.40994
0.26259	-0.95258	0.15372	-0.56711	-0.02347	0.82331	0.78066	0.30337	0.54638
0.37977	-0.26873	0.88519	-0.75710	-0.64014	0.13047	-0.53159	0.71972	0.44656
-0.32428	0.15784	0.93270	0.88891	-0.28638	0.35752	-0.32354	-0.94502	0.04744
-0.08695	0.96299	0.25513	0.99619	0.08223	0.02914	-0.00708	-0.25669	0.96647
-0.94844	0.21007	0.23736	-0.11616	-0.92710	0.35635	0.29492	0.31040	0.90370
-0.19387	0.89787	0.39527	0.94923	0.06993	0.30671	-0.24774	-0.43467	0.86585

-0.84160	-0.17778	0.51000	0.53998	-0.25734	0.80137	-0.01122	0.94983	0.31257
0.97217	-0.23248	0.02913	-0.23302	-0.94640	0.22366	0.02443	0.22423	0.97423
0.12984	-0.44145	0.88784	0.87210	0.47690	0.10959	-0.47180	0.76005	0.44691
0.22358	-0.74381	0.62989	-0.96480	-0.07706	0.25146	0.13850	0.66394	0.73485
-0.46608	-0.82850	0.31041	-0.86165	0.50470	0.05333	0.20085	0.24261	0.94911
0.74134	-0.66442	0.09470	-0.05121	0.08470	0.99509	-0.66918	-0.74255	0.02877
0.06634	-0.77893	0.62359	0.11626	0.62674	0.77050	-0.99100	0.02138	0.13214
-0.73145	-0.40245	0.55047	-0.13803	0.87793	0.45846	0.66778	-0.25936	0.69771
-0.68998	0.61313	0.38471	-0.15632	-0.64517	0.74788	0.70675	0.45588	0.54100
-0.45205	-0.29823	0.84066	0.15073	0.90336	0.40153	0.87917	-0.30822	0.36341
-0.89047	0.08347	0.44731	0.24241	-0.74491	0.62157	0.38509	0.66192	0.64309
0.31326	-0.37455	0.87269	-0.54458	0.68199	0.48819	-0.77802	-0.62817	0.00967
-0.27318	-0.26528	0.92466	0.93582	-0.29588	0.19159	0.22276	0.91765	0.32908
-0.51570	-0.33958	0.78660	0.85676	-0.20945	0.47128	0.00472	0.91696	0.39895
-0.63607	-0.57122	0.51878	0.65168	-0.03765	0.75756	-0.41320	0.81994	0.39620
-0.74297	-0.58182	0.33087	-0.00729	0.50134	0.86522	0.66928	-0.64043	0.37672
-0.76607	-0.58530	0.26564	0.64083	-0.66342	0.38629	-0.04986	0.46615	0.88330
0.27551	-0.41039	0.86930	-0.95327	-0.00004	0.30211	0.12395	0.91191	0.39122
-0.36478	-0.90431	0.22170	-0.89691	0.40521	0.17709	0.24998	0.13425	0.95890
-0.24377	-0.88509	0.39647	-0.57746	0.46090	0.67388	0.77918	0.06467	0.62346
-0.96294	-0.06745	0.26114	0.20121	-0.82439	0.52905	0.17960	0.56199	0.80741
-0.17920	0.92350	0.33916	0.91080	0.02539	0.41207	-0.37194	-0.38275	0.84568
-0.64043	-0.10258	0.76114	0.56319	-0.73654	0.37461	0.52218	0.66857	0.52947
-0.24814	-0.85016	0.46439	0.96225	-0.27164	0.01687	0.11180	0.45104	0.88547
-0.33663	-0.82347	0.45670	-0.49478	0.56734	0.65827	0.80117	0.00437	0.59842
0.36580	-0.68935	0.62529	-0.01165	0.66841	0.74370	-0.93062	-0.27933	0.23647
0.93683	-0.33311	0.10668	-0.32944	-0.73784	0.58912	0.11752	0.58705	0.80098
-0.17723	-0.78196	0.59760	-0.97298	0.23054	0.01311	0.14802	0.57913	0.80169

8.2.2 2D Orientation Data

Table 8.14. *Table showing 2D orientation data for Lewis cliff (LEW) 85311 and Murchison*

Lewis Cliff 85311	Murchison
Major Axis Angle (relative to top of image)	**Major Axis Angle (relative to top of image)**
164.243	172.53
70.515	50.322
95.203	59.659
96.938	88.198
137.099	72.878
149.9	164.232
173.271	68.425
108.413	113.1
91.591	138.766
174.762	158.914
37.875	3.532
45.484	179.507
101.463	73.153
90.473	163.417
24.054	6.491
78.338	2.675
95.678	151.729
36.529	171.437
85.28	173.845
60.842	139.433
49.517	161.536
87.224	11.486
100.635	17.119
3.108	0.027
179.976	4.001
9.098	179.205
55.447	170.153
111.172	10.672
46.687	177.792
157.477	177.089
164.196	5.129
56.477	6.323
152.86	125.423
59.253	153.157
84.732	5.058
85.322	67.647
168.596	156.907

149.924	5.383
4.474	37.093
163.176	72.168
61.519	159.958
74.583	86.49
74.386	147.707
35.565	179.851
84.795	126.681
150.423	24.531
89.36	170.732
25.697	18.96
11.403	103.807
88.495	36.933
38.42	141.162
141.613	0.283
179.177	5.466
122.938	173.694
109.46	131.804
25.462	18.224
78.502	132.282
72.864	171.486
143.336	137.484
138.705	31.829
84.253	57.03
121.459	57.374
30.565	162.554
112.688	161.849
8.232	45.471
167.243	20.956
19.523	173.673
72.005	128.632
58.237	23.637
162.015	15.668
100.933	2.663
84.96	1.439
41.894	176.519
104.802	25.575
91.545	13.282
14.046	94.355
148.054	19.108
55.59	14.881
80.253	156.191
90.349	27.957
17.771	178.187
162.073	3.725
42.271	32.028
137.104	1.36
92.391	72.437
7.555	24.1
9.572	147.002
61	115.244
32.558	125.834
131.465	3.721
63.469	125.138
156.308	150.151
15.262	135.763
12.997	58.926
104.89	172.858
57.698	109.191
0.978	27.9
17.709	165.898
94.781	161.243
128.031	12.206
46.391	9.602
161.631	163.129
49.909	175.728
0.479	18.284
48.692	115.783
170.441	166.955
51.983	150.741
151.768	104.872
106.15	165.665
37.502	9.407
74.709	157.087
143.417	120.015

28.119	159.443
0.683	175.513
114.311	157.983
103.884	1.13
121.132	151.625
34.544	142.152
47.958	153.306
93.156	160.517
132.035	141.02
2.708	176.385
140.605	20.744
13.052	178.25
20.129	41.306
65.407	16.417
99.444	124.951
44.363	159.615
105.251	65.412
117.424	164.655
110.26	104.333
145.346	103.891
173.135	162.162
-	119.95
-	52.228
-	11.073
-	4.308
-	22.773
-	5.639
-	146.566

8.2.3 Chondrule Shape Data

Table 8.15. Table of chondrule shape characteristics of CM chondrites examined

Sample	Lithology	Chondrule Shape (%)										Total Number of Chondrules
		Compact	Compact Platy	Compact Bladed	Compact Elongate	Platy	Bladed	Elongate	Very Platy	Very Bladed	Very Elongate	
Aguas Zarcas	L1	19 (18.63)	4 (3.92)	36 (35.29	22 (21.57)	1 (0.98)	6 (5.88)	13 (12.75)	0 (0)	0 (0)	1 (0.98)	102
	L2	34 (32.69)	7 (6.73)	24 (23.08)	35 (33.65)	0 (0)	1 (0.96)	3 (2.88)	0 (0)	0 (0)	0 (0)	104
	L3	26 (24.30)	9 (8.41)	30 (28.04)	17 (15.89)	0 (0)	10 (9.35)	15 (14.02)	0 (0)	0 (0)	0 (0)	107
Cold Bokkeveld	L1	31 (32.63)	6 (6.32)	27 (28.42)	16 (16.84)	1 (1.05)	7 (7.37)	7 (7.37)	0 (0)	0 (0)	0 (0)	95
	L2	4 (9.52)	7 (16.67)	13 (30.95)	10 (23.81)	3 (7.14)	5 (11.90)	0 (0)	0 (0)	0 (0)	0 (0)	42
	L3	17 (27.42)	8 (12.90)	17 (27.42)	12 (19.35)	0 (0)	3 (4.84)	4 (6.45)	0 (0)	0 (0)	1 (1.61)	62
LEW 85311	-	52 (33.55)	9 (5.81)	36 (23.23)	39 (25.16)	1 (0.65)	7 (4.52)	11 (7.10)	0 (0)	0 (0)	0 (0)	155
Murchison	-	55 (30.56)	24 (13.33)	42 (23.33)	29 (16.11)	2 (1.11)	9 (5.00)	19 (10.56)	0 (0)	0 (0)	0 (0)	180
Winchcombe	L1	18 (28.13)	5 (7.81)	19 (29.69)	15 (23.44)	1 (1.56)	1 (1.56)	5 (7.81)	0 (0)	0 (0)	0 (0)	64
	L2	16 (21.33)	5 (6.67)	22 (29.33)	16 (21.33)	0 (0)	5 (6.67)	10 (13.33)	0 (0)	0 (0)	1 (1.33)	75

8.2.4 3D Axes Lengths

Table 8.16. *Table showing 3D axis lengths observed in Aguas Zarcas*

Aguas Zarcas L1 Chondrules			Aguas Zarcas L2 Chondrules			Aguas Zarcas L3 Chondrules		
PEllipsoid Rad1 (mm)	PEllipsoid Rad2 (mm)	PEllipsoid Rad3 (mm)	PEllipsoid Rad1 (mm)	PEllipsoid Rad2 (mm)	PEllipsoid Rad3 (mm)	PEllipsoid Rad1 (mm)	PEllipsoid Rad2 (mm)	PEllipsoid Rad3 (mm)
0.464212	0.421541	0.267968	0.188182	0.182235	0.123765	0.242361	0.221444	0.189503
0.548955	0.429849	0.405064	0.242161	0.237414	0.164227	0.17275	0.152279	0.0962169
0.369211	0.299859	0.272146	0.262898	0.193002	0.153844	0.588967	0.391843	0.264984
0.154749	0.0995669	0.0862081	0.186867	0.161344	0.133001	0.172982	0.153514	0.137614
0.127906	0.110909	0.0895915	0.185224	0.15486	0.119207	0.212564	0.112503	0.0773318
0.156593	0.112819	0.0962448	0.155998	0.142021	0.119328	0.122561	0.0945926	0.0789854
0.230558	0.17725	0.139361	0.272713	0.253708	0.167084	0.202205	0.151659	0.120282
0.216417	0.132623	0.110777	0.167617	0.133609	0.0965465	0.128425	0.102127	0.0559763
0.160497	0.102276	0.0898331	0.15523	0.13614	0.119738	0.241105	0.153804	0.10097
0.170613	0.15676	0.129986	0.157583	0.106577	0.0984988	0.154835	0.13614	0.133205
0.329836	0.237563	0.188601	0.200168	0.164515	0.141439	0.170254	0.106326	0.103191
0.164246	0.122124	0.112133	0.190226	0.137624	0.113823	0.1497	0.140126	0.117311
0.252175	0.239443	0.194882	0.300193	0.200689	0.171793	0.101741	0.0815326	0.074647
0.120122	0.103983	0.0795059	0.18559	0.148425	0.097492	0.138873	0.111057	0.106761
0.108949	0.0897673	0.0780142	0.210649	0.144628	0.138359	0.345825	0.19566	0.136104
0.209538	0.122771	0.0838682	0.205323	0.174351	0.152919	0.31647	0.189192	0.131553
0.0852881	0.0621115	0.058428	0.152375	0.110074	0.103119	0.283432	0.200276	0.167404
0.118614	0.103867	0.0779704	0.125589	0.106734	0.0933826	0.134836	0.109777	0.0959967
0.104591	0.0758129	0.0688463	0.223735	0.172379	0.14904	0.344198	0.278454	0.154637
0.18714	0.152624	0.127853	0.174271	0.131749	0.10063	0.173213	0.145347	0.116817
0.408451	0.225139	0.200631	0.143415	0.109764	0.0731324	0.139551	0.135523	0.112192
0.264189	0.235534	0.181781	0.134697	0.111278	0.0912168	0.142266	0.103192	0.0834103
0.205857	0.157804	0.114908	0.231266	0.201005	0.166822	0.21481	0.158343	0.127394
0.203805	0.178828	0.148836	0.145652	0.115553	0.087839	0.158557	0.0899424	0.0822855
0.290014	0.223437	0.142124	0.142614	0.127634	0.10874	0.22314	0.131798	0.105168
0.165496	0.0974014	0.0732646	0.236614	0.146862	0.119558	0.177894	0.145839	0.107946
0.0942395	0.0778102	0.0527667	0.226773	0.15701	0.124677	0.213125	0.161872	0.132053
0.279981	0.263834	0.207802	0.235112	0.125933	0.115839	0.170864	0.122568	0.0972575
0.175581	0.150655	0.111604	0.152862	0.141771	0.132141	0.113814	0.0808739	0.0719977
0.294688	0.205718	0.186913	0.163605	0.116048	0.111961	0.186145	0.164679	0.150393
0.15648	0.121141	0.101801	0.184889	0.122467	0.10364	0.229007	0.145191	0.122375
0.237033	0.119917	0.0983586	0.135357	0.114737	0.0862071	0.183963	0.154739	0.101765
0.185326	0.12156	0.111718	0.285155	0.254687	0.202899	0.161292	0.138233	0.0917619
0.117304	0.112825	0.0907609	0.205419	0.140961	0.132373	0.139161	0.123424	0.119786
0.131792	0.0958678	0.0749343	0.131037	0.130158	0.086369	0.18706	0.145888	0.103796
0.227261	0.1237	0.110762	0.178529	0.122822	0.106651	0.31135	0.2462	0.156284
0.46492	0.391716	0.242731	0.197811	0.146799	0.131426	0.257366	0.167383	0.109461
0.102135	0.0874213	0.076815	0.260789	0.207885	0.173659	0.147038	0.117714	0.100959
0.198398	0.133355	0.100627	0.197773	0.135761	0.127155	0.229147	0.177347	0.10444
0.135038	0.126795	0.114047	0.177112	0.16197	0.131131	0.133614	0.065608	0.0499506
0.407376	0.296119	0.212318	0.20908	0.191324	0.178811	0.161173	0.133539	0.103195
0.199832	0.168134	0.134436	0.131718	0.107025	0.0822882	0.202722	0.187682	0.169744
0.193199	0.116249	0.106613	0.124261	0.122899	0.08915	0.191797	0.157159	0.0922303
0.394317	0.188707	0.17269	0.137122	0.117905	0.101978	0.106653	0.0826213	0.0718588
0.143923	0.10833	0.0918145	0.153546	0.134522	0.110712	0.276819	0.14544	0.127376
0.171046	0.140668	0.117734	0.184901	0.128951	0.109524	0.100795	0.0854757	0.0694155
0.282926	0.188037	0.140941	0.16193	0.126105	0.115422	0.147818	0.130996	0.0777781
0.0782745	0.0611583	0.0531962	0.131925	0.0956098	0.0881357	0.137423	0.0907581	0.0792823
0.236784	0.188037	0.159725	0.124099	0.087454	0.0772328	0.16354	0.149923	0.0893924
0.252139	0.146962	0.107622	0.1226	0.0834522	0.0713435	0.15927	0.148638	0.0959169
0.17374	0.112545	0.0959748	0.24624	0.206434	0.19723	0.205293	0.0979809	0.0868479
0.415499	0.310819	0.277699	0.120226	0.0779287	0.0642788	0.143598	0.113938	0.0813238
0.199356	0.109525	0.0889288	0.182182	0.161531	0.144345	0.180742	0.150411	0.0972662
0.111361	0.0961106	0.0683902	0.126024	0.0997167	0.0971775	0.156257	0.117301	0.0928885
0.513321	0.29922	0.234969	0.215969	0.1758	0.128172	0.148676	0.128673	0.094952
0.168144	0.124002	0.10237	0.182106	0.088202	0.0737091	0.199191	0.143783	0.12715
0.177277	0.127628	0.0873667	0.0877962	0.084768	0.0747293	0.294283	0.168892	0.122106
0.328784	0.157251	0.0863346	0.126116	0.0931826	0.07907	0.256978	0.191082	0.183693
0.116664	0.0989712	0.0822143	0.22997	0.128325	0.119338	0.248205	0.203835	0.164691
0.197197	0.106865	0.100277	0.122268	0.0901277	0.0831125	0.138938	0.110112	0.0972758
0.23566	0.171751	0.125315	0.126684	0.116928	0.0933968	0.189129	0.101025	0.0986966
0.15923	0.118714	0.0859613	0.155206	0.107886	0.0978261	0.193729	0.14499	0.103822
0.140409	0.112831	0.0698603	0.230305	0.205109	0.134982	0.16381	0.129261	0.114401
0.175917	0.0902712	0.0760961	0.130671	0.109339	0.0843854	0.212004	0.207505	0.161647
0.119665	0.110168	0.0862674	0.340379	0.308314	0.265763	0.130066	0.111491	0.0961564

0.229317	0.154535	0.125886	0.166624	0.148827	0.117528	0.145594	0.116372	0.104585
0.0901934	0.0655114	0.0646231	0.14063	0.0993603	0.0760455	0.205673	0.0984983	0.0853313
0.217672	0.123581	0.112958	0.124919	0.0954226	0.0764999	0.166294	0.13718	0.127666
0.149028	0.119279	0.0993988	0.217149	0.151954	0.132756	0.179293	0.123503	0.0769517
0.128996	0.106788	0.0755257	0.12601	0.106737	0.0855143	0.27628	0.179543	0.144389
0.140506	0.118339	0.084146	0.1259	0.110423	0.0840685	0.239346	0.138507	0.115178
0.142332	0.109904	0.0707071	0.0933561	0.0739615	0.0724936	0.178294	0.160499	0.10706
0.110596	0.0848511	0.0662747	0.219882	0.146426	0.11815	0.178024	0.135413	0.104664
0.355516	0.278875	0.218939	0.210526	0.16418	0.128219	0.254115	0.119904	0.0984376
0.278773	0.248586	0.186967	0.131186	0.0934321	0.0668776	0.193726	0.134456	0.105558
0.193285	0.177934	0.141145	0.130819	0.113336	0.078311	0.194968	0.158502	0.123297
0.354588	0.203962	0.170938	0.297418	0.186047	0.129628	0.270002	0.234672	0.212758
0.262107	0.154912	0.100493	0.241996	0.162122	0.126727	0.178291	0.143841	0.109041
0.245854	0.16385	0.14054	0.169133	0.129066	0.114496	0.23763	0.196424	0.13336
0.219032	0.173387	0.135424	0.198189	0.154747	0.142599	0.266717	0.22032	0.160935
0.161833	0.135249	0.109284	0.220679	0.125762	0.118394	0.12427	0.112053	0.106665
0.106317	0.0936801	0.074195	0.24027	0.191209	0.156279	0.22691	0.145869	0.124165
0.21059	0.145686	0.11063	0.133746	0.108603	0.0752193	0.185282	0.143177	0.133363
0.299722	0.20002	0.128459	0.0981649	0.0878108	0.0612226	0.323157	0.227541	0.177985
0.124492	0.0944959	0.0777038	0.199975	0.154475	0.129925	0.14859	0.139373	0.104527
0.129955	0.0978726	0.0845416	0.176578	0.10118	0.0949506	0.141061	0.121962	0.0712617
0.210614	0.158767	0.119256	0.0876012	0.084461	0.0674405	0.333661	0.166431	0.109014
0.182003	0.113838	0.0873325	0.171821	0.134849	0.129286	0.223772	0.134057	0.0925559
0.0949043	0.0852931	0.0802836	0.136187	0.0897324	0.0852859	0.182284	0.121298	0.100055
0.147094	0.139997	0.108368	0.136215	0.104361	0.096207	0.216346	0.18143	0.149948
0.143042	0.105218	0.0999543	0.111813	0.094453	0.0787563	0.164233	0.115685	0.0996986
0.178161	0.141647	0.101902	0.180561	0.152403	0.129433	0.123017	0.11322	0.0881711
0.147215	0.132389	0.0978827	0.196044	0.13514	0.121184	0.202353	0.183701	0.122374
0.155868	0.116095	0.100612	0.232078	0.142342	0.10793	0.220679	0.159095	0.126083
0.166933	0.155019	0.139683	0.150311	0.115483	0.0991971	0.0865693	0.0816126	0.0715674
0.234466	0.174633	0.126189	0.124553	0.113914	0.0927283	0.142115	0.126539	0.105052
0.164507	0.139121	0.134778	0.203786	0.136121	0.114403	0.220245	0.117947	0.0854728
0.251455	0.210042	0.14546	0.219061	0.184222	0.15828	0.149666	0.10451	0.0903178
0.209118	0.182337	0.0969351	0.167492	0.127727	0.1096	0.225812	0.103094	0.0888153
0.15101	0.121651	0.0963015	0.170885	0.137911	0.123587	0.153659	0.113987	0.0861832
0.122452	0.103026	0.0810546	0.171486	0.147819	0.103384	0.223246	0.193638	0.157738
0.172778	0.145761	0.110805	0.156737	0.115299	0.105154	0.206964	0.175785	0.104314
			0.133011	0.119005	0.0945851	0.189363	0.176251	0.161051
			0.136786	0.105344	0.0819296	0.334279	0.229475	0.140966
						0.185423	0.120965	0.0968642
						0.279538	0.186334	0.114374
						0.383861	0.299591	0.244986

Table 8.17. *Table showing 3D axis lengths observed in Cold Bokkeveld*

Cold Bokkeveld L1 Chondrules			Cold Bokkeveld L1 Metal Grains			Cold Bokkeveld L2 Chondrules			Cold Bokkeveld L3 Chondrules		
PEllipsoid Rad1 (mm)	PEllipsoid Rad2 (mm)	PEllipsoid Rad3 (mm)	PEllipsoid Rad1 (mm)	PEllipsoid Rad2 (mm)	PEllipsoid Rad3 (mm)	PEllipsoid Rad1 (mm)	PEllipsoid Rad2 (mm)	PEllipsoid Rad3 (mm)	PEllipsoid Rad1 (mm)	PEllipsoid Rad2 (mm)	PEllipsoid Rad3 (mm)
0.544	0.447	0.398	0.080	0.076	0.061	0.181	0.113	0.111	0.139	0.117	0.100
0.235	0.193	0.183	0.062	0.059	0.055	0.133	0.122	0.068	0.146	0.130	0.114
0.316	0.252	0.151	0.055	0.041	0.035	0.220	0.182	0.118	0.265	0.185	0.155
0.167	0.155	0.142	0.137	0.042	0.035	0.327	0.291	0.164	0.154	0.142	0.130
0.190	0.181	0.159	0.110	0.078	0.070	0.109	0.100	0.087	0.195	0.150	0.108
0.312	0.214	0.136	0.086	0.083	0.069	0.221	0.148	0.095	0.243	0.202	0.186
0.394	0.309	0.232	0.063	0.057	0.048	0.340	0.285	0.208	0.125	0.114	0.086
0.228	0.173	0.141	0.132	0.115	0.098	0.122	0.111	0.078	0.154	0.146	0.114
0.306	0.248	0.150	0.078	0.070	0.059	0.393	0.285	0.195	0.109	0.086	0.076
0.480	0.327	0.264	0.104	0.092	0.063	0.175	0.119	0.115	0.133	0.103	0.094
0.185	0.148	0.101	0.104	0.068	0.049	0.181	0.144	0.093	0.132	0.111	0.100
0.206	0.170	0.118	0.116	0.085	0.076	0.226	0.207	0.123	0.233	0.149	0.131
0.272	0.233	0.168	0.072	0.054	0.033	0.199	0.157	0.132	0.940	0.059	0.047
0.589	0.356	0.284	0.046	0.044	0.040	0.111	0.099	0.076	0.167	0.143	0.098
0.303	0.286	0.216	0.053	0.037	0.034	0.190	0.138	0.104	0.116	0.087	0.066
0.148	0.116	0.091	0.066	0.056	0.042	0.134	0.127	0.111	0.145	0.080	0.071
0.211	0.207	0.112	0.197	0.094	0.068	0.151	0.113	0.097	0.091	0.079	0.062
0.307	0.205	0.187	0.066	0.039	0.030	0.126	0.117	0.084	0.145	0.134	0.095
0.237	0.200	0.187	0.043	0.042	0.038	0.161	0.105	0.073	0.217	0.179	0.130
0.214	0.147	0.145	0.062	0.042	0.031	0.119	0.096	0.082	0.113	0.074	0.071
0.200	0.177	0.127	0.063	0.029	0.027	0.248	0.155	0.138	0.173	0.155	0.153
0.193	0.180	0.142	0.067	0.045	0.034	0.241	0.193	0.147	0.189	0.166	0.154

0.320	0.222	0.171	0.059	0.048	0.043
0.385	0.287	0.274	0.047	0.040	0.023
0.471	0.385	0.302	0.065	0.061	0.031
0.373	0.212	0.182	0.088	0.073	0.054
0.178	0.171	0.123	0.047	0.039	0.036
0.180	0.167	0.151	0.051	0.042	0.023
0.374	0.155	0.130	0.160	0.043	0.032
0.214	0.185	0.171	0.144	0.133	0.072
0.263	0.181	0.146	0.053	0.043	0.038
0.247	0.225	0.143	0.083	0.064	0.050
0.376	0.297	0.239	0.049	0.043	0.039
0.480	0.367	0.292	0.076	0.062	0.058
0.277	0.260	0.223	0.105	0.100	0.096
0.287	0.186	0.160	0.095	0.069	0.045
0.212	0.153	0.121	0.057	0.047	0.042
0.131	0.125	0.106	0.109	0.085	0.079
0.257	0.204	0.154	0.122	0.059	0.047
0.167	0.142	0.115	0.065	0.050	0.040
0.210	0.186	0.146	0.136	0.051	0.039
0.275	0.186	0.168	0.037	0.032	0.022
0.227	0.156	0.128	0.082	0.058	0.044
0.216	0.134	0.113	0.059	0.048	0.043
0.196	0.170	0.144	0.065	0.063	0.058
0.237	0.162	0.114	0.105	0.058	0.051
0.188	0.179	0.142	0.064	0.052	0.047
0.255	0.159	0.113	0.106	0.070	0.057
0.235	0.146	0.114	0.095	0.049	0.045
0.238	0.206	0.194	0.047	0.036	0.030
0.177	0.149	0.119	0.071	0.042	0.030
0.163	0.156	0.118	0.089	0.056	0.042
0.156	0.112	0.093	0.057	0.051	0.049
0.520	0.396	0.372	0.099	0.041	0.031
0.261	0.217	0.186	0.045	0.041	0.030
0.304	0.201	0.183	0.079	0.042	0.026
0.225	0.183	0.139	0.093	0.088	0.084
0.288	0.196	0.159	0.110	0.099	0.078
0.225	0.183	0.124	0.057	0.041	0.027
0.192	0.148	0.088	0.069	0.052	0.043
0.244	0.180	0.125	0.068	0.058	0.055
0.143	0.114	0.103	0.060	0.047	0.037
0.287	0.177	0.136	0.048	0.038	0.027
0.155	0.142	0.112	0.050	0.048	0.044
0.224	0.218	0.158	0.060	0.052	0.048
0.137	0.124	0.101	0.066	0.063	0.062
0.156	0.117	0.092	0.045	0.040	0.034
0.343	0.223	0.184	0.088	0.052	0.040
0.200	0.167	0.114	0.059	0.046	0.040
0.227	0.171	0.133	0.061	0.043	0.035
0.262	0.224	0.184	0.065	0.053	0.046
0.306	0.267	0.140	0.156	0.098	0.092
0.327	0.220	0.161	0.094	0.087	0.077
0.262	0.219	0.209	0.093	0.058	0.038
0.179	0.142	0.125	0.044	0.041	0.037
0.185	0.160	0.128	0.113	0.054	0.039
0.213	0.205	0.172	0.109	0.053	0.039
0.139	0.127	0.106	0.065	0.043	0.041
0.224	0.165	0.115	0.123	0.098	0.082
0.129	0.123	0.100	0.087	0.075	0.043
0.303	0.296	0.256	0.053	0.045	0.034
0.232	0.175	0.137	0.045	0.039	0.037
0.245	0.172	0.102	0.068	0.044	0.034
0.220	0.174	0.131	0.055	0.051	0.046
0.243	0.233	0.159	0.077	0.074	0.058
0.271	0.241	0.192	0.091	0.069	0.062
0.209	0.147	0.126	0.067	0.040	0.031
0.210	0.156	0.110	0.113	0.070	0.038
0.153	0.144	0.114	0.109	0.050	0.039
0.251	0.207	0.144	0.053	0.049	0.048
0.196	0.150	0.133	0.056	0.049	0.044
0.371	0.329	0.226	0.112	0.101	0.076
0.322	0.201	0.156	0.069	0.065	0.033
0.307	0.193	0.170	0.160	0.144	0.059
0.245	0.235	0.183	0.056	0.043	0.041

0.106	0.100	0.069
0.259	0.209	0.102
0.247	0.207	0.121
0.175	0.138	0.109
0.246	0.161	0.094
0.256	0.221	0.128
0.100	0.080	0.068
0.165	0.116	0.086
0.218	0.143	0.137
0.148	0.120	0.076
0.291	0.224	0.189
0.186	0.138	0.115
0.108	0.098	0.083
0.105	0.095	0.089
0.106	0.080	0.071
0.199	0.143	0.098
0.224	0.142	0.118
0.173	0.116	0.093
0.187	0.107	0.097
0.197	0.179	0.122

0.113	0.089	0.075
0.147	0.116	0.087
0.131	0.090	0.076
0.082	0.072	0.055
0.110	0.084	0.078
0.409	0.355	0.221
0.160	0.143	0.109
0.211	0.173	0.138
0.154	0.145	0.124
0.147	0.135	0.085
0.130	0.116	0.077
0.157	0.116	0.109
0.161	0.125	0.101
0.276	0.229	0.211
0.150	0.149	0.114
0.091	0.084	0.060
0.151	0.104	0.082
0.302	0.211	0.158
0.596	0.455	0.320
0.256	0.167	0.107
0.163	0.147	0.102
0.098	0.085	0.069
0.138	0.094	0.086
0.174	0.134	0.132
0.156	0.102	0.093
0.149	0.133	0.087
0.124	0.090	0.078
0.167	0.119	0.081
0.118	0.092	0.087
0.095	0.080	0.057
0.163	0.077	0.073
0.161	0.119	0.083
0.147	0.086	0.064
0.136	0.075	0.065
0.155	0.093	0.082
0.085	0.063	0.055
0.113	0.098	0.092
0.127	0.101	0.085
0.115	0.093	0.065
0.363	0.287	0.144

***Table 8.18**. Table showing 3D axis lengths observed in LEW 85311, Muchison, Winchcombe L1 and Winchcombe L2*

Lewis Cliff 85311 Chondrules			Murchison Chondrules			Winchcombe L1 Chondrules			Winchcombe L2 Chondrules		
PEllipsoid Rad1 (mm)	PEllipsoid Rad2 (mm)	PEllipsoid Rad3 (mm)	PEllipsoid Rad1 (mm)	PEllipsoid Rad2 (mm)	PEllipsoid Rad3 (mm)	PEllipsoid Rad1 (mm)	PEllipsoid Rad2 (mm)	PEllipsoid Rad3 (mm)	PEllipsoid Rad1 (mm)	PEllipsoid Rad2 (mm)	PEllipsoid Rad3 (mm)
0.122	0.099	0.090	0.308	0.289	0.217	0.118	0.087	0.069	0.062	0.048	0.039
0.053	0.051	0.046	0.292	0.209	0.138	0.108	0.088	0.077	0.097	0.068	0.065
0.062	0.048	0.042	0.196	0.129	0.101	0.133	0.074	0.060	0.124	0.096	0.081
0.299	0.224	0.186	0.334	0.188	0.168	0.055	0.038	0.033	0.079	0.068	0.049
0.111	0.080	0.046	0.288	0.250	0.157	0.060	0.051	0.041	0.083	0.054	0.040
0.202	0.105	0.072	0.291	0.247	0.189	0.106	0.082	0.058	0.096	0.081	0.051
0.135	0.113	0.099	0.113	0.105	0.088	0.074	0.063	0.054	0.103	0.052	0.051
0.063	0.059	0.055	0.141	0.125	0.115	0.071	0.052	0.051	0.103	0.087	0.076
0.080	0.059	0.051	0.198	0.143	0.127	0.110	0.090	0.081	0.065	0.058	0.046
0.086	0.067	0.048	0.236	0.129	0.083	0.108	0.058	0.040	0.122	0.095	0.067
0.191	0.162	0.109	0.119	0.114	0.080	0.060	0.056	0.044	0.124	0.095	0.055
0.067	0.054	0.042	0.156	0.120	0.094	0.077	0.075	0.039	0.059	0.057	0.051
0.088	0.061	0.054	0.178	0.153	0.089	0.209	0.148	0.116	0.086	0.082	0.064
0.066	0.043	0.032	0.152	0.120	0.087	0.087	0.057	0.045	0.048	0.038	0.033
0.083	0.064	0.054	0.191	0.127	0.119	0.107	0.092	0.048	0.094	0.056	0.047
0.084	0.049	0.041	0.355	0.247	0.230	0.212	0.165	0.147	0.138	0.091	0.080
0.114	0.067	0.064	0.434	0.200	0.193	0.092	0.067	0.048	0.119	0.105	0.099
0.111	0.074	0.049	0.226	0.205	0.177	0.065	0.062	0.051	0.109	0.088	0.079
0.064	0.051	0.036	0.241	0.164	0.132	0.074	0.071	0.040	0.108	0.107	0.094
0.047	0.036	0.031	0.160	0.137	0.134	0.152	0.130	0.111	0.130	0.056	0.049
0.105	0.091	0.078	0.154	0.131	0.119	0.069	0.048	0.043	0.120	0.100	0.061
0.070	0.055	0.044	0.345	0.316	0.264	0.052	0.046	0.044	0.054	0.041	0.035
0.046	0.037	0.026	0.166	0.108	0.096	0.070	0.056	0.045	0.118	0.111	0.064
0.129	0.063	0.050	0.205	0.173	0.154	0.061	0.046	0.032	0.089	0.050	0.041
0.136	0.117	0.107	0.095	0.075	0.054	0.069	0.049	0.037	0.101	0.091	0.081
0.147	0.128	0.104	0.337	0.174	0.149	0.057	0.042	0.034	0.124	0.086	0.052
0.065	0.058	0.049	0.508	0.377	0.262	0.054	0.049	0.041	0.105	0.087	0.054
0.087	0.066	0.046	0.126	0.107	0.089	0.087	0.061	0.051	0.055	0.053	0.041
0.039	0.032	0.025	0.115	0.086	0.082	0.143	0.089	0.080	0.165	0.095	0.072
0.071	0.058	0.039	0.330	0.291	0.246	0.103	0.083	0.078	0.137	0.112	0.095
0.066	0.055	0.039	0.134	0.128	0.095	0.170	0.104	0.081	0.075	0.054	0.050
0.096	0.065	0.053	0.237	0.202	0.127	0.047	0.041	0.033	0.133	0.101	0.088
0.079	0.057	0.054	0.366	0.203	0.138	0.098	0.075	0.051	0.111	0.083	0.069
0.229	0.139	0.112	0.318	0.150	0.106	0.047	0.038	0.036	0.035	0.034	0.033
0.087	0.082	0.059	0.185	0.144	0.132	0.149	0.109	0.099	0.131	0.122	0.075
0.096	0.062	0.047	0.364	0.320	0.225	0.094	0.066	0.048	0.095	0.088	0.060
0.138	0.102	0.072	0.215	0.134	0.126	0.109	0.070	0.068	0.130	0.062	0.051
0.041	0.029	0.026	0.471	0.291	0.233	0.071	0.067	0.053	0.067	0.055	0.045
0.062	0.050	0.042	0.238	0.224	0.203	0.085	0.055	0.047	0.221	0.193	0.142
0.150	0.127	0.101	0.438	0.358	0.265	0.064	0.064	0.046	0.096	0.075	0.064
0.093	0.076	0.052	0.134	0.115	0.092	0.050	0.039	0.032	0.123	0.081	0.072
0.124	0.098	0.086	0.224	0.156	0.133	0.144	0.083	0.059	0.061	0.055	0.049
0.086	0.060	0.057	0.372	0.314	0.274	0.065	0.064	0.042	0.067	0.053	0.047
0.095	0.093	0.082	0.203	0.143	0.102	0.050	0.041	0.030	0.086	0.069	0.058
0.177	0.114	0.089	0.187	0.171	0.127	0.102	0.074	0.065	0.059	0.049	0.043
0.120	0.084	0.072	0.209	0.134	0.110	0.091	0.074	0.061	0.126	0.088	0.072
0.063	0.059	0.055	0.242	0.210	0.186	0.088	0.062	0.049	0.048	0.043	0.040
0.074	0.072	0.066	0.192	0.154	0.150	0.104	0.069	0.064	0.089	0.073	0.059
0.070	0.062	0.055	0.108	0.096	0.071	0.084	0.073	0.064	0.094	0.073	0.042
0.115	0.080	0.076	0.273	0.241	0.188	0.074	0.063	0.058	0.157	0.096	0.073
0.099	0.077	0.067	0.743	0.307	0.242	0.124	0.109	0.075	0.118	0.098	0.072
0.117	0.087	0.080	0.127	0.116	0.089	0.085	0.054	0.036	0.089	0.077	0.054
0.138	0.098	0.080	0.309	0.230	0.199	0.049	0.044	0.032	0.120	0.074	0.069
0.041	0.035	0.033	0.201	0.100	0.087	0.073	0.047	0.038	0.094	0.062	0.055
0.087	0.062	0.058	0.162	0.158	0.113	0.148	0.072	0.063	0.143	0.096	0.087
0.064	0.057	0.055	0.411	0.393	0.231	0.072	0.066	0.056	0.084	0.067	0.058
0.120	0.103	0.098	0.161	0.119	0.100	0.077	0.060	0.047	0.123	0.104	0.093
0.052	0.051	0.047	0.201	0.152	0.130	0.096	0.082	0.067	0.115	0.098	0.066
0.059	0.051	0.041	0.220	0.144	0.127	0.062	0.059	0.046	0.120	0.095	0.079
0.057	0.051	0.043	0.234	0.196	0.145	0.062	0.047	0.039	0.072	0.052	0.033
0.068	0.047	0.034	0.377	0.206	0.155	0.085	0.066	0.052	0.229	0.212	0.146
0.072	0.054	0.038	0.212	0.144	0.107	0.090	0.063	0.053	0.109	0.068	0.060
0.072	0.052	0.045	0.329	0.274	0.161	0.095	0.065	0.060	0.126	0.086	0.075
0.138	0.093	0.065	0.136	0.091	0.071	0.076	0.054	0.042	0.105	0.087	0.062
0.089	0.084	0.067	0.281	0.213	0.170				0.270	0.121	0.106
0.296	0.108	0.094	0.176	0.159	0.111				0.144	0.116	0.098
0.087	0.061	0.050	0.210	0.142	0.105				0.116	0.077	0.060

0.041	0.039	0.038	0.535	0.429	0.318
0.190	0.085	0.064	0.232	0.194	0.169
0.074	0.058	0.044	0.267	0.266	0.229
0.110	0.099	0.066	0.431	0.387	0.244
0.144	0.112	0.080	0.307	0.203	0.131
0.070	0.058	0.042	0.233	0.193	0.151
0.051	0.045	0.033	0.141	0.127	0.108
0.073	0.058	0.035	0.262	0.158	0.126
0.116	0.078	0.066	0.237	0.178	0.145
0.088	0.082	0.061	0.254	0.196	0.160
0.085	0.067	0.053	0.358	0.227	0.191
0.096	0.082	0.064	0.169	0.160	0.145
0.112	0.058	0.056	0.254	0.221	0.210
0.063	0.060	0.055	0.336	0.268	0.232
0.141	0.122	0.074	0.211	0.179	0.155
0.100	0.068	0.060	0.268	0.208	0.153
0.069	0.054	0.042	1.018	0.524	0.400
0.076	0.057	0.051	0.171	0.143	0.133
0.100	0.067	0.060	0.170	0.143	0.112
0.050	0.040	0.036	0.134	0.103	0.086
0.094	0.050	0.033	0.248	0.184	0.124
0.068	0.059	0.037	0.287	0.182	0.158
0.072	0.056	0.038	0.192	0.148	0.132
0.179	0.126	0.120	0.337	0.271	0.176
0.047	0.041	0.033	0.231	0.165	0.119
0.170	0.136	0.100	0.162	0.143	0.123
0.095	0.080	0.066	0.166	0.132	0.093
0.140	0.122	0.084	0.175	0.142	0.117
0.080	0.079	0.077	0.163	0.116	0.103
0.068	0.061	0.054	0.223	0.190	0.168
0.104	0.076	0.061	0.164	0.122	0.121
0.044	0.039	0.034	0.300	0.187	0.166
0.090	0.075	0.039	0.075	0.070	0.049
0.037	0.035	0.034	0.186	0.161	0.115
0.072	0.064	0.057	0.246	0.219	0.163
0.160	0.106	0.102	0.337	0.316	0.224
0.044	0.041	0.039	0.158	0.102	0.083
0.087	0.063	0.056	0.236	0.164	0.144
0.072	0.054	0.047	0.181	0.141	0.105
0.067	0.065	0.059	0.222	0.184	0.112
0.076	0.064	0.063	0.174	0.131	0.102
0.108	0.087	0.080	0.204	0.202	0.192
0.117	0.110	0.093	0.441	0.317	0.244
0.074	0.065	0.053	0.193	0.150	0.118
0.100	0.092	0.073	0.204	0.181	0.148
0.080	0.058	0.044	0.232	0.179	0.138
0.073	0.057	0.052	0.390	0.294	0.209
0.048	0.045	0.039	0.233	0.195	0.161
0.058	0.054	0.044	0.314	0.276	0.218
0.094	0.092	0.069	0.232	0.227	0.222
0.089	0.069	0.061	0.251	0.143	0.102
0.049	0.042	0.031	0.201	0.173	0.141
0.090	0.063	0.052	0.213	0.146	0.097
0.091	0.064	0.046	0.187	0.161	0.133
0.093	0.056	0.053	0.206	0.143	0.124
0.134	0.121	0.072	0.341	0.176	0.145
0.103	0.076	0.063	0.220	0.207	0.128
0.076	0.054	0.048	0.196	0.161	0.146
0.112	0.080	0.072	0.141	0.100	0.099
0.058	0.049	0.045	0.417	0.248	0.180
0.051	0.044	0.039	0.387	0.249	0.183
0.085	0.059	0.054	0.192	0.163	0.142
0.040	0.036	0.034	0.363	0.290	0.183
0.063	0.047	0.045	0.435	0.284	0.185
0.114	0.073	0.059	0.330	0.255	0.164
0.052	0.046	0.042	0.201	0.171	0.159
0.085	0.065	0.041	0.339	0.250	0.239
0.092	0.071	0.065	0.206	0.172	0.158
0.062	0.060	0.045	0.139	0.138	0.123
0.056	0.038	0.032	0.123	0.102	0.082
0.099	0.073	0.065	0.351	0.330	0.221
0.123	0.081	0.053	0.233	0.213	0.145
0.049	0.044	0.042	0.203	0.125	0.108
0.177	0.157	0.140	0.173	0.153	0.133
0.117	0.090	0.072	0.251	0.200	0.188

0.131	0.114	0.109
0.145	0.132	0.105
0.110	0.084	0.060
0.095	0.090	0.066
0.249	0.126	0.070
0.246	0.099	0.081
0.090	0.059	0.036
0.109	0.088	0.063

0.060	0.058	0.056	0.359	0.347	0.242
0.108	0.096	0.076	0.379	0.182	0.166
0.094	0.077	0.068	0.496	0.343	0.233
0.232	0.134	0.091	0.133	0.113	0.095
0.071	0.069	0.062	0.236	0.135	0.122
0.158	0.097	0.082	0.536	0.296	0.234
0.041	0.040	0.037	0.144	0.112	0.102
0.090	0.081	0.061	0.151	0.114	0.106
0.100	0.086	0.057	0.178	0.152	0.140
0.090	0.065	0.057	0.235	0.208	0.153
0.076	0.057	0.048	0.149	0.092	0.081
0.125	0.075	0.058	0.299	0.282	0.235
0.070	0.060	0.049	0.227	0.191	0.134
			0.286	0.168	0.150
			0.247	0.187	0.144
			0.363	0.225	0.155
			0.238	0.164	0.141
			0.187	0.163	0.104
			0.441	0.273	0.138
			0.164	0.134	0.128
			0.119	0.112	0.085
			0.258	0.180	0.163
			0.218	0.190	0.142
			0.241	0.206	0.110
			0.257	0.230	0.221
			0.189	0.180	0.150
			0.373	0.270	0.197
			0.209	0.173	0.159
			0.223	0.197	0.124
			0.175	0.160	0.120
			0.142	0.124	0.120
			0.214	0.202	0.147
			0.245	0.144	0.115
			0.161	0.140	0.095
			0.193	0.178	0.139
			0.235	0.192	0.174
			0.279	0.222	0.188
			0.544	0.289	0.214

8.2.5 2D Axis Lengths

Table 8.19. *Table of 2D axis lengths of LEW 85311 and Murchison*

Lewis Cliff 85311 Chondrules			Murchison Chondrules		
Major Axis (mm)	**Minor Axis (mm)**	**Aspect Ratio**	**Major Axis (mm)**	**Minor Axis (mm)**	**Aspect Ratio**
0.148	0.113	1.310	0.072	0.059	1.223
0.084	0.059	1.424	0.108	0.059	1.840
0.179	0.127	1.409	0.204	0.148	1.377
0.166	0.145	1.145	0.107	0.080	1.337
0.391	0.341	1.147	0.310	0.250	1.242
0.243	0.136	1.787	0.328	0.225	1.461
0.181	0.108	1.676	0.076	0.068	1.106
0.074	0.051	1.451	0.632	0.498	1.269
0.111	0.073	1.521	0.377	0.223	1.689
0.422	0.291	1.450	0.118	0.097	1.223
0.128	0.111	1.153	0.321	0.285	1.128
0.240	0.125	1.920	0.174	0.085	2.046
0.103	0.085	1.212	0.071	0.066	1.083
0.181	0.160	1.131	0.196	0.095	2.072
0.182	0.174	1.046	0.114	0.081	1.414
0.155	0.121	1.281	0.104	0.090	1.157
0.100	0.081	1.235	0.124	0.102	1.214
0.090	0.072	1.250	0.111	0.061	1.838
0.091	0.072	1.264	0.177	0.117	1.505
0.079	0.070	1.129	0.532	0.380	1.400
0.138	0.131	1.053	0.307	0.138	2.232
0.092	0.063	1.460	0.102	0.076	1.336
0.170	0.120	1.417	0.198	0.122	1.621
0.367	0.203	1.808	0.208	0.175	1.188

0.061	0.056	1.089	0.174	0.102	1.713
0.290	0.157	1.847	0.295	0.187	1.575
0.093	0.085	1.094	0.192	0.089	2.149
0.155	0.133	1.165	0.221	0.148	1.487
0.285	0.148	1.926	0.099	0.070	1.417
0.266	0.155	1.716	0.224	0.108	2.068
0.192	0.165	1.164	0.159	0.105	1.515
0.207	0.157	1.318	0.109	0.099	1.102
0.469	0.242	1.938	0.108	0.088	1.234
0.186	0.185	1.005	0.154	0.087	1.776
0.170	0.100	1.700	0.692	0.456	1.518
0.126	0.112	1.125	0.187	0.125	1.502
0.082	0.056	1.464	0.168	0.147	1.140
1.140	0.606	1.881	0.335	0.167	2.009
0.205	0.152	1.349	0.186	0.155	1.200
0.140	0.103	1.359	0.157	0.124	1.258
0.912	0.815	1.119	0.217	0.187	1.159
0.152	0.110	1.382	0.187	0.098	1.907
0.293	0.156	1.878	0.091	0.074	1.221
0.458	0.297	1.542	0.653	0.498	1.312
0.120	0.077	1.558	0.122	0.096	1.278
0.159	0.115	1.383	0.130	0.105	1.235
0.205	0.153	1.340	0.194	0.168	1.156
0.333	0.302	1.103	0.235	0.107	2.195
0.147	0.125	1.176	0.292	0.261	1.121
0.197	0.155	1.271	0.176	0.161	1.093
0.082	0.067	1.224	0.074	0.042	1.742
0.265	0.150	1.767	0.165	0.107	1.551
0.160	0.139	1.151	0.110	0.092	1.191
0.082	0.074	1.108	0.071	0.059	1.202
0.132	0.067	1.970	0.199	0.174	1.146
0.945	0.781	1.210	0.095	0.073	1.304
0.145	0.113	1.283	0.106	0.073	1.459
0.207	0.158	1.310	0.292	0.186	1.574
0.354	0.246	1.439	0.162	0.093	1.742
0.095	0.092	1.033	0.498	0.337	1.477
0.164	0.123	1.333	0.208	0.169	1.234
0.130	0.106	1.226	0.180	0.145	1.240
0.154	0.132	1.167	0.202	0.188	1.075
0.363	0.224	1.621	0.292	0.223	1.310
0.151	0.130	1.162	0.135	0.103	1.307
0.206	0.107	1.925	0.101	0.067	1.515
0.137	0.105	1.305	0.118	0.105	1.123
0.580	0.396	1.465	0.067	0.055	1.213
0.802	0.694	1.156	0.171	0.110	1.558
0.205	0.123	1.667	0.247	0.191	1.289
0.167	0.119	1.403	0.178	0.144	1.237
0.068	0.060	1.133	0.193	0.130	1.482
0.146	0.114	1.281	0.197	0.119	1.662
0.232	0.130	1.785	0.076	0.070	1.087
0.291	0.226	1.288	0.154	0.126	1.219
0.318	0.287	1.108	0.105	0.074	1.420
0.213	0.200	1.065	0.155	0.119	1.310
0.131	0.101	1.297	0.111	0.055	2.020
0.128	0.096	1.333	0.154	0.146	1.053
0.152	0.109	1.394	0.072	0.064	1.130
0.190	0.140	1.357	0.130	0.064	2.038
0.173	0.152	1.138	0.075	0.062	1.213
0.324	0.208	1.558	0.112	0.082	1.367
0.132	0.104	1.269	0.347	0.179	1.940
0.221	0.174	1.270	0.095	0.062	1.523
0.076	0.061	1.246	0.144	0.121	1.190
0.081	0.066	1.227	0.076	0.056	1.354
0.097	0.072	1.347	0.185	0.172	1.073
0.265	0.097	2.732	0.055	0.049	1.115
0.096	0.077	1.247	0.138	0.080	1.718
0.150	0.101	1.485	0.091	0.073	1.251
0.166	0.129	1.287	0.118	0.061	1.924
0.231	0.219	1.055	0.107	0.080	1.344
0.256	0.220	1.164	0.099	0.091	1.098
0.170	0.169	1.006	0.494	0.381	1.298
0.247	0.219	1.128	0.096	0.080	1.197
0.094	0.076	1.237	0.103	0.088	1.172
0.086	0.079	1.089	0.081	0.046	1.765
0.299	0.160	1.869	0.137	0.077	1.765

0.104	0.087	1.195
0.523	0.393	1.331
0.184	0.135	1.363
0.359	0.225	1.596
0.157	0.073	2.151
0.131	0.093	1.409
0.341	0.307	1.111
0.078	0.060	1.300
0.096	0.081	1.185
0.065	0.055	1.182
0.248	0.225	1.102
0.149	0.112	1.330
0.122	0.095	1.284
0.156	0.146	1.068
0.308	0.266	1.158
0.079	0.060	1.317
0.141	0.099	1.424
0.257	0.241	1.066
0.152	0.127	1.197
0.063	0.058	1.086
0.132	0.085	1.553
0.211	0.171	1.234
0.141	0.104	1.356
0.131	0.099	1.323
0.237	0.178	1.331
0.269	0.263	1.023
0.167	0.121	1.380
0.084	0.075	1.120
0.351	0.308	1.140
0.085	0.065	1.308
0.125	0.116	1.078
0.079	0.076	1.039
0.188	0.158	1.190
0.082	0.072	1.139

0.637	0.504	1.263
0.503	0.363	1.386
0.324	0.203	1.593
0.139	0.072	1.931
0.177	0.130	1.362
0.173	0.155	1.116
0.082	0.065	1.265
0.078	0.073	1.080
0.170	0.130	1.310
0.211	0.118	1.781
0.201	0.145	1.390
0.082	0.075	1.087
0.108	0.098	1.100
0.456	0.310	1.470
0.179	0.090	1.980
0.096	0.071	1.349
0.262	0.172	1.529
0.220	0.173	1.276
0.167	0.147	1.129
0.118	0.061	1.943
0.225	0.159	1.412
0.118	0.086	1.379
0.132	0.096	1.379
0.402	0.252	1.595
0.103	0.070	1.465
0.154	0.110	1.401
0.132	0.099	1.334
0.208	0.193	1.077
0.211	0.120	1.758
0.099	0.086	1.153
0.152	0.117	1.292
0.105	0.090	1.172
0.293	0.153	1.908
0.146	0.117	1.250
0.213	0.119	1.796
0.188	0.111	1.699
0.322	0.245	1.315
0.107	0.065	1.660
0.079	0.063	1.252
0.325	0.167	1.951
0.149	0.135	1.098

List of References

Abdullah A., and Mohammed A. 2018. Scanning Electron Microscopy (SEM): A Review. *Proceedings of 2018 International Conference on Hydraulics and Pneumatics* 77–85.

Adams J., and Mccord T. 1970. Remote sensing of lunar surface mineralogy - Implications from visible and near-infrared reflectivity of Apollo 11 samples. *Geochimica et Cosmochimica Acta Supplement* 1:1937.

Alexander C. M. O. D., Bowden R., Fogel M. L., Howard K. T., Herd C. D. K., and Nittler L. R. 2012. The provenances of asteroids, and their contributions to the volatile inventories of the terrestrial planets. *Science* 337:721–723.

Alexander C. M. O. D., Howard K. T., Bowden R., and Fogel M. L. 2013. The classification of CM and CR chondrites using bulk H, C and N abundances and isotopic compositions. *Geochimica et Cosmochimica Acta* 123:244–260.

Als-Nielsen J., and McMorrow D. 2011. *Elements of Modern X-ray Physics: Second Edition,* John Wiley and Sons.

Amano K. et al. 2023. Reassigning CI chondrite parent bodies based on reflectance spectroscopy of samples from carbonaceous asteroid Ryugu and meteorites. *Science advances* 9:eadi3789.

Ambrose J. 1973. Computerized transverse axial scanning (tomography): II. Clinical application. *British Journal of Radiology* 46:1023–1047.

Amelin Y., Krot A. N., Hutcheon I. D., and Ulyanov A. A. 2002. Lead isotopic ages of chondrules and calcium-aluminum-rich inclusions. *Science* 297:1678–1683.

Arnold J. R., Testa J. P., Friedman P. J., and Kambic G. X. 1983. Computed tomographic analysis of meteorite inclusions. *Science* 219:383–384.

Asphaug E. 2009. Growth and evolution of asteroids. *Annual Review of Earth and Planetary Sciences* 37:413–448.

Asphaug E., Jutzi M., and Movshovitz N. 2011. Chondrule formation by partial accretion of planetesimals. *Lunar and Planetary Science Conference* #1647.

Bazilevskaya G. A. et al. 2008. Cosmic ray induced ion production in the atmosphere. *Space Science Reviews* 137:149–173.

Benito S., Cuervo C., Pöhl F., and Theisen W. 2019. Improvements on the recovery of 3D particle size distributions from 2D sections. *Materials Characterization* 156.

Bennett C. J., Pirim C., and Orlando T. M. 2013. Space-weathering of solar system bodies: A laboratory perspective. *Chemical Reviews* 113:9086–9150.

Bhattacharya S. K., Goswami J. N., and Lal D. 1973. Semiempirical rates of formation of cosmic ray tracks in spherical objects exposed in space: Preatmospheric and postatmospheric depth profiles. *Journal of Geophysical Research* 78:8356–8363.

Birlan M., Popescu M., Irimiea L., Binzel R., Birlan M., Popescu M., Irimiea L., and Binzel R. 2016. M4AST - A Tool for Asteroid Modelling. *DPS* 48:325.17.

Bischoff A., and Schultz L. 2004. Abundance and meaning of regolith breccias among meteorites (abstract). *Meteoritics and Planetary Science* 39.

Bischoff A., Scott E. R. D., Metzler K., and Goodrich C. A. 2006. Nature and origins of meteoritic breccias. In *Meteorites and the Early Solar System II*. pp. 679–712

Bischoff A., Ebert S., Metzler K., and Lentfort S. 2017. Breccia classification of CM chondrites. In *Meteoritical Society*. p. 48149

Bischoff A., Patzek M., Ebert S., Pack A., Kerraouch I., and Zolensky M. E. 2018. A Lage, Light Fragment in the Murchison (CM) Breccia - A Unique, Highly-Metamorphosed Chondrite as a Xenolith in a CM chondrite. *81st Meeting of the Meteoritical Society* Abstract #.

Biswas S. 2000. Solar Energetic Particles. In *Cosmic Perspectives in Space Physics*, 1st ed. Springer, Dordrecht. pp. 233–282

Bland P. A., Collins G. S., Davison T. M., Abreu N. M., Ciesla F. J., Muxworthy A. R., and Moore J. 2014. Pressure-temperature evolution of primordial solar system solids during impact-induced compaction. *Nature Communications* 5.

Bland P. A., and Travis B. J. 2017. Giant convecting mud balls of the early solar system. *Science Advances* 3:e1602514.

Blandford R., and Eichler D. 1987. Particle acceleration at astrophysical shocks: A theory of cosmic ray origin. *Physics Reports* 154:1–75.

Blott S. J., and Pye K. 2001. Gradistat: A grain size distribution and statistics package for the analysis of unconsolidated sediments. *Earth Surface Processes and Landforms* 26:1237–1248.

Boley A. C., and Durisen R. H. 2008. Gravitational Instabilities, Chondrule Formation, and the FU Orionis Phenomenon. *The Astrophysical Journal* 685:1193–1209.

Borovička J., Popova O., and Spurný P. 2019. The Maribo CM2 meteorite fall—Survival of weak material at high entry speed. *Meteoritics and Planetary Science* 54:1024–1041.

Borovička J., Bettonvil F., Baumgarten G., Strunk J., Hankey M., Spurný P., and Heinlein D. 2021. Trajectory and orbit of the unique carbonaceous meteorite Flensburg. *Meteoritics and Planetary Science* 56:425–439.

Boss A. P., and Durisen R. H. 2005. Chondrule-forming Shock Fronts in the Solar Nebula: A Possible Unified Scenario for Planet and Chondrite Formation. *The Astrophysical Journal* 621:L137–L140.

Bottke W. F., Cellino A., Paolicchi P., and Binzel R. P. 2021. An Overview of the Asteroids: In *Asteroids III*. pp. 3–16

Bouvier A., and Wadhwa M. 2010. The age of the Solar System redefined by the oldest Pb–Pb age of a meteoritic inclusion. *Nature Geoscience 2010 3:9* 3:637–641.

Braukmüller N., Wombacher F., Hezel D. C., Escoube R., and Münker C. 2018. The chemical composition of carbonaceous chondrites: Implications for volatile element depletion, complementarity and alteration. *Geochimica et Cosmochimica Acta* 239:17–48.

Brearley A. J. 2006. The Action of Water. *Meteorites and the early solar system II*, 587–624.

Britt D. T., Yeomans D., Housen K., and Consolmagno G. 2002. Asteroid Density, Porosity, and Structure. In *Asteroids III*, edited by Bottke W. F., Cellino A., Paolicchi P., and Binzel R. P. pp. 485–500.

Brown P. G. et al. 2000. The fall, recovery, orbit, and composition of the Tagish Lake meteorite: A new type of carbonaceous chondrite. *Science* 290:320–325.

Brownlee D. E., and Rajan R. S. 1973. Micrometeorite craters discovered on chondrule-like objects from Kapoeta meteorite. *Science* 182:1341–1344.

Bruck Syal M., Michael Owen J., and Miller P. L. 2016. Deflection by kinetic impact: Sensitivity to asteroid properties. *Icarus* 269:50–61.

Brunetto R., Loeffler M. J., Nesvorný D., Sasaki S., and Strazzulla G. 2015. Asteroid surface alteration by space weathering processes. In *Asteroids IV*. University of Arizona Press. pp. 597–616.

Bunch T. E., and Chang S. 1980. Carbonaceous chondrites—II. Carbonaceous chondrite phyllosilicates and light element geochemistry as indicators of parent body processes and surface conditions. *Geochimica et Cosmochimica Acta* 44:1543–1577.

Buratti B. J. et al. 2013. Vesta, vestoids, and the HED meteorites: Interconnections and differences based on Dawn Framing Camera observations. *Journal of Geophysical Research: Planets* 118:1991–2003.

Burbine T. H. 2000. Forging Asteroid-Meteorite Relationships through Reflectance Spectroscopy. Massachusetts Institute of Technology.

Bus S. J., and Binzel R. P. 2002a. Phase II of the small main-belt asteroid spectroscopic survey. A feature-based taxonomy. *Icarus* 158:146–177.

Bus S. J., and Binzel R. P. 2002b. Phase II of the small main-belt asteroid spectroscopic survey. The observations. *Icarus* 158:106–145.

Caffee M. W., Goswami J. N., Hohenberg C. M., and Reedy R. C. 1988. Irradiation records in meteorite. In *Meteorites and the early solar system*, edited by Kerridge J. F., and Matthews M. S. Tuscon: University of Arizona Press. pp. 205–245.

Cain P. M., McSween H. Y., and Woodward N. B. 1986. Structural deformation of the Leoville chondrite. *Earth and Planetary Science Letters* 77:165–175.

Cane H. V., Richardson I. G., and Von Rosenvinge T. T. 2010. The properties of cycle 23 solar energetic proton events. In *AIP Conference Proceedings*. AIP Publishing. pp. 687–690.

Carry B. 2012. Density of asteroids. *Planetary and Space Science* 73:98–118.

Chapman C. R., and Salisbury J. W. 1973. Comparisons of meteorite and asteroid spectral reflectivities. *Icarus* 19:507–522.

Chapman C. R., Morrison D., and Zellner B. 1975. Surface properties of asteroids: A synthesis of polarimetry, radiometry, and spectrophotometry. *Icarus* 25:104–130.

Chapman C. R. 1976. Asteroids as meteorite parent-bodies: the astronomical perspective. *Geochimica et Cosmochimica Acta* 40:701–719.

Chapman C. R. 1996. S-type asteroids, ordinary chondrites, and space weathering: The evidence from Galileo's fly-bys of Gaspra and Ida. *Meteoritics and Planetary Science* 31:699–725.

Charles C. R. J., Robin P. Y. F., Davis D. W., and McCausland P. J. A. 2018. Shapes of chondrules determined from the petrofabric of the CR2 chondrite NWA 801. *Meteoritics & Planetary Science* 53:935–951.

Chizmadia L. J., and Brearley A. J. 2008. Mineralogy, aqueous alteration, and primitive textural characteristics of fine-grained rims in the Y-791198 CM2 carbonaceous chondrite: TEM observations and comparison to ALHA81002. *Geochimica et Cosmochimica Acta* 72:602–625.

Choe W. H., Huber H., Rubin A. E., Kallemeyn G. W., and Wasson J. T. 2010. Compositions and taxonomy of 15 unusual carbonaceous chondrites. *Meteoritics and Planetary Science* 45:531–554.

Clark B. E., Hapke B., Pieters C., and Britt D. 2002. Asteroid Space Weathering and Regolith Evolution. *Asteroids III* 585–600.

Clark B. E. et al. 2010. Spectroscopy of B-type asteroids: Subgroups and meteorite analogs. *Journal of Geophysical Research: Planets* 115.

Connelly J. N., Bizzarro M., Krot A. N., Nordlund Å., Wielandt D., and Ivanova M. A. 2012. The absolute chronology and thermal processing of solids in the solar protoplanetary disk. *Science* 338:651–655.

Connolly H. C., and Jones R. H. 2016a. Chondrules: The canonical and noncanonical views. *Journal of Geophysical Research: Planets* 121:1885–1899.

Consolmagno G. J., Britt D. T., and Macke R. J. 2008. The significance of meteorite density and porosity. *Chemie der Erde* 68:1–29. www.elsevier.de/chemer (Accessed August 24, 2023).

Le Corre L. et al. 2018. Ground-based characterization of Hayabusa2 mission target asteroid 162173 Ryugu: Constraining mineralogical composition in preparation for spacecraft operations. *Monthly Notices of the Royal Astronomical Society* 475:614–623.

Corrigan C. M., Zolensky M. E., Dahl J., Long M., Weir J., Sapp C., and Burkett P. J. 1997. The porosity and permeability of chondritic meteorites and interplanetary dust particles. *Meteoritics and Planetary Science* 32:509–515.

Crozaz G., Pellas P., Bourot-Denise M., de Chazal S. M., Fiéni C., Lundberg L. L., and Zinner E. 1989. Plutonium, uranium and rare earths in the phosphates of ordinary chondrites-the quest for a chronometer. *Earth and Planetary Science Letters* 93:157–169.

Cuzzi J. N., Hogan R. C., Paque J. M., and Dobrovolskis A. R. 2001. Size-selective Concentration of Chondrules and Other Small Particles in Protoplanetary Nebula Turbulence. *The Astrophysical Journal* 546:496–508.

Cuzzi J. N., and Olson D. M. 2017. Recovering 3D particle size distributions from 2D sections. *Meteoritics and Planetary Science* 52:532–545.

Daly R. A. 1946. Origin of the Moon and Its Topography. *Proceedings of the American Philosophical Society* 90:104–119.

DeMeo F. E., Binzel R. P., Slivan S. M., and Bus S. J. 2009. An extension of the Bus asteroid taxonomy into the near-infrared. *Icarus* 202:160–180.

DeMeo F. E., Alexander C. M. O. D., Walsh K. J., Chapman C. R., and Binzel R. P. 2015. The compositional structure of the asteroid belt. In *Asteroids IV*. pp. 13–41.

DeMeo F. E. et al. 2022. Connecting asteroids and meteorites with visible and near-infrared spectroscopy. *Icarus* 380.

Desch S. J., and Cuzzi J. N. 2000. The Generation of Lightning in the Solar Nebula. *Icarus* 143:87–105.

Desch S. J., Ciesla F. J., Hood L. L., and Nakamoto T. 2005. Heating of Chondritic Materials in Solar Nebula Shocks. *Chondrites and the Protoplanetary Disk* 341:849.

Desch S. J., Morris M. A., Connolly H. C., and Boss A. P. 2010. A critical examination of the x-wind model for chondrule and calcium-rich, aluminum-rich inclusion formation and radionuclide production. *Astrophysical Journal* 725:692–711.

Desch S. J., Morris M. A., Connolly H. C., and Boss A. P. 2012. The importance of experiments: Constraints on chondrule formation models. *Meteoritics and Planetary Science* 47:1139–1156.

Dodd R. T. 1965. Preferred orientation of chondrules in chondrites. *Icarus* 4:308–316.

Dodd R. T. 1982. Objects We Call Chondrules. In *Chondrules and their Origins*. Houston: Lunar and Planetary Institute. 15.

Durante M., and Cucinotta F. A. 2011. Physical basis of radiation protection in space travel. *Reviews of Modern Physics* 83.

Ebel D. S., Greenberg M., Rivers M. L., and Newville M. 2009. Three-dimensional textural and compositional analysis of particle tracks and fragmentation history in aerogel. *Meteoritics and Planetary Science* 44:1445–1463.

Eicken H. 1993. Automated image analysis of ice thin sections — instrumentation, methods and extraction of stereological and textural parameters. *Journal of Glaciology* 39:341–352.

Eisenhour D. D. 1996. Determining chondrule size distributions from thin-section measurements. *Meteoritics and Planetary Science* 31:243–248.

Eugster O., Herzog G. F., Marti K., and Caffee M. W. 2006. Irradiation Records , Cosmic-Ray Exposure Ages , and Transfer Times of Meteorites. *Meteorites and the Early Solar System II* 829-851.

Fan Y. et al. 2022. Shidian meteorite, a new fall analog of near-Earth asteroid (101955) Bennu. *Meteoritics and Planetary Science* 57:2192–2215.

Fendrich K. V., and Ebel D. S. 2021. Comparison of the Murchison CM2 and Allende CV3 chondrites. *Meteoritics and Planetary Science* 56:77–95.

Fischer B. E., and Spohr R. 1983. Production and use of nuclear tracks: Imprinting structure on solids. *Reviews of Modern Physics* 55:907–948.

Fleischer R. L., Price P. B., Walker R. M., and Hubbard E. L. 1964. Track registration in various solid-state nuclear track detectors. *Physical Review* 133.

Fleischer R. L., Price P. B., and Walker R. M. 1965a. Solid-State Track Detectors: Applications to Nuclear Science and Geophysics. *Annual Review of Nuclear Science* 15:1–28.

Fleischer R. L., Price P. B., and Walker R. M. 1965b. Tracks of charged particles in solids. *Science* 149:383–393.

Fleischer R. L., Price P. B., and Walker R. M. 1965c. Ion explosion spike mechanism for formation of charged-particle tracks in solids. *Journal of Applied Physics* 36:3645–3652.

Fleischer R. L., Price P. B., and Walker R. M. 1965d. Effects of temperature, pressure, and ionization of the formation and stability of fission tracks in minerals and glasses. *Journal of Geophysical Research* 70:1497–1502.

Fleischer R. L., Price P. B., and Walker R. M. 1975. *Nuclear tracks in solids: principles and applications*. University of California Press.

Floyd C. J., and Lee M. R. 2022. The CIS method: A proposed standardised protocol for measuring and reporting sizes of chondrules and other chondritic objects (abstract# 6087). In *85th Annual Meeting of the Meteoritical Society*.

Flynn G. J., Moore L. B., and Klöck W. 1999. Density and Porosity of Stone Meteorites: Implications for the Density, Porosity, Cratering, and Collisional Disruption of Asteroids. *Icarus* 142:97–105.

Flynn G. J., Durda D. D., Patmore E. B., Clayton A. N., Jack S. J., Lipman M. D., and Strait M. M. 2015. Hypervelocity cratering and disruption of porous pumice targets: Implications for crater production, catastrophic disruption, and momentum transfer on porous asteroids. In *Planetary and Space Science*. pp. 64–76.

Folk R. L., and Ward W. C. 1957. Brazos River bar [Texas]; a study in the significance of grain size parameters. *Journal of Sedimentary Research* 27:3–26.

Forbush S. E. 1946. Three unusual cosmic-ray increases possibly due to charged particles from the sun. *Physical Review* 70:771–772.

Forman L. V. et al. 2016. Hidden secrets of deformation: Impact-induced compaction within a CV chondrite. *Earth and Planetary Science Letters* 452:133–145.

Forman L. V., Daly L., Bland P. A., Benedix G. K., and Corrigan C. 2023. Impacts on the CV parent body: A coordinated, multiscale fabric analysis of the Allende meteorite. *Meteoritics and Planetary Science* 58:529–545.

Friedlander M. 2000. *A Thin Cosmic Rain: Particles from Outer Space*, 2nd ed. Cambridge: Harvard University Press

Friedrich J. M., Wignarajah D. P., Chaudhary S., Rivers M. L., Nehru C. E., and Ebel D. S. 2008. Three-dimensional petrography of metal phases in equilibrated L chondrites-Effects of shock loading and dynamic compaction. *Earth and Planetary Science Letters* 275:172–180.

Friedrich J. M., Weisberg M. K., Ebel D. S., Biltz A. E., Corbett B. M., Iotzov I. V, Khan W. S., and Wolman M. D. 2015. Chondrule size and related physical properties: a compilation and evaluation of current data across all meteorite groups. *Geochemistry* 75:419–443.

Friedrich J. M., Glavin D. P., Rivers M. L., and Dworkin J. P. 2016. Effect of a synchrotron X-ray microtomography imaging experiment on the amino acid content of a CM chondrite. *Meteoritics and Planetary Science* 51:429–437.

Friend P., Hezel D. C., Barrat J. A., Zipfel J., Palme H., and Metzler K. 2018. Composition, petrology, and chondrule-matrix complementarity of the recently discovered Jbilet Winselwan CM2 chondrite. *Meteoritics and Planetary Science* 53:2470–2491.

Fuchs L. H., Olsen E., and Jensen K. J. 1973. Mineralogy, Mineral-Chemistry, and Composition of the Murchison (C2) Meteorite. *Smithsonian Contributions to the Earth Sciences* 1–39.

Fujimura A., Kato M., and Kumazawa M. 1983. Preferred orientation of phyllosilicate [001] in matrix of Murchison meteorite and possible mechanisms of generating the oriented texture in chondrites. *Earth and Planetary Science Letters* 66:25–32.

Fujiwara A. et al. 2006. The rubble-pile asteroid Itokawe as observed by Hayabusa. *Science* 312:1330–1334.

Fujiya W., Sugiura N., Hotta H., Ichimura K., and Sano Y. 2012. Evidence for the late formation of hydrous asteroids from young meteoritic carbonates. *Nature Communications*. 627

Gaffey M. J. 2011. Mineralogy of asteroids. In *AIP Conference Proceedings*. American Institute of PhysicsAIP. pp. 129–169

Garver J. I. 2003. Etching zircon age standards for fission-track analysis. *Radiation Measurements* 37:47–53.

Gerling E., and Levskii L. 1956. On the Origin of the Rare Gases in Stoney Meteorites. *Doklady Akademii Nauk SSSR* 110.

Gleeson L. J., and Axford W. I. 1968. Solar Modulation of Galactic Cosmic Rays. *The Astrophysical Journal* 154:1011.

Gold T. 1955. The Lunar Surface. *Monthly Notices of the Royal Astronomical Society* 115:585.

Goldstein J. I., Newbury D. E., Echlin P., Joy D. C., Fiori C., and Lifshin E. 1992. *Scanning Electron Microscopy and X-ray Microanalysis: a text for Biologists, Materials Scientists, and Geologists.*, Second Edi. New York: Plenum Press

Goldstein J. I., Newbury D. E., R M. J., Ritchie N. W. M., Scott J. H. J., and Joy D. C. 2017. *Scanning Electron Microscopy and X-ray Microanalysis*, Fourth. New York: Springer.

Gooding J. L., and Keil K. 1981. Relative abundances of chondrule primary textural types in ordinary chondrites and their bearing on conditions of chondrule formation. *Meteoritics* 16:17–43.

Goswami J. N., Hutcheon I. D., and MacDougall J. D. 1976. Microcraters and Solar Flare Tracks in Crystals from Carbonaceous Chondrites and Luncar Breccias. *In: Proc. Lunar Science Conference, 7th,* 1:543–562.
Goswami J. N., and Lal D. 1979. Formation of the parent bodies of the carbonaceous chondrites. *Icarus* 40:510–521.
Goswami J. N., and Macdougall J. D. 1983. Nuclear track and compositional studies of olivines in CI and CM chondrites. *Journal of Geophysical Research* 88:755–764.
Goswami J. N., Lal D., and Wilkening L. L. 1984. Gas-rich meteorites: Probes for particle environment and dynamical processes in the inner solar system. *Space Science Reviews* 37:111–159.
Grimm R. E., and Mcsween H. Y. 1989. Water and the thermal evolution of carbonaceous chondrite parent bodies. *Icarus* 82:244–280.
Hamilton V. E. et al. 2019. Evidence for widespread hydrated minerals on asteroid (101955) Bennu. *Nature Astronomy* 3:332–340.
Hanna R. D., Ketcham R. A., and Hamilton V. E. 2012. Inclusion Foliation in Murchison as Revealed by High Resolution X-Ray CT. In *43rd Lunar and Panetary Science Conference*. Houston.
Hanna R. D., Ketcham R. A., Zolensky M., and Behr W. M. 2015. Impact-induced brittle deformation, porosity loss, and aqueous alteration in the Murchison CM chondrite. *Geochimica et Cosmochimica Acta* 171:256–282.
Hanna R. D., and Ketcham R. A. 2017. X-ray computed tomography of planetary materials: A primer and review of recent studies. *Chemie der Erde* 77:547–572.
Hanna R. D., and Ketcham R. A. 2018. Evidence for accretion of fine-grained rims in a turbulent nebula for CM Murchison. *Earth and Planetary Science Letters* 481:201–211.
Hanna R. D., Ketcham R. A., Edey D. R., and O'Connell J. 2022. 3D porosity structure of the earliest solar system material. *Scientific Reports* 12.
Hapke B. 2001. Space weathering from Mercury to the asteroid belt. *Journal of Geophysical Research: Planets* 106:10039–10073.
Harries D., and Wild P. 2017a. Olivine Grains Extracted From the Jbilet Winselwan CM2 Chondrite – A Reference for the Regolith of C-Group Asteroids? In *80th Annual Meeting of the Meteoritical Society 2017*.
Harries D., and Wild P. 2017b. Particle track densities in olivine of the heated Jbilet Winselwan CM2 chondrite: Constraints on regolith heating? In *Hayabusa 2017: 5th Symposium of Solar System Materials*
Harris A. W., and D'Abramo G. 2015. The population of near-Earth asteroids. *Icarus* 257:302–312.
Hasegawa S., Kuroda D., Yanagisawa K., and Usui F. 2017. Follow-up observations for the asteroid catalog using AKARI spectroscopic observations. *Publications of the Astronomical Society of Japan* 69:99–100.
Hassler D. M. et al. 2014. Mars' surface radiation environment measured with the Mars science laboratory's curiosity rover. *Science* 343.
Hewins R. H. 1997. Chondrules. *Annu. Rev. Earth Planet. Sci* 25:61–83. www.annualreviews.org (Accessed January 29, 2020).
Hewins R. H., Connolly H. C., Lofgren G. E., and Libourel G. 2005. Experimental constraints on Chondrule Formation. In *Chondrites and the Protoplanetary Disk*. pp. 1183–1188.
Hewins R. H. et al. 2014. The Paris meteorite, the least altered CM chondrite so far. *Geochimica et Cosmochimica Acta* 124:190–222.

Hezel D. C., Russell S. S., Ross A. J., and Kearsley A. T. 2008. Modal abundances of CAIs: Implications for bulk chondrite element abundances and fractionations. *Meteoritics and Planetary Science* 43:1879–1894.

Hillas A. M. 2005. Can diffusive shock acceleration in supernova remnants account for high-energy galactic cosmic rays? *Journal of Physics G: Nuclear and Particle Physics* 31.

Hodoroaba V. D. 2019. Energy-dispersive X-ray spectroscopy (EDS). In *Characterization of Nanoparticles: Measurement Processes for Nanoparticles*, edited by Hodoroaba V. D., Unger W. E. S., and Shard A. G. Elsevier. pp. 397–417.

Hood L. L. 1998. Thermal processing of chondrule precursors in planetesimal bow shocks. *Meteoritics and Planetary Science* 33:97–107.

Hounsfield G. N. 1995. Computerized transverse axial scanning (tomography): Part I. Description of system. 1973. *The British journal of radiology* 68:H166-72.

Housen K. R., Sweet W. J., and Holsapple K. A. 2018. Impacts into porous asteroids. *Icarus* 300:72–96.

Howard K. T., Benedix G. K., Bland P. A., and Cressey G. 2009. Modal mineralogy of CM2 chondrites by X-ray diffraction (PSD-XRD). Part 1: Total phyllosilicate abundance and the degree of aqueous alteration. *Geochimica et Cosmochimica Acta* 73:4576–4589.

Howard K. T., Benedix G. K., Bland P. A., and Cressey G. 2011. Modal mineralogy of CM chondrites by X-ray diffraction (PSD-XRD): Part 2. Degree, nature and settings of aqueous alteration. *Geochimica et Cosmochimica Acta* 75:2735–2751. www.elsevier.com/locate/gca (Accessed May 25, 2023).

Howard K. T., Alexander C. M. O., Schrader D. L., and Dyl K. A. 2015. Classification of hydrous meteorites (CR, CM and C2 ungrouped) by phyllosilicate fraction: PSD-XRD modal mineralogy and planetesimal environments. *Geochimica et Cosmochimica Acta* 149:206–222.

Hsieh J. 2022. *Computed Tomography: Principles, Design, Artifacts, and Recent Advances, Fourth Edition*, 2nd ed. 1000 20th Street, Bellingham, WA 98227-0010 USA: SPIE.

Huss G. R., Rubin A. E., and Grossman J. N. 2006. Thermal Metamorphism in Chondrites. In *Meteorites and the Early Solar System II*. pp. 567–586.

Jacquet E. 2021. Collisions and compositional variability in chondrule-forming events. *Geochimica et Cosmochimica Acta* 296:18–37.

Jarosewich E. 1990. Chemical analyses of meteorites: A compilation of stony and iron meteorite analyses. *Meteoritics* 25:323–337.

Jaumann R. et al. 2019. Images from the surface of asteroid Ryugu show rocks similar to carbonaceous chondrite meteorites. *Science* 365:817–820.

Jenniskens P. et al. 2012. Radar-enabled recovery of the Sutter's Mill meteorite, a carbonaceous chondrite regolith breccia. *Science* 338:1583–1587.

Johansen A., and Okuzumi S. 2018. Harvesting the decay energy of 26 Al to drive lightning discharge in protoplanetary discs. *Astronomy and Astrophysics* 609:31.

Johnson T. V., and Fanale F. P. 1973. Optical properties of carbonaceous chondrites and their relationship to asteroids. *Journal of Geophysical Research* 78:8507–8518.

Johnson B. C., Bowling T. J., and Melosh H. J. 2014. Jetting during vertical impacts of spherical projectiles. *Icarus* 238:13–22.

Johnson B. C., Minton D. A., Melosh H. J., and Zuber M. T. 2015. Impact jetting as the origin of chondrules. *Nature* 517:339–341.

Johnson B. C., Ciesla F. J., Dullemond C. P., and Melosh H. J. 2018. Formation of Chondrules by Planetesimal Collisions. *Chondrules: Records of Protoplanetary Disk Processes* 343–360.

Jones R. H., Lee T., Connolly Jr. H. C., Love S. G., and Shang H. 2000. Formation of Chondrules and CAIs: Theory VS. Observation. *Protostars and planets IV* 927–962.

Jones R. H. 2012. Petrographic constraints on the diversity of chondrule reservoirs in the protoplanetary disk. *Meteoritics and Planetary Science* 47:1176–1190.

Jones R. H., Villeneuve J., and Libourel G. 2018. Thermal Histories of Chondrules: Petrologic Observations and Experimental Constraints. In *Chondrules: Records of Protoplanetary Disk Processes*, edited by Russell S. S., Connolly Jr. H. C., and Krot A. N. Cambridge University Press. pp. 57–90.

Jourdan F. et al. 2023. Rubble pile asteroids are forever. *Proceedings of the National Academy of Sciences of the United States of America* 120:e2214353120.

Jutzeler M., Proussevitch A. A., and Allen S. R. 2012. Grain-size distribution of volcaniclastic rocks 1: A new technique based on functional stereology. *Journal of Volcanology and Geothermal Research* 239–240:1–11.

Kallemeyn G. W., and Wasson J. T. 1979. Refractory element fractionations among carbonaceous chondrite groups [11]. *Nature* 282:827–829.

Kallemeyn G. W., and Wasson J. T. 1982. The compositional classification of chondrites: III. Ungrouped carbonaceous chondrites. *Geochimica et Cosmochimica Acta* 46:2217–2228.

Kaneko H., Sato K., Ikeda C., and Nakamoto T. 2023. Cooling Rates of Chondrules after Lightning Discharge in Solid-rich Environments. *The Astrophysical Journal* 947:15.

Kastner J., and Heinzl C. 2018. X-Ray Tomography. In *Handbook of Advanced Non-Destructive Evaluation*, edited by Ida N., and Meyendorf N. Cham: Springer, Cham. pp. 1–72.

Keller L. P., and MacKay D. S. 1993. Discovery of vapor deposits in the lunar regolith. *Science* 261:1305–1307.

Keller L. P., and McKay D. S. 1997. The nature and origin of rims on lunar soil grains. *Geochimica et Cosmochimica Acta* 61:2331–2341.

Keller L. P., and Berger E. L. 2014. A transmission electron microscope study of itokawa regolith grains. *Earth, Planets and Space* 66.

Keller L. P., Berger E. L., Zhang S., and Christoffersen R. 2021. Solar energetic particle tracks in lunar samples: A transmission electron microscope calibration and implications for lunar space weathering. *Meteoritics and Planetary Science* 56:1685–1707.

Kerraouch I. et al. 2019. A light, chondritic xenolith in the Murchison (CM) chondrite – Formation by fluid-assisted percolation during metasomatism? *Chemie der Erde* 79.

Kerraouch I. et al. 2021. The polymict carbonaceous breccia Aguas Zarcas: A potential analog to samples being returned by the OSIRIS-REx and Hayabusa2 missions. *Meteoritics and Planetary Science* 56:277–310.

Ketcham R. A., and Carlson W. D. 2001. Acquisition, optimization and interpretation of x-ray computed tomographic imagery: Applications to the geosciences. *Computers and Geosciences* 27:381–400.

Ketcham R. A. 2005a. Computational methods for quantitative analysis of three-dimensional features in geological specimens. *Geosphere* 1:32–41.

Ketcham R. A. 2005b. Three-dimensional grain fabric measurements using high-resolution X-ray computed tomography. *Journal of Structural Geology* 27:1217–1228.

Kieffer S. W. 1971. Shock metamorphism of the Coconino Sandstone at Meteor Crater, Arizona. *Journal of Geophysical Research* 76:5449–5473.

Kimura M., Imae N., Komatsu M., Barrat J. A., Greenwood R. C., Yamaguchi A., and Noguchi T. 2020. The most primitive CM chondrites, Asuka 12085, 12169, and 12236, of subtypes 3.0–2.8: Their characteristic features and classification. *Polar Science* 26:100565.

King T. V. V., and King E. A. 1978. Grain size and petrography of C2 and C3 carbonaceous chondrites. *Meteoritics* 13:47–72.

King T. V. V., and King E. A. 1979. Size frequency distributions of fluid drop chondrules in ordinary chondrites. *Meteoritics* 14:91–96.

King A. J., Russell S. S., Schofield P. F., Humphreys-Williams E. R., Strekopytov S., Abernethy F. A. J., Verchovsky A. B., and Grady M. M. 2018. The alteration history of the Jbilet Winselwan CM carbonaceous chondrite: An analog for C-type asteroid sample return. *Meteoritics & Planetary Science* 54:maps.13224.

King A. J., Bates H. C., Krietsch D., Busemann H., Clay P. L., Schofield P. F., and Russell S. S. 2019. The Yamato-type (CY) carbonaceous chondrite group: Analogues for the surface of asteroid Ryugu? *Chemie der Erde* 79:125531.

King A. J., Bates H. C., Schofield P. F., and Russell S. S. 2021. The Bulk Mineralogy Aand Water Contents Of The Carbonaceous Chondrite Falls Kolang And Tarda. In *52nd Lunar and Planetary Science Conference 2021*.

King A. J. et al. 2022. The Winchcombe meteorite, a unique and pristine witness from the outer solar system. *Science Advances* 8:eabq3925.

van Kooten E. M. M. E., Kubik E., Siebert J., Heredia B. D., Thomsen T. B., and Moynier F. 2022. Metal compositions of carbonaceous chondrites. *Geochimica et Cosmochimica Acta* 321:52–77. http://creativecommons.org/licenses/by/4.0/ (Accessed May 31, 2024).

Krishnaswami S., Lal D., Prabhu N., and Tamhane A. S. 1971. Olivines: Revelation of tracks of charged particles. *Science* 174:287–291.

Krot A. N., Keil K., Scott E. R. D., Goodrich C. A., and Weisberg M. K. 2007. Classification of Meteorites. In *Treatise on Geochemistry*. Pergamon. pp. 1–52.

Krot A. N., Keil K., Scott E. R. D., Goodrich C. A., and Weisberg M. K. 2013. *Classification of Meteorites and Their Genetic Relationships*, 2nd ed. Elsevier Ltd.

Krot A. N., Keil K., Scott E. R. D., Goodrich C. A., and Weisberg M. K. 2014. Classification of Meteorites and Their Genetic Relationships. *Treatise on Geochemistry: Second Edition* 1:1–63.

Krot A. N. 2019. Refractory inclusions in carbonaceous chondrites: Records of early solar system processes. *Meteoritics and Planetary Science* 54:1647–1691.

Kuiper G. P. 1954. On the Origin of the Lunar Surface Features. *Proceedings of the National Academy of Sciences* 40:1096–1112.

Lal D., Muralli A. V., Rajan R. S., Tamhane A. S., Lorin J. C., and Pellas P. 1968. Techniques for proper revelation and viewing of etch-tracks in meteoritic and terrestrial minerals. *Earth and Planetary Science Letters* 5:111–119.

Lal D., and Rajan R. S. 1969. Observations on space irradiation of individual crystals of gas-rich meteorites. *Nature* 223:269–271.

Lal D. 1972. Hard rock cosmic ray archaeology. *Space Science Reviews* 14:3–102.

Lantz C., Brunetto R., Barucci M. A., Fornasier S., Baklouti D., Bourçois J., and Godard M. 2017. Ion irradiation of carbonaceous chondrites: A new view of space weathering on primitive asteroids. *Icarus* 285:43–57.
Lauretta D. S., Nagahara H., and Alexander C. M. O. 2006. Petrology and Origin of Ferromagnesian Silicate Chondrules. In *Meteorites and the Early Solar System II*, edited by Lauretta D. S., and Mcsween Jr. H. Y. University of Arizona Press. pp. 431–460.
Lauretta D. S. et al. 2017. OSIRIS-REx: Sample Return from Asteroid (101955) Bennu. *Space Science Reviews* 212:925–984.
Lauretta D. S. et al. 2019. The unexpected surface of asteroid (101955) Bennu. *Nature* 568:55–60.
Lee M. R., and Smith C. L. 2006. Scanning transmission electron microscopy using a SEM: Applications to mineralogy and petrology. *Mineralogical Magazine* 70:579–590.
Lee M. R., and Ellen R. 2008. Aragonite in the Murray (CM2) carbonaceous chondrite: Implications for parent body compaction and aqueous alteration. *Meteoritics and Planetary Science* 43:1219–1231.
Lee M. R., Lindgren P., and Sofe M. R. 2014. Aragonite, breunnerite, calcite and dolomite in the CM carbonaceous chondrites: High fidelity recorders of progressive parent body aqueous alteration. *Geochimica et Cosmochimica Acta* 144:126–156.
Lee M. R., Cohen B. E., King A. J., and Greenwood R. C. 2019. The diversity of CM carbonaceous chondrite parent bodies explored using Lewis Cliff 85311. *Geochimica et Cosmochimica Acta* 264:224–244.
Lee M. R., Floyd C., Martin P. E., Zhao X., Franchi I. A., Jenkins L., and Griffin S. 2023. Extended time scales of carbonaceous chondrite aqueous alteration evidenced by a xenolith in LaPaz Icefield 02239 (CM2). *Meteoritics and Planetary Science* 58:672–687.
Lentfort S., Bischoff A., Ebert S., and Patzek M. 2020. Classification of CM chondrite breccias—Implications for the evaluation of samples from the OSIRIS-REx and Hayabusa 2 missions. *Meteoritics and Planetary Science* 21:1–21.
Leroux H., Cuvillier P., Zanda B., and Hewins R. H. 2015. GEMS-like material in the matrix of the Paris meteorite and the early stages of alteration of CM chondrites. *Geochimica et Cosmochimica Acta* 170:247–265.
de Leuw S., Rubin A. E., Schmitt A. K., and Wasson J. T. 2009. 53Mn-53Cr systematics of carbonates in CM chondrites: Implications for the timing and duration of aqueous alteration. *Geochimica et Cosmochimica Acta* 73:7433–7442.
Lindgren P., Lee M. R., Sofe M. R., and Zolensky M. E. 2013. Clasts in the CM2 carbonaceous chondrite Lonewolf Nunataks 94101: Evidence for aqueous alteration prior to complex mixing. *Meteoritics and Planetary Science* 48:1074–1090.
Lindgren P., Hanna R. D., Dobson K. J., Tomkinson T., and Lee M. R. 2015. The paradox between low shock-stage and evidence for compaction in CM carbonaceous chondrites explained by multiple low-intensity impacts. *Geochimica et Cosmochimica Acta* 148:159–178.
Lipschutz M. E., and Schultz L. 2014. Chapter 28 – Meteorites. In *Encyclopedia of the Solar System*. pp. 625–655.
Love S. G., Hörz F., and Brownlee D. E. 1993. Target Porosity Effects in Impact Cratering and Collisional Disruption. *Icarus* 105:216–224.

Macke R. J., Consolmagno G. J., and Britt D. T. 2011. Density, porosity, and magnetic susceptibility of carbonaceous chondrites. *Meteoritics and Planetary Science* 46:1842–1862.
Mackinnon I. D. R., and Zolensky M. E. 1984. Proposed structures for poorly characterized phases in C2M carbonaceous chondrite meteorites. *Nature* 309:240–242.
MacPherson G. J. 2007. Calcium–Aluminum-Rich Inclusions in Chondritic Meteorites. *Treatise on Geochemistry* 1–9:1–47.
Malhotra R. 2012. Orbital resonances in planetary systems. *Encyclopedia of Life Support Systems - Celestial Mechanics* 6:31.
Martin P. M., and Mills A. A. 1980. Preferred chondrule orientations in meteorites. *Earth and Planetary Science Letters* 51:18–25.
Matsuoka M. et al. Space weathering acts strongly on the uppermost surface of Ryugu.
Maurette M., Pellas P., and Walker R. M. 1964. Cosmic-ray-induced particle tracks in a meteorite. *Nature* 204:821–823.
Mccord T. B., Adams J. B., and Johnson T. V. 1970. Asteroid Vesta: Spectral reflectivity and compositional implications. *Science* 168:1445–1447.
Mckay D. S., Heiken G., Basu A., Blanford G., Simon S., Reedy R., French B. M., and Papike J. 1991. The Lunar Regolith -. In *Lunar sourcebook : A user's guide to the Moon*, 1st ed., edited by Heiken G., Vaniman D., and French B. M. Cambridge University Press. pp. 285–356.
Meier M. M. M., S G., Maden C., and Busemann H. 2016. Do we have meteorites from the Veritas asteroid break-up event 8Ma ago? (abstract #6291). *Meteoritics & Planelary Science* 51:6291.
Metzler K., Bischoff A., and Stöffler D. 1992. Accretionary dust mantles in CM chondrites: Evidence for solar nebula processes. *Geochimica et Cosmochimica Acta* 56:2873–2897.
Metzler K. 2004. Formation of accretionary dust mantles in the solar nebula: Evidence from preirradiated olivines in CM chondrites. *Meteoritics and Planetary Science* 39:1307–1319.
Metzler K. 2018. From 2D to 3D chondrule size data: Some empirical ground truths. *Meteoritics and Planetary Science* 53:1489–1499.
Metzler K. et al. 2021. The Loongana (CL) group of carbonaceous chondrites. *Geochimica et Cosmochimica Acta* 304:1–31.
Michel R., Leya I., and Borges L. 1996. Production of cosmogenic nuclides in meteoroids: Accelerator experiments and model calculations to decipher the cosmic ray record in extraterrestrial matter. *Nuclear Instruments and Methods in Physics Research, Section B: Beam Interactions with Materials and Atoms* 113:434–444.
Miura H., Nakamoto T., and Doi M. 2008. Origin of three-dimensional shapes of chondrules: I. Hydrodynamics simulations of rotating droplet exposed to high-velocity rarefied gas flow. *Icarus* 197:269–281.
Miyahara M., Edanaga J., Yamaguchi A., Kobayashi T., Sekine T., and Nakamura A. 2021. Chondrule Flattening by Shock Recovery Experiments on Unequilibrated Chondrites. *Journal of Geophysical Research: Planets* 126.
Morbidelli A. 1999. Origin and Evolution of Near Earth Asteroids. *International Astronomical Union Colloquium* 172:39–50.
Morbidelli A., and Michel P. 2014. Origin and Evolution of Near-Earth Objects Origin and Evolution of Near-Earth Objects. 409–422.
Muranushi T. 2010. Dust-dust collisional charging and lightning in protoplanetary discs. *Monthly Notices of the Royal Astronomical Society* 401:2641–2664.

Nakamoto T., Hayashi M. R., Kita N. T., and Tachibana S. 2005. Chondrule-forming Shock Waves in the Solar Nebula by X-Ray Flares. *Chondrites and the Protoplanetary Disk* 341:883.

Nakamura T., Tomeoka K., Sekine T., and Takeda H. 1993. Shock metamorphism of carbonaceous chondrites: textural diversity of experimentally shocked Allende in various conditions. *Meteoritics* 28:408.

Nakamura T. et al. 2011. Itokawa Dust Particles: A Direct Link Between S-Type Asteroids and Ordinary Chondrites. *Science* 333:1113–1116.

Nishiizumi K., Regnier S., and Marti K. 1980. Cosmic ray exposure ages of chondrites, pre-irradiation and constancy of cosmic ray flux in the past. *Earth and Planetary Science Letters* 50:156–170.

Noguchi T. et al. 2011. Incipient space weathering observed on the surface of itokawa dust particles. *Science* 333:1121–1125.

Nordheim T. A., Jasinski J. M., and Hand K. P. 2019. Galactic Cosmic-Ray Bombardment of Europa's Surface. *The Astrophysical Journal* 881:L29.

Oakeshott R. B. S., and Edwards S. F. 1992. On the stereology of ellipsoids and cylinders. *Physica A: Statistical Mechanics and its Applications* 189:208–233.

Okada T. et al. 2020. Highly porous nature of a primitive asteroid revealed by thermal imaging. *Nature* 579:1–5.

Palmer E. E., and Lauretta D. S. 2011. Aqueous alteration of kamacite in CM chondrites. *Meteoritics and Planetary Science* 46:1587–1607.

Partsch P. 1843. Die Meteoriten oder von Himmel gefallenen Stein- und Eisenmassen im K. K. Holfmineraliekabinette zu Wien. *Catalog of Vienna Collection*.

Pellas P., Poupeau G., Lorin J. C., Reeves H., and Audouze J. 1969a. Primitive low-energy particle irradiation of meteoritic crystals. *Nature* 223:272–274.

Pieters C., and McFadden L. 1994. Meteorite and Asteroid Reflectance Spectroscopy: Clues to Early Solar System Processes. *Annual Review of Earth and Planetary Sciences* 22:457–497.

Pieters C. M., Taylor L. A., Noble S. K., Keller L. P., Hapke B., Morris R. V., Allen C. C., McKAY D. S., and Wentworth S. 2000. Space weathering on airless bodies: Resolving a mystery with lunar samples. *Meteoritics and Planetary Science* 35:1101–1107.

Pieters C. M., and Noble S. K. 2016. Space Weathering on Airless Bodies. *Journal of Geophysical Research: Planets* 121:1865–1884.

Pinto G. A., Marrocchi Y., Morbidelli A., Charnoz S., Eugenia Varela M., Soto K., Martínez R., and Olivares F. 2021. Constraints on Planetesimal Accretion Inferred from Particle-size Distribution in CO Chondrites. *The Astrophysical Journal Letters* 917:L25.

Price P. B., and Walker R. M. 1962. Chemical etching of charged-particle tracks in solids. *Journal of Applied Physics* 33:3407–3412.

Price P. B., Hutcheon I. D., Braddy D., MacDougall D., Price P. B., Hutcheon I. D., Braddy D., and MacDougall D. 1975. Track studies bearing on solar-system regoliths. In *6th Lunar and Planetary Conference*. pp. 3449–3469

Ramsay J., Huber M., and Lisle R. 1983. *The Techniques of Modern Structural Geology*, Elsevier Science.

Raymond S. N., Kokubo E., Morbidelli A., Morishima R., and Walsh K. J. 2014. Terrestrial Planet Formation at Home and Abroad. In *Protostars and Planets VI*.

Reddy V., Dunn T. L., Thomas C. A., Moskovitz N. A., and Burbine T. H. 2015. Mineralogy and surface composition of asteroids. In *Asteroids IV*. pp. 43–63

Riebe M. 2012. Cosmic ray tracks in chondritic material with focus on silicate mineral inclusions in chromite. 297.
Roeller K., and Trepmann C. 2010. Stereo32. Institut für Geologie, Ruhr University Bochum, Boc.
Roig F., Nesvorný D., and Ferraz-Mello S. 2002. Asteroids in the 2 : 1 resonance with Jupiter: Dynamics and size distribution. *Monthly Notices of the Royal Astronomical Society* 335:417–431.
Rozitis B. et al. 2020. Asteroid (101955) Bennu's weak boulders and thermally anomalous equator. *Science Advances* 6.
Rubin A. E., and Wasson J. T. 1986. Chondrules in the Murray CM2 meteorite and compositional differences between CM-CO and ordinary chondrite chondrules. *Geochimica et Cosmochimica Acta* 50:307–315.
Rubin A. E. 1989. Size-frequency distributions of chondrules in CO3 chondrites. *Meteoritics* 24:179–189.
Rubin A. E., Trigo-Rodríguez J. M., Huber H., and Wasson J. T. 2007. Progressive aqueous alteration of CM carbonaceous chondrites. *Geochimica et Cosmochimica Acta* 71:2361–2382.
Rubin A. E. 2012. Collisional facilitation of aqueous alteration of CM and CV carbonaceous chondrites. *Geochimica et Cosmochimica Acta* 90:181–194.
Rubin A. E. 2015. An American on Paris: Extent of aqueous alteration of a CM chondrite and the petrography of its refractory and amoeboid olivine inclusions. *Meteoritics and Planetary Science* 50:1595–1612.
Ruzicka A. M., and Hugo R. C. 2018. Electron backscatter diffraction (EBSD) study of seven heavily metamorphosed chondrites: Deformation systematics and variations in pre-shock temperature and post-shock annealing. *Geochimica et Cosmochimica Acta* 234:115–147.
Sahagian D. L., and Proussevitch A. A. 1998. 3D particle size distributions from 2D observations: stereology for natural applications. *Journal of Volcanology and Geothermal Research* 84:173–196.
Schindelin J. et al. 2012. Fiji: an open-source platform for biological-image analysis. *Nature Methods 2012 9:7* 9:676–682.
Schmitt-Kopplin P., Gabelica Z., Gougeon R. D., Fekete A., Kanawati B., Harir M., Gebefuegi I., Eckel G., and Hertkorn N. 2010. High molecular diversity of extraterrestrial organic matter in Murchison meteorite revealed 40 years after its fall. *Proceedings of the National Academy of Sciences of the United States of America* 107:2763–2768.
Van Schmus W. R., and Wood J. A. 1967. A chemical-petrologic classification for the chondritic meteorites. *Geochimica et Cosmochimica Acta* 31:747.
Scott E. R. D., Keil K., and Stöffler D. 1992. Shock metamorphism of carbonaceous chondrites. *Geochimica et Cosmochimica Acta* 56:4281–4293. https://linkinghub.elsevier.com/retrieve/pii/001670379290268N (Accessed June 17, 2020).
Scott E. R. D., and Krot A. N. 2013. Chondrites and Their Components. In *Treatise on Geochemistry: Second Edition*. Elsevier. pp. 65–137
Shanmugaraju A., Vijayalakshmi P., Lawrance M. B., Moon Y. J., and Ebenezer E. 2023. Solar active region magnetic parameters and their relationship with the properties of halo coronal mass ejections. *Journal of Atmospheric and Solar-Terrestrial Physics* 249:106106.
Shen W., Liang Z., Zou T., Yang Z., Hou W., Zhou M., and Gong J. 2022. A Review of Research on Grove Mountains CM-Type Chondrites. *Minerals* 12:619.

Shu F. H., Shang H., and Lee T. 1996. Toward an astrophysical theory of chondrites. *Science* 271:1545–1552.
Shu F. H., Shang H., Glassgold A. E., and Lee T. 1997. X-rays and fluctuating x-winds from protostars. *Science* 277:1475–1479.
Shu F. H., Shang H., Gounelle M., Glassgold A. E., and Lee T. 2001. The Origin of Chondrules and Refractory Inclusions in Chondritic Meteorites. *The Astrophysical Journal* 548:1029–1050.
Simpson J. A. 1983. Elemental and Isotopic composition of the Galactic Cosmic Rays. *Ann. Rev. Nucl. Part. Sci* 33:323–381.
Sneed E. D., and Folk R. L. 1958. Pebbles in the Lower Colorado River, Texas a Study in Particle Morphogenesis. *The Journal of Geology* 66:114–150.
Sneyd D. S., McSween H. Y., Sugiura N., Strangway D. W., and Nord G. L. 1988. Origin of Petrofabrics and Magnetic Anisotropy in Ordinary Chondrites. *Meteoritics* 23:139–149.
Snickt G. van der. 2012. James Ensor's Pigments Studied by Means of Portable and Synchrotron. University of Antwerp
Stacey F. D., Lovering J. F., and Parry L. G. 1961. Thermomagnetic properties, natural magnetic moments, and magnetic anisotropies of some chondritic meteorites. *Journal of Geophysical Research* 66:1523–1534.
Stöffler D., Bischoff A., Buchwald V., and Rubin A. E. 1988. Shock Effects in Meteorites. In *Meteorites and the Early Solar System*, edited by Kerridge J. F., and Matthews M. S. University of Arizona Press. pp. 165–202.
Stöffler D., Keil K., and Scott E. 1991. shock metamorphism of ordinary chondrites. *Geochimica et Cosmochimica Acta* 55:3845–3867.
Stöffler D., Hamann C., and Metzler K. 2018. Shock metamorphism of planetary silicate rocks and sediments: Proposal for an updated classification system. *Meteoritics and Planetary Science* 53:5–49.
Sugita S. et al. 2013. Visible Spectroscopic Observations of Asteroid 162173 (1999 JU3) with the Gemini-S Telescope. *44th Lunar and Planetary Science Conference* 162173:LPSC-2013-1486.
Suttle M. D., Genge M. J., and Russell S. S. 2017. Shock fabrics in fine-grained micrometeorites. *Meteoritics and Planetary Science* 52:2258–2274.
Suttle M. D., Greshake A., King A. J., Schofield P. F., Tomkins A., and Russell S. S. 2021a. The alteration history of the CY chondrites, investigated through analysis of a new member: Dhofar 1988. *Geochimica et Cosmochimica Acta* 295:286–309.
Suttle M. D., King A. J., Schofield P. F., Bates H., and Russell S. S. 2021b. The aqueous alteration of CM chondrites, a review. *Geochimica et Cosmochimica Acta* 299:219–256.
Suttle M. D. et al. 2022. The Winchcombe meteorite—A regolith breccia from a rubble pile CM chondrite asteroid. *Meteoritics and Planetary Science*.
Swindle T. D., Davis A. M., Hohenberg C. M., MacPherson G., and Nyquist L. E. 1996. Formation times of chondrules and Ca-Al-rich inclusions: constraints from short-lived radionuclides. In *Chondrules and the Protoplanetary Disk*, edited by Hewins R. H., Jones R. H., and Ed Scott. Cambridge. pp. 77–86.
Tedesco E. F., and Desert F.-X. 2002. The Infrared Space Observatory Deep Asteroid Search. *The Astronomical Journal* 123:2070–2082.
Teitler S. A., Paque J. M., Cuzzi J. N., and Hogan R. C. 2011. Statistical Tests of Chondrule Sorting.
The Meteoritical Society. 2023. Meteoritical Bulletin: Search the Database. https://www.lpi.usra.edu/meteor/ (Accessed November 1, 2023).
Tholen D. James. 1984. Asteroid Taxonomy From Cluster Analysis of Photometry.

Tomeoka K., and Buseck P. R. 1985. Indicators of aqueous alteration in CM carbonaceous chondrites: Microtextures of a layered mineral containing Fe, S, O and Ni. *Geochimica et Cosmochimica Acta* 49:2149–2163.

Tomeoka K., Yamahana Y., and Sekine T. 1999. Experimental shock metamorphism of the Murchison CM carbonaceous chondrite. *Geochimica et Cosmochimica Acta* 63:3683–3703.

Trigo-Rodríguez J. M., Rimola A., Tanbakouei S., Soto V. C., and Lee M. 2019. Accretion of Water in Carbonaceous Chondrites: Current Evidence and Implications for the Delivery of Water to Early Earth. *Space Science Reviews* 215.

Trigo-Rodriguez J. M., Rubin A. E., and Wasson J. T. Non-nebular origin of dark mantles around chondrules and inclusions in CM chondrites.

Tsuchiyama A., Shigeyoshi R., Kawabata T., Nakano T., Uesugi K., and Shirono S. 2003. Three-dimensional structures of chondrules and their high-speed rotation. *Lunar Planet. Sci. Conf. XXXIV* 1271.

Tsuda Y. et al. 2022. Mission Objectives, planning, and achievments of Hayabusa2. In *Hayabusa2 Asteroid Sample Return Mission*, edited by Hirabayashi M., and Tsuda Y. Elsevier. pp. 5–23.

Urey H. C. 1952. Chemical fractionation in the meteorites and the abundance of the elements. *Geochimica et Cosmochimica Acta* 2:269–282.

Urey H. C. 1967. Parent bodies of the meteorites and the origin of chondrules. *Icarus* 7:350–359.

Vacher L. G., Marrocchi Y., Villeneuve J., Verdier-Paoletti M. J., and Gounelle M. 2018. Collisional and alteration history of the CM parent body. *Geochimica et Cosmochimica Acta* 239:213–234.

Vacher L. G., Piani L., Rigaudier T., Thomassin D., Florin G., Piralla M., and Marrocchi Y. Hydrogen in chondrites: Influence of parent body alteration and atmospheric contamination on primordial components.

Vilas F., and Gaffey M. J. 1989. Phyllosilicate absorption features in main-belt and outer-belt asteroid reflectance spectra. *Science* 246:790–792.

Vilas F. 2008. Spectral characteristics of Hayabusa 2 near-Earth asteroid targets 162173 1999 JU3 and 2001 QC34. *Astronomical Journal* 135:1101–1105.

Vinegar H. J., and Wellington S. L. 1987. Tomographic imaging of three-phase flow experiments. *Review of Scientific Instruments* 58:96–107.

Visser R., John T., Whitehouse M. J., Patzek M., and Bischoff A. 2020. A short-lived 26Al induced hydrothermal alteration event in the outer solar system: Constraints from Mn/Cr ages of carbonates. *Earth and Planetary Science Letters* 547:116440.

Vogt S., Herzog G. F., and Reedy R. C. 1990. Cosmogenic nuclides in extraterrestrial materials. *Reviews of Geophysics* 28:253.

W. C. Krumbein. 1936. Application of Logarithmic Moments to Size Frequency Distributions of Sediments. *SEPM Journal of Sedimentary Research* Vol. 6:35–47.

Walsh K. J., Morbidelli A., Raymond S. N., O'brien D. P., and Mandell A. M. 2011. A low mass for Mars from Jupiter's early gas-driven migration.

Walsh K. J., Morbidelli A., Raymond S. N., O'Brien D. P., and Mandell A. M. 2012. Populating the asteroid belt from two parent source regions due to the migration of giant planets-"The Grand Tack". *Meteoritics and Planetary Science* 47:1941–1947.

Wasson J. T., Krot A. N., Lee M. S., and Rubin A. E. 1995. Compound chondrules. *Geochimica et Cosmochimica Acta* 59:1847–1869.

Watanabe S. ichiro, Tsuda Y., Yoshikawa M., Tanaka S., Saiki T., and Nakazawa S. 2017. Hayabusa2 Mission Overview. *Space Science Reviews* 208:3–16.

Weidenschilling S. J., Marzari F., and Hood L. L. 1998. The origin of chondrules at Jovian resonances. *Science* 279:681–684.

Weisberg M. K., Mccoy T. J., and Krot A. N. 1988. Systematics and Evaluation of Meteorite Classification. In *Meteorites and the early solar system*

Weisberg M. K., McCoy T. J., and Krot A. N. 2006. Systematics and Evaluation of Meteorite Classification. In *Meteorites and the early solar system II*, edited by Lauretta D. S., and McSween H. Y. University of Arizona Press. pp. 19–52

Wellington S. L., and Vinegar H. J. 1987. X-Ray Computerized Tomography. *JPT, Journal of Petroleum Technology* 39:885–898.

Whipple F. L. 1966. A Suggestion as to the Origin of sundae. *Science* 153:54–56.

Wlotzka F. 1983. Composition of Chondrules , Fragments and Matrix in the Unequilibrated Ordinary Chondrites Tieschitz and Sharps. In *Chondrules and their Origins*. pp. 296–318.

Wlotzka F. 1993. A weathering scale for the ordinary chondrites. *Meteoritics* 28:460.

Wolfendale A., and Erlykin A. 2014. Understanding galactic cosmic rays. *Astroparticle Physics* 53:115–119.

Woodcock N. H., and Naylor M. A. 1983. Randomness testing in three-dimensional orientation data. *Journal of Structural Geology* 5:539–548.

Wurm G., Teiser J., Bischoff A., Haack H., and Roszjar J. 2010. Experiments on the photophoretic motion of chondrules and dust aggregates-Indications for the transport of matter in protoplanetary disks. *Icarus* 208:482–491.

Yada T. et al. 2022. Preliminary analysis of the Hayabusa2 samples returned from C-type asteroid Ryugu. *Nature Astronomy* 6:214–220.

Yang X., Hanna R. D., Davis A. M., Neander A. I., and Heck P. R. 2022. A record of post-accretion asteroid surface mixing preserved in the Aguas Zarcas meteorite. *Nature Astronomy* 6:1051–1058.

Yokoyama T. et al. 2023. Samples returned from the asteroid Ryugu are similar to Ivuna-type carbonaceous meteorites. *Science (New York, N.Y.)* 379:eabn7850.

Yoshikawa M., Kawaguchi J., Fujiwara A., and Tsuchiyama A. 2021. The Hayabusa mission. In *Sample Return Missions*, edited by Longobardo A. Elsevier. pp. 123–146.

Zanda B. 2004. Chondrules. *Earth and Planetary Science Letters* 224:1–17.

Zanetta P. M., Leroux H., Le Guillou C., Zanda B., and Hewins R. H. 2021. Nebular thermal processing of accretionary fine-grained rims in the Paris CM chondrite. *Geochimica et Cosmochimica Acta* 295:135–154.

Zanetta P. M., Le Guillou C., Leroux H., Zanda B., Hewins R., and Bellino G. 2022. Processes and temperatures of FGR formation in chondrites. *Geochimica et Cosmochimica Acta* 319:94–117.

Zega T. J., and Buseck P. R. 2003. Fine-grained-rim mineralogy of the Cold Bokkeveld CM chondrite. *Geochimica et Cosmochimica Acta* 67:1711–1721.

Zellner B., Tholen D. J., and Tedesco E. F. 1985. The eight-color asteroid survey: Results for 589 minor planets. *Icarus* 61:355–416.

Zhou W., Apkarian R., Wang Z. L., and Joy D. 2007. Fundamentals of scanning electron microscopy (SEM). In *Scanning Microscopy for Nanotechnology: Techniques and Applications*, edited by Zhou W., and Wang Z. L. Springer. pp. 1–40.

Zolensky M. E., Mittlefehldt D. W., Lipschutz M. E., Wang M. S., Clayton R. N., Mayeda T. K., Grady M. M., Pillinger C., and Barber D. 1997. CM chondrites exhibit the complete petrologic range from type 2 to 1. *Geochimica et Cosmochimica Acta* 61:5099–5115.